COMPACTION EFFECTS ON UNIFORMITY, MOISTURE DIFFUSION, AND MECHANICAL PROPERTIES OF ASPHALT PAVEMENTS

A Dissertation

by

EMAD ABDEL-RAHMAN KASSEM

Submitted to the Office of Graduate Studies of
Texas A&M University
in partial fulfillment of the requirements for the degree of

DOCTOR OF PHILOSOPHY

December 2008

Major Subject: Civil Engineering

COMPACTION EFFECTS ON UNIFORMITY, MOISTURE DIFFUSION, AND MECHANICAL PROPERTIES OF ASPHALT PAVEMENTS

A Dissertation

by

EMAD ABDEL-RAHMAN KASSEM

Submitted to the Office of Graduate Studies of
Texas A&M University
in partial fulfillment of the requirements for the degree of

DOCTOR OF PHILOSOPHY

Approved by:

Chair of Committee,	Eyad Masad
Committee Members,	Robert Lytton
	Amy Epps Martin
	Ibrahim Karaman
Head of Department,	David Rosowsky

December 2008

Major Subject: Civil Engineering

ABSTRACT

Compaction Effects on Uniformity, Moisture Diffusion, and Mechanical Properties of Asphalt Pavements. (December 2008)

Emad Abdel-Rahman Kassem, B.S., Zagazig University, Egypt;

M.S., Texas A&M University

Chair of Advisory Committee: Dr. Eyad Masad

Field compaction of asphalt mixtures is an important process that influences performance of asphalt pavements; however there is very little effort devoted to evaluate the influence of compaction on the uniformity and properties of asphalt mixtures. The first part of this study evaluated relationships between different field compaction patterns and the uniformity of air void distribution in asphalt pavements. A number of projects with different asphalt mixture types were compacted, and cores were taken at different locations from these projects. The X-ray Computed Tomography (X-ray CT) system was used to capture the air void distributions in these cores. The analysis results have revealed that the uniformity of air void distribution is highly related to the compaction pattern and the sequence of different compaction equipment. More importantly, the efficiency of compaction (reducing air voids) at a point was found to be a function of the location of this point with respect to the compaction roller width. The results in this study supported the development of the "Compaction Index (CI)," which quantifies the degree of field compaction. The CI is a function of the number of passes at a point and the position of the point with respect to the compaction roller width. This index was found to correlate reasonably well with percent air voids in the pavement. The CI calculated from field compaction was also related to the slope of the compaction curve obtained from the Superpave gyratory compactor. This relationship offers the opportunity to predict field compactability based on laboratory measurements. The compaction of longitudinal joints was investigated, and recommendations were put forward to improve joint compaction. The air void distributions in gyratory specimens were related to the mixture mechanical properties measured using the Overlay and Hamburg tests.

The second part of this study focused on studying the relationship between air void distribution and moisture diffusion. A laboratory test protocol was developed to measure the diffusion coefficient of asphalt mixtures. This important property has not measured before. The results revealed that the air void phase within the asphalt mixtures controls the rate of moisture diffusion. The measured diffusion coefficients correlated well with the percent and size of connected air voids. The measured diffusion coefficient is a necessary parameter in modeling moisture transport and predicting moisture damage in asphalt mixtures.

The last part of this study investigated the resistance of asphalt mixtures with different percent air voids to moisture damage by using experimental methods and a fracture mechanics approach that accounts for fundamental material properties.

DEDICATION

To my parents

To my wife and my daughter

To my sisters, brothers and nephews

ACKNOWLEDGEMENTS

I am deeply grateful to my committee chair, Dr. Eyad Masad, for providing me with the support needed to complete this research. Words cannot convey my gratitude to Dr. Masad. During my study years, he has been a brother for me before being my supervisor. He had his door open all the time to listen to my inquiries and provide me with professional feedback. Dr. Masad always appreciated the hard work which encouraged me to do better. He provided me with the support to attend a number of conferences and workshops across the nation which had a great impact on me. It was my good fortune to have a brilliant person like Dr. Masad at the top of my committee.

Thanks are due to Dr. Robert Lytton. I owe him so much. His courses provided me with extensive knowledge in the area of materials and pavements engineering. His hard work and commitment to research is remarkable and inspiring. I enjoyed my academic discussions with him. Thanks extended to Dr. Amy Epps Martin and Dr. Ibrahim Karaman for serving as members of my graduate committee. Dr. Epps Martin was an excellent mentor for me when I served as a teaching assistant.

My gratitude is extended to the following individuals who helped me during this research: Arif Chowdhury, Andrew Muras, Rick Canatella and Jeff Perry. I appreciate the support of my colleagues: Dr. Edith Arambula, Chein-Wei Haung and Enad Mahmoud.

Special thanks are to the Texas Department of Transportation (TxDOT) for funding this research project and to Dr. German Claros for his insightful and useful comments and feedback during the study.

TABLE OF CONTENTS

TABLE OF CONTENTS (Continued)

TABLE OF CONTENTS (Continued)

TABLE OF CONTENTS (Continued)

LIST OF FIGURES

LIST OF FIGURES (Continued)

LIST OF FIGURES (Continued)

LIST OF FIGURES (Continued)

LIST OF FIGURES (Continued)

LIST OF FIGURES (Continued)

LIST OF FIGURES (Continued)

LIST OF FIGURES (Continued)

LIST OF TABLES

CHAPTER I
INTRODUCTION AND BACKGROUND

OVERVIEW

Compaction is the process by which the volume of an asphalt mixture is reduced, leading to an increase in unit weight of the mixture and interlock among aggregate particles (Corps of Engineers 2000; Roberts et al. 1996). The performance of asphalt mixtures is significantly influenced by the degree of compaction. Insufficient compaction leads to poor asphalt pavement performance even if all desirable mixture design characteristics are met. Poor compaction can result in premature permanent deformation or rutting, excessive aging, and moisture damage.

There are many factors that affect the compaction process; these factors include the properties of the materials in the mixture, environmental variables, conditions at the lay down site, and the method of compaction. A number of studies were carried out in order to evaluate the relationship between laboratory and field compaction methods and mechanical properties of asphalt mixtures (Consuegra et al. 1989; Harvey and Monismith 1993; Peterson et al. 2004; Tashman et al. 2001). Based on the published literature, it can be seen that very little effort has been devoted in the past to evaluate the effect of changes in field compaction patterns on degree of compaction and uniformity of air void distribution in asphalt pavements. This uniformity leads to asphalt pavements with more uniform properties and improved performance. Additionally, there is still a need to relate field compaction to laboratory compaction in order to predict asphalt mixture compactability based on laboratory measurements.

The effect of the air void distribution on moisture diffusion, as an important cause of moisture damage in asphalt pavements, also needs to be investigated. Most studies have focused on permeability as a measure of the infiltration of water in the mixture (Masad et al. 2006a). However, evidence of severe moisture damage in pavements in

---

This dissertation follows the style of the *Journal of Materials in Civil Engineering*.

areas with low levels of annual rainfall, such as Arizona and New Mexico (Caro et al. 2007), implies that the diffusion of water vapor could be an important source of moisture damage in pavements. The diffusion coefficient is an important input for modeling moisture transport and predicting moisture damage in asphalt mixtures. Developing an experimental procedure for measuring the diffusion coefficient of asphalt mixtures and evaluating the effect of the air void distribution on the moisture diffusion is one objective of this study.

The percent and size of air voids is an important factor that influences asphalt pavement performance. Experimental methods and a fracture mechanics approach were employed to evaluate the resistance of asphalt mixtures with different percent air voids to moisture damage. The proposed fracture model accounts for fundamental material properties of asphalt mixtures.

PROBLEM STATEMENT AND OBJECTIVES

The degree of compaction has a significant influence on asphalt mixture performance in the field. Providing all desirable mixture design characteristics without adequate compaction will lead to poor asphalt pavement performance. Poor compaction has been associated with premature permanent deformation or rutting, excessive aging, and moisture damage. There is no method currently available to assess the compactability of asphalt mixtures in the field based on laboratory measurements. A few studies were carried out in the past to study the effect of changes in field compaction patterns on mechanical properties and degree of compaction and air void distribution in asphalt pavements. This study aimed at providing better understanding of the compaction factors that influence uniformity and degree of compaction and resulting mechanical properties of asphalt mixtures. This understanding is necessary in order to compact more uniform asphalt pavements with improved performance. In addition, this study investigated the effect of air void distribution on moisture diffusion. Moisture diffusion is one of the important modes of moisture damage which might occur as a result of poor compaction. The effect of air void distribution on moisture damage was investigated using a fracture mechanics approach. The primary objectives of this study were as follows:

1) Develop a method to quantify the level of pavement compaction and its uniformity,
2) Predict degree of compaction in the field based on laboratory measurements ,
3) Determine the influence of different compaction patterns on asphalt pavement uniformity,
4) Develop a test procedure for measuring moisture diffusion in asphalt mixtures,
5) Use a fracture mechanics approach to assess moisture damage in asphalt mixtures and its relationship to air void distribution.

RESEARCH PLAN

The objectives of this study were achieved by executing the tasks described in this section.

Task 1: Conduct Literature Search

A comprehensive literature search was conducted in order to collect pertinent information on:

- Compaction in both the field and the laboratory and the factors that influence this process
- Field and laboratory compaction equipment,
- Influence of compaction methods on mixture properties and performance,
- Influence of compaction methods on the internal structure of asphalt mixtures,
- Effect of compaction temperature on the air void distribution of asphalt mixtures,
- Analysis and experimental measurements of moisture diffusion, and
- Methods for measuring mixture resistance to moisture damage.

Task 2: Conduct Field Compaction with Different Compaction Patterns

Roadway projects with different types of mixtures, compaction patterns and compaction equipment were identified. Different compaction patterns were followed in the field. Field cores were obtained from the test sections. Number of passes and the position of each compactor's pass

were recorded across the mat, and their influence on measured percent air voids in the recovered field cores were studied. The data and samples collected during the field projects included:

- ambient, surface, and mixture temperature.
- density data measured using nuclear and non-nuclear density gauges,
- equipment used in the project, (screed, dump truck or materials transfer device, roller): size, weight, pattern, sequence, number of passes, etc.,
- cores for Saturated Surface Dry (SSD) density, vacuum sealed density, X-ray CT, and performance testing,
- plant mixture and virgin aggregate and binder for further testing.

Task 3: Analyze Air Void Distribution

X-ray Computed Tomography (CT) is a nondestructive test used to capture the internal structure of materials (Masad 2004). The CT images were analyzed by techniques such as those available in Image-Pro® Plus software (1999). Three-dimensional maps of air void distribution in pavement sections were generated by inputting percent air voids as a function of depth (from X-ray CT images) and the location of cores in the pavement to the Matlab 7.1 software (2004). This application is considered valuable because it provides an estimate of percent air voids at any point in the pavement section every 1 mm of depth. As such, one can determine the detailed three-dimensional distribution of air voids. The uniformity of air void distribution was quantified using mathematical indices.

Task 4: Evaluate Field Compactability and Laboratory Compactability

In the field, the location of the compactors across the mat during the compaction process was recorded for each pass by measuring the distance from the edge of the compactor with respect to the longitudinal joint of the mat. The compactability of asphalt mixtures in the field was evaluated by considering the number of passes of the rollers and the relative location of each pass. In the laboratory, a number of laboratory Superpave gyratory compactor (SGC) specimens were compacted for the same asphalt mixtures studied in the field. The compactability of the laboratory mixtures was quantified by determining the slope of the percent air voids to number of gyrations on a logarithmic

scale for each sample at a certain percent air voids. The compactability of asphalt mixtures in the laboratory was compared to the compactability of the same mixtures in the field.

Task 5: Study Influence of Compaction on Mechanical Properties

The mechanical response of laboratory specimens and field cores were measured using the Hamburg wheel tracking device, the overlay tester, and a permeability test in order to compare the properties of laboratory and field specimens. Permeability tests were conducted on field and SGC compacted samples following ASTM Standard D5084 "Standard Test Methods for Measurement of Hydraulic Conductivity of Saturated Porous Materials Using a Flexible Wall Permeameter" (ASTM 2006). The permeability measures the ability of the asphalt mixture to transmit and drain the surface water. Overlay tests were conducted following the recommendations by Zhou and Scullion (2003) and recently adopted in TxDOT standard Tex-248-F "Overlay Test". The overlay test was used to identify the crack resistance of asphalt mixtures. The Hamburg test was conducted following TxDOT standard Tex-242-F "Hamburg Wheel-tracking Test.". The Hamburg test was used to measure rutting and stripping susceptibility of asphalt mixtures.

Task 6: Measure Diffusion Coefficients of Asphalt Mixtures and Evaluate Effect of Air Void Distribution

The presence of moisture in asphalt pavements has detrimental effects on the bond between the aggregate and binder and the bond within the binder. The loss of these bonds leads to the deterioration of asphalt pavements. In regions with low rainfall, moisture diffusion is an important source of moisture transport. The diffusion coefficient is an essential input for any model to simulate moisture damage in asphalt pavements. In this task, an experimental protocol was developed for measuring the moisture diffusion coefficient, which has not been measured yet for asphalt mixtures. A test procedure similar to the drying test for measuring the diffusion coefficients for soil (Mitchell 1979) was developed. The diffusion coefficient was measured by the drying (evaporation) test in which the change of the total suction in a wet asphalt mixture specimen was monitored

as a function of time. X-ray CT was used to characterize the internal structure of the test samples to evaluate the effect of the internal structure on the permeation of water vapor though the asphalt mixtures.

Task 7: Use Fracture Mechanics Approach to Assess Moisture Damage

The effect of air voids in asphalt mixtures on moisture susceptibility was evaluated using a fracture mechanics approach that accounts for fundamental material properties. Asphalt mixture samples with different percent air voids were prepared. Test samples were subjected to dynamic loading under different conditions: dry (unconditioned) and wet (moisture-conditioned). The crack growth index developed by Lytton et al. (1993) and later modified by Masad et al. (2006b) and Arambula (2007) was employed in order to assess moisture susceptibility of asphalt mixtures. The parameters required for the crack growth index were obtained through a relaxation modulus test, a tensile test, a dynamic tensile test, and surface energy tests.

Task 8: Document the Main Findings

The research results and findings were documented in this dissertation. The dissertation includes the test methods, analysis approaches and results of all the tasks listed in this chapter.

ORGANIZATION OF DISSERTATION

This dissertation documents the research efforts outlined in Task 1 through 8. Chapter I provides the introduction, background, and the list of tasks conducted under this research project. Chapter II summarizes the comprehensive literature review conducted under Task 1. Chapter III provides a brief description of the field projects and field testing. Chapter IV documents the evaluation of the relationship between different field compaction patterns and the uniformity of air void distribution. It presents the detailed testing efforts and analyses procedure of air voids distribution using X-ray CT. Chapter V provides the testing efforts and results from a comparative performance study between field compacted and laboratory compacted specimens. Chapter VI documents the effort to evaluate the effect of the air void distribution on the performance of HMA

using an overlay tester and a Hamburg wheel tester. The efforts to evaluate the effect of temperature on laboratory compacted specimens are presented in Chapter VII. Chapter VIII describes the testing and results from four forensic projects studied under this research project. Chapter IX documents the research efforts to develop an experimental procedure for measuring the diffusion coefficient of full asphalt mixtures and to evaluate the effect of air voids on moisture diffusion. Chapter X discusses the fracture mechanics approach and the experimental tests used to assess the moisture damage of asphalt mixtures with different percent air voids. Chapter XI presents the overall conclusions inferred under various tasks.

CHAPTER II
LITERATURE REVIEW

INTRODUCTION

Compaction is the process by which the volume of asphalt mixture is reduced (Corps of Engineers, 2000). As a result of the compaction process, the aggregate interlock and interparticle friction increases, percent air voids decreases, and unit weight increases. The compaction process has a significant influence on HMA properties and performance. Providing all desirable mix-design characteristics without adequate compaction will lead to poor asphalt pavement performance. HMA pavements with poor compaction will be exposed to permanent deformation "rutting" as a result of further densification under the subsequent traffic especially in the first few years of service. Studies show that percent air voids should not fall below 3 to 4 percent for the dense-graded mixtures in order to maintain good resistance to permanent deformation (Roberts et al., 1996). Adequate compaction decreases rutting, increases fatigue life, decreases moisture damage, and decreases low temperature cracking (Corps of Engineers, 2000).

FACTORS AFFECTING COMPACTION

The factors that affect HMA compaction include the properties of materials used in the mixture, environmental variables, conditions at the laydown site, and the method of compaction being used (Corps of Engineers, 2000).

Properties of the Materials

Aggregate

Aggregate characteristics influence the compactive effort required to obtain a proper level of density (Corps of Engineers, 2000). The compactive effort increases with an increase in aggregate angularity, nominal maximum aggregate size, and aggregate hardness. More densification effort is required to compact angular aggregate due to its resistance to reorientation. Smooth aggregates are easier to compact than aggregates with rough surfaces. Rounded shape aggregates require less compaction effort than cubical or

block-shaped aggregates. Dense-graded mixtures need less compaction effort than open-graded mixture.

Asphalt Binder

The ability to densify the asphalt mixtures is influenced by the amount and the grade of asphalt binder (Corps of Engineers, 2000). Asphalt mixtures fabricated with high grade binder are usually stiff and require more compactive effort to obtain the desired density. Asphalt mixtures that include too little asphalt binder are stiff and usually require more compaction effort than the mixtures with high asphalt binder content.

The temperature susceptibility of the asphalt binder affects the workability and the time available for compaction (Corps of Engineers, 2000). A mix containing high temperature-susceptible asphalt binder has less time available for compaction as a result of losing the temperature and being stiffer.

Environmental Variables

The time available for compaction is the time for the mix to cool from its laydown temperature to a minimum compaction temperature. The time available for compaction was determined for various HMA mixtures in the early 1970s by the U.S. Army Corps of Engineers (2000). A study by the U.S. Army of Engineers (2000) defined this minimum compaction temperature to be 80^{o}C. Below this temperature the compaction process is not effective and little density gain is achieved. Six variables were found to influence the available time for compaction in this study. These factors were layer thickness, air temperature, base temperature, mix laydown temperature, wind velocity and solar radiation. The relationships between these variables and the time available for compaction are illustrated in Figures 2-1 and 2-2. Wind velocity and solar radiation are assumed to be constants in this study.

Layer Thickness

Layer thickness significantly influences the time available for compaction. It can be seen from Figure 2-1 that if a mix laydown temperature is 120^{o}C (250^{o}F) and a base temperature is 15^{o}C (60^{o}F), the available time to compact a mat with a thickness of 2

inches is 12 minutes. If a mat thickness is doubled, the time available for compaction increases from 12 minutes to 36 minutes. It can be seen from Figures 2-1 and 2-2 that there is limited time available for compaction for a thick layer, especially in cold weather.

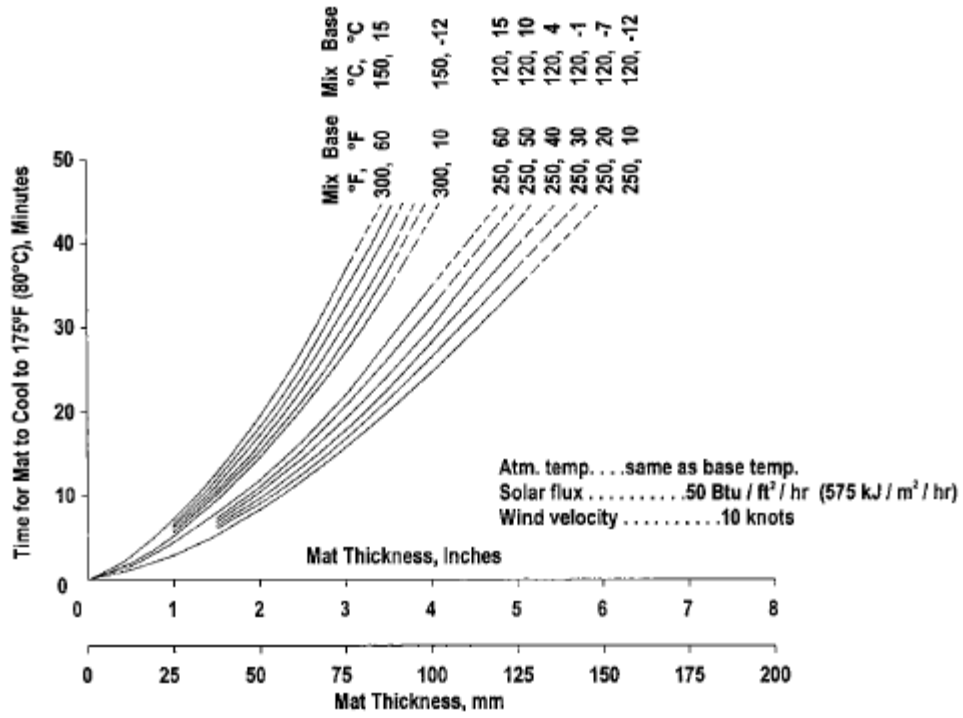

Figure 2-1. Time for Mat to Cool to 80°C versus Mat Thickness for Lines of Constant Mix and Base Temperatures 120°C or 150°C behind Paver (Corps of Engineers, 2000).

Air and Base Temperature

An asphalt layer loses heat to both air and the layer on which the new layer is placed. Usually, the air temperature and the base temperature are assumed to be the same. The base temperature is considered more important than the air temperature as the cooling rate at the base is more rapid than at the upper surface (Corps of Engineers, 2000). Figures 2-1 and 2-2 show that the time available for compaction increases with an increase in base temperature.

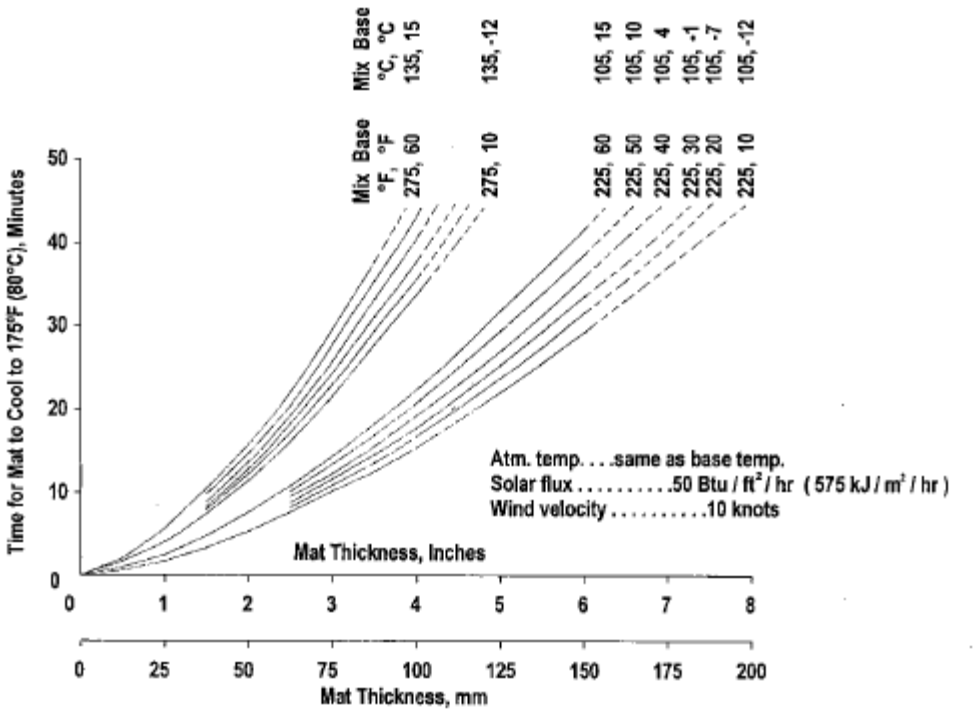

Figure 2-2. Time for Mat to Cool to 80°C versus Mat Thickness for Lines of Constant Mix and Base Temperatures 105°C or 135°C behind Paver (Corps of Engineers, 2000).

Mix Laydown Temperature

Usually, the temperatures of producing asphalt mixtures are between 130°C (270°F) and 165°C (325°F). The plant mixing temperature is not as important in determining the time available for compaction as the mix laydown temperature. It can be seen from Figures 2-1 and 2-2 that the time available for compaction increases with an increase in the initial mix temperature. The initial mix temperature is a more significant factor in affecting compaction of thin layers in cold weather (Corps of Engineers, 2000).

Wind Velocity

The cooling rate of the asphalt layer increases if there is a strong wind during compaction. The wind influences the time available for compaction for a thin layer more than a thick one. A crust forms at the top of asphalt layer and should be broken down by a roller before compaction.

Solar Flux

Solar flux is the amount of radiant energy available from the sun, and depends on many variables such as the position of the sun above the horizon, and the distance above the sea level. The solar flux affects the temperature of the base layer. The temperature of the base layer is higher than the ambient temperate on a sunny day. A high base temperature will increase the time available for compaction.

Laydown Site Conditions

As mentioned earlier, layer thickness is the most important factor affecting the compaction ability in order to obtain the desired density level. If the asphalt layer thickness varies in depth due to rutting in the old surface, it is difficult to densify the mix in order to achieve a given density. A pneumatic tire roller is more helpful than a static steel wheel roller in this case because static steel wheel rollers tend to bridge over the ruts, especially when they are narrow and deep.

Compaction Equipment

The density of asphalt mixtures is influenced by the method of compaction. Different compaction equipment produces asphalt mixtures with different density levels at the same number of passes. In this section, the field compaction equipment and laboratory compaction equipment are discussed.

Field Compaction Equipment

Compaction decreases air voids and increases the unit weight of asphalt mixtures by applying external forces. Self-propelled compactors are used to provide the compaction energy. This compaction train usually consists of two more rollers in order to achieve the following objectives (Roberts et al., 1996):

1) Achieve the desired density and comply with the specifications, and
2) Provide the mat with a smooth surface.

There are three types of self-propelled compactor equipment; static steel wheel rollers, pneumatic tire rollers, and vibratory steel wheel rollers.

- Static Steel Wheel Rollers

  A static steel wheel roller is shown in Figure 2-3. The weight of static steel wheel is between 3 to 14 tons. The actual compactive effort is determined by the contact pressure between the steel drum and the asphalt layer (Roberts et al., 1996). The contact pressure is dependent on the depth of penetration. As the penetration depth increases, the contact pressure decreases due to the large contact area. As a result, the compaction effort supplied to the mix decreases. The penetration depth decreases gradually under the subsequent passes of the roller as a result of densification of the mix. Large drums have lower angles of contact at a given pressure and a lower component of horizontal force that pushes against the asphalt layer (Roberts et al., 1996).

- Pneumatic Tire Rollers

  Pneumatic tire rollers shown in Figure 2-4 are employed for intermediate rolling after a static steel wheel or vibratory steel wheel roller and before a static steel finish roller. However, they can be operated in the initial or finish rolling. The compactive effort provided by the pneumatic roller is influenced by the wheel load of the machine, tire pressure, tire design, and depth of penetration of the tire into the mixtures (Corps of Engineers, 2000). As the contact pressure between the tires and the mix increases, the compactive effort supplied by the pneumatic roller increases. The desired compaction pressure of the mat can be produced by changing the inflation pressure in the tires (Roberts et al., 1996).

Figure 2-3. Static Steel Wheel Roller.

Low pressure is preferable for the tender mix (mix that tends to move under compaction equipment) as low tire pressure will displace the mix less than higher pressure does. Usually, the pressure of the tires should be maintained constant in the same project, especially if the pneumatic roller is used in the intermediate position. The tire of the pneumatic roller might pickup the mix, so water may be sprayed or a release agent may be applied. There are many advantages of using pneumatic rollers when compacting dense-graded aggregate (Roberts et al., 1996):

- A more uniform degree of compaction is provided by pneumatic roller than by a steel wheel rollers.
- The density provided by a pneumatic roller, occasionally can not be achieved by a steel wheel roller.

- Pneumatic rollers do not cause checking during compaction and help in removing checking that might occur under the steel wheel roller. Checking is the term used to describe fine, hairline, transverse cracks which occur at the surface of the mat.

Figure 2-4. Pneumatic Tire Roller.

- Vibratory Steel Wheel Rollers

Vibratory steel wheel rollers shown in Figure 2-5 apply static and dynamic forces. The dynamic component is produced by a rotating eccentric weight inside its drum. Both of static and dynamic loads affect the compactive effort provided by the vibratory rollers; however the dynamic load is more significant in densification of the mat. Vibration reduces mechanical friction during compaction, but yields an increase of mechanical interlock after that (Roberts et al., 1996). In order to achieve a given density level, the frequency and amplitude of a vibratory roller must be selected. Generally, higher amplitude and a lower frequency are needed for a thicker mat than a thinner one.

Figure 2-5. Vibratory Steel Wheel Roller.

Laboratory Compaction Equipment

Laboratory compaction equipment is used to produce asphalt mixtures specimens similar to field cores. There is a verity of laboratory compaction equipment. This equipment includes Marshall impact compactor, mobile steel wheel simulator, Arizona vibratory-kneading compactor, California kneading compactor, Texas gyratory shear device, and Superpave gyratory compactor (SGC). The focus of the discussion will be on the SGC.

The Superpave gyratory compactor, shown in Figure 2-6, is used to produce asphalt mixtures specimens in the laboratory. The compactive effort provided by the SGC is influenced by the vertical pressure, the angle of gyration, and the number of gyrations. For the Superpave design procedure, the vertical pressure is set at 600 kPa, while the angle of gyration is set at 1.25^{o}. The Superpave gyratory specimens are either 6 inches (15 cm) or 4 inches (10 cm) in diameter.

Figure 2-6. Superpave Gyratory Compactor.

EFFECT OF COMPACTION METHODS ON MECHANICAL PROPERTIES OF ASPHALT MIXTURES

Different compaction methods produce HMA specimens with different internal structures which are represented by air void distribution, aggregate orientation, and aggregate contacts. The difference in internal structure is manifested in different mechanical properties. In this section, some of the previous studies on this topic are reviewed and their findings are presented.

Consuegra et al. (1989)

The main objective of the study was to insure that laboratory asphalt specimens are fabricated in a manner that adequately simulates field compaction and yield engineering properties similar to field cores. The specific goal was to evaluate the ability of different compaction devices to simulate the compaction in the field in terms of the mechanical properties. Five different laboratory compaction methods were used in this study. These methods were (a) Texas gyratory compactor, (b) California kneading

compactor, (c) Marshall impact compactor, (d) mobile steel wheel simulator, and (e) Arizona vibratory-kneading compactor.

Field cores and samples of asphalt, aggregate, and loose mix from the drum were collected and transported to the laboratory. Laboratory specimens were prepared by reheating the loose mix in the laboratory and compacting it at the same percentage of the air content of the field cores. In the field, the following compaction patterns were used:

- vibratory rolling for breakdown compaction followed by static rolling for finish compaction,
- static rolling for breakdown compaction followed by pneumatic rolling for intermediate compaction and static rolling for finish compaction, and
- pneumatic rolling for breakdown compaction followed by static rolling for finish compaction.

The field cores and the laboratory specimens were evaluated for indirect tensile strength, indirect tensile creep, and diametral resilient modulus. An average absolute difference (ΔD) is used to evaluate the average differences in means for each of the laboratory compaction methods from the field cores. ΔD was represented by the following equation:

$$\Delta D = \frac{\sum_{i=1}^{n}\left(\frac{MP_c - MP_s}{MP_c}\right)}{n} \qquad (2\text{-}1)$$

where, MP_C = average materials property measured on the field cores, which is taken to be a target value, MP_S = average materials property measured on the laboratory specimens, n = number of data point for each compaction device.

Table 2-1 presents the average absolute difference (ΔD) for the different compaction methods. The mean square error (MSE) is used also to compare the mechanical properties for the laboratory specimens to the field cores as a desired value. MSE results are summarized in Table 2-2.

The results analysis showed that the engineering mechanical properties of asphalt mixtures were dependent on the compaction method. A Texas gyratory compactor was found to be the best method among those used in this study in terms of lower MSE and less average absolute difference value. The study ranked the compaction methods in terms of simulation of mechanical properties of field cores. The ranking was as follows: (1) Texas gyratory compactor, (2) California kneading compactor, (3) mobile steel wheel simulator, (4) Arizona vibratory-kneading compactor, and (5) Marshall mechanical hammer.

Table 2-1. Summary of Average Differences between Field Cores and Laboratory Compacted Specimens (Consuegra et al., 1989).

Compaction Device	Creep Compliance at 77°F	Indirect Tensile Strength	Tensile Strain at Failure	Resilient Modulus
Arizona Compactor	0.77	0.51	0.47	0.41
Marshall Hammer	0.80	0.35	0.45	0.55
California Kneading	0.59	0.21	0.27	0.42
Steel Wheel Simulator	0.51	0.31	0.11	0.26
Texas Gyratory Shear Compactor	0.44	0.14	0.16	0.37

Note: A zero difference indicates that the laboratory specimens had identical properties of the cores (no difference).

Table 2-2. Mean Squared Error (MSE) Comparison of Compaction Data (Consuegra et al., 1989.)

Laboratory Compaction Method	Average MSE Rankings by Mixture		
	Project	Property	Temperature
Arizona Compactor	5.0	4.8	4.7
California Kneading	2.0	2.0	2.0
Marshall Hammer	4.0	3.5	3.3
Mobile Steel Wheel	1.7	2.8	2.0
Texas Gyratory	2.0	1.5	1.3

Sousa et al. (1991)

The objective of this study was to determine the effect of compaction method on the fundamental engineering properties of HMA. Sousa et al. (1991) stated that laboratory specimens must simulate the in-service mixtures produced by mixing, placement, and compaction in the field in order to for laboratory tests to provide meaningful results. Three compaction methods were evaluated in this study: (a) Texas gyratory compactor, (b) California kneading compactor, and (c) rolling-wheel compactor. The study evaluated the effect of different compaction methods on the permanent deformation and fatigue properties of asphalt mixtures. The main findings of this study in regard to the effect of compaction method on the performance of the asphalt mixture can be summarized as follows:

- The engineering properties of asphalt mixture are significantly influenced by the compaction method used to prepare the laboratory specimens.
- Specimens prepared using the kneading compactor were the most resistant to permanent deformation, followed by the specimens fabricated using the rolling-wheel compactor and the Texas gyratory compactor. The results of the effect of compaction method on resistance to permanent deformation are summarized in Table 2-3. In general, specimens prepared using the kneading

compactor were the most sensitive to aggregate characteristics, and the specimens prepared using rolling-wheel compactor were more sensitive to asphalt characteristics.

- Texas gyratory specimens have the most resistance to fatigue followed by the specimens fabricated by the rolling wheel and kneading compactor. The results of the effect of compaction method on resistance to fatigue are presented in Table 2-4.
- The kneading compactor is very effective in producing asphalt mixtures with maximum interparticle contact. This might help in understanding the cause of higher resistance of kneading specimens to permanent deformation than the specimens prepared using other compaction methods. Kneading specimens are sensitive to the aggregate angularity and surface texture.

Table 2-3. Effect of Compaction Method on Resistance to Permanent Deformation (Sousa et al., 1991).

Compaction Method	Test	Overall Resistance	Ranking in the Twelve Mixtures and Test Variable Comparisons of Tables 4.1 and 4.2		
			Strongest	Intermediate	Weakest
Gyratory	Compressive Creep	Weakest	None	4 Times	8 Times
	Shear Creep	Weakest	1 Time	None	11 Times
Kneading	Compressive Creep	Strongest	10 Times	1 Time	1 Time
	Shear Creep	Strongest	2 Times	2 Times	None
Rolling wheel	Compressive Creep	Intermediate	2 Times	7 Times	3 Times
	Shear Creep	Intermediate	1 Time	10 Times	1 Time

Table 2-4. Effect of Compaction Method on Resistance to Fatigue (Sousa et al., 1991).

Compaction Method	Test	Overall Resistance	Ranking in the Twelve Mixtures and Test Variable Comparisons of Tables 4.6 and 4.7		
			Strongest	Intermediate	Weakest
Gyratory	Flexural Fatigue	N/A	N/A	N/A	N/A
	Diametral Fatigue	Strongest	6 Times	3.5 Times	2.5 Times
Kneading	Flexural Fatigue	Intermediate	3 Times	9 Times	N/A
	Diametral Fatigue	Weakest	None	7.5 Times	4.5 Times
Rolling Wheel	Flexural Fatigue	Strongest	9 Times	3 Times	N/A
	Diametral Fatigue	Intermediate	6 Times	1 Time	5 Times

Harvey and Monismith (1993)

The main objective of the study was to determine the effects of laboratory preparation variables on the mechanical properties of asphalt mixtures, which relate to permanent deformation, fatigue, and flexural stiffness. The mixes used in this study differed in binder type, aggregate type, fines content, air void content, mixing viscosity, and compaction viscosity.

The laboratory compaction methods evaluated were (a) Texas gyratory compactor, (b) University of California at Berkley rolling wheel compactor, and (c) California kneading compactor. The results revealed that the compaction methods produce specimens that are significantly different in terms of resistance to permanent deformation. The results from the repetitive shear permanent deformation are represented in Table 2-5. The analysis of the results indicated that the kneading specimens have the most permanent shear deformation resistance, the rolling wheel specimens have intermediate resistance, and gyratory compacted specimens have the least resistance. This study indicated that the effect of laboratory compaction method on the mix performance is at least equivalent to the effect of aggregate type, binder type, fines content, or air void content. The results also demonstrated that compaction methods can not be used interchangeably to produce HMA specimens with similar mechanical properties.

Button et al. (1994)

This study was carried out in order to determine which of four different compaction methods most closely simulates field compaction. The compaction methods that were studied included: (a) Exxon rolling wheel compactor, (b) Texas gyratory compactor, (c) rotating base hammer, and (d) Elf linear kneading compactor.

Table 2-5. Average Permanent Deformation Results: Conventional Asphalts (Harvey and Monismith, 1993).

		Air Voids (%)	N_f (reps)	Air void content	
				low 4% N_f (reps)	High 8% N_f (reps)
Asphalt Type	Valley Ar-4000	5.8	951	1652	191
	Boscan Ac-30	6.2	6432	12663	200
	% difference		148.5	153.8	4.6
Aggregate Type	Pleasanton Gravel	5.9	975	1778	173
	Watsonville Granite	6.1	6189	11716	200
	% difference		145.6	147.3	14.5
Fines Content	Low (2.5%)	6.2	2502	4762	241
	Normal (5.5%)	5.8	4723	8961	132
	% difference		61.5	61.2	58.4
Air-void Content	Low	4.1	6946		
	High	8.0	187		
	% difference		189.5		
Compaction Method	Gyratory	6.0	91	111	69
	Rolling Wheel	5.9	572	951	193
	Kneading	6.0	10464	20610	298
Mix Viscosity	Low	5.8	5594	10517	260
	Normal	6.2	1595	2935	255
	% difference		111.3	112.7	1.9
Compaction Viscosity	Low	6.0	5750	11382	118
	Normal	6.0	1605	2851	255
	% difference		112.7	119.9	73.5

Percent difference = (difference/average) *100 percent

Thirty field cores were taken from five pavement sites. The same aggregate and binder used in the field were used to fabricate laboratory specimens. The laboratory specimens were compacted in order to simulate the range of the air content in the field cores. The air content in the field cores varied from about 3 to 8 percent. Laboratory tests were utilized in order to evaluate specimens compacted by different compaction methods. These laboratory tests included indirect tension at 25°C, resilient modulus at 0°C, Marshall stability, Hveem stability, and uniaxial repetitive compressive creep followed by compression to failure. The statistical analyses of the results are presented in Table 2-6.

Table 2-6. Consolidated Results from Statistical Analysis (Button et al., 1994).

Site	Compaction Method	Resilient Modulus,		IDT Strength	Marshall Stability	Hveem Stability	Compressive Dilation Ration	Creep Test Compressive Strength
		25°C	0°C					
Casa Grande	Gyratory	E	H	H	E	E	E	E
	Marshal	E	H	E	E	-	-	-
	Exxon	L	E	E	E	E	E	E
	Elf	E	H	E	E	E	E	L
Flagstaff	Gyratory	D	E	E	D	E	E	H
	Marshal	H	E	E	E	-	-	-
	Exxon	L	E	L	E	L	E	D
Alberta	Gyratory	E	H	D	E	E	E	E
	Marshal	E	H	H	E	-	-	-
	Exxon	E	E	E	E	L	E	E
	Elf	E	E	E	E	L	E	L
Manitoba	Gyratory	E	E	H	E	H	-	-
	Marshal	H	E	H	H	-	-	-
	Exxon	L	L	L	E	L	E	E
Michigan	Gyratory	E	E	E	E	E	E	E
	Marshal	H	E	H	H	-	-	-

E = Equivalent to
L= Less than
H = Higher than
D = Difference from
} the field compaction

All four compaction methods were not used to prepare specimens from all five locations.

Results of comparisons are described by four categories as follows: equivalent to (E), less than (L), higher than (H), or different from (D) the field cores. Total number of Es was summed for each compaction method and was expressed in a percent of the

maximum possible number of Es. The Texas gyratory compactor simulated field cores 24 times out of a possible 33 times (73 percent). Exxon rolling wheel compaction simulated field cores 18 times out of a possible 28 times (64 percent). Elf linear kneading compaction simulated field cores 9 times out of a possible 14 times (64 percent). The author stated that these differences are not statically significant (at $\alpha = 0.05$).

Peterson et al. (2004)

This study evaluated the resemblance of laboratory compaction to field compaction by measuring the mechanical properties of asphalt mixtures. The performance characteristics of asphalt mixtures were evaluated by the Superpave shear tester. A Superpave gyratory compactor was used to prepare the asphalt mixture specimens. The specific objective was to determine the influence of various SGC control parameters on properties of asphalt mixtures. These control parameters included the angle of gyration, specimen height, gyratory compaction pressure, and the temperatures of the gyratory mold and the base plates. The field samples were cored from three different field sections that were compacted using different compaction patterns. HMA was collected from the field and delivered to the laboratory for compaction at the same percent air void as the asphalt pavements. The results revealed that a 1.5^{o} angle of gyration along with a specimen height of 50 to 75 mm would better simulate the mechanical properties of the field cores. Also, the results demonstrate that similar compaction results can be obtained by using the current 1.25^{o} angle along with 400 kPa pressure in case the angle of gyration of the gyratory compactor can not be modified.

EFFECT OF COMPACTION METHODS ON AIR VOID DISTRIBUTION USING IMAGE ANALYSIS TECHNIQUES

Compaction methods influence the mechanical properties of asphalt mixtures. An asphalt mix exhibits different mechanical properties when it is compacted using different compaction methods at the same air content due to the differences in the internal structure. A number of studies on the effect of compaction methods on the internal structure of asphalt mixtures are discussed in the following subsections.

Masad et al. (1999a)

This study quantifies the internal structure of asphalt mixtures. The Superpave gyratory compactor and linear kneading compactor (LKC) were used to prepare specimens. The HMA internal structure was quantified by aggregate orientation, aggregate contacts, and air void distribution. X-ray CT was utilized to capture the air void structure in asphalt mixtures.

X-ray Computed Tomography (CT)

X-ray CT is a nondestructive method to capture the internal structure of materials. Figure 2-7 shows the components of X-ray CT. The test specimen is placed between an X-ray source and a detector. X-rays that pass through the test specimen along several different paths in several different directions produce a set of CT images. The intensity of X-rays is measured before it enters the specimen and after it passes through it. Scanning of a slice is complete after collecting the intensity measurements for a full rotation of the specimen. The specimen is then shifted vertically by a fixed amount (the slice thickness) and the entire procedure is repeated to generate additional slices. The resulting X-ray CT image is a map of the spatial distribution of density.

Once images of the internal structure are captured, imaging techniques can be used to extract significant information from the image. Figure 2-8 illustrates the process of analyzing the air void distribution in an asphalt mix specimen using the X-ray CT system and image analysis techniques. The captured image consists of 256 levels of gray intensity that correspond to different densities within the specimen. Air voids (low density) are shown in black (Figure 2-9). Using a suitable gray intensity threshold value, air voids can be separated from other mix constituents (aggregate and mastic). The threshold level represents a boundary value below which pixels in the analyzed image are considered as part of the air voids. Pixels that have intensity values above the threshold value are considered to belong to the remaining phases. The analysis is capable of quantifying the vertical and horizontal distributions of air voids, size distribution of air voids, and connectivity of air voids.

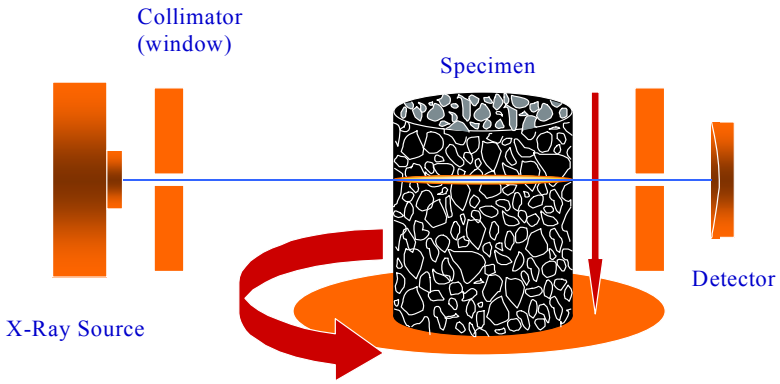

Figure 2-7. Components of X-Ray Computed Tomography System (Masad et al.,1999a).

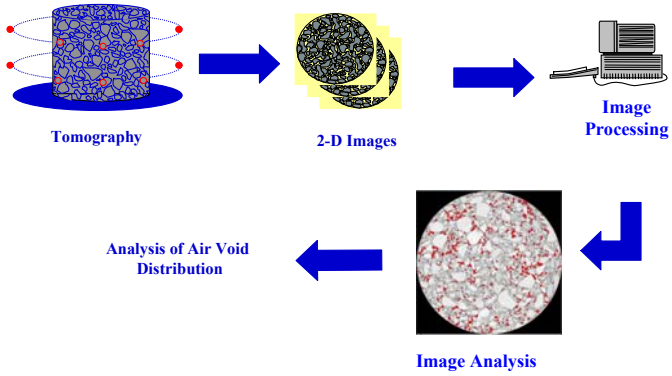

Figure 2-8. The Process of Analyzing Air Void Distribution in Asphalt Mix Specimens Using X-ray CT and Image Analysis Techniques (Masad et al., 1999a).

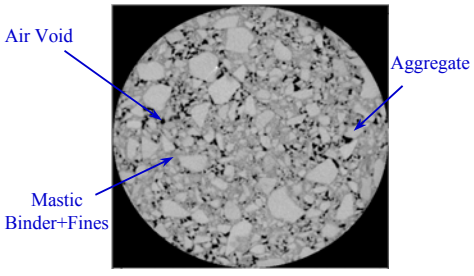

Figure 2-9. An Example of an X-ray CT Image (Masad et al., 1999a).

Aggregate Orientation

The orientation of the aggregate is measured by the angle (θ_k) between the major axis of an aggregate and the horizontal axis of the image (Figure 2-10). The major axis of the aggregate can be defined as the greatest distance between two pixels. After calculating (θ_k), the vector magnitude (Δ) (Equation 2-2), and average angle of inclination (θ) are used to quantify the directional distribution of aggregates. The vector magnitude parameter and average angle of inclination are calculated using Equations 2-2 and 2-3, respectively.

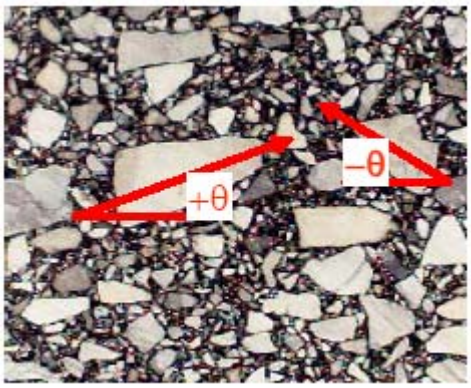

Figure 2-10. Angle of Inclination (θ_k) (Masad et al.,1999a).

$$\Delta = \frac{100}{N}\sqrt{(\sum \sin 2\theta_K)^2 + (\sum cos\ 2\theta_K)^2} \tag{2-2}$$

$$\theta = \frac{\sum|\theta_k|}{N} \tag{2-3}$$

where, θ_k = the orientation of an individual aggregate, from -90 to +90°, N = number of aggregates on the image

The vector magnitude parameter (Δ) varies from 0 to 100 percent. Zero percent means that aggregates have complete random distribution, while 100 percent means the aggregates have exactly the same direction.

Aggregate Contacts

The method to calculate the number of contacts is based on the erosion operation. Erosion is a morphological operation in which pixels are removed from a binary image according to the number of surrounding pixels that have different colors. The effect of the sequence of erosion operations on an image is illustrated in Figure 2-11. At the points of object contact, white pixels are surrounding the black ones. Consequently, the black pixels in contact are removed during the erosion operation. Simultaneously, the size of objects shrinks, and the small particles disappear after a sufficient number of operations are conducted.

The results from the study revealed the following findings:

- The distribution of the air void in both SGC and LKC is not uniform. The SGC specimens have higher percentage of air void at the top and the bottom compared to the middle part, while the percentage of air voids in LKC specimens increases with the depth as shown in Figure 2-12.
- The number of contacts in LKC specimens was more than in SGC specimens.
- The orientation results showed that the aggregates have more of a random distribution in kneading specimens compared to the gyratory specimens which have preferred orientation toward the horizontal direction.

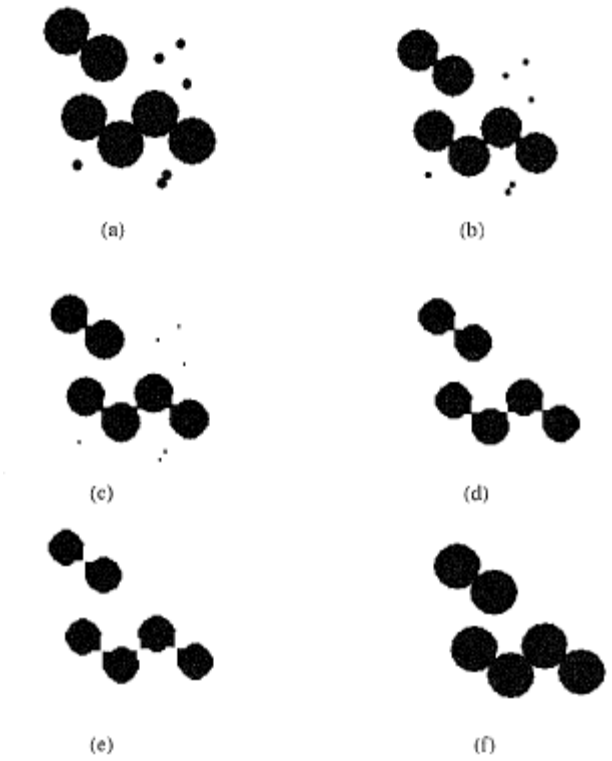

Figure 2-11. Determination of Number of Contacts by Erosion Techniques (Masad et al., 1999a).

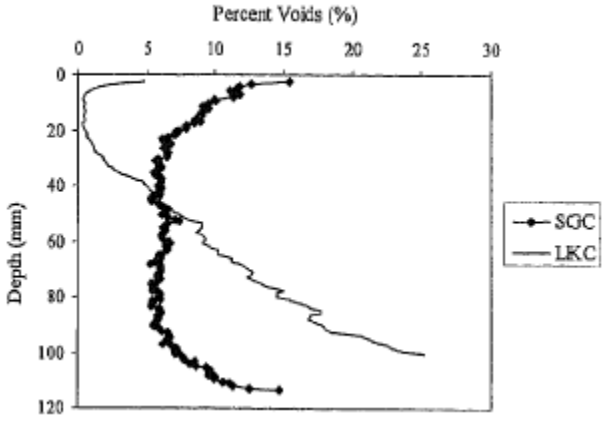

Figure 2-12. Air Void Distribution in SGC and LKC Specimens (Masad et al., 1999a).

Masad et al. (1999b)

This study was carried out in order to develop image analysis-based methods to quantify the internal structure of asphalt mixtures. In this study the internal structure included the air void distribution, aggregate orientation, and gradation. The internal structure was quantified for SGC specimens prepared at different compaction levels and was compared to the internal structure of field cores.

The results of the air void distribution for gyratory compacted specimens which were compacted at different compaction levels and the air void distribution in field cores are presented in Figures 2-13 and 2-14, respectively. The results from the analysis of gyratory compacted specimens revealed that the air void distribution is not uniform and there is higher air void content at the top and the bottom than in the middle. The compaction of the middle part increases with an increase in compaction. In the field cores, the air void distribution was different than the one in the gyratory compacted specimens.

The vector magnitude, average angle of inclination, and percent of air void were calculated for both the gyratory compacted specimen and field cores, and the results are illustrated in Figure 2-15. These results demonstrated that the average angle of inclination decreases with the compaction levels until a certain level. The orientation angle tends to increase after this certain compaction level. Conversely, the vector magnitude tends to increase until it reached the same certain compaction level and then starts to decrease with further compaction. The authors stated that preferred orientation increased with compaction until it reached a maximum value which was called the optimum compaction level. In this study, the optimum compaction level was found at about 100 gyrations. Once the orientation reached this maximum value, further compaction caused aggregates to lose preferred orientation and become more random.

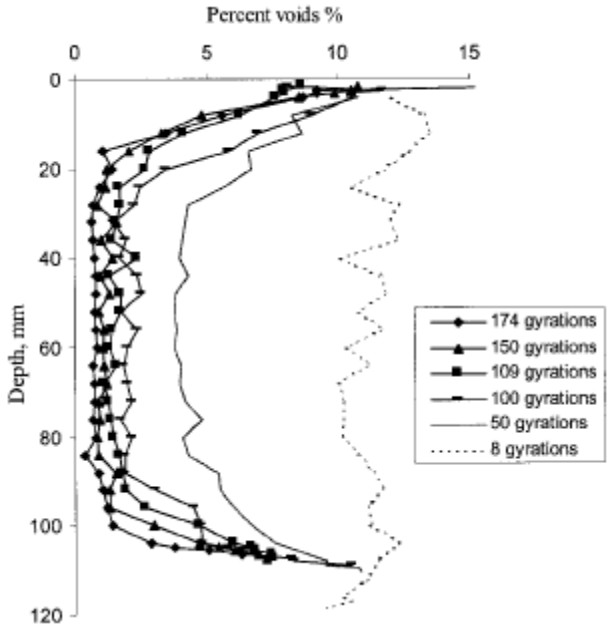

Figure 2-13. Distribution of Voids in Gyratory Specimens (Masad et al., 1999b).

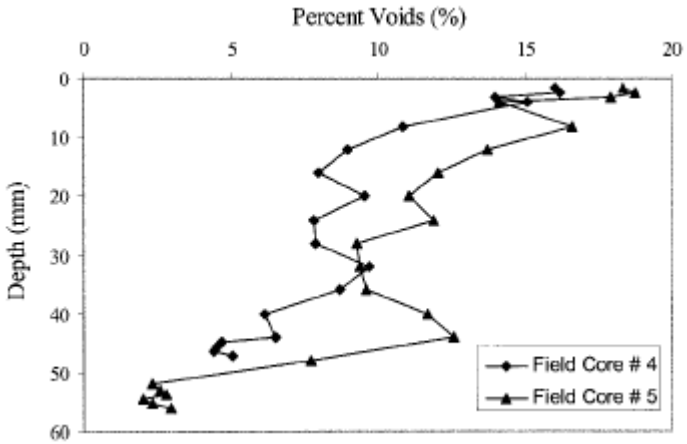

Figure 2-14. Distribution of Voids in Field Cores (Masad et al., 1999b).

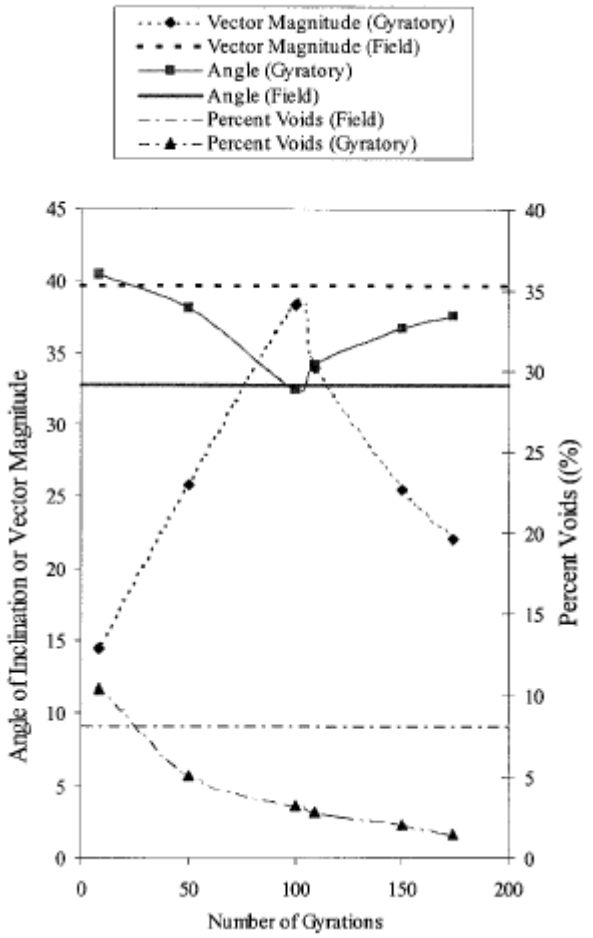

Figure 2-15. Variation of Vector Magnitude, Angle of Inclination, and Percent Void with Compaction (Masad et al., 1999b).

Shashidhar (1999)

The main objective of this study was to promote better understanding of the aggregate structure in asphalt concrete by utilizing X-Ray CT. X-ray CT was used for imaging the internal structure of laboratory compacted specimens and field cores. X-ray CT was found to be an excellent technique for capturing the internal structure of asphalt mixtures. This study has shown qualitatively that air void distribution and aggregate interlock are related to mixture performance.

Tashman et al. (2001)

This study was carried out in order to evaluate the ability of SGC to produce laboratory specimens that closely simulate the internal structure of field cores. Also, this study evaluated the influence of different field compaction patterns on the internal structure of field cores. Three field test sections were constructed using different compaction patterns.

The results of the air void distributions in laboratory compacted specimens revealed that there is a high percentage of air void at the top and the bottom compared to the middle part. The air void distribution in laboratory specimens is illustrated in Figure 2-16a. Different compaction patterns produced air void distributions in field cores similar to those shown in Figure 2-16b. Field cores always had a higher percentage of air void at the top than the bottom. The study evaluated the air void distribution in SGC specimens compacted using two different mold temperatures. Using a higher temperature produced more uniform distribution of air voids (Figure 2-17).

The different field compaction patterns did not affect aggregate orientation. However, it was found that both gyration angle and height of specimen affected the aggregate orientation. The authors suggested that aggregate orientation is controlled by the shear action which is represented in the angle of gyration and specimen height. The aggregate orientation results illustrated in Figure 2-18 show that the short specimens (50 mm and 75 mm) at angle of gyration of 1.5^{o} adequately simulated field cores.

The shear frequency sweep test measured the mechanical response of field cores and gyratory compacted specimens. The results showed that the gyratory specimens compacted at an angle of gyration of 1.5^{o} adequately simulated field cores in terms of the stiffness results.

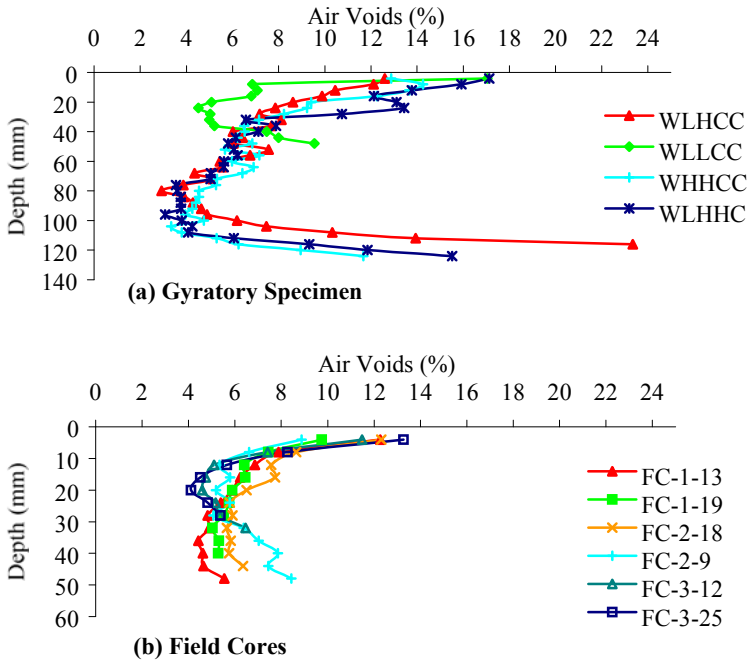

Figure 2-16. Vertical Distribution of Air Voids in Gyratory Specimens and Field Cores (Tashman et al., 2001).

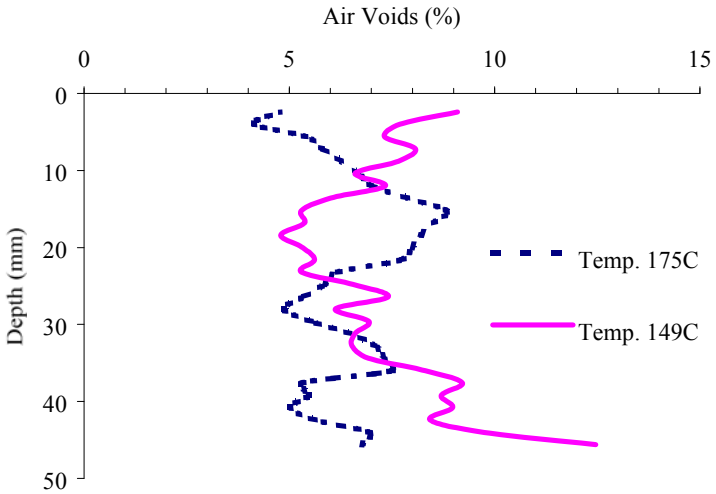

Figure 2-17. Effect of the Base Plates and Mold Temperature on the Vertical Distribution of Air Voids in Gyratory Specimens (Tashman et al., 2001).

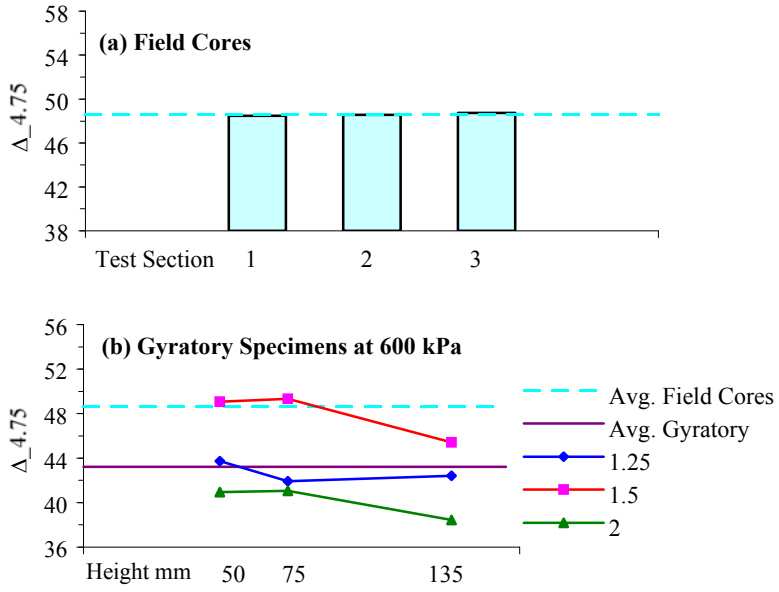

Figure 2-18. Vector Magnitude of Aggregate Orientation (Tashman et al., 2001).

Partl et al. (2003 and 2007)

One aim of these studies was examining the difference in homogeneity and isotropy in asphalt mixtures compacted using different compaction methods. The compaction methods were the Marshall compactor, Superpave gyratory compactor, and rolling-wheel compactor. The air void distribution was investigated at different compaction levels using X-ray CT.

Marshall and gyratory specimens were cored from the center and cut horizontally. Marshall specimens were cut into three parts (top, middle, bottom), while the gyratory compacted specimens were cut into 4 parts (top, upper middle, lower middle, and bottom). Rolling-wheel compacted specimens were cut into 40 pieces as shown in Figure 2-19. The findings of these studies can be summarized as follows:

- The air void distribution in Marshall compacted specimens showed that there is a difference in the air void content between the core and exterior of the specimens. This difference was clear at the initial compaction, as it reached 3.5 percent. This

difference decreased with further compaction. The air void content distribution is illustrated in Figure 2-20.

- In gyratory compacted specimens, the middle part of the core was more compacted than the top and the bottom parts as shown in Figure 2-21. It is believed that the kneading action at the top and the bottom of the base plates is not effective.
- The air void content distribution in rolling-wheel compaction after the initial compaction level was fairly even as shown in Figures 2-22 and 2-23. However, the air void distribution became uneven with more compaction and the minimum percent of air voids was located at the center of the bottom part. After the final compaction level, it was obvious that the bottom part is less compacted than the top part.
- The comparison between the different compaction methods showed that the relationship between the decrease of air void content and compaction effort varied from one compaction method to another as illustrated in Figure 2-24. This relationship looks linear for the Marshall compactor while it is nonlinear for the Superpave gyratory compactor. In regard to the rolling-wheel compactor, the relationship appears to be intermediate behavior between linear and nonlinear.

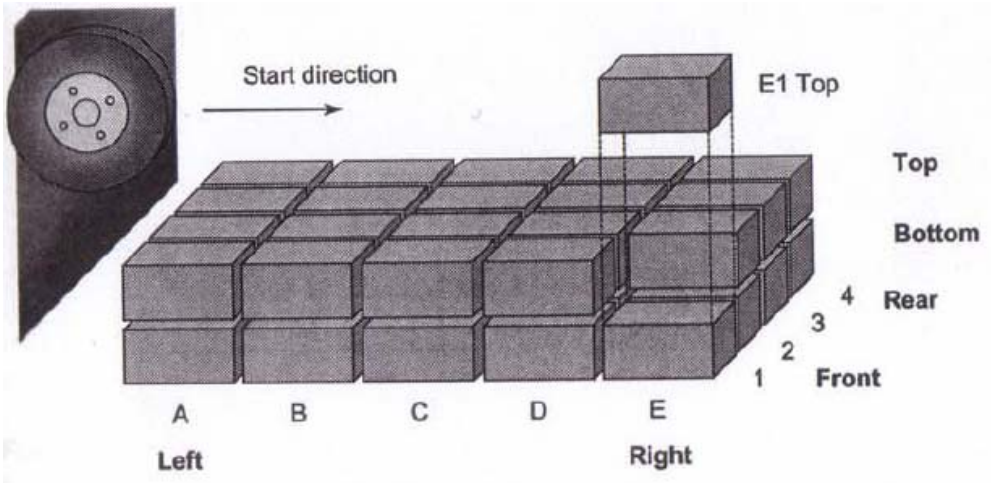

Figure 2-19. Rolling Wheel Compacted Specimens (Partl et al., 2007).

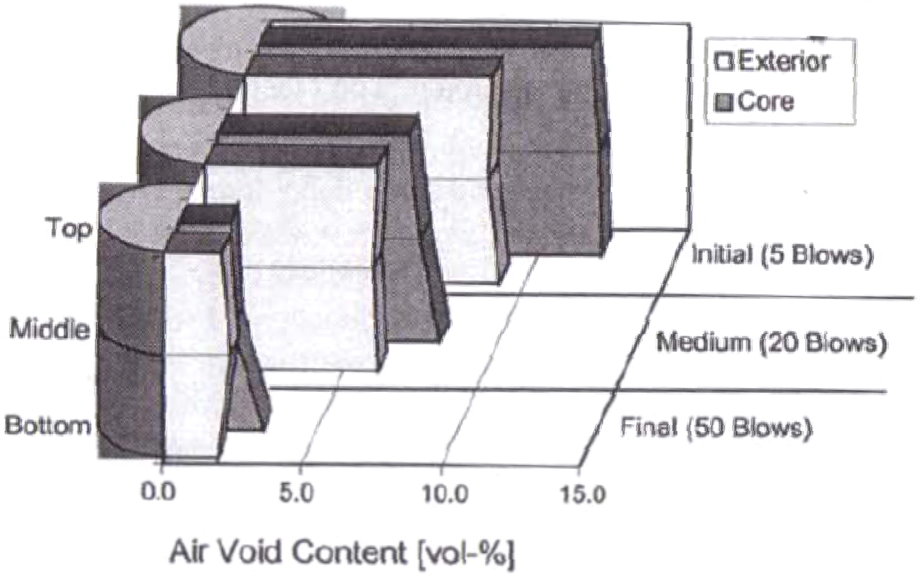

Figure 2-20. Air Void Distribution in Marshall Specimen (Partl et al., 2007).

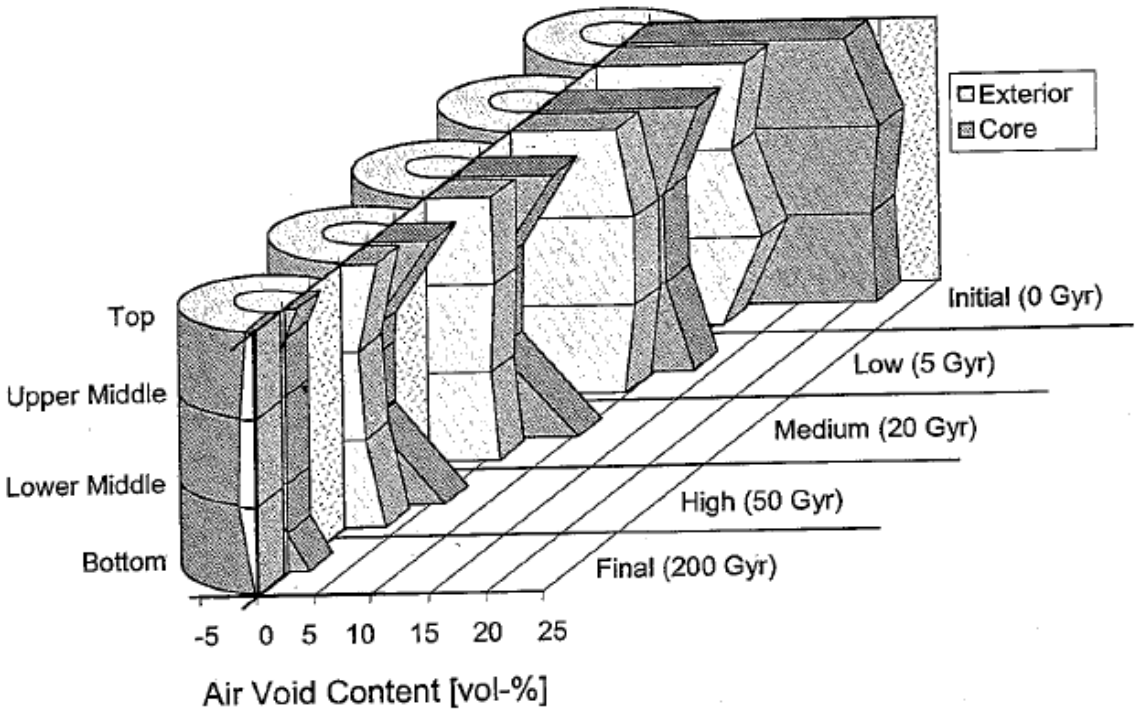

Figure 2-21. Air Void Distribution in Gyratory Compacted Specimens (Partl et al., 2003).

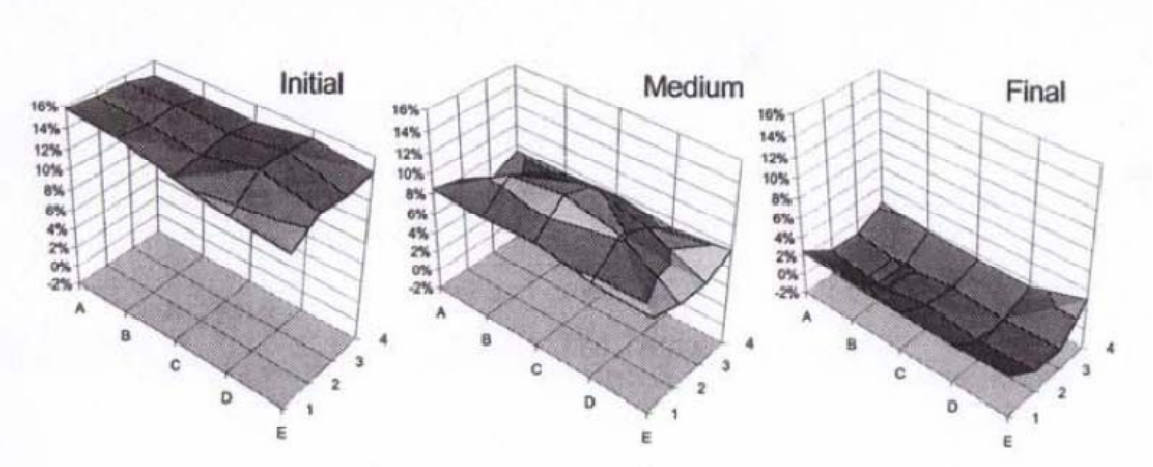

Figure 2-22. Air Void Content in the Top Part of Rolling Wheel Compacted Specimens (Partl et al., 2007).

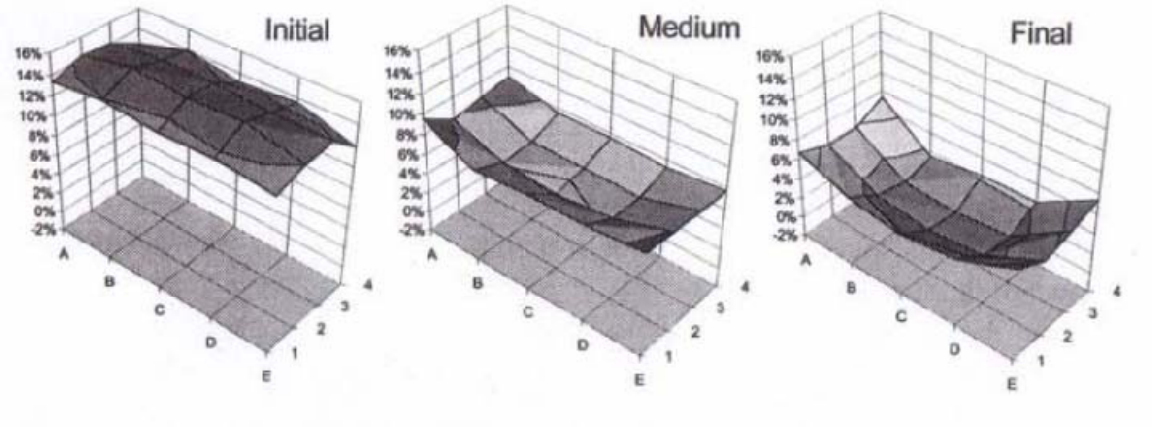

Figure 2-23. Air Void Content in the Bottom Part of Rolling Wheel Compacted Specimens (Partl et al., 2007).

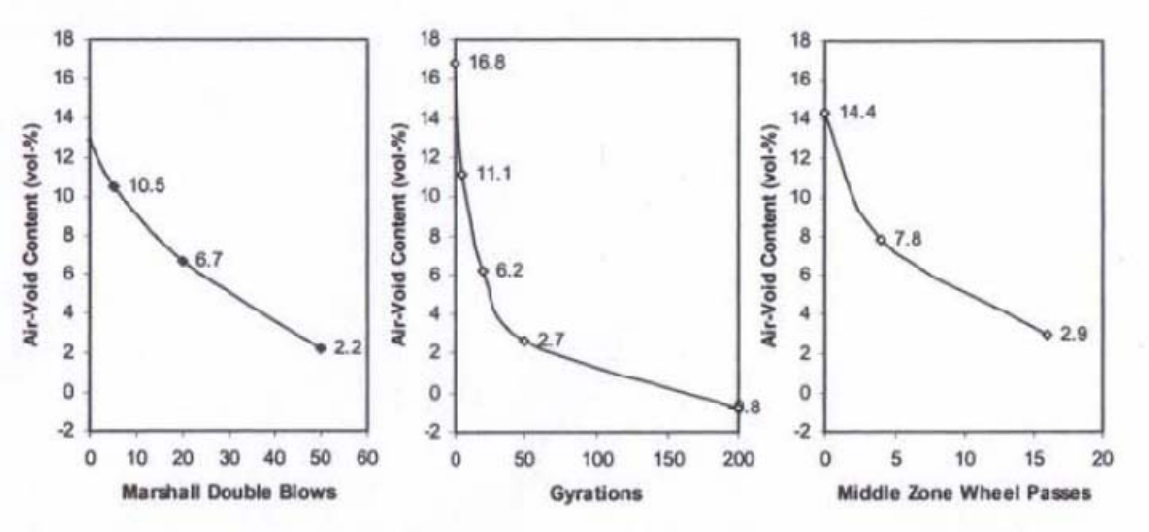

Figure 2-24. A Decrease of Air Content with the Compaction Level (Partl et al., 2007).

MODELING COMPACTION OF ASPHALT MIXES

Very little research has been directed towards modeling HMA compaction and the material properties that influence compactability. Guler et al. (2002) have proposed the use of a porous elasto-plastic (using a modified Gurson-Tvergaard yield function) compaction model. In order to achieve this purpose, an incremental constitutive relation for the porous material was developed. The researchers focused on obtaining a correlation between asphalt mixture characteristics and the proposed model parameters. Simple linear models were built to predict the model parameters. The displacement field used to represent 3-D compaction is an approximation of the actual motion in an SGC. Also, the model is formulated assuming small strain theory, is time independent, and assumes isothermal conditions (no changes in temperature).

Huerne (2004) from the Netherlands used a modified form of soil critical state theory in modeling asphalt mixture compaction. The granular material performance is described by the critical state theory using means of a closed yield locus. Huerne's implementation simulates void reduction by means of plastic volume changes. The Hveem device was used for determining the model's parameters. This theory is developed assuming small strain deformation that is limited in modeling the high strains

involved in the compaction process. The model also has many parameters that are not directly linked to mixture properties.

Krishnan and Rao (2000) developed a constitutive model for asphalt mixtures using mixture theory to model the one-dimensional compaction of asphalt mixtures under a static load. This model employs the fundamental balance laws to describe the behavior and characteristics of asphalt mixtures. While their work places the modeling within the context of a general framework that takes into account the balance laws of mechanics, it ignores certain critical issues concerning the material response such as the fact that the "natural configuration" of the material being compacted evolves with the compaction process. Also, such an approach to modeling compaction of asphalt mixtures is limited by the available experimental techniques to measure the various characteristics included in the proposed model.

CHAPTER III
DESCRIPTION OF FIELD COMPACTION PROJECTS

INTRODUCTION

Several field projects were identified with the help of the TxDOT. Assistance was sought from different districts to volunteer for candidate HMA projects. A number of districts volunteered to participate in the modification of field compaction patterns. Test sections from the following roadways were evaluated:

1. US 281 in Pharr District
2. FM 649 in Laredo District
3. IH 35 in Waco District
4. SH 36 in Yoakum District
5. US 87 in Yoakum District
6. US 259 in Tyler District
7. SH 21 in Austin District
8. SH 44 in Laredo District
9. SH 6 in Bryan District
10. SL 1 in Austin District
11. US 290 in Houston District
12. FM 529 in Houston
13. SL 368 in San Antonio
14. SH 114 in Fort Worth

Projects 11 through 14 are included in forensic evaluation part of this task. This chapter will focus on the first ten projects that were used to analyze the influence of field compaction patterns on air void distribution and mechanical properties. The research team recorded field compaction effort; conducted tests in the field; obtained field cores, plant mix, and virgin materials; and conducted laboratory tests on laboratory compacted specimens and field cores. Table 3-1 provides a description of mixtures used in these seven projects, and Table 3-2 summarizes the compaction patterns. The following

sections briefly describe the research efforts and construction projects included in this part of the study.

US 281 IN PHARR DISTRICT

In February 2006, the first construction job located on northbound US 281 near the Pharr city limit was conducted. This stretch of highway was totally new construction and had very thick asphalt layers. The focus of this study was only on the SMA layer compacted on top of a recently compacted Superpave mixture. This SMA layer was later overlaid with PFC mixture. Initially there was an expectation of changing the compaction pattern in this job. Due to some unavoidable circumstances the idea of changing the compaction pattern was dropped. The original compaction pattern adopted by the paving contractor (Bellinger Corp.) was recorded, and samples obtained from the site.

The SMA mixture was designed using a local river gravel from Fordyce Gravels (Shower quarry). The mixture contained 6.3 percent PG 76-22S binder from Valero Asphalt. The lift thickness was 2 inches (5 cm). The paving contractor used a tri-dem steel wheeled roller, a large truck loaded heavy load at the rear end (Figure 3-1), as well as regular pneumatic tire roller as compactor.

FM 649 IN LAREDO DISTRICT

Two different rolling patterns were evaluated in FM 649 in Laredo in March 2006. FM 649 is a two-lane, undivided highway in rural area. A two-inch thick Type C mixture was placed on this highway. The mixture contained limestone from the Martin Marietta Beckmann quarry in San Antonio. The mixture contained 4.9 percent PG 76-22 binder from Valero asphalt. This is the only project where the contractor used a vibratory pneumatic roller. Figure 3-2 shows the finish roller.

Figure 3-1. Unusual Compaction Equipment.

Table 3-1. Summary of Mixture Designs Used in Compaction Study.

Highway ID	Mixture Type	Date of Field Testing	Aggregate (major)	Binder	Optimum AC %	Max Rice Sp Gr.	VMA at Op. AC.	Design Air Void, %
US 281, PHR	SMA	Feb 2006	Siliceous River Gravel	PG 76-22S	6.3	2.383	18.3	4.0
FM 649, LRD	Type C	March 2006	Limestone	PG 76-22	4.9	2.427	15.0	4.0
IH 35, WAC	SMA	May 2006	Traprock & Limestone	PG 76-22	6.0	2.563	18.3	4.0
SH 36, YKM	Type D	July 2006	Limestone	PG 64-22	4.9	2.447	15.1	3.5
US 87, YKM	Type C	Oct 2006	Siliceous River Gravel	PG 76-22S	4.3	2.460	13.8	4.0
US 259, TYL	Type C	March 2007	Sandstone & Limestone	PG 70-22S	4.3	2.478	13.1	3.0
SH 21, AUS	Type C	June 2007	Limestone	PG 70-22	4.7	2.467	14.3	3.0
SH 44 LRD	Type B	Jan 2008	Siliceous River Gravel	PG 76-22	4.2	2.443	13.5	4
SH 6 BRY	SMA	June 2008	Sandstone & Limestone	PG 76-22	6.4	2.419	17.5	3
SL 1 AUS	SMA	June 2008	Sandstone & Limestone	PG 76-22	6.2	2.352	17.5	4

Table 3-2. Description of Compaction Patterns.

Highway ID	Compaction Pattern 1			Compaction Pattern 2		
	BD	**IM**	**FS**	**BD**	**IM**	**FS**
US 281, PHR	Steel Wheel Static	Steel wheeled vibratory, Heavy pneumatic (truck wheel) and Regular Pneumatic tire roller	Steel Wheel Static	N/A	N/A	N/A
FM 649, LRD	Steel Wheel Vibratory Roller	Pneumatic Wheel	Steel Wheel Static	Pneumatic wheeled vibratory	Steel wheeled vibratory roller	Static steel wheeled
IH 35, WAC	Two Steel Wheel Vibratory Rollers	N/A	Steel Wheel Static	N/A	N/A	N/A
SH 36, YKM	Steel Wheel Vibratory and Steel Wheel Static	Pneumatic Wheel (High Speed – 10 mph)	Steel Wheel Static	Steel Wheel Vibratory	Pneumatic Wheel (High Speed – 10 mph)	Steel Wheel Static
US 87, YKM	Steel Wheel Vibratory and Steel Wheel Static	Pneumatic Wheel	Steel Wheel Static	Pneumatic Wheel	Steel Wheel Vibratory	Steel Wheel Static
US 259, TYL	Steel Wheel Vibratory	Pneumatic Wheel	Pneumatic Wheel	Steel Wheel Vibratory (progressive motion)	Pneumatic Wheel	Pneumatic Wheel
SH 21, AUS	Steel Wheel Vibratory	Pneumatic Wheel	Steel Wheel Static	Pneumatic Wheel	Steel Wheel Vibratory	Steel Wheel Static
SH 44 LRD	Steel Wheel Vibratory	Steel Wheel Static	Pneumatic Wheel	N/A	N/A	N/A
SH 6 BRY	Steel Wheel Vibratory	N/A	Steel Wheel Static	N/A	N/A	N/A
SL 1 AUS	Steel Wheel Vibratory	N/A	Steel Wheel Static	N/A	N/A	N/A

BD: Breakdown, IM: Intermediate, FS: Finish

IH 35 IN WACO DISTRICT

This test section was located on southbound inside lane between Waco and Hillsboro. Only one type of compaction pattern was studied in this project. The overlay in this project used SMA mixture with traprock and limestone. The binder content of this mixture was 6.0 percent (PG 76-22). The SMA mixture was laid on top of a freshly placed seal coat. The lift thickness was 2.0 inches (5 cm). The contractor (Young Brothers) used two steel wheel vibratory rollers side by side as breakdown rollers to cover the entire paving width. The paving width was approximately 15 ft (4.57 m) including the inside shoulder.

Figure 3-2. Finish Roller on FM 649.

SH 36 IN YOAKUM DISTRICT

This project site was located in Austin County under the Yoakum District. The project was executed under the supervision of Victoria area office. SH 36 is a two-lane undivided highway. The research team took part in this project site in July 2006. Type D

mixture with 2 inches (5 cm) compacted mat thickness was laid on top of recently applied seal coat. Hunter Industries, the paving contractor, hauled the mixture from their Rosenberg plant (approximately 25 miles from the job site). This Type D mixture had limestone from Colorado materials and 11 percent field sand, 4.9 percent PG 64-22 binder, and one percent lime.

The research team intended to use a pneumatic roller as a breakdown roller in the compaction Pattern 2. But this roller was static and rather small, so the modified rolling pattern consisted of breakdown with vibratory steel wheel roller. Figure 3-3 shows the coring layout on SH 36.

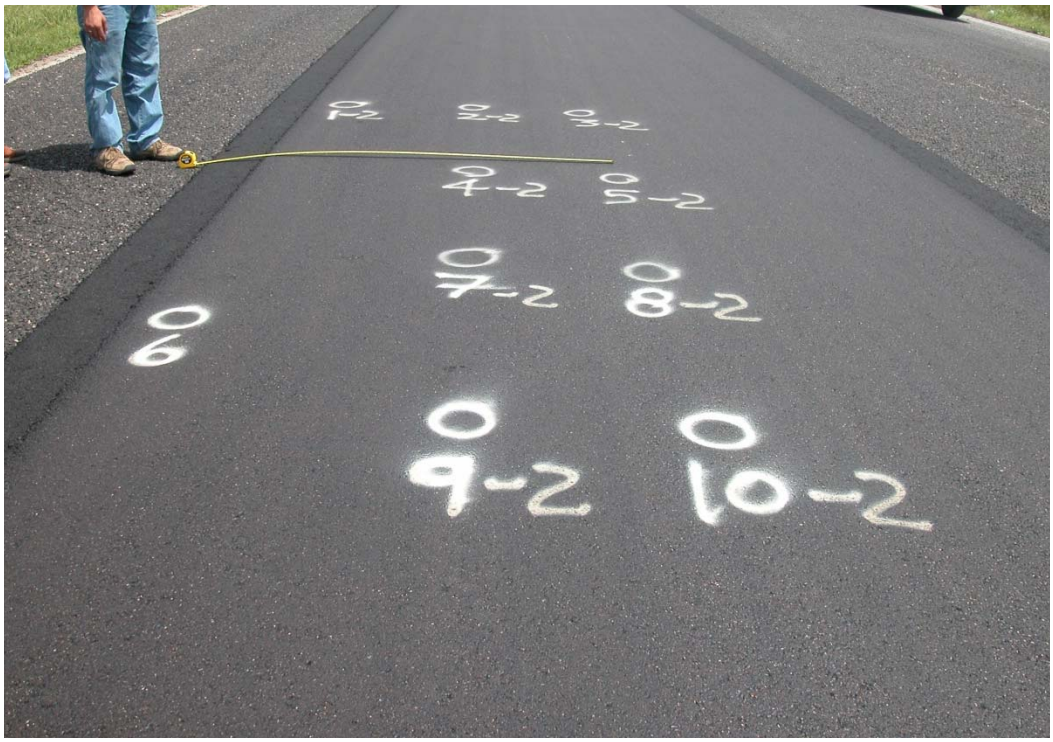

Figure 3-3. Field Coring Layout on SH 36.

US 87 IN YOAKUM DISTRICT

The research team worked the US 87 job near Port Lavaca in Calhoun County in October 2006. Hunter Industries was the paving contractor for this job. They hauled their mixture from their Colorado Materials Plant in Nursery, Texas which is about 50 miles

from the jobsite. US 87 is a four-lane divided highway. The test sections were located on northbound outside lane. The mixture was Type C (TxDOT 1993 Specification) designed with Fordyce Gravel and Colorado Materials limestone screening with 4.3 percent PG 76-22s binder. This Type C mixture was laid on Type B mat and according to the construction plan, TxDOT will lay another PFC layer on top of the Type C layer. The thickness of the Type C layer was 2 inches (5 cm).

The paving contractor laid the mixture with a 16 ft (4.8 m) mat width, of which 1.5 ft (45 cm) on one side was tapered. Specimens were obtained from wheel path, between the wheel path, and longitudinal joint (retrained and unrestrained) from each of those two sections. Figure 3-4 shows the coring layout on US 87.

Figure 3-4. Field Coring Layout on US 87.

US 259 IN TYLER DISTRICT

This project was visited in February 2007. This section of US 259, which is four-lane divided highway, is located in Rusk County. The overlay in this project used a Type C surface mixture compacted in 2 inch (5 cm) lift thickness. The coarse part of the aggregate was sandstone while the intermediate and fine size particles were limestone. The mix had 11 percent field sand and 4.3 percent PG 70-22S binder. The paving contractor A. L. Helmcamp, Inc. hauled the mixture from a plant located in Timpson (approximately 20 miles from the jobsite).

The test sections were in the southbound outside lane. Type C mix was laid on top of recently compacted Type D level-up course. The paving width was approximately 15 ft (4.57 m) (including shoulder). The contractor maintained vertical longitudinal joint. The general rolling pattern can be described as breakdown by steel wheel vibratory roller and pneumatic wheel roller as both intermediate and finish type. In the modified roller pattern the vibratory steel wheel roller was moved progressively in transverse directions. Like the original pattern, the pneumatic wheel roller acted as both intermediate and finish roller. Field cores were obtained from the wheelpath, between the wheelpath, and near the longitudinal joints for both test sections. The coring layout on US 259 is shown in Figure 3-5.

Figure 3-5. Coring Layout on US 259.

SH 21 IN AUSTIN DISTRICT

The research team participated in the construction on SH 21 in Lee County under Austin District in May 2007. This part of SH 21 is a four-lane undivided highway without any center lane and limited or no shoulder on either side. At one area there is a turning lane of almost 1000 ft (300 m) in length. Local TxDOT personnel offered that turning lane for testing and sample collection. The research team with the help of the construction inspector divided that 1000 ft turning lane into two sections for two different types of roller patterns.

The mixture in this project was Type C surface mix including limestone from two different sources and 10 percent field sand. PG 70-22 binder (4.7 percent) from Martin Asphalt was used in this mixture. The lift thickness of the surface mix was approximately 2 inches (5 cm). Prior to the surface mix, there was a recent Type D level-up course followed by a one layer seal coat. Figure 3-6 shows the coring layout on SH 21.

Figure 3-6. Coring Layout on SH 21.

SH 44 IN LAREDO DISTRICT

This construction site was located about 1 mile east of Freer in Duvall County of Laredo District. Test was conducted on the eastbound outside lane and shoulder in January 2008. The inside edge of the HMA mat was restrained while the outside edge was unrestrained. Hass Anderson, the contractor of this project, placed a 2-inch thick Type B mixture. Type B mixture was placed on recently constructed flexible base. The contractor also applied prime coat on flexible base right before the placement of Type B mixture as shown in Figure 3-7. Finally one course seal coat layer was placed on HMA surface as a final surface. The research team was focused only on the compaction of HMA layer. This Type B mixture included primarily crushed river gravel with 4.2 percent PG 76-22 binder.

Figure 3-7. Application of Prime Coat on Flexible Base

SH 6 IN BRYAN DISTRICT

This construction site was located south of Hearne in Robertson County of Bryan District. Test was conducted on southbound outside lane in June 2008. Both side of the HMA mat was restrained. The contractor Knife River Corporation placed 2-ich thick SMA after milling off existing layer. Before placement of SMA they also applied tack coat. This SMA mixture was designed using sandstone, limestone, and mineral filler with 6.4 percent PG 76-22 binder. This SMA layer was again covered with one layer seal coat and PFC. The research team concentrated only the compaction of SMA layer. Figure 3-8 shows the coring layout on SH 6.

Figure 3-8. Coring Layout on SH 6.

SL 1 IN AUSTIN DISTRICT

This construction site was located in the City of Austin in the Austin District. It was a SMA overlay project. Test was conducted on southbound outside lane in June 2008. Both side of the HMA mat were restrained. Earlier the existing surface layer was milled off followed by placement of one-layer seal coat. Due to high traffic volume entire paving of this project was done during night. This SMA mixture was designed using sandstone, limestone, fly ash, and limestone screening with 6.2 percent PG 76-22 binder.

CHAPTER IV
RELATIONSHIP OF FIELD COMPACTION PATTERN TO AIR VOID DISTRIBUTION*

INTRODUCTION

This chapter includes the evaluation of the relationship between different field compaction patterns and the uniformity of air void distribution in asphalt pavements. A number of projects with different hot mix asphalt (HMA) types were compacted and cores were taken at different locations from these projects. The X-ray Computed Tomography (X-ray CT) system was used to capture the air void distributions in these cores. The images were used to develop maps of air void distributions across the pavement surface and depth that were useful to study the uniformity of air void distributions. These distributions were further quantified by computing a Uniformity Index and the differences in percent air voids across the depth.

The analysis results revealed that the uniformity of air void distribution is highly related to the compaction pattern and the sequence of different compaction equipment. More importantly, the efficiency of compaction (reducing air voids) at a point is a function of the location of this point with respect to the roller compactor width. The results in this chapter have supported the development of an index termed the "Compaction Index (CI)" that is a function of number of passes at a point and the position of the point with respect to the compaction roller width.

OBJECTIVES, SIGNIFICANCE, AND TASKS

The primary objective was to investigate the influence of different compaction patterns on asphalt pavement uniformity in terms of air void distribution. The findings of this study assist in providing a better understanding of the compaction factors that

---

*Reprinted with the permission from "Influence of Field Compaction Pattern on Asphalt Pavement Uniformity" by Kassem, E., Masad, E., Chowdhury, A., and Claros G., 2008, *Journal of the Association of Asphalt Paving Technologists*, AAPT, in press.

influence uniformity. This understanding is necessary in order to compact more uniform asphalt pavements with improved performance. The objective was achieved by executing the following tasks:

1) Conduct field compaction of a number of asphalt pavement using different compaction patterns.
2) Obtain field cores from different locations in the pavement.
3) Measure the air void distribution in the cores using X-ray CT and image analysis techniques.
4) Develop maps of horizontal and vertical air void distributions in the pavement.
5) Quantify the uniformity of air void distributions using mathematical functions and indices.
6) Relate air void distribution to the compaction pattern, and put forward recommendations for improving pavement uniformity.
7) Compact laboratory samples and compare laboratory compaction data with field compaction data.

FIELD EXPERIMENTS

The research team recorded field compaction information such as type of compaction equipment, number of passes, location of each pass and mat temperature. In addition, they conducted tests in the field and obtained field cores, plant mix, and virgin materials. The description of the field projects is given in Chapter III. Specimens were obtained from the wheel path, between the wheel path, the center of lane, and the longitudinal joint (restrained and unrestrained) from each of those test sections. Typically, longitudinal joints samples were obtained 1 ft away from the joint. Field core locations of all the test sections were not uniform since the paving width and rolling patterns were different. In some cases, there were also restrictions regarding the number of cores that can be taken from a roadway. Figure 4-1 shows an example of field coring layout from the SH 21 test section.

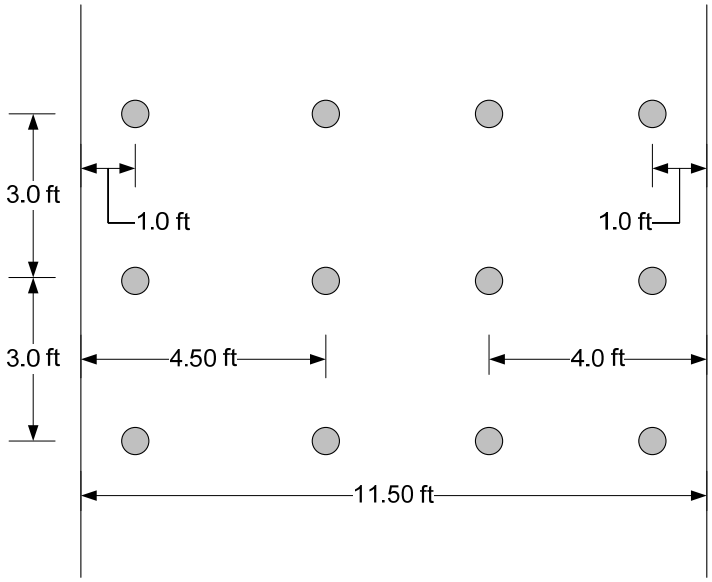

Figure 4-1. An Example of Field Coring Layout on SH 21.

RELATIONSHIP BETWEEN COMPACTION PATTERN AND PERCENT AIR VOIDS

The percent air void of each core was measured using the Saturated Surface Dry (SSD) Procedure (AASHTO 2002a). Then the percent air voids was plotted along with the number of roller passes and location as shown in the examples in Figures 4-2 through 4-4. Each point represents the average percent of air voids of at least two cores taken longitudinally at a given distance from the pavement section edge. Figures A-1 through A-9 in Appendix A present the results for the other test sections. The r-squared value (R^2) was used to evaluate the correlation of the percent of air voids with the number of passes of different rollers as shown in Table 4-1. It can be seen from Table 4-1 that there is a weak correlation, if any, between percent air voids and number of passes of different rollers. It should be pointed out that, test sections from IH 35, SH 36, US 87, US 259, and SH 21 were evaluated in developing the Compaction index (CI) while test sections from SH 44, SH 6, and SL 1 were conducted after the CI was developed.

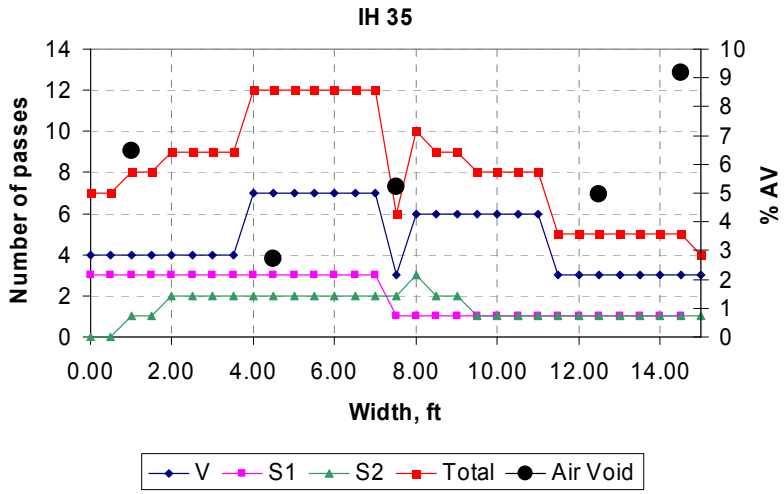

Note: Breakdown roller: vibratory (V), intermediate roller: static (S1), finish roller: static (S2).

Figure 4-2. Number of Passes and Percent of Air Voids across the Mat in the IH 35 Test Section.

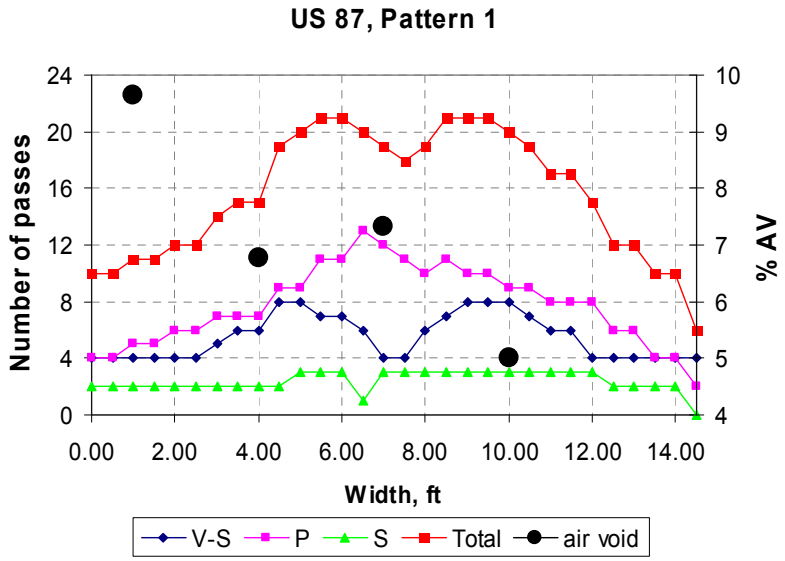

Note: Breakdown roller: vibratory then static (V-S), intermediate roller: pneumatic (P), finish roller: static (S).

Figure 4-3. Number of Passes and Percent of Air Voids across the Mat in the US 87 Test Section (Pattern 1).

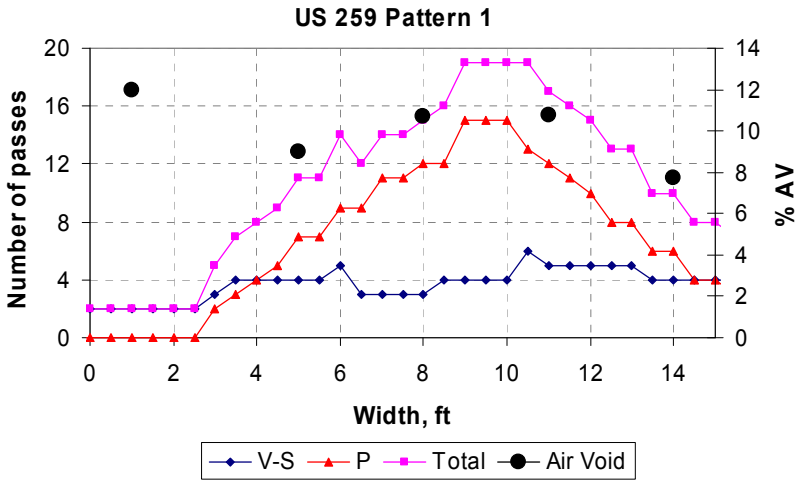

Note: Breakdown roller: vibratory and static (V-S), finish roller: pneumatic (P).

Figure 4-4. Number of Passes and Percent of Air Voids across the Mat in the US 259 Test Section (Pattern 1).

Table 4-1. R-Squared Value.

		Total Number of Passes		
Highway ID	**Compaction Pattern #**	**All Rollers**	**Pneumatic Roller**	**Vibratory and Static Rollers**
IH 35	1	0.47	*	0.47
SH 36	1	(-)0.19	(-)0.15	(-)0.24
	2	(-)0.02	(-)0.02	(-)0.02
US 87	1	0.73	0.25	0.87
	2	0.80	0.47	0.93
US 259	1	0.04	0.02	0.25
	2	0.43	0.32	0.62
SH 21	1	0.44	0.23	0.04
	2	0.24	0.49	0.15
	Average R^2	0.33	0.20	0.34

* Not applicable
(-) Correlation in the opposite direction

Research team observed that cores compacted close to the center of the roller width (static or vibratory) tended to have a higher density than cores compacted at the edge of the compactor even if cores were taken from the middle of the mat and away

from the joint. However, there was no relationship between the location of the core with respect to the pneumatic tire compactor and change in percent air voids. Therefore a statistical correlation analysis was conducted to determine the relationship of percent air voids as a function of number of passes of static and vibratory rollers and the location of the core with respect to the compactor width. Each pass was multiplied by an effectiveness factor which is a function of the location of the core with respect to roller width. Consequently, the percent air voids was plotted versus the summation of number of passes multiplied by the effectiveness factor corresponding to each pass. This summation is termed here the Compaction Index (CI).

Examples of the different effectiveness factors across the roller width are shown in Figure 4-5. The y-axis in these plots represents the effectiveness factor, while the x-axis represents the distance from the roller edge. The numbers shown next to the plots are the R^2 values obtained between CI and percent air voids when these effectiveness factors are used.

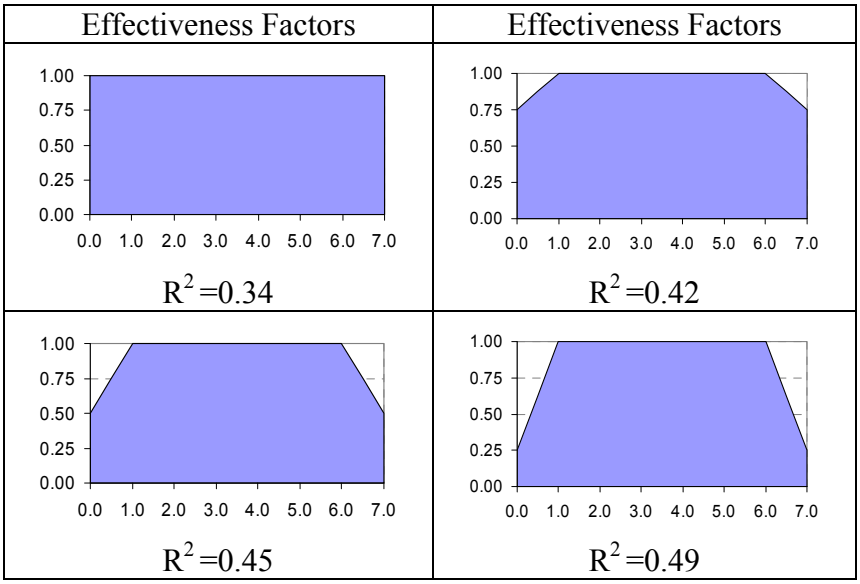

Figure 4-5. Examples of Different Effectiveness Factors of R^2 Values Obtained between Compaction Index and Percent Air Voids when These Factors Are Used.

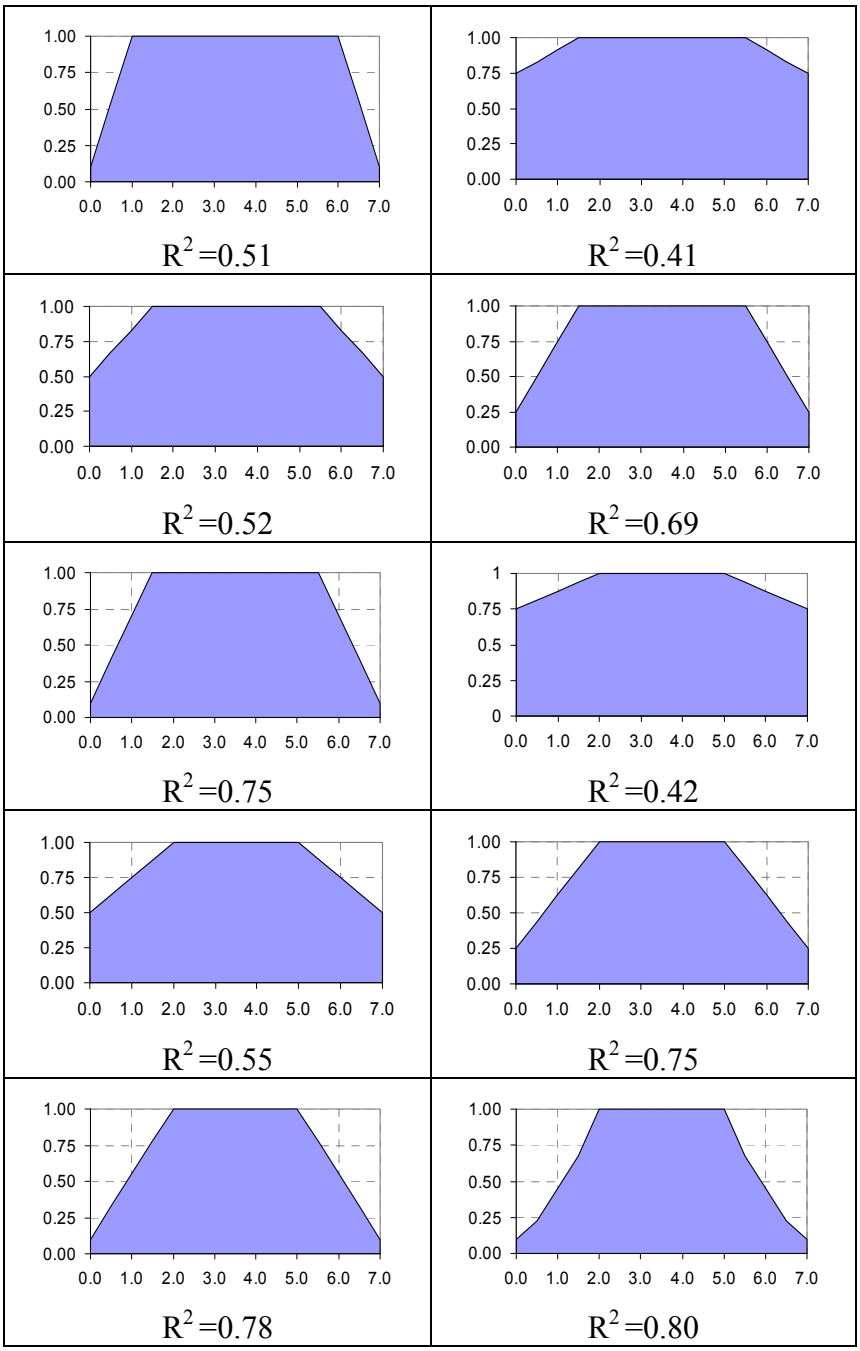

Note: The x-axis is the distance from a roller edge in ft and y-axis is the effectiveness factor.

Figure 4-5. Continued.

The best correlation (R^2 equal to 0.8) between percent air voids and CI was achieved by using the last effectiveness factor in Figure 4-5. The results indicate that the effectiveness of compaction decreases as the distance from the roller edge decreases to less than 2 ft. Examples of the relationships of number of passes and CI with percent air voids are shown Figures 4-6 through 4-10. Figures A-10 through A-16 in Appendix A show the results for the remaining test sections.

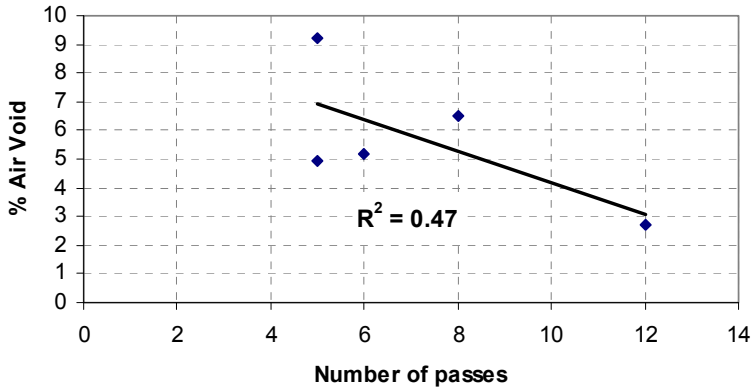

(a)

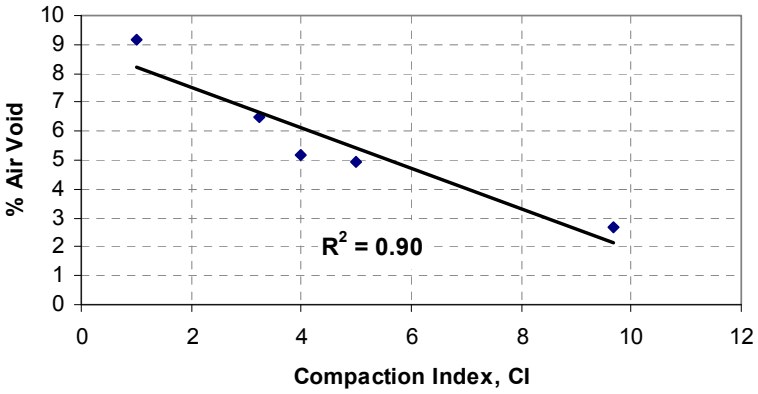

(b)

Figure 4-6. (a) Number of Passes versus the Percent of Air Voids in the IH 35 Test Section, (b) CI versus the Percent of Air Voids in the IH 35 Test Section.

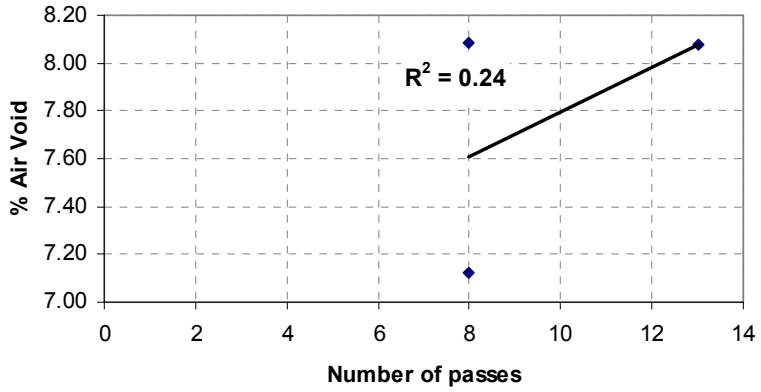

(a)

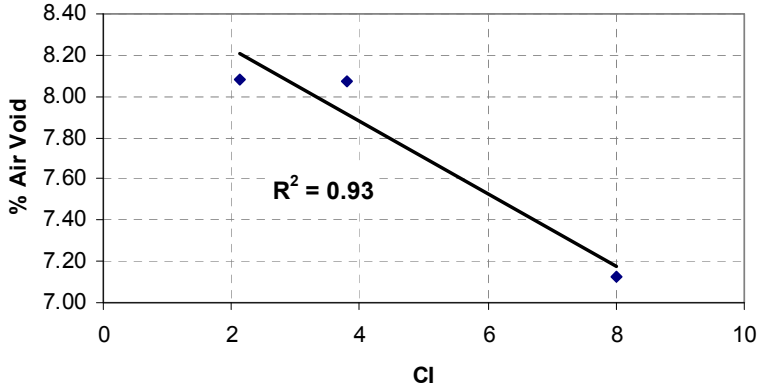

(b)

Figure 4-7. (a) Number of Passes versus the Percent of Air Voids in the SH 36 Test Section (Pattern 1), (b) CI versus the Percent of Air Voids in the SH 36 Test Section (Pattern 1).

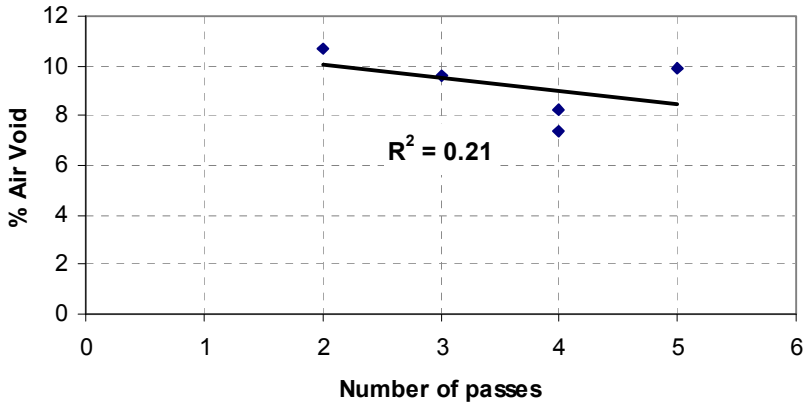

(a)

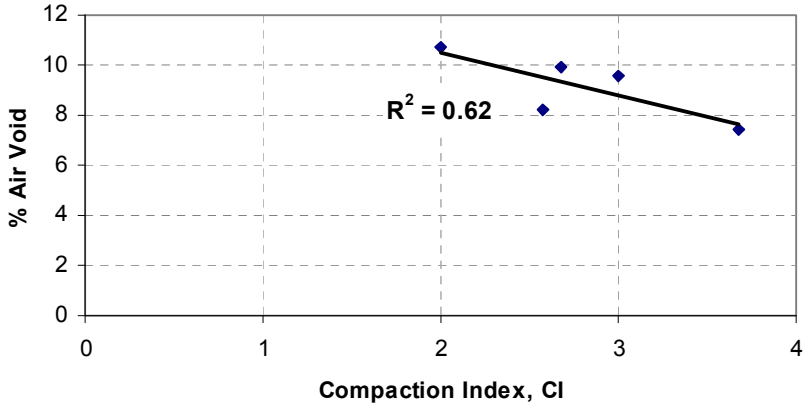

(b)

Figure 4-8. (a) Number of Passes versus the Percent of Air Voids in the US 259 Test Section (Pattern 1), (b) CI versus the Percent of Air Voids in the US 259 Test Section (Pattern 1).

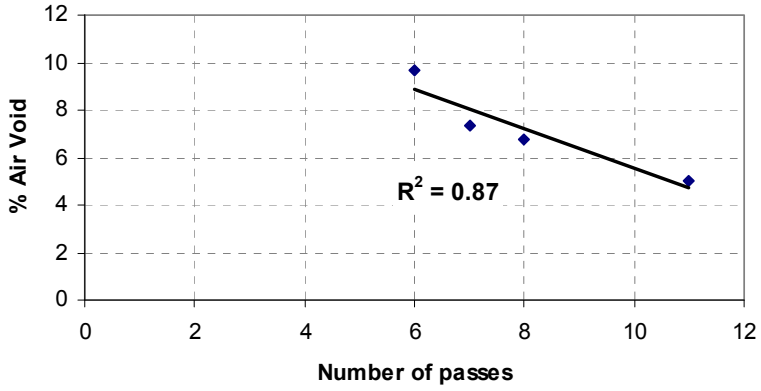

(a)

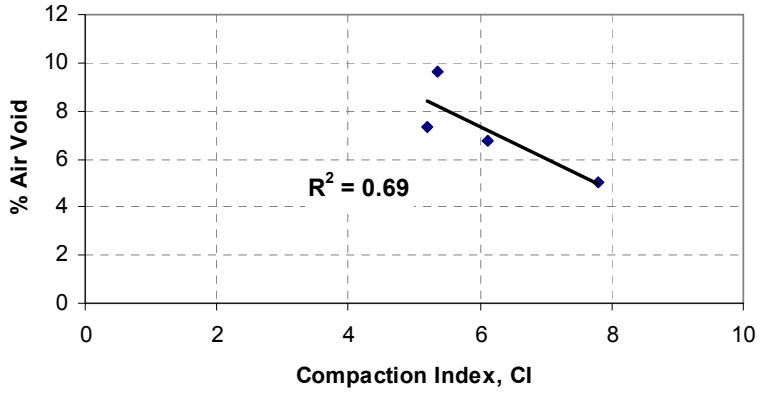

(b)

Figure 4-9. (a) Number of Passes versus the Percent of Air Voids in the US 87 Test Section (Pattern 1), (b) CI versus the Percent of Air Voids in the US 87 Test Section (Pattern 1).

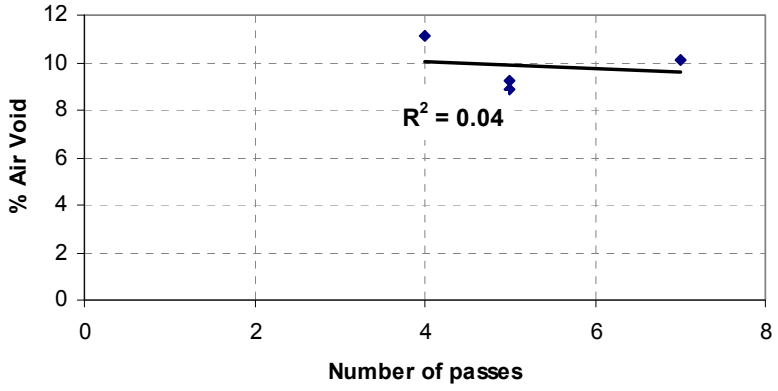

(a)

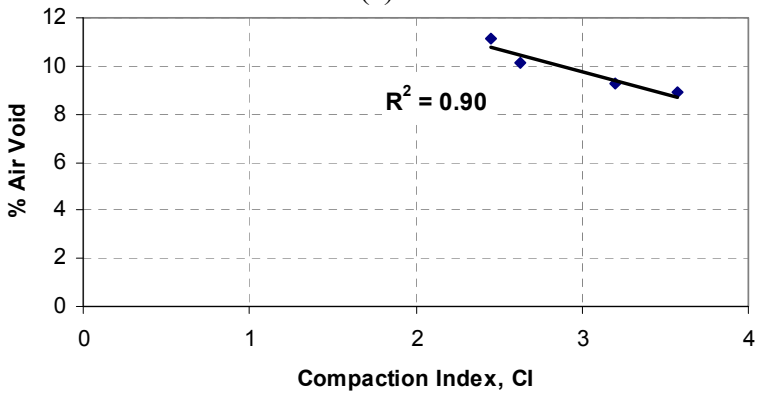

(b)

Figure 4-10: (a) Number of Passes versus the Percent of Air Voids in the SH 21 Test Section (Pattern 1), (b) CI versus the Percent of Air Voids in the SH 21 Test Section (Pattern 1).

APPLICATIONS OF THE COMPACTION INDEX

The relationship between percent air voids and CI can be very useful to setup the compaction pattern (number of passes and location of these passes). The compaction pattern can be adjusted to achieve uniform CI distribution across the pavement section, which corresponds to uniform air void distribution. This point is illustrated in Figures 4-11 and 4-12, which were generated by inputting the location of each core and its percent air voids to the Matlab 7.1 software (2004). Then an interpolation algorithm in Matlab was used to predict percent air voids in the whole pavement section. Figures A-17 through A-26 in Appendix A show the results for the remaining test sections

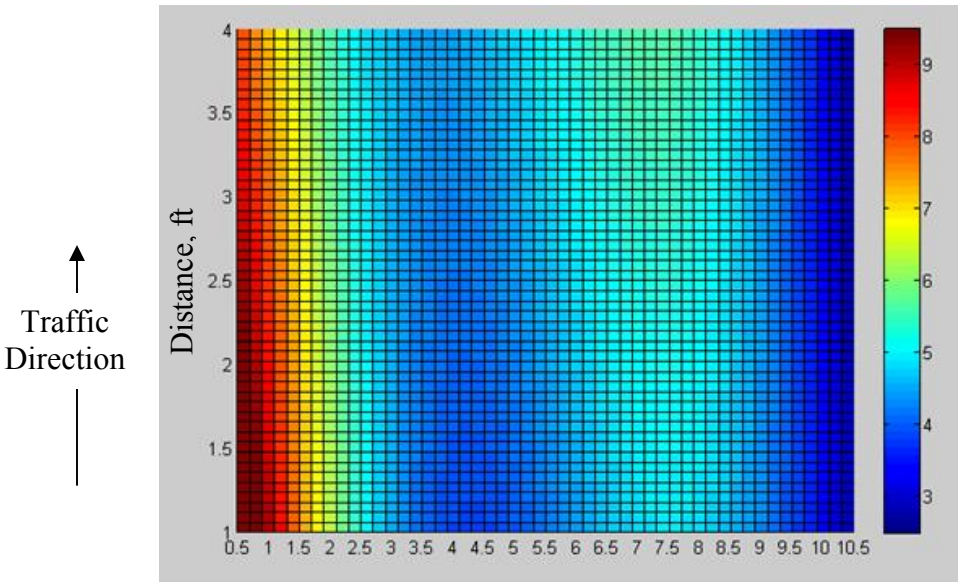

(a)

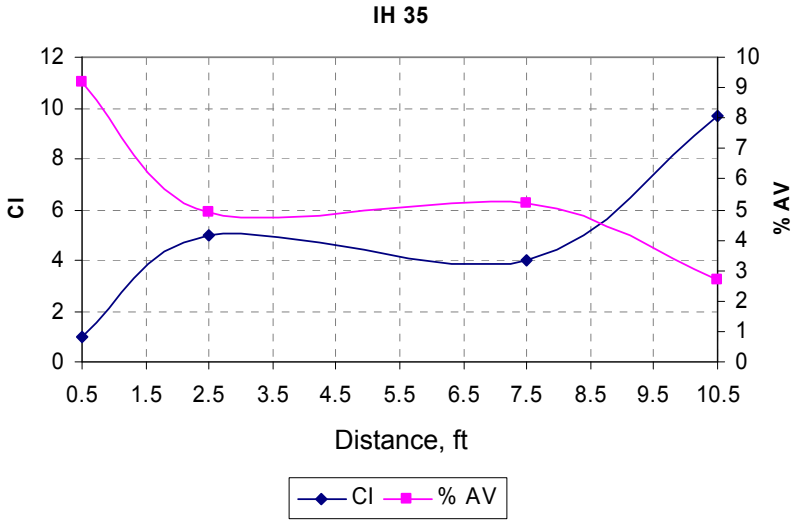

(b)

Note: the total width of the mat is 15 ft.

Figure 4-11. (a) Air Void Distribution (%) across the Mat for the IH 35 Job (b) The CI and Average Percent of Air Voids across the Mat for the IH 35 Test Section.

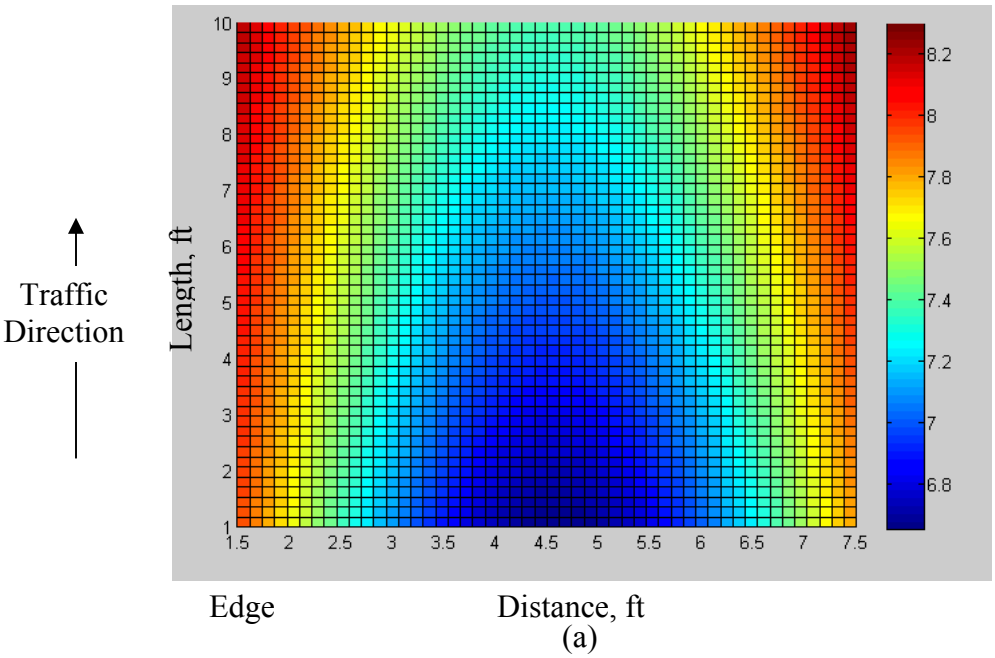

(a)

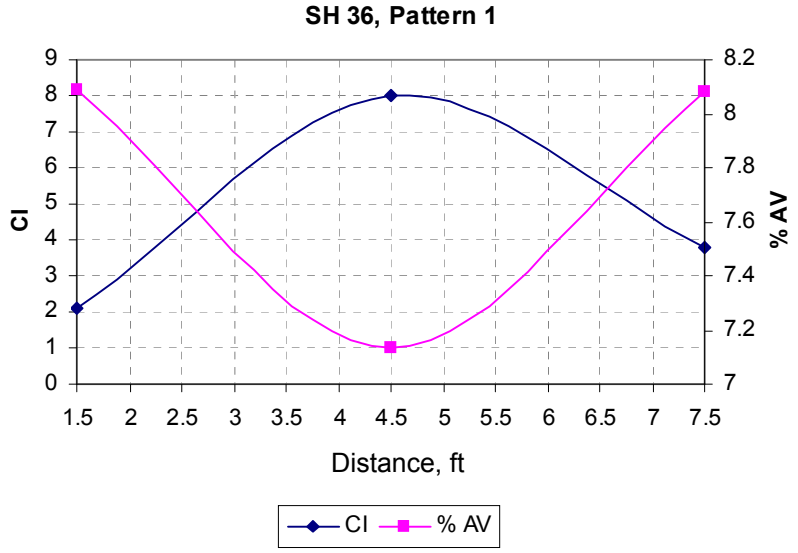

(b)

Note: The total width of the mat is 14 ft.

Figure 4-12. (a) Air Void Distribution (%) across the Mat for SH 36 Test Section (Pattern 1), (b) The CI and Average Percent of Air Voids across the Mat for SH 36 Test Section (Pattern 1).

The CI can also be used to determine the sensitivity of a mixture to the compaction effort. Relationships of CI to percent air voids are shown in Figure 4-13. Percent air voids changes at different rates as more compaction effort is applied (increase in CI). It is interesting to note that the SH 36 mixture was not as sensitive to changes in CI compared to the other mixtures. The SH 36 mixture consisted of small size relatively soft limestone aggregates with a 9.5 mm nominal maximum size. The results in Figure 4-13 indicate that this mixture can be easily compacted using relatively small compaction effort. Continuing increase in compaction effort (increase in CI) did not help in decreasing percent air voids.

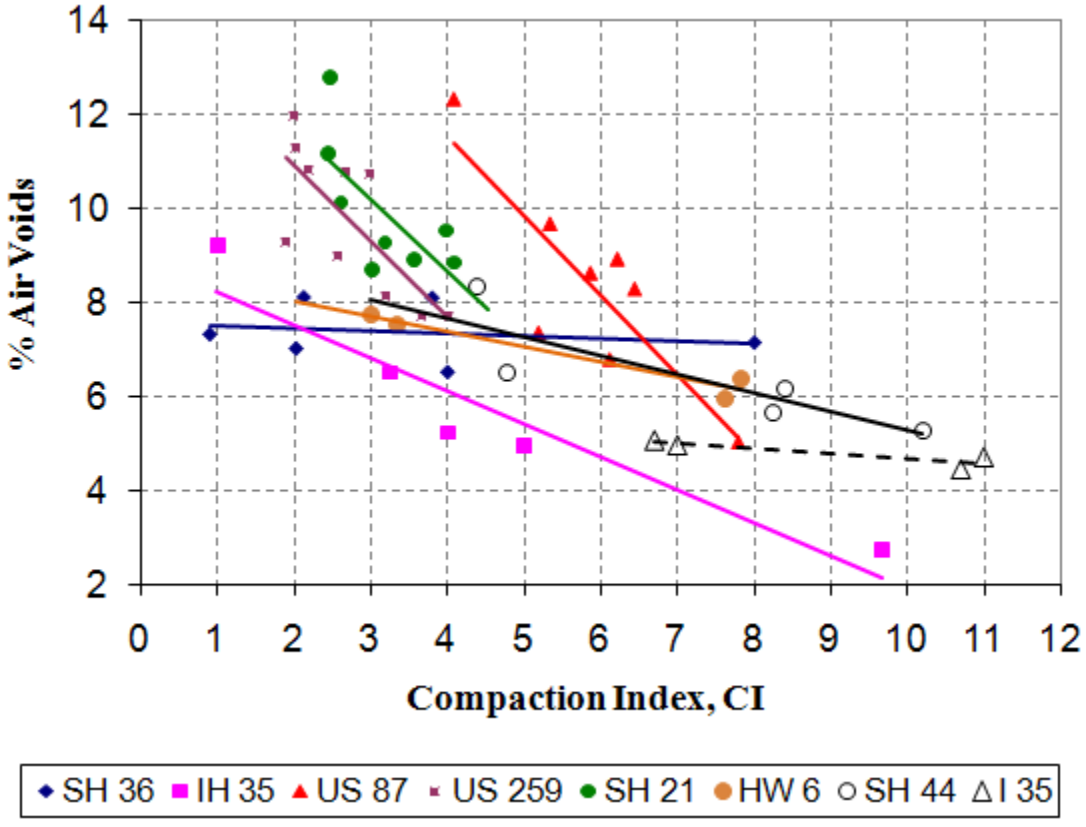

Figure 4-13. The CI versus the Percent of Air Voids.

RELATIONSHIP OF LABORATORY COMPACTION TO FIELD COMPACTION

Four SGC specimens (150 mm diameter and approximately 63.5 mm in height) were compacted at a 1.25° gyration angle, and two specimens were compacted at a 2.0° gyration angle from each mixture. Slope of percent air voids to number of gyrations in logarithmic scale was calculated. Figure 4-14 shows the relationship between the average slope up to 8 percent air voids in the laboratory versus the CI at this percent air voids. Samples with higher slope in the laboratory needed less CI in the field (less compaction effort). This relationship offers the potential to estimate the required compaction effort in the field (i.e., CI) based on the slope of number of gyrations and percent air voids in the laboratory. It should be pointed out that the compactability of SH 44 at 8 percent air voids could not be assessed in the field since the extracted cores had relatively low percent air voids

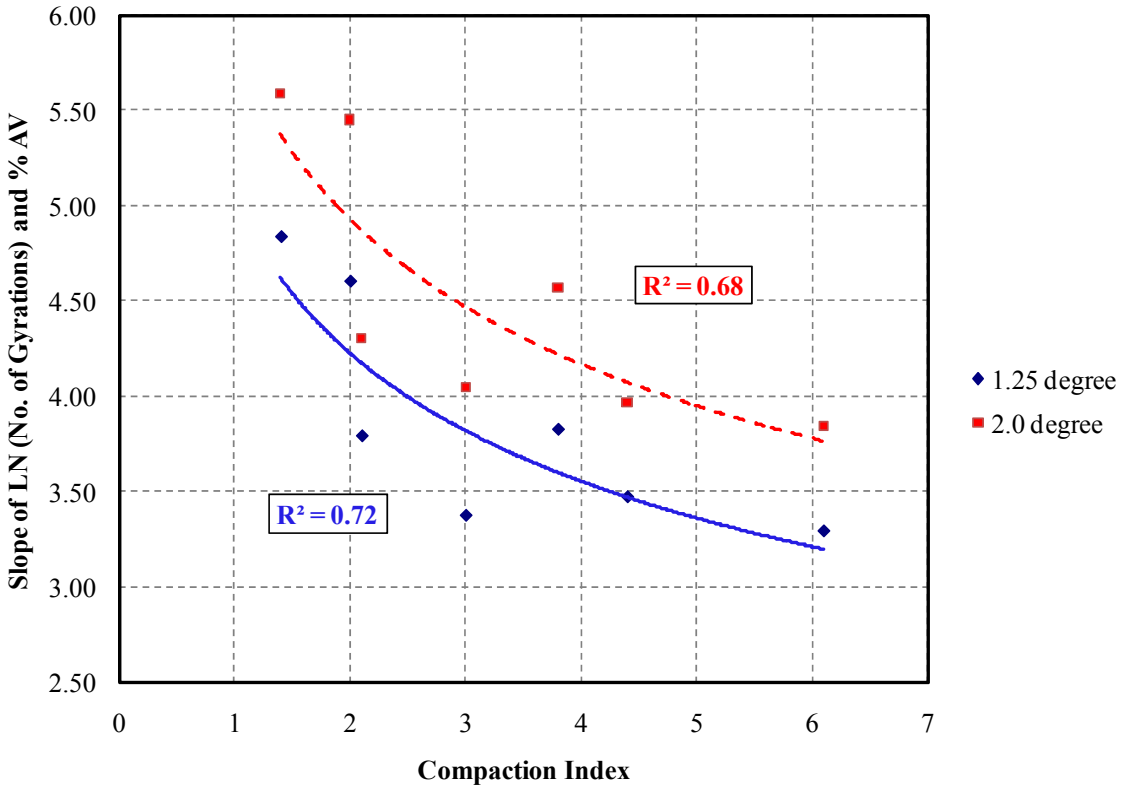

Figure 4-14. Compaction Index versus the Slope of LN (No. of Gyrations) and Percent Air Voids Curve at 8 Percent Air Voids for Different Mixes.

INFLUENCE OF COMPACTION PATTERN ON UNIFORMITY OF AIR VOID DISTRIBUTION

X-ray Computed Tomography

X-ray CT is a nondestructive test used to capture the internal structure of materials. Various applications of this method are discussed by Masad (2004). The X-ray CT setup at Texas A&M University is shown in Figures 4-15 and 4-16. This setup includes two separate systems placed in the same shielding cabinet. The mini-focus system has a 350 kV X-ray source and a linear detector, while the micro-focus system has a 225 kV X-ray source and an area detector.

The mini-focus source can penetrate thicker and denser specimens than the micro-focus source. The micro-focus system is capable of achieving a better resolution than the mini-focus system. All the experimental measurements in this study were conducted using the mini-focus 350 kV X-ray source system which has the necessary power to penetrate the asphalt mix specimens with a reasonable resolution. More details on the different X-ray CT configurations and their capabilities can be found in the paper by Masad (2004)

The densities of the different components of the mixture are represented in an image that consists of 256 gray intensity levels as low density material is represented by a darker color. The images were captured every 1 mm in the vertical direction and with a horizontal resolution equal to about 0.17 mm/pixel. The X-ray CT images were processed in order to separate air voids from the other mix constituents (aggregate and asphalt), and these images were analyzed to determine average percent air voids in each image ($\%AV_{image}$) as shown in Equation 4-1:

$$\%AV_{image} = \frac{A_{TV}}{A_T} \tag{4-1}$$

where, A_{TV} is the total area of the air voids in a CT image and A_T is the total cross-sectional area of a CT image. The analysis was conducted using macros that were developed in Image-Pro® Plus software (1999).

Figure 4-15. X-Ray CT System at Texas A&M University.

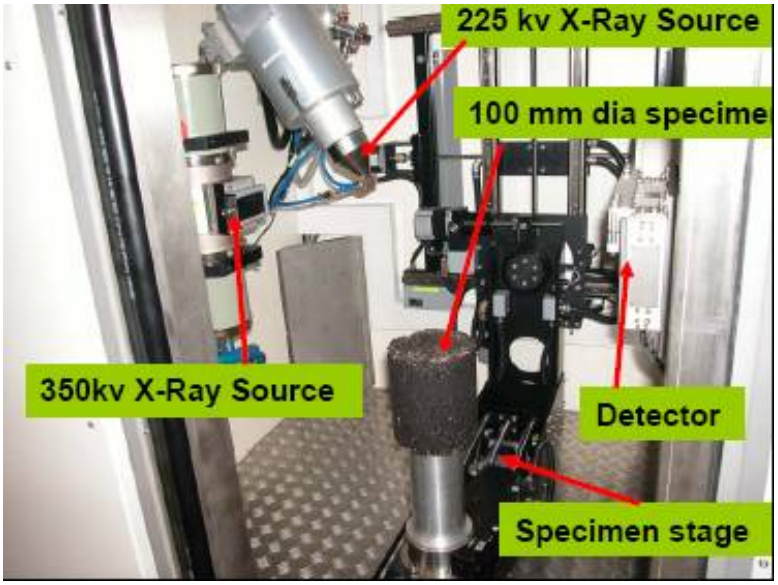

Figure 4-16. Components of X-Ray Computed Tomography System.

Three-Dimensional Air Void Distribution Maps

Three-dimensional maps of air void distribution in pavement sections were generated by inputting percent air voids as a function of depth (from X-ray CT images) and the location of cores in the pavement to the Matlab 7.1 software. This application provides an estimate of percent air voids at any point in the pavement section every 1 mm of depth. As such, one can determine the detailed three-dimensional distribution of air voids.

Figures 4-17 through 4-20 show examples of the vertical distribution of air voids in pavement sections. Figures A-27 through A-33 in Appendix A show the results for more test sections. The results from compaction patterns 1 have all shown that the middle part of the pavement has less percent of air voids or is more compacted than the top and the bottom parts. It is interesting to note that the use of a pneumatic tire compactor in the breakdown stage in projects US 87 and SH 21 resulted in a more uniform distribution and a higher density in the top two- thirds of the pavement thickness. This can be seen by comparing Figure 4-18 versus Figure 4-17 and Figure 4-20 versus Figure 4-19. In order to better illustrate this point, Figure 4-21 shows the percent air voids for the SH 21 test section in 5 mm increments across the depth for both compaction patterns. The results confirm that the top 25 mm had more uniform percent air voids and was more compacted in compaction Pattern 2, where a pneumatic tire roller was used in breakdown, compared with Pattern 1.

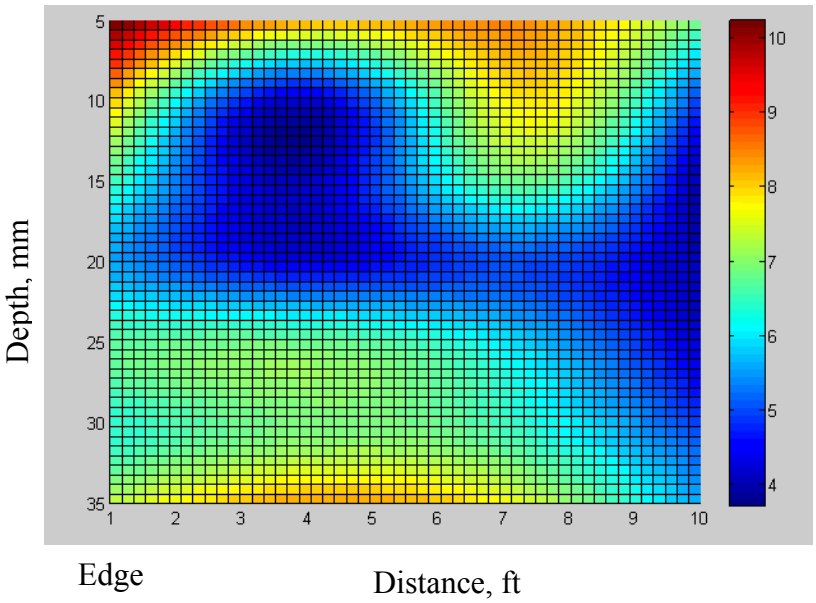

Note: Total width of the mat is 14.5 ft.

Figure 4-17. Air Void Distribution (%) along the Depth of the Mat for the US 87 Test Section (Pattern 1).

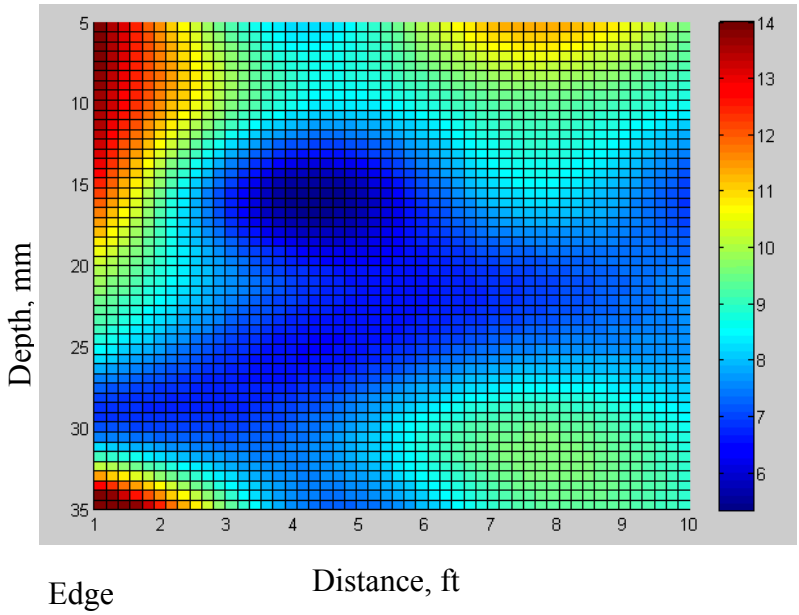

Note: Total width of the mat is 14.5 ft.

Figure 4-18. Air Void Distribution (%) along the Depth of the Mat for the US 87 Test Section (Pattern 2).

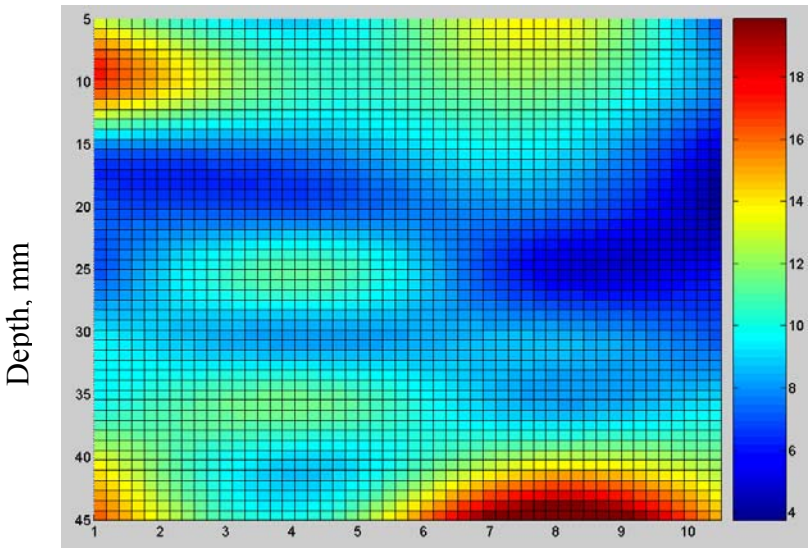

Note: Total width of the mat is 11.5 ft.

Figure 4-19. Air Void Distribution (%) along the Depth of the Mat for the SH 21 Test Section (Pattern 1).

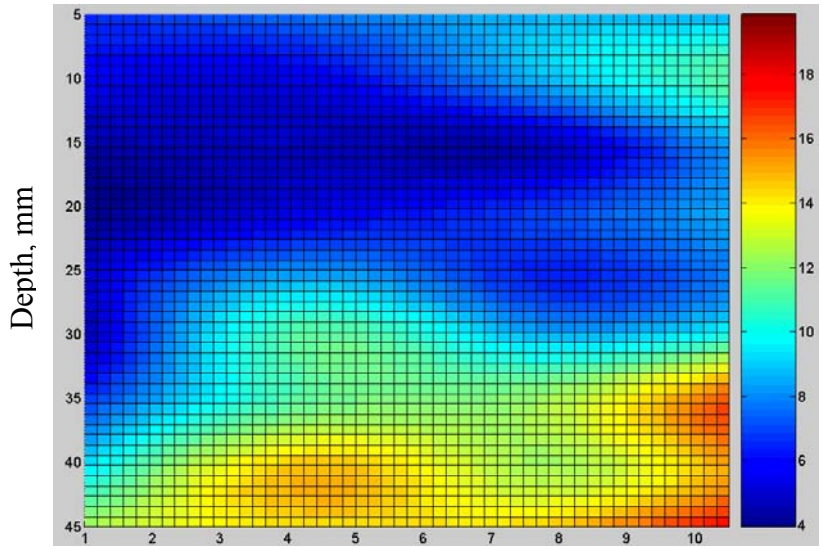

Note: Total width of the mat is 11.5 ft.

Figure 4-20. Air Void Distribution (%) along the Depth of the Mat for the SH 21 Test Section (Pattern 2).

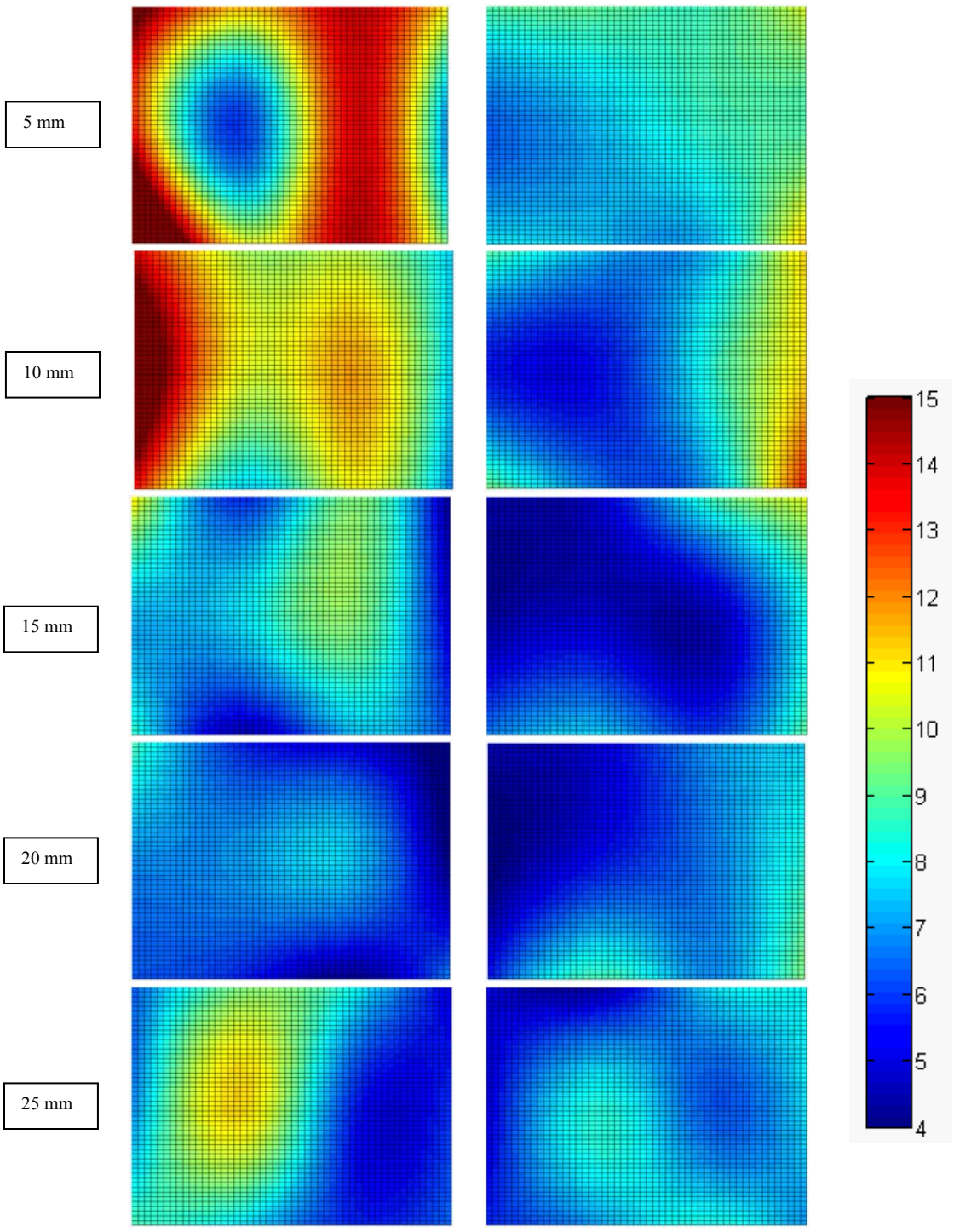

Figure 4-21. Air Void Distribution (%) across the Mat at Different Depths for the SH 21 Test Section.

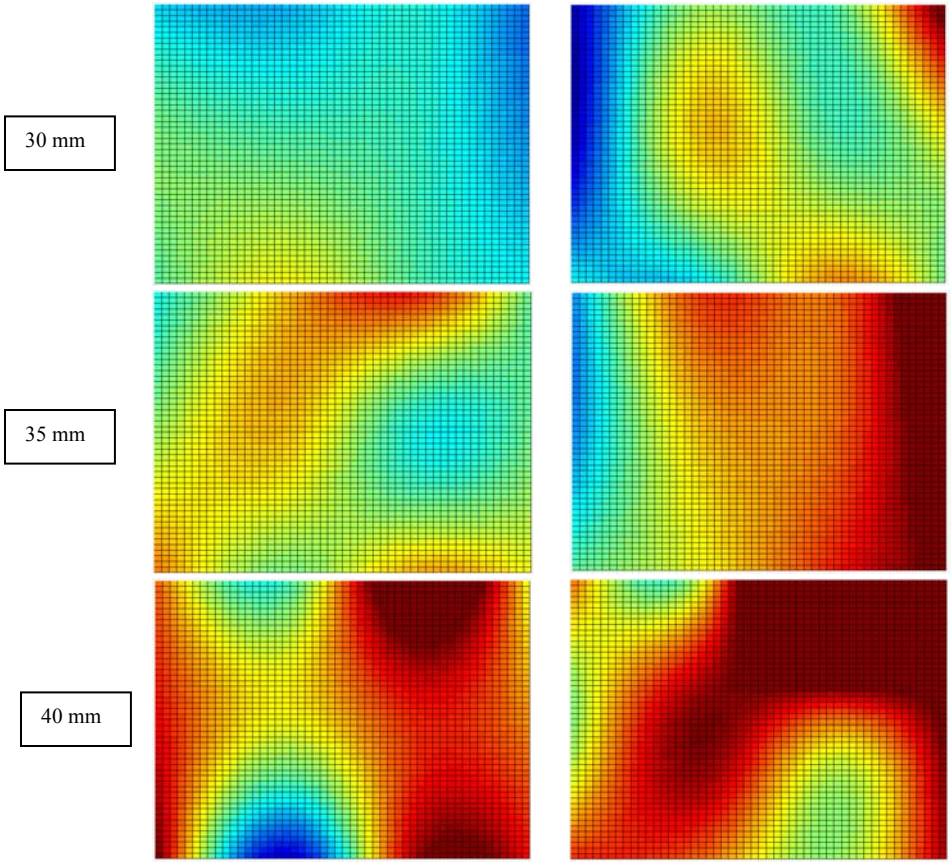

Note: The x-axis is 9.5 ft, and y-axis is 6 ft (a) Pattern 1 (b) Pattern 2.

Figure 4-21. Continued.

Quantifying Uniformity of Air Void Distribution

The uniformity of air void distribution is quantified using two indices. The first index is the difference in air voids between the top and bottom halves of a core (%AV (Top) - %AV (Bottom). The second index is termed the Uniformity Index (UI) and is calculated as follows:

1. Plot percent air voids *f(x)* against the core depth x.
2. Fit a fourth order polynomial for *f(x)*.
3. Calculate the derivate *f'(x)* of the function *f(x)*.
4. Calculate the UI using Equation 4-2.

$$UI = \frac{1}{b-a}\int_{a}^{b}\left[f'(x)\right]^2 dx \qquad (4\text{-}2)$$

The fourth order polynomial was found to fit the percent air voids function very well. The UI is equal to zero for a straight line function representing uniform distribution, and it increases with an increase in nonuniformity. The integration limits depend on the thickness over which the analysis is conducted. For a core with thickness equal to h, the analysis is conducted for the whole core (a=0, b = h), for the top half (a=0, b=h/2), and for the bottom half (a=h/2 and b=h).

Some results are presented in Figures 4-22 through 4-25. In these figures, the field cores are labeled according to their locations in the mat as follows; right longitudinal joint (RJ), right wheel path (RW), center of paving lane (Cen.), left wheel path (LW), and left longitudinal joint (LJ). The results for US 87 are shown in Figures 4-22 and 4-23. The use of the pneumatic tire roller in breakdown in the second compaction pattern resulted in less percent air voids in the top as indicated with the mostly negative values in Figure 4-22b compared with the mostly positive values in Figure 4-22a. Also, the second compaction pattern results in less UI (more uniform air void distribution) especially in the top half as indicated in Figure 4-23. These results support the discussion in the previous section that the use of the pneumatic tire roller in breakdown is more effective in inducing more compaction toward the pavement surface.

The results for SH 21 are shown in Figures 4-24 and 4-25. The difference in percent air voids between the top and the bottom became more negative in Pattern 2 indicating less percent air voids in the top. The uniformity in the top improved (UI decreased) in compaction Pattern 2 compared with compaction Pattern 1. These results are consistent with the findings from US 87. Figures A-34 through A-51 in Appendix A show the findings for the remaining test sections.

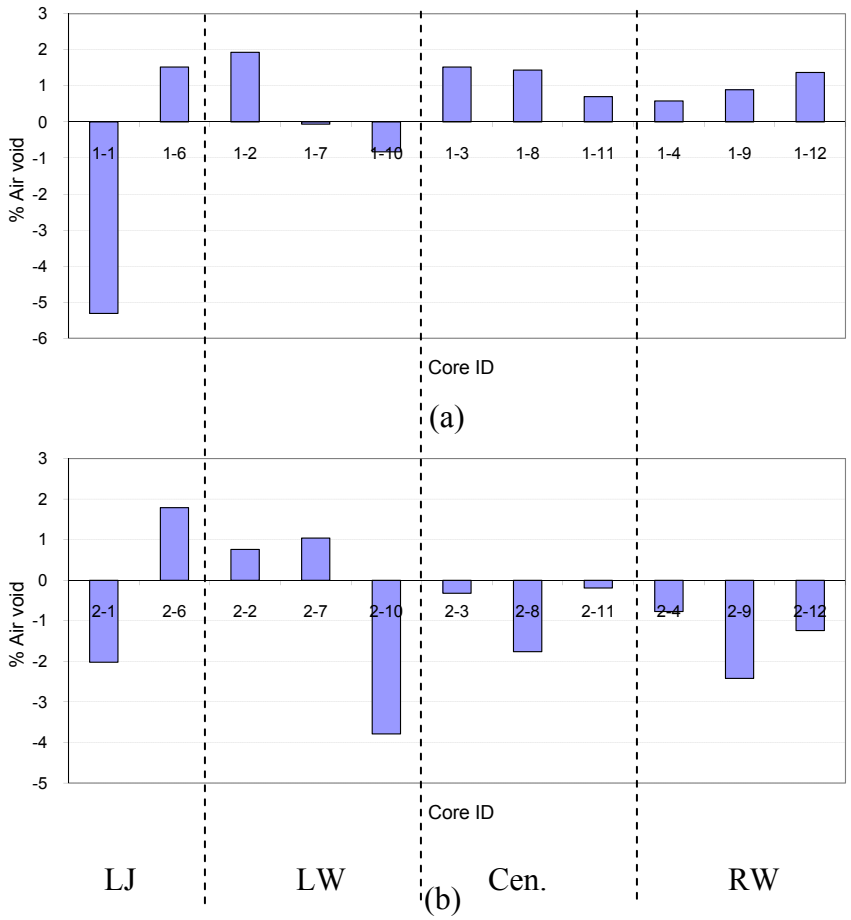

Figure 4-22. Difference between the Percent of Air Voids at the Top and Bottom Parts for the US 87 Test Section (a) Pattern 1, (b) Pattern 2.

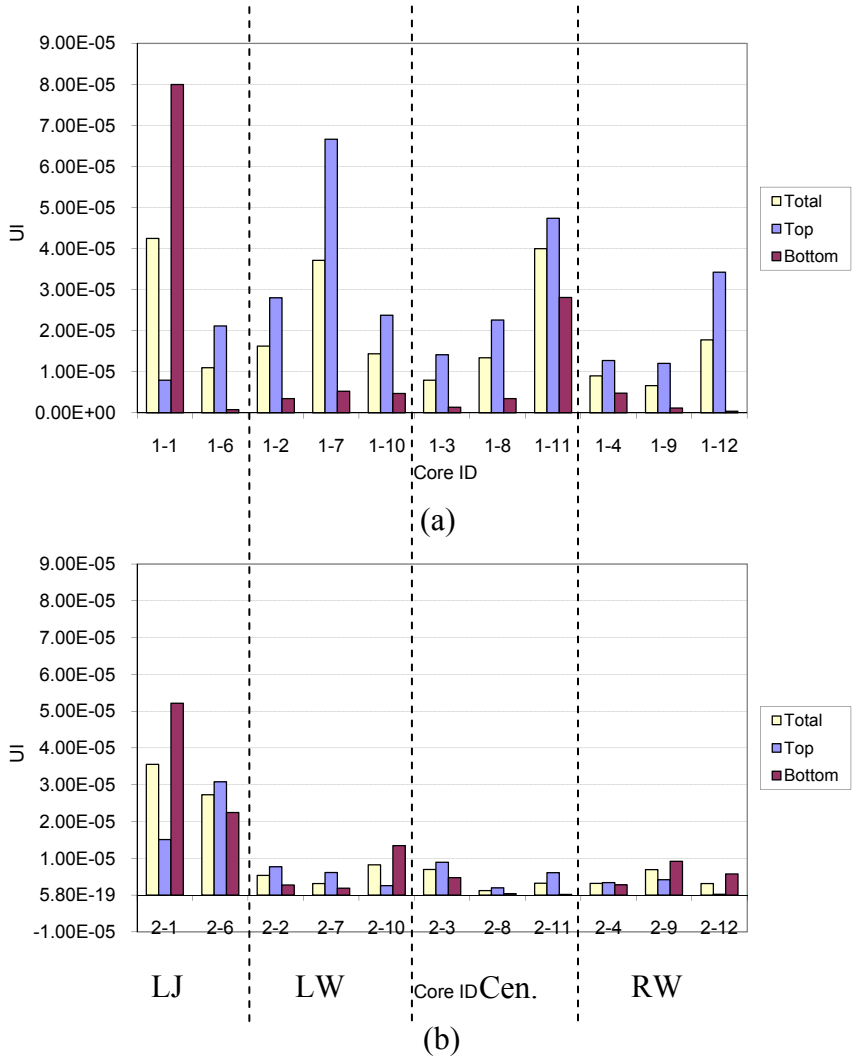

Figure 4-23. UI for the US 87 Test Section (a) Pattern 1, (b) Pattern 2.

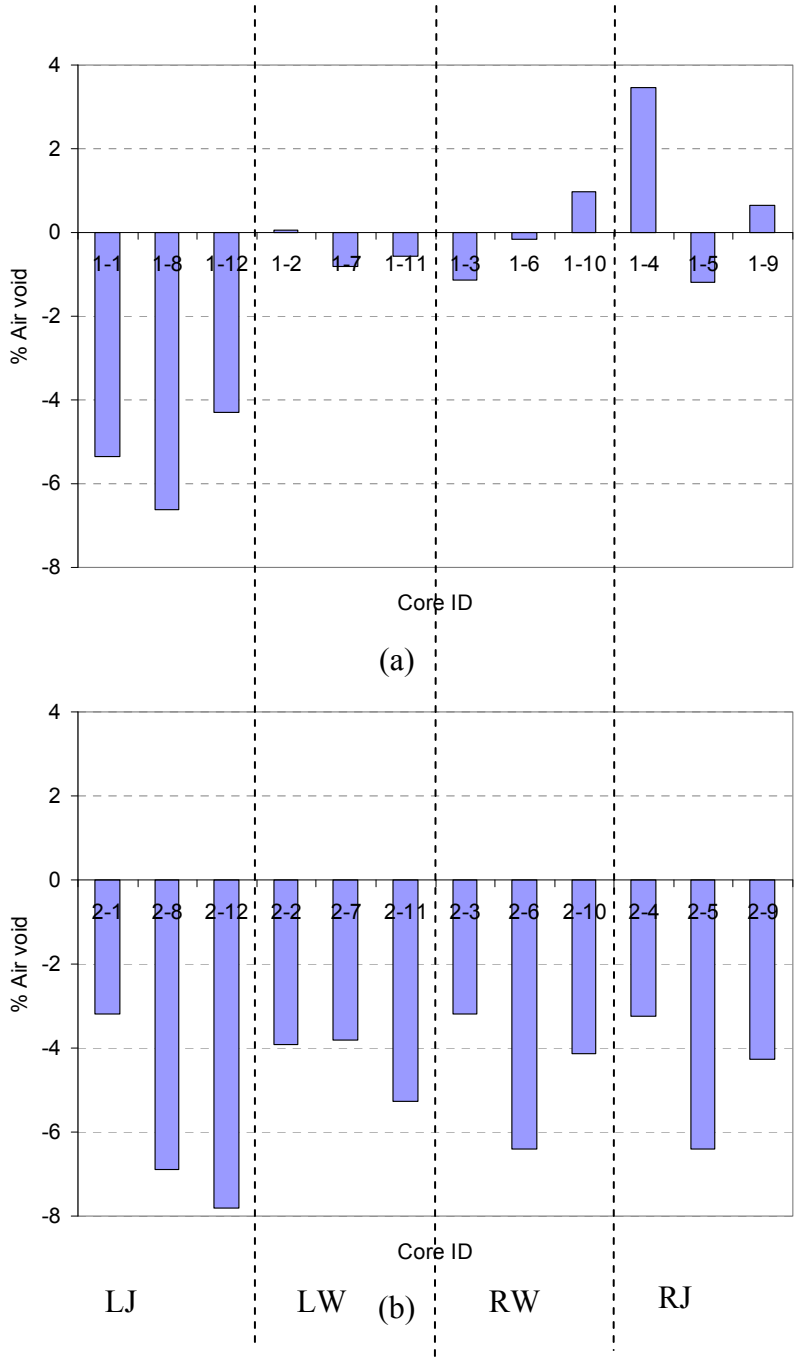

Figure 4-24. Difference between the Percent of Air Voids at the Top and the Bottom Parts for the SH 21 Test Section (a) Pattern 1, (b) Pattern 2.

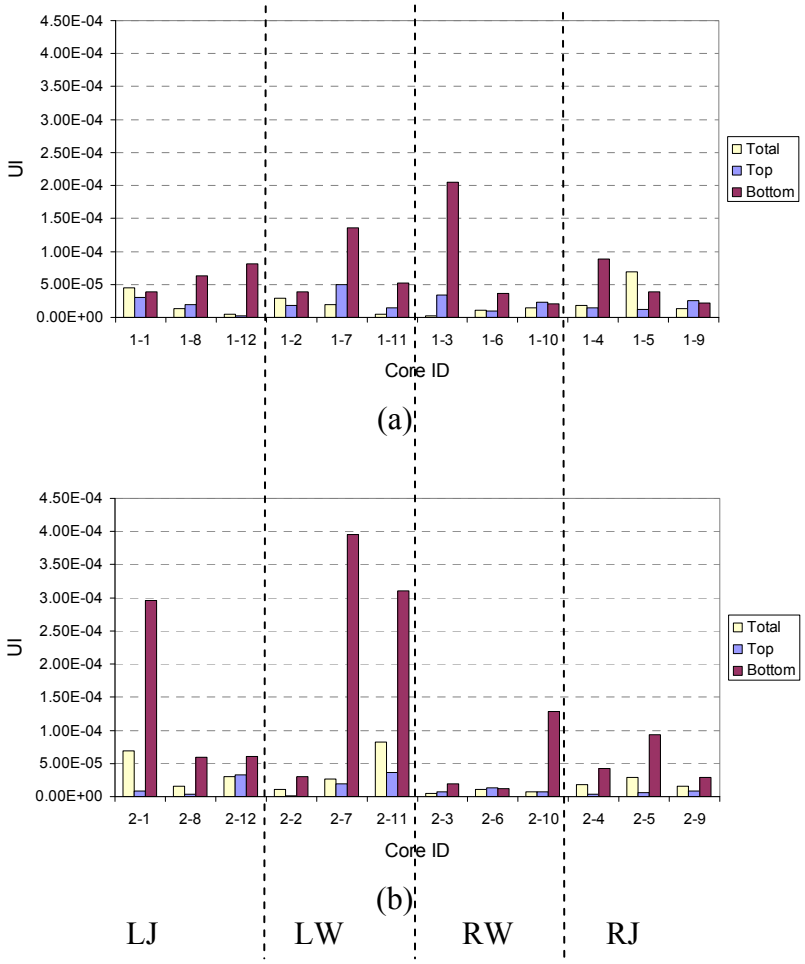

Figure 4-25. UI for the SH 21 Test Section (a) Pattern 1, (b) Pattern 2.

COMPACTION OF LONGITUDINAL JOINTS

It is well accepted that asphalt pavement close to the longitudinal joint tends to be less compacted than toward the center of the pavement. This is caused by the tendency to apply fewer passes at the joints. Also, the low confinement at some types of joints (unrestricted or unconfined joints) and the higher rate at which the mixture at the joint loses heat reduce the efficiency of compaction at the joint compared with the pavement center. In this study, the compaction of longitudinal joints and the possible methods that can improve this compaction are discussed in this section.

The research team obtained field cores from different locations of the mat as well as from near the longitudinal joints. The joint construction was not the same for all

projects (vertical versus tapered or confined versus unconfined). Left and right longitudinal joints of the IH 35 test section were confined and unconfined vertical joints, respectively. Both edges of the SH 36 mat had unconfined tapered (wedge) longitudinal joints. Left and right longitudinal joints of the US 87 test section were confined and unconfined tapered joints, respectively. The right edge of the US 259 mat was free (shoulder), whereas the left edge of the same mat had a vertical longitudinal joint. Both edges of the SH 21 test section mat had tapered confined longitudinal joints.

As expected, the air void of specimens near the longitudinal joints had a higher percent of air voids than the other parts across the mat. However, percent air voids near the confined or restrained longitudinal joints were closer to that at the center of the mat compared with the unconfined joints.

In this study as discussed in Figure 4-5, it was found that the effectiveness factor decreases at the edge of the roller. An important aspect influencing joint compaction is overhanging of roller edge at a distance of about 1.5 ft to 2 ft from the longitudinal joint. One example is given in Figure 4-26 which shows the percent of air void distribution and CI across the mat in the US 259 test section. As can be seen, the cores taken from the right edge (restrained joint) had the lowest percent of air voids which corresponds to the highest CI across the mat. In this particular case, the steel wheel roller had 2 ft overhanging from the restrained joint, resulting in a higher CI at that location. Interestingly, there are some areas within the mat that have less density than the ones at the restrained longitudinal joints. These areas were subjected to a lower CI as a result of poor overlapping.

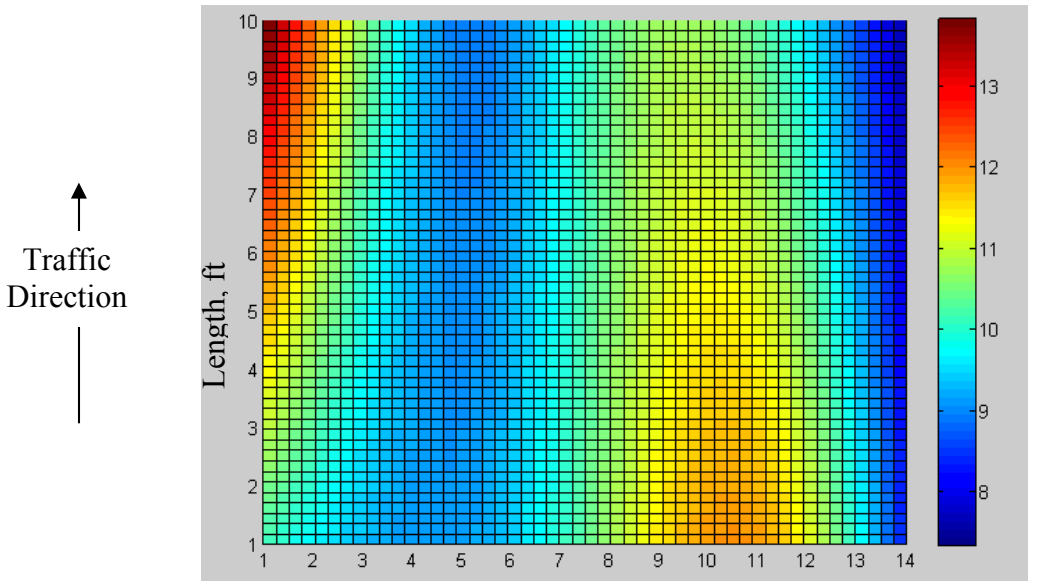

(a)

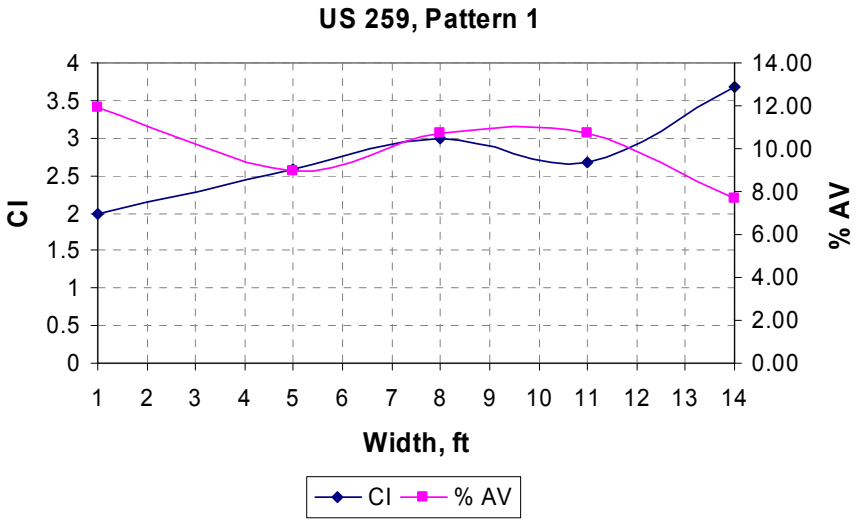

(b)

Note: The total width of the mat is 15 ft.

Figure 4-26. (a) Air Void Distribution (%) across the Mat for the US 259 Test Section (Pattern 1), (b) The CI and Average Percent of Air Voids across the Mat for the US 259 Test Section (Pattern 1).

The air void distribution was found to be more uniform at the restrained joint than at the unrestrained one as can be seen from Figure 4-27. The UI, explained in Equation 4-2, for total depth at unrestrained joint samples is higher than the UI of samples obtained

from restricted joint. The authors recommend the overhanging of steel rollers to be at least 2 ft.

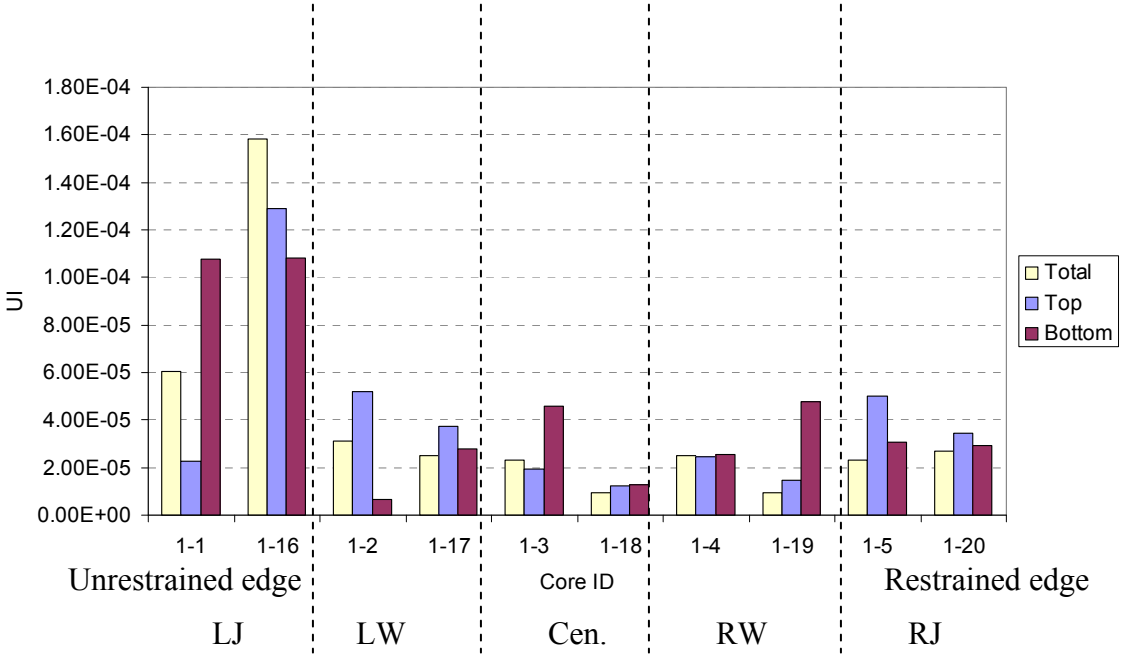

Figure 4-27. UI for the US 259 Test Section (Pattern 1).

CONCLUSIONS

This study provided experimental evaluation of the influence of the field compaction pattern on level of compaction and the uniformity of air void distribution in asphalt pavements. The findings showed that the efficiency of compaction at a given point in the pavement is a function of the location of the roller with respect to this point. The efficiency of compaction at the center of the roller is better than at the edge of the roller. Therefore, a new index referred to as the Compaction Index (CI) is proposed to quantify the compaction effort at any point in the pavement. This index is the summation of the multiplication of each pass with an effectiveness factor, which is a function of distance from the edge of the roller. The CI is useful to set up the compaction pattern in order to achieve the desired percent air voids uniformly across the pavement section; a more uniform CI corresponds to more uniform air void distribution. In terms of compaction sequence, the use of the

pneumatic roller in the breakdown stage was found to be effective in reducing the percent air voids and improving uniformity in the top half of the lift thickness.

The CI can also be used to determine the sensitivity of a mixture to the compaction effort. Some mixtures achieve a certain level of percent air voids and further increase in compaction effort or CI does not help in reducing percent air voids.

This study demonstrated that there is a relationship between slope of a laboratory compaction curve and CI values. This relationship can be used to determine the required field compaction effort based on laboratory compaction data.

It has been reported in the past that the mixture near longitudinal joints is usually less compacted than the rest of the pavement section. This has been attributed to the lower confinement, typically lower number of passes and the faster rate of heat loss at the joint compared with the center of the pavement. Based on the results of this study, the low compaction at the joint is also attributed to the low effectiveness factor because a joint is typically compacted using the roller edge. Consequently, joints need to be compacted to a higher CI compared with the center of the pavement in order to compensate for the other factors that reduce joint compactability. This can be achieved by overhanging of the steel rollers by at least 2 ft.

CHAPTER V
COMPARISON OF LABORATORY AND FIELD MECHANICAL PROPERTIES

INTRODUCTION

The research team obtained field cores from the ten construction projects discussed in Chapter III. Field cores from all projects were tested to measure density (both vacuum sealed or CoreLok and Saturated Surface Dry or SSD methods), air void distribution using X-ray CT, permeability, rutting resistance using Hamburg wheel tracking device, and fatigue resistance using overlay tester. In addition, specimens were compacted in the laboratory using virgin materials obtained from the HMA plants for selected projects where compaction patterns were varied in the field (FM 649, SH 36, US 87, US 259, and SH 21). Plant mixes obtained from the field sites were tested to determine maximum specific gravity, binder content, and gradation. Table 5-1 presents the summary of tests conducted with specimens obtained from each construction projects.

HAMBURG TEST RESULTS

The Hamburg test was conducted following TxDOT standard Tex-242-F "Hamburg Wheel-tracking Test." Laboratory specimens were compacted using both 1.25° and 2.0° gyratory angles to achieve 7±1 percent air void. Table 5-2 summarizes the Hamburg test results.

All the tests were set to run for 20,000 cycles or 12.5 mm rut depth, whichever came first. In some cases the specimens failed (rut depth of 0.5 inch or 12.5 mm) before reaching 20,000 cycles and in some cases the test stopped slightly before a 12.5 mm rut depth. In order to compare the results, the average rutting rate was calculated as the rutting depth in mm divided by Log (number of cycles). The shaded cells in Table 5-2 represent those results where the tests were continued until the rut depth reached 12.5 mm.

Table 5-1. Laboratory Tests Conducted with Different Mixtures from Field Compaction Study.

Highway ID	Comment	Tests with Field Cores					Tests with Lab Mixed Lab Compacted Specimens					
		Density	X-ray CT	Ham-burg	Perme-ability	Over-lay	Comment	Density	X-ray CT	Ham-burg	Perme-ability	Over-lay
US 281, PHR	One Compaction Pattern	CoreLok & SSD	Yes	Yes	Yes	Yes	1.25° angle	CoreLok & SSD	Yes	N/A	N/A	N/A
FM 649, LRD	Two Compaction Patterns	CoreLok & SSD	Yes	Yes	Yes	Yes	1.25° & 2.0° angle	CoreLok & SSD	Yes	Yes	Yes	Yes
IH 35, WAC	One Compaction Pattern	CoreLok & SSD	Yes	Yes	Yes	Yes	1.25° angle	CoreLok & SSD	Yes	N/A	N/A	N/A
SH 36, YKM	Two Compaction Patterns	CoreLok & SSD	Yes	Yes	Yes	Yes	1.25° & 2.0° angle	CoreLok & SSD	Yes	Yes	Yes	Yes
US 87, YKM	Two Compaction Patterns	CoreLok & SSD	Yes	Yes	Yes	Yes	1.25° & 2.0° angle	CoreLok & SSD	Yes	Yes	Yes	Yes
US 259, TYL	Two Compaction Patterns	CoreLok & SSD	Yes	Yes	Yes	Yes	1.25° & 2.0° angle	CoreLok & SSD	Yes	Yes	Yes	Yes
SH 21, AUS	Two Compaction Patterns	CoreLok & SSD	Yes	Yes	Yes	Yes	1.25° & 2.0° angle	CoreLok & SSD	Yes	Yes	Yes	Yes
SH 44, LRD	One Compaction Pattern	CoreLok & SSD	Yes	Yes	Yes	Yes	1.25° angle	CoreLok & SSD	Yes	Yes	Yes	Yes
SH 6, BRY	One Compaction Pattern	CoreLok & SSD	Yes	Yes	Yes	Yes	1.25° angle	CoreLok & SSD	Yes	N/A	N/A	N/A
SL 1, AUS	One Compaction Pattern	CoreLok & SSD	Yes	Yes	Yes	Yes	1.25° angle	CoreLok & SSD	Yes	N/A	N/A	N/A

Table 5-2. Hamburg Test Results.

Highway ID	Load cycle or rut depth		Average	Average Rutting Rate
	Left Wheel	Right Wheel		
FM 649 Field Compaction 1	13925	11820	12873	3.04
FM 649 Field Compaction 2	14480	15400	14940	2.99
FM 649_1.25 D _Lab Molded	3.82	3.53	3.68	0.86
FM 649_2.0 D _Lab Molded	2.75	3.26	3.01	0.70
SH 36_Field Compaction 1	6501	3901	5201	3.36
SH 36_Field Compaction 2	7250	6350	6800	3.26
SH 36_1.25 D _Lab Molded	5950	7002	6476	3.28
SH 36_2.0 D _Lab Molded	9885	9421	9653	3.14
US 87 Field Compaction 1	5.54	3.87	4.7	1.09
US 87 Field Compaction 2	6.82	7.58	7.2	1.67
US 87_1.25 D _Lab Molded	3.55	4.17	3.86	0.90
US 87_2.0 D _Lab Molded	3.03	3.05	3.04	0.71
FM 529 Field	4.39	4.09	4.24	0.99
US 290 Field	3.34	N/A	3.34	0.78
IH 35_Waco Field	11.65	9.82	10.74	2.50
US 281_Pharr Field	4301	6151	5226	3.36
US 259 Field Compaction 1	21000	17400	19200	2.92
US 259_1.25 D _Lab Molded	14300	15200	14750	3.00
US 259_2.0 D _Lab Molded	22800	17800	20300	2.90
SH 21 Field Compaction 1	6.13	8.56	7.35	1.71
SH 21 Field Compaction 2	4.78	5.29	5.04	1.17
SH 21_1.25 D _Lab Molded	3.02	2.85	2.94	0.68
SH 21_2.0 D _Lab Molded	2.75	2.59	2.67	0.62
SH 44 Field	2.56	2.17	2.37	0.55
SH 44_1.25 D _Lab Molded	2.11	2.10	2.11	0.49
SH 6 Field	7.92	10.70	9.31	2.16
SL 1 Field	10.72	8.49	9.61	2.23

Note: Rut depth is given in mm.

As shown by the average rutting rate in Table 5-2, specimens compacted in the lab using a 2.0° gyratory angle performed slightly better than samples compacted with a 1.25° gyratory angle. In Figure 5-1, the performance of gyratory compacted samples was comparable to the performance of field samples when the field air void was close to 7 percent (US 87 and SH 36). Field samples from FM 649 (both compaction patterns) performed much worse than that of corresponding gyratory compacted samples because field cores from FM 649 had almost 11 percent air voids.

Among these construction projects US 87, SH 21, IH 35 and SH 44 performed very well in Hamburg tests with both lab and field samples. US 87 Pattern 2 field sample

performed slightly worse than Pattern 1. This can be attributed to the difference in percent air voids because US 87 Pattern 2 had almost 2 to 3 percent higher air voids than Pattern 1. The effect of the change of the compaction pattern on rutting of cores from SH 21 project was clear. Cores extracted from Pattern 2 performed better than the corresponding ones in compaction Pattern 1. The average percent of air voids in the test samples from both patterns were comparable. It is believed that the air void structure in Pattern 2 provided better resistance to rutting. The field cores from Pattern 2 had less percent of air void at the top part compared with the bottom one as indicated in Figure 4-23 in Chapter IV. These results agree with project FM 649. All cores from compaction Pattern 2 showed that the top part had less air voids than the bottom part. The Hamburg results revealed that compaction Pattern 2 performed slightly better than compaction Pattern 1 (Table 5-2). It seems that having a less percent of air void at the top might help in resisting the rutting.

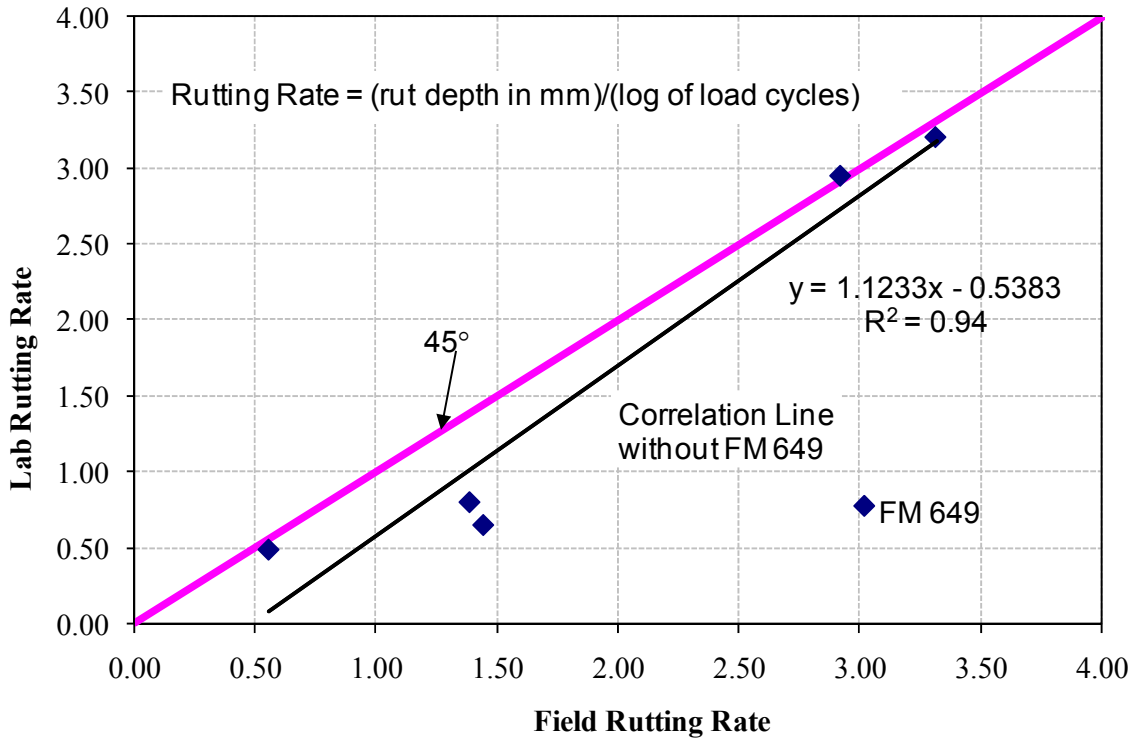

Figure 5-1. Comparison of Field and Lab Compacted Hamburg Specimens.

SH 36 samples (both lab and field) performed relatively poorly. US 259 field samples passed the TxDOT criteria and it was comparable to the corresponding lab samples compacted at a 2.0° gyratory angle. However, samples compacted at a 1.25° gyratory angle barely failed TxDOT criteria of maximum 12.5 mm rut depth at 15,000 cycles for mixtures with PG 70-22 binder.

In project US 259, the Hamburg results presented in Table 5-2 demonstrate that the field cores taken from the left wheel path performed better than the cores extracted from the right wheel path. The field cores taken from the right wheel path had higher percent of air void than the cores from the left wheel path.

The IH 35 SMA mixture field sample passed TxDOT criteria. On the other hand the US 281 SMA mixture failed very poorly. Visual observation of these sample show that there was not much aggregate interlock in US 281 samples. Overall the results indicate that the percent air voids is a critical factor in affecting the relationship between lab and field rutting results. The compaction angle has only slight difference on the Hamburg rut depth results.

OVERLAY TEST RESULTS

Overlay tests were conducted on both field and lab compacted samples following the recommendations by Zhou and Scullion and recently adopted TxDOT standard Tex-248-F "Overlay Test." Figure 5-2 depicts the key parts of the overlay apparatus. This overlay tester consists of two steel plates; one is fixed, and the other moves horizontally to simulate the opening and closing of joints or cracks in the old pavements beneath an overlay. The load is applied in a cyclic, triangular waveform with constant magnitude. The overlay test is run at room temperature (77ºF) in a controlled displacement mode at a loading rate of one cycle per 10 seconds with a maximum displacement of 0.025 inch until failure occurs (Zhou and Scullion, 2003).

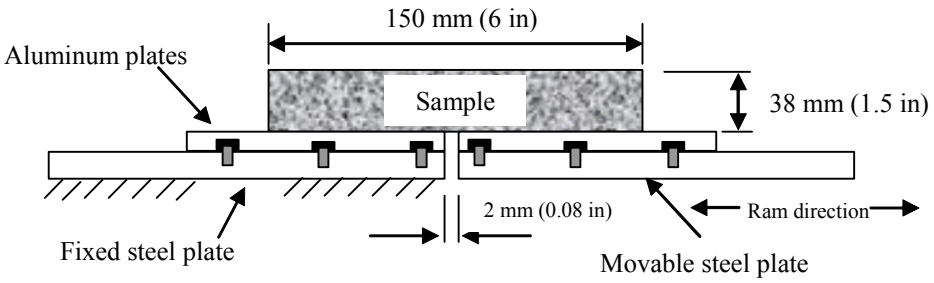

Figure 5-2. Schematic Diagram of TTI Overlay Tester System (Zhou and Scullion, 2003).

Lab samples were compacted at 1.25° and 2.0° angles of gyrations with a Superpave gyratory compactor and field samples were obtained from each compaction pattern by coring. Prismatic specimens (6 inch × 3 inch × 1.5 inch) were sawed from SGC compacted or field cores before testing. Lab samples were prepared for testing only for those highways where the research team was able to change compaction pattern. Test results from field samples and lab compacted samples are presented in Table 5-3 and Table 5-4, respectively.

Field cores from SMA mixture in IH 35, SH 6, and SL 1 performed very well, while the SMA mixture in US 281 did not (Table 5-3). The compaction pattern does not seem to influence the overlay testing results for the mixtures evaluated in this study. Lab compacted samples for FM 649, SH 36, and US 87 failed at a very low number of load cycles regardless of compaction angle. US 259 and SH 21 lab samples performed very good and reasonably well, respectively. For a given mixture, the compaction angle (1.25° or 2.0° angle) did not make much difference for overlay testing.

Table 5-3. Overlay Test Results with Field Compacted Samples.

Highway	Compaction Pattern	Number of Cycles at Failure			
		Spec 1	Spec 2	Spec 3	Avg.
FM 649	1	3	1	N/A	2
	2	2	1	N/A	2
SH 36	1	1	6	4	4
	2	7	11	6	8
US 87	1	205	61	31	99
	2	38	31	78	49
IH 35	N/A	900+	600+	600+	700+
US 281	N/A	86	24	N/A	55
US 259	1	34	71	110	72
SH 21	1	7	8	4	6
	2	14	26	13	18
SH 44	N/A	34	8	222	88
SH 6	N/A	900+	900	900+	900+
SL 1	N/A	900+	900+	900+	900+

Table 5-4. Overlay Test Results with Lab Compacted Samples.

Highway	Angle of Gyration	Number cycles At failure			
		Spec 1	Spec 2	Spec 3	Average
FM 649	1.25°	2	1	1	1
	2.00°	1	1	1	1
SH 36	1.25°	2	3	2	2
	2.00°	3	2	3	3
US 87	1.25°	2	2	1	2
	2.00°	2	2	1	2
US 259	1.25°	776	650	230	552
	2.00°	800	467	326	531
SH 21	1.25°	171	63	209	148
	2.00°	166	168	138	158
SH 44	1.25°	141	25	175	114

PERMEABILITY TEST

Permeability tests were conducted on field and gyratory compacted samples. This test was conducted following ASTM Standard D5084 “Standard Test Methods for Measurement of Hydraulic Conductivity of Saturated Porous Materials Using a Flexible Wall Permeameter” (ASTM 2006). In some cases, field cores had to be saw cut in order to separate them from the underlying layer or seal coat at the bottom. Research team believes that during saw cutting sufficient heat is produced to melt the binder which may ultimately seal some voids.

In general, field samples obtained near longitudinal joint had higher permeability than the cores obtained from inside the lane. Figures 5-3 through 5-11 show the permeability test results from SH 36, FM 649, US 87, SH 21, US 259, IH 35, SH 44, SH 6, and SL 1 projects. Field samples from FM 649 had higher permeability than gyratory compacted samples. This is attributed to the fact that samples from this road had about 4

percent air voids more than the lab samples. On the contrary, the field samples from SH 36 and US 87 had a much lower permeability than corresponding lab compacted samples. The air voids of field samples from both roads were close to lab air voids. The probable reason could be the saw cutting of field samples from SH 36 and US 87. Field samples from FM 649 were not saw cut at the bottom. The permeability of the field cores from SH 44 projects was comparable to the laboratory specimens. In general, there is no trend indicating that permeability in gyratory specimens compacted at a certain angle are higher than the other.

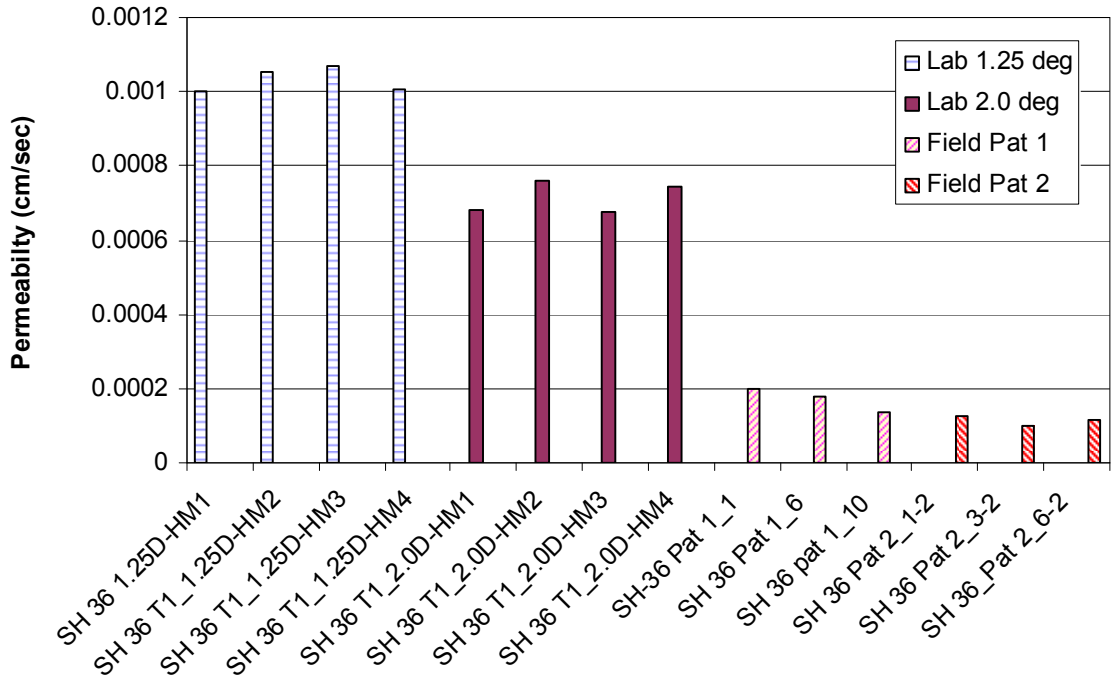

Figure 5-3. Permeability Test Results with SH 36 Samples.

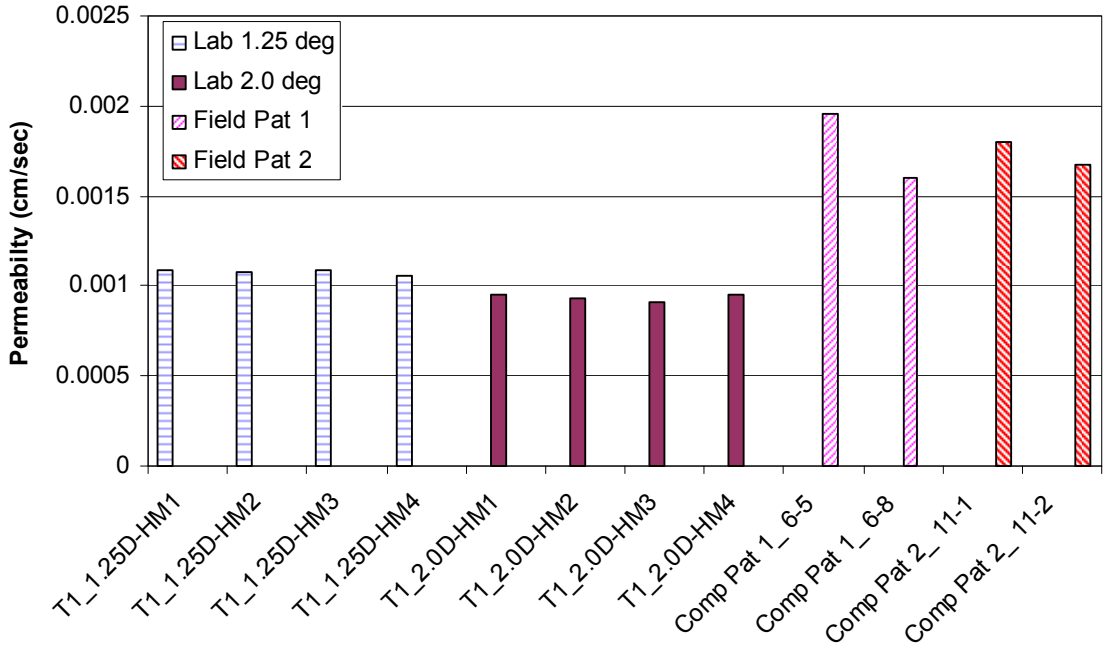

Figure 5-4. Permeability Test Results with FM 649 Samples.

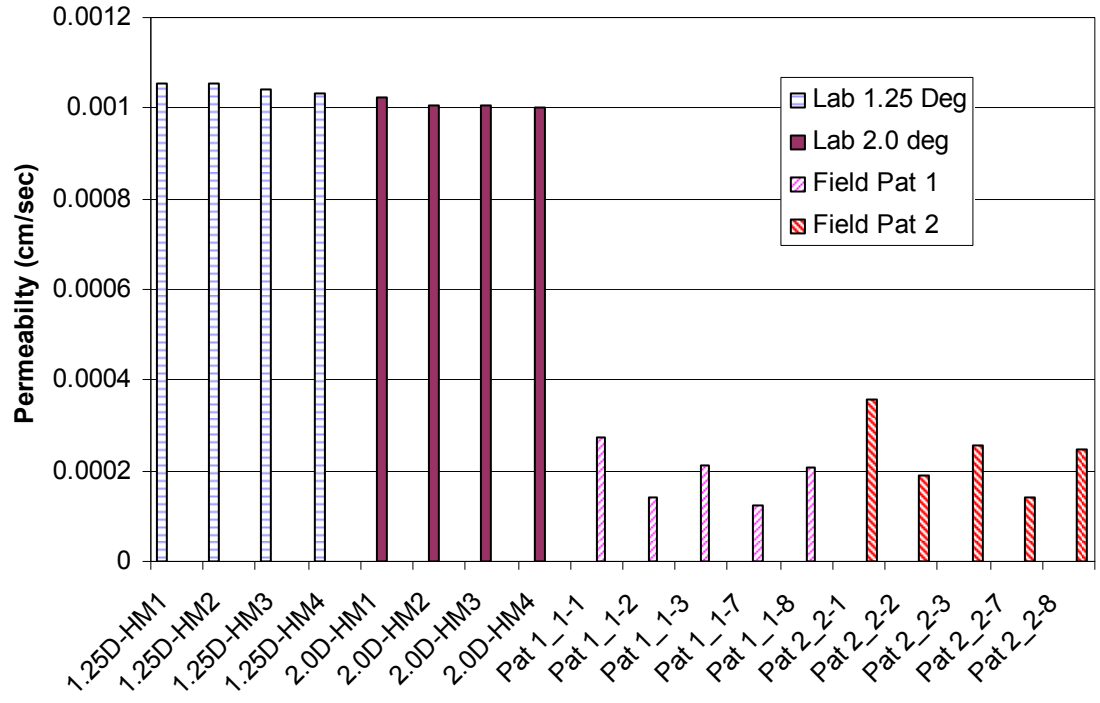

Figure 5-5. Permeability Test Results with US 87 Samples.

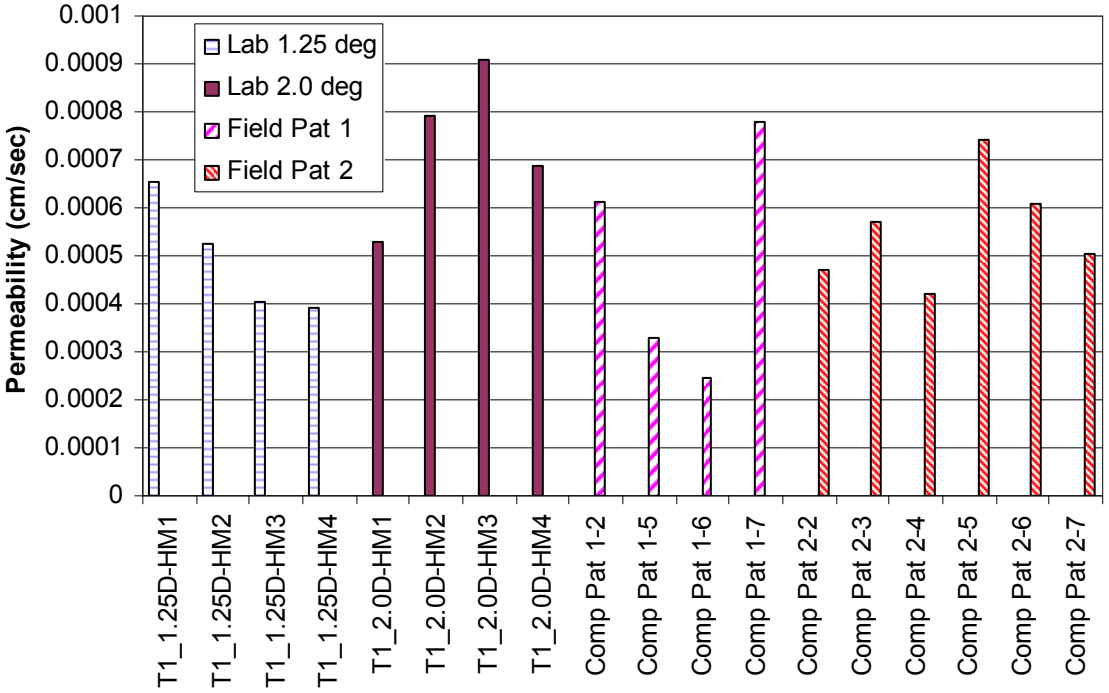

Figure 5-6. Permeability Test Results with SH 21 Samples.

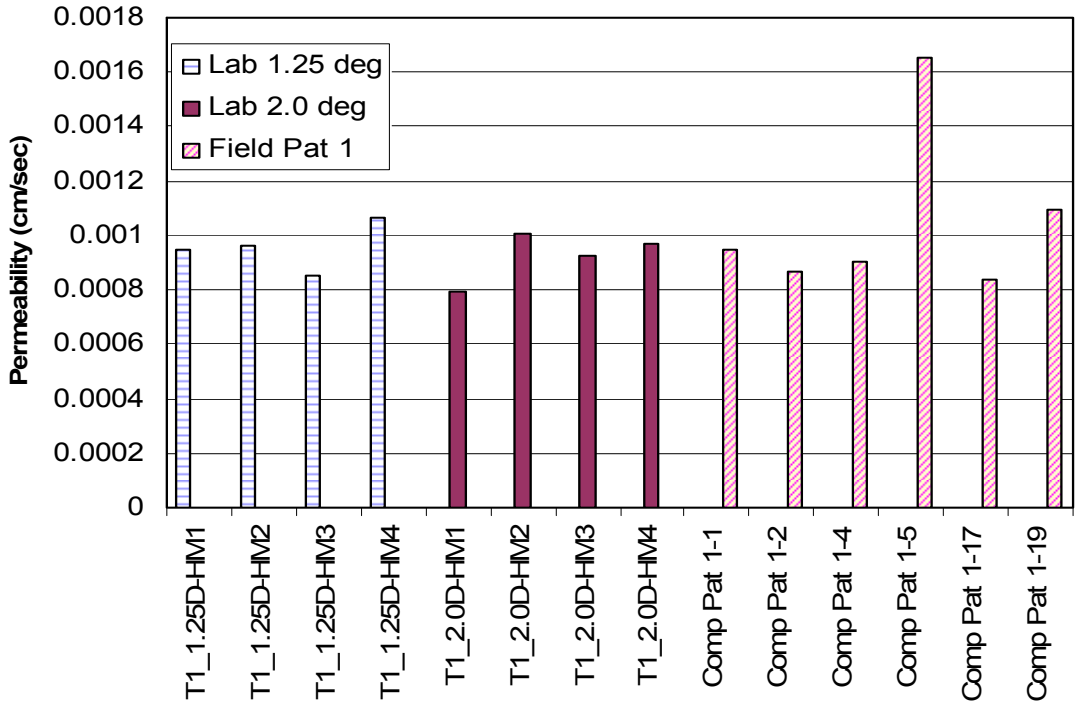

Figure 5-7. Permeability Test Results with US 259 Samples.

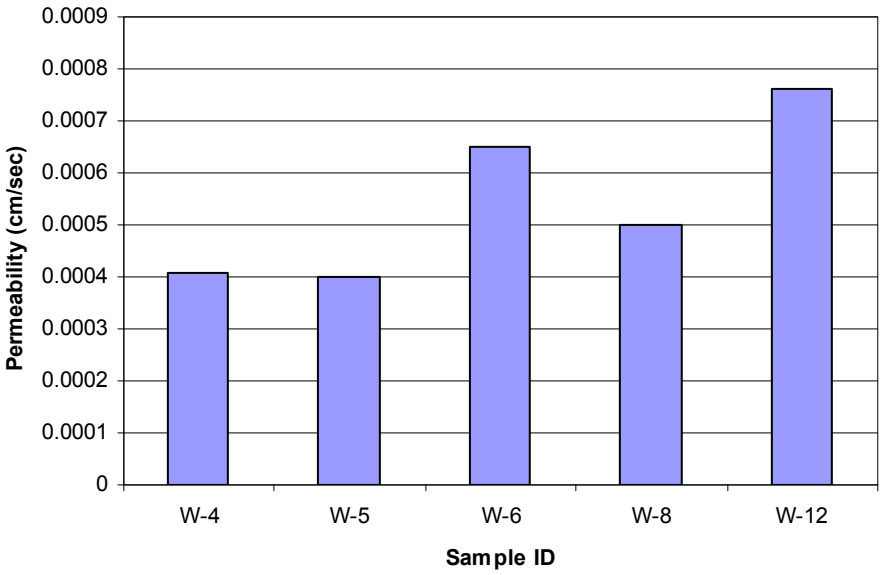

Figure 5-8. Permeability Test Results with IH 35 Field Samples.

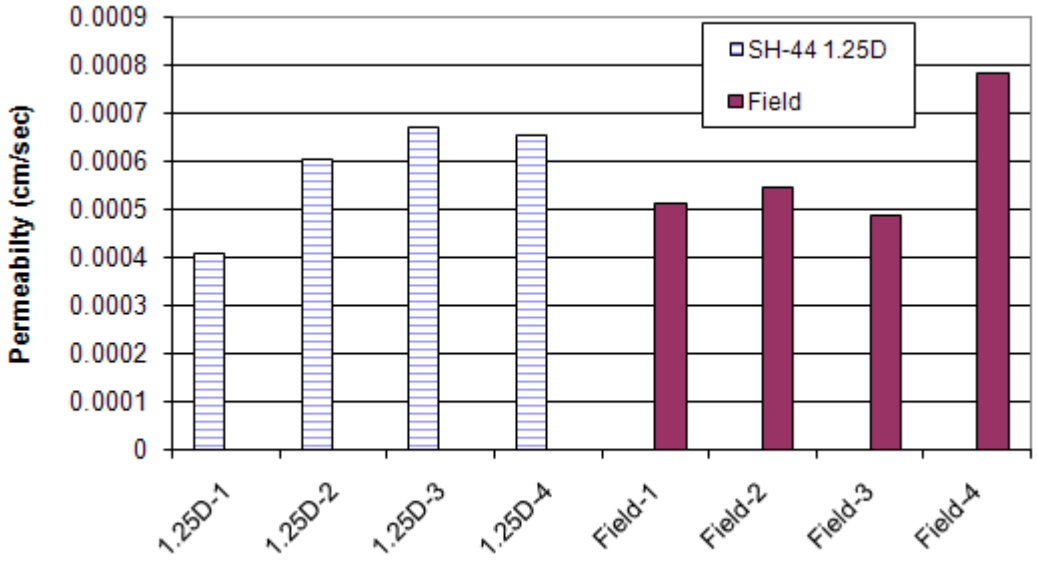

Figure 5-9. Permeability Test Results with SH 44 Samples.

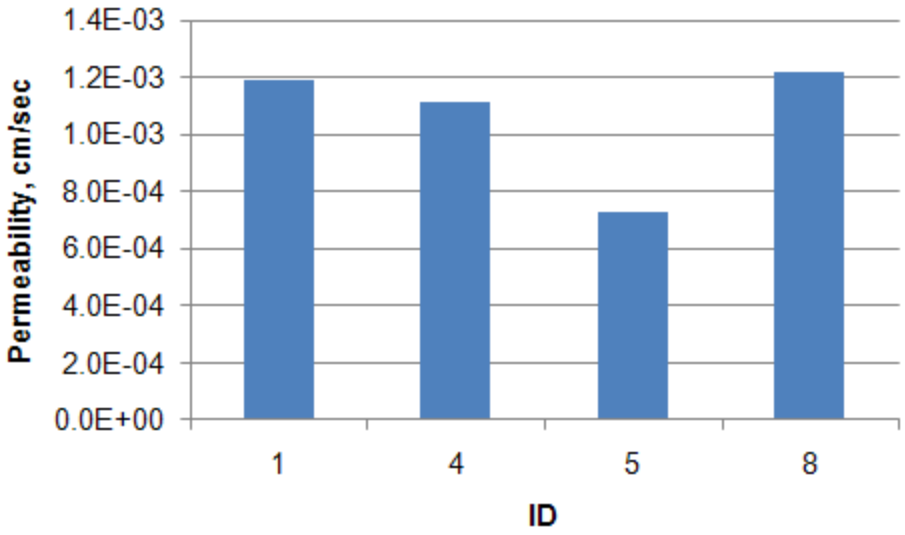

Figure 5-10. Permeability Test Results with SH 6 Field Samples.

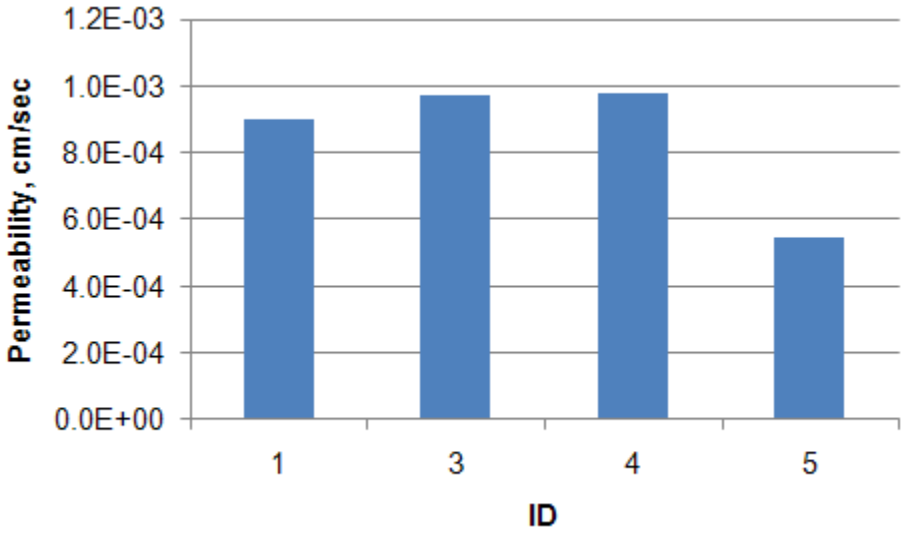

Figure 5-11. Permeability Test Results with SL 1 Field Samples.

SUMMARY OF FINDINGS

Based on three laboratory testings of lab compacted specimens and field cores, the following findings can be summarized:

- In general, laboratory specimens compacted using a 2.0° gyratory angle performed slightly better in Hamburg tests than specimens compacted using 1.25° gyratory angle.
- Overlay test results did not show any difference among the lab prepared specimens compacted using a 1.25° or 2.0° angle.
- There is no trend indicating that permeability in gyratory specimens is influenced by the angle of gyration.
- Laboratory compacted samples had comparable rut depth to field cores when percent air voids was similar.
- There was a slight influence of compaction pattern on the Hamburg results. However, there was no trend indicating an influence of compaction pattern on the overlay testing results or permeability results. The variability in the overlay testing results might have overshadowed the influence of compaction pattern or resistance to fracture as measured using the overlay tester.
- Hamburg results were found to be more related to the average percent of air void rather than the air void structure. Field cores with a less average percent of air void performed better than the ones that had a higher percent of air void.

CHAPTER VI
THE EFFECT OF THE AIR VOID DISTRIBUTION ON THE OVERLAY TEST AND HAMBURG RESULTS

EFFECT OF THE AIR VOID DISTRIBUTION ON THE OVERLAY TEST

Introduction

In this section, the effect of the air void distribution along the depth of the laboratory samples on the performance of these samples was evaluated using the overlay test. The overlay tester system is described in Chapter V. Gyratory specimens with 150 mm height and 150 mm in diameter were prepared. The X-ray CT system described in Chapter II was utilized to capture the air void distribution along the height of these samples. The samples were cut into short samples of about 37.5 mm height in such a way that the cut specimens had similar average percent air voids but different air void distributions. The cut samples were classified into five groups according to the air void distribution.

Materials and Test Procedure

SGC specimens were fabricated using crushed river gravel aggregates with PG 64-22 binder. The aggregate blend includes 18 percent of Fordyce C rock, 57 percent of Fordyce D/F rock, 10 percent of manufactured sand, 14 percent of limestone screening and 1 percent of lime. The gradation and the proportions of each material are shown in Table 6-1. The asphalt content was 5.6 percent by weight of the mixture.

X-ray CT was utilized to scan the test samples in order to capture the air void distribution along the depth of the samples. The average percent of air void was measured using the Saturated Surface Dry and CoreLok procedures. The X-ray results were used to cut the specimens into smaller ones. The cut samples had similar average percent air voids and different air void distributions. Each cut specimen was 150 mm in diameter and about 37.5 mm in height and had 7.5 $\pm$ 0.50 percent air voids. The cut samples were classified into five groups according to the distribution of air voids. The overlay tester was used to test the samples according to the parameters that were previously discussed

in Chapter V. The failure criterion in this test was taken to be the number of cycles at which a reduction of 7 percent of the initial load was achieved.

Table 6-1. Aggregate Gradation

	Fordyce C		Fordyce D/F		Man. Sand		limestone Scr.		Lime		Cumulative
Sieve Size (mm)	Pass (%)	Total (%)	Pass (%)	Total (%)	Pass (%)	Total (%)	Pass (%)	Total (%)	Pass (%)	Total (%)	Total (%)
19.000	100.0	18.0	100.0	57.0	100.0	10.0	100.0	14.0	100.0	1.0	100.0
12.500	70.0	12.6	100.0	57.0	100.0	10.0	100.0	14.0	100.0	1.0	94.6
9.500	10.0	1.8	95.0	54.2	100.0	10.0	100.0	14.0	100.0	1.0	81.0
4.750	5.0	0.9	50.0	28.5	100.0	10.0	100.0	14.0	100.0	1.0	54.4
2.360	3.0	0.5	15.0	8.6	99.0	9.9	92.0	12.9	100.0	1.0	32.9
1.180	2.5	0.5	5.0	2.9	79.0	7.9	72.0	10.1	100.0	1.0	22.4
0.600	2.0	0.4	4.0	2.3	49.0	4.9	54.0	7.6	100.0	1.0	16.2
0.300	1.5	0.3	3.0	1.7	23.0	2.3	41.0	5.7	100.0	1.0	11.0
0.150	1.0	0.2	2.0	1.1	7.0	0.7	33.0	4.6	100.0	1.0	7.6
0.075	0.5	0.1	1.0	0.6	3.0	0.3	25.0	3.5	100.0	1.0	5.5

Test Results and Discussion

The air void distributions are presented in Figures 6-1 through 6-5 for the different cases. Figure 6-1 shows the air void distribution for case number 1 which is uniform across the sample height. Figure 6-2 shows the air void distribution for case number 2 in which the top part of the sample has a higher percent of air void than the bottom part. Case number 3 is similar to case 2 except that the air void distribution is more uniform at the bottom as shown in Figure 6-3. Figures 6-4 and 6-5 represent the air void distribution for cases number 4 and 5, respectively. Both case 4 and 5 have less percent at the top part than the bottom one. However, the air void distribution at the top is more uniform in case 5 than the one at top in case 4 as shown Figure 6-5.

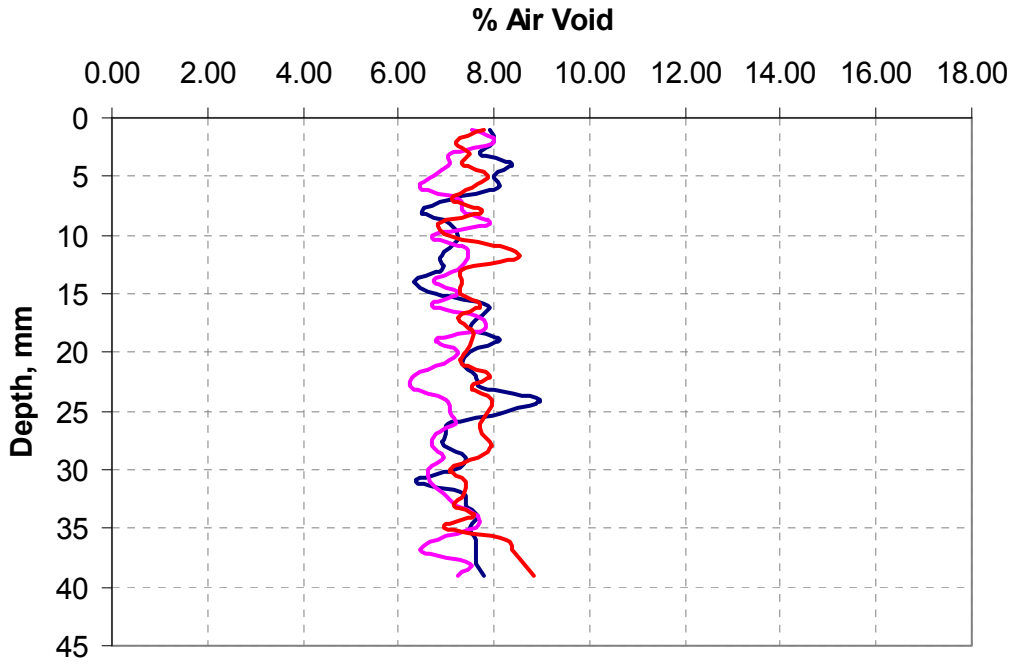

Figure 6-1. Air Void Distribution across the Depth of the Samples for Case 1.

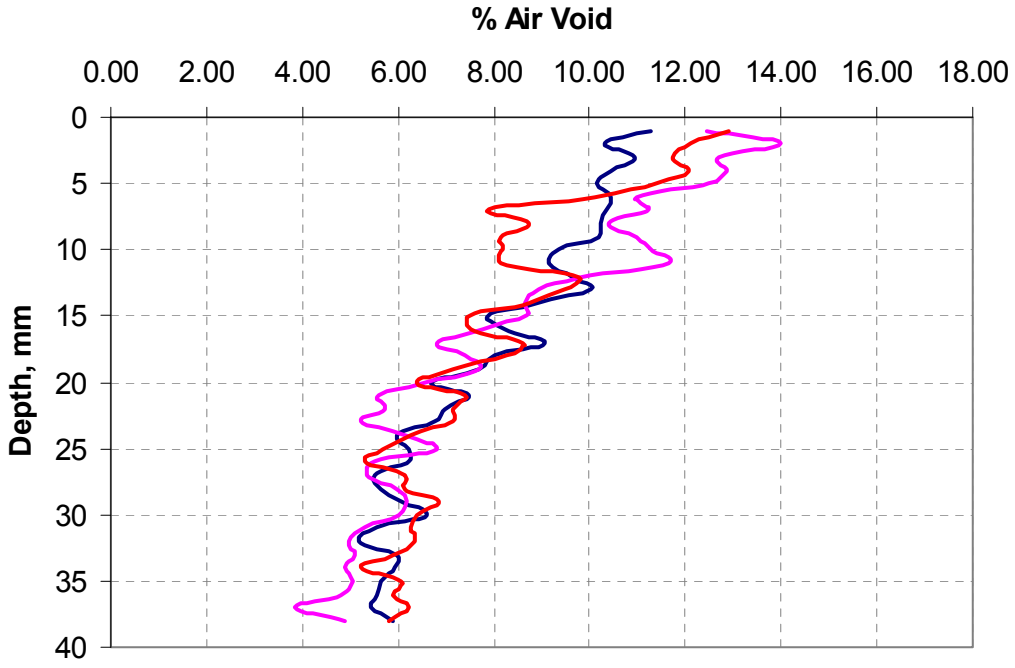

Figure 6-2. Air Void Distribution across the Depth of the Samples for Case 2.

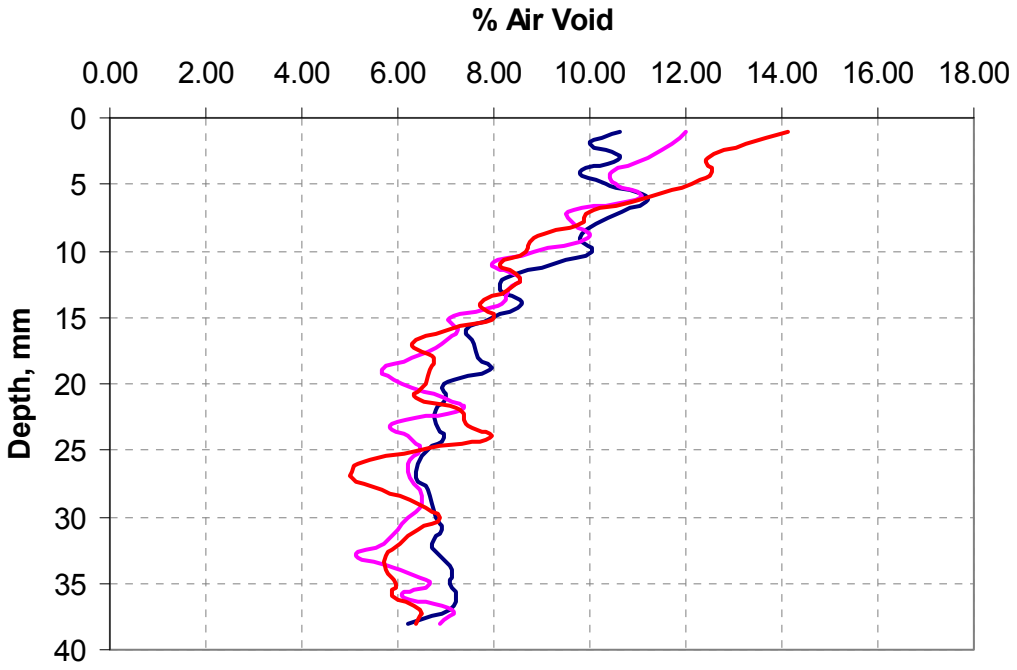

Figure 6-3. Air Void Distribution across the Depth of the Samples for Case 3.

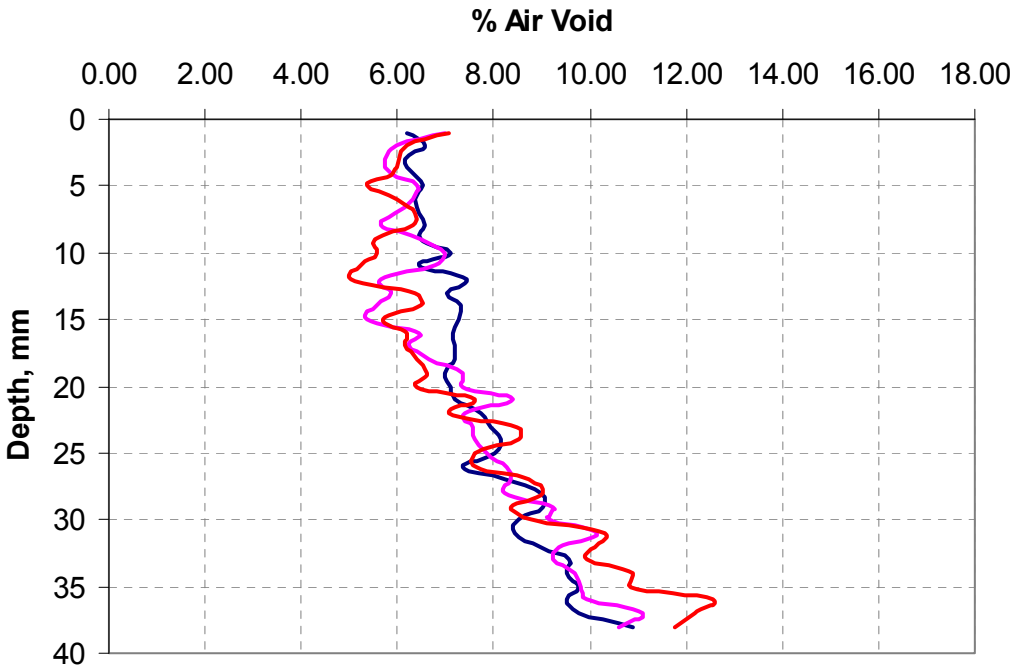

Figure 6-4. Air Void Distribution across the Depth of the Samples for Case 4.

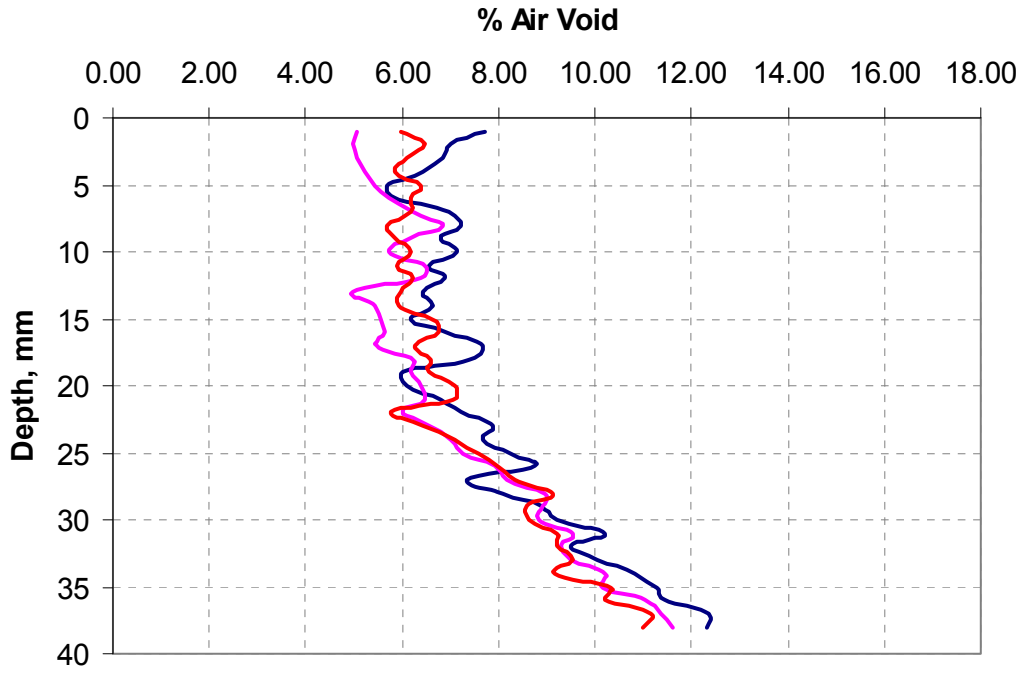

Figure 6-5. Air Void Distribution across the Depth of the Samples for Case 5.

The overlay test results are shown in Figures 6-6 and 6-7. Given the high variability in four of the five cases, it is difficult to judge whether air void distribution has a significant effect of the overlay test average results or not. However, the results clearly show that case number 1 with a uniform air void distribution had less variation in the failure number of cycles than all other cases.

Recently, the air void distribution across the depth of 4.5 inch and 2.5 inch samples were studied for three different asphalt mixtures; TxDOT type B, TxDOT type C and TxDOT type D. The height of the sample affects the air void distribution across its depth. Figures 6-8 and 6-9 show the ratio of air void distribution across the depth of 4.5 inch and 2.5 inch samples, respectively. The air void ratio is the percent air voids at any height relative to the average percent air voids for the whole sample. Both samples have higher air void ratio at the top and the bottom, however the middle part of the 4.5 inch sample has more uniform air void distribution than the middle part of the 2.5 inch sample. Figure 6-10 show the UI for air void distribution of overlay samples cut from the

middle part of 4.5 inch and 2.5 inch. It can be seen that the overlay samples cut form 4.5 inch sample had less UI, which mean more uniform air void distribution, than the ones cut from 2.5 inch samples. The preliminary test results provide by TxDOT (Izzo 2008) show that cutting overlay samples from 4.5 inch samples reduce significantly the variability of the overlay test results. It can be concluded that having more uniform air void across the test samples in the overlay test will reduce the variability of the test results which makes it more reliable test.

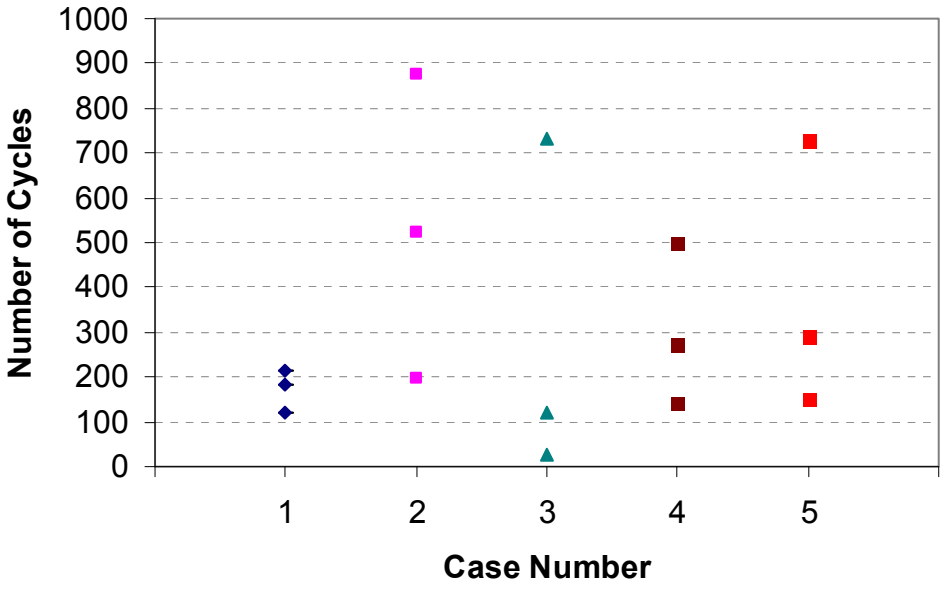

Figure 6-6. Overlay Test Results.

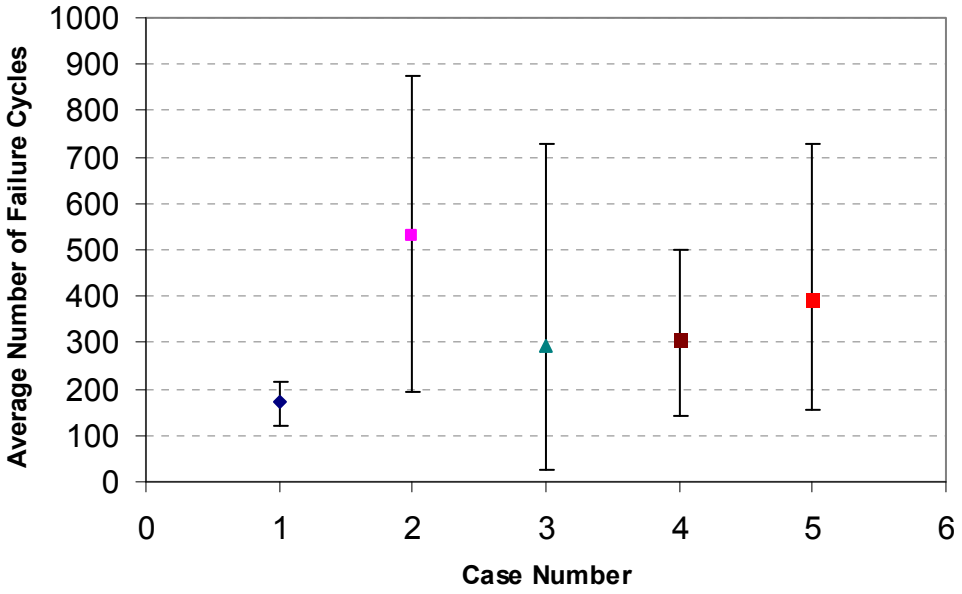

Figure 6-7. Average Number of Failure Cycles.

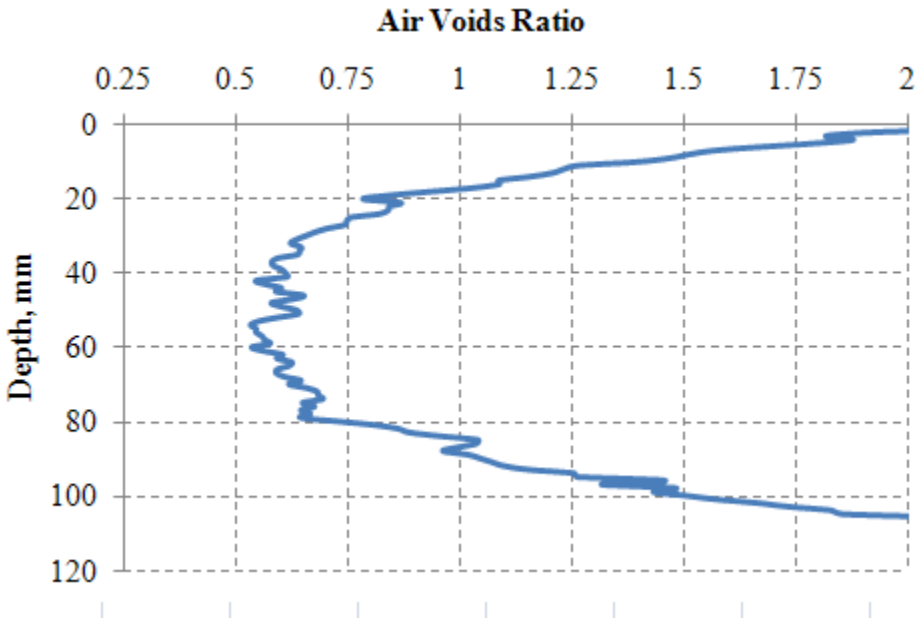

Figure 6-8. Example of Air Void Ratio across the Depth of 4.5 inch Specimen.

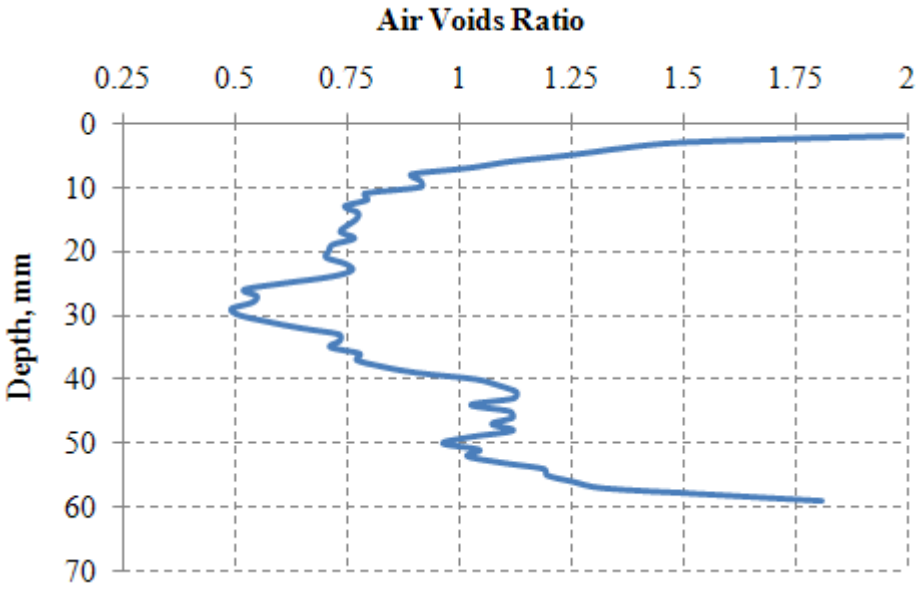

Figure 6-9. Example of Air Void Ratio across the Depth of 2.5 inch Specimen.

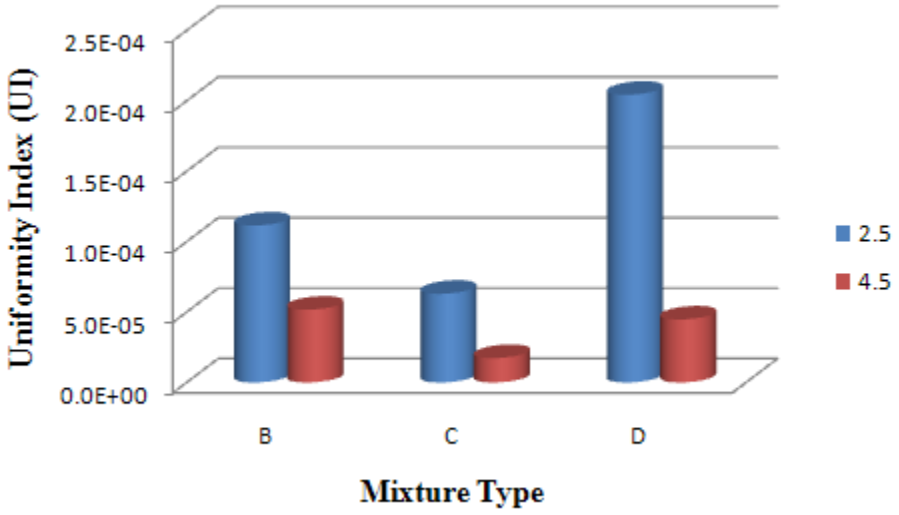

Figure 6-10. Average Uniformity Index of Air Void Distribution for Overlay Specimens Cut form 4.5 inch and 2.5 inch Specimens.

EFFECT OF THE AIR VOID DISTRIBUTION ON THE HAMBURG TEST

In this section, the effect of the air void distribution on the Hamburg results was evaluated. The Hamburg results for the field cores, as discussed in Chapter V, were influenced by the average percent air void in the test cores. The effect of the air void distribution on the Hamburg results was not easy to evaluate for the following reasons:

- The field cores had a dissimilar percent of air voids which made it difficult to correlate the Hamburg results with the air void structure without considering the effect of the percent of air voids.
- The field cores which had similar percent air voids did not have the similar air void distribution in all the projects in this study.

For the previous two reasons, it was difficult to get a comprehensive conclusion for all the projects. In order to overcome this problem, a side study was initiated in order to eliminate the dissimilarity of the percent of the air voids and the average air void distribution. This study included testing a number of laboratory samples fabricated in such a way to induce different air void distributions along the height of the samples. These samples had 7 percent air voids ± 0.50 percent air voids. US 259 mix were used in this study as it has experienced a considerable amount of the rutting.

Initially, SGC samples (4-inch height and 6-inch diameter) were prepared. X-ray CT was used to capture the air void distribution along the height of the samples. The samples were cut at specific locations into 2.5 inch samples to induce different air void distributions along the height of the samples; however they had comparable average percent air void (7±0.5 percent). Four cases were considered. Three cases (2.5 inch height) were cut from long samples (4 inch height) and one case (case 4) was compacted at 2.5 inch directly such as the conventional way. The average percent air voids in the top part, bottom part, whole samples were shown in Figure 6-11. Case 1 had relatively higher percent air voids at the top than the bottom part, while case 2 has less percent air voids at the top than the bottom. Case 3 had equal percent air voids at the top and the bottom part. Case 4, which was compacted directly to 2.5 inch sample, had higher percent air voids at the top than the bottom but with less degree compared to case 1. The Hamburg results are

shown in Figure 6-12 for each case. It can seen that there is no significant difference in the rutting results from one case to another, since all the test samples passed the TxDOT criteria (the rutting is less than 12.5 mm after 20,000 cycles). It can be concluded that unlike the overlay tester, the Hamburg test is less sensitive to the air void distribution within the test samples and it is more influenced by the average percent air voids within the test samples.

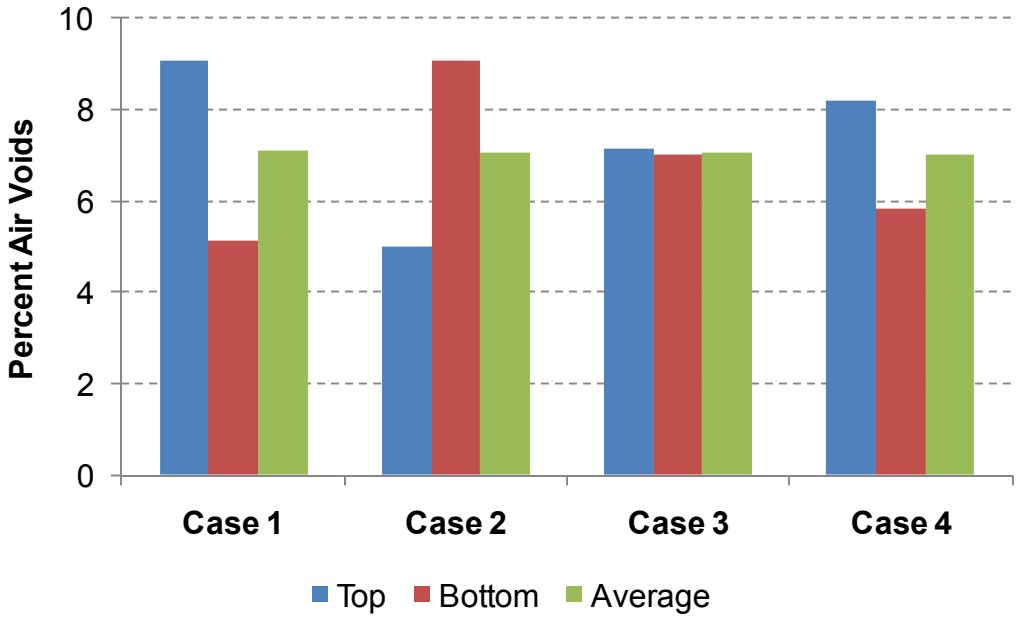

Figure 6-11. The Average, Top and Bottom Percent of Air Voids for Different Cases.

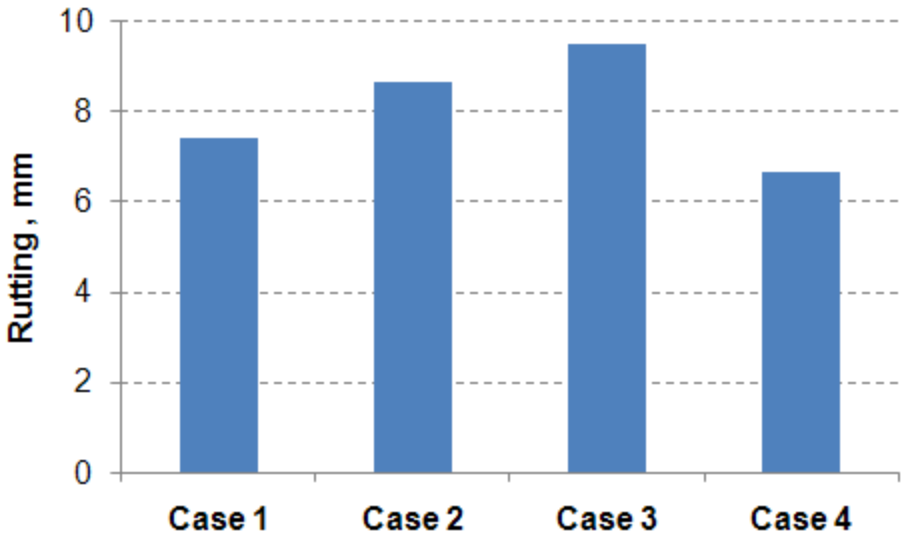

Figure 6-12. Hamburg Test Results for Different Cases

SUMMARY

In this chapter the effect of air void distribution on the overlay and Hamburg test results was evaluated. Asphalt mixtures specimens were prepared to have similar average percent air voids but with different air void distributions. In overlay test, the results showed that specimens with a uniform air void distribution had less variation in the failure number of cycles. Producing specimens with more uniform air void distribution could be good practice to reduce the known variability of the overlay test results. The Hamburg test found to be insensitive to the air void distribution in test specimens. As can be seen From Chapter V, the Hamburg test is more influenced by the average percent air voids in test specimens.

CHAPTER VII
THE EFFECT OF THE COMPACTION TEMPERATURE ON THE AIR VOID DISTRIBUTION

INTRODUCTION

Several studies demonstrated that the air void distribution in Superpave gyratory specimen is nonuniform; the top and bottom have more air voids than the middle. It has been postulated that this is caused by the restriction of aggregate movement close to the plates compared with the middle and the faster rate of heat loss at the top and bottom. Loss of heat causes the mix to become less mobilized which causes higher percent air voids. In order to evaluate the influence of temperature on air void distribution, an experiment was conducted in which the temperatures of a top plate, a base plate and a mold in the SGC were varied. Consequently, X-ray CT was used to measure air void distribution and analysis was conducted to examine the uniformity of air void distribution.

EXPERIMENTS

Laboratory SGC samples 6.5 inches (165 mm) height by 6 inches (150 mm) diameter were prepared using two binders PG 76-22 and PG 64-22 and crushed river gravel aggregate. Temperatures of the top plate, base plate and mold were varied according to the cases shown in Table 7-1. Three specimens were evaluated from each case.

Table 7-1. Cases Analyzed for Varying Plates and Mold Temperatures.

	Temperature of Mold	Temperature of Base Plate	Temperature of Upper Plate	Temperature of Mix
Case 1	Tc	Tc	30 ^{o}C	Tc
Case 2	Tc + 30 ^{o}C	Tc + 30 ^{o}C	30 ^{o}C	Tc
Case 3	Tc	Tc	Tc	Tc

Note: Tc = the compaction temperature

The temperature distribution along the height of asphalt specimens was measured using a setup that consisted of a two-piece infrared temperature measurement system with a miniature sensing head and electronics. A schematic view of the temperature measurement system is shown in Figure 7-1.

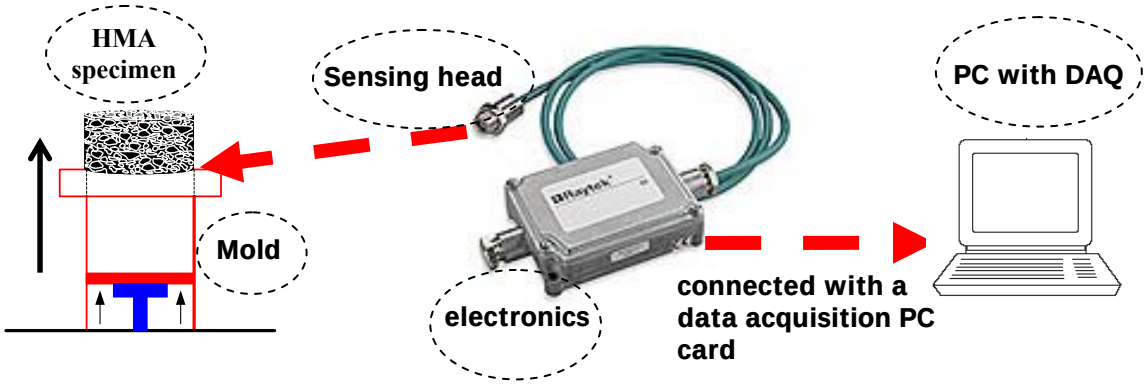

Figure 7-1. A Schematic View of the Temperature Measurement System.

The miniature infrared sensor is a noncontact device that can be used to measure temperature from distance. This device measures the amount of energy emitted from a certain object and then converts it to a signal. The sensor consists of two pieces. The first piece is a miniature sensing a head and the second piece is a separate electronics box. The range of temperature that can be measured by these sensors is 40^{o}C to 600^{o}C. The sensing head is connected to the electronics box. The accuracy of the system is $\pm$ 1^{o}C. The system has 10:1 optical resolution which is expressed as a ratio of the distance to the measurement spot divided by the diameter of the spot. The system has a response time of 150ms which is as fast or faster than many advanced systems.

Three miniature infrared sensors were employed in this experiment. First, the sensors were inserted into a 10 inch (25 cm) diameter PVC pipe as shown in Figures 7-2a and 7-2b. The PVC pipe was used as a holder for the infrared sensors. The head of the infrared sensors was inside the holder (Figure 7-2b). Right after the compaction and before extraction of a specimen from the compaction mold (Figure 7-2c), the sensors'

holder was placed around the compaction mold and the test sample was pushed out of the compaction mold as shown in Figure 7-2d.

(a)

(b)

(c)

(d)

Figure 7-2. Experimental Setup.

The height of the bottom sensor was adjusted to be at the end of the height of the test sample when the sample was pushed all the way out from the compaction mold. The sensor at the middle was 2 inches (5 cm) away from the bottom sensor and the distance between the middle sensor and the top one was 2 inches (5 cm). The sensor at the bottom

recorded the temperature profile for the full height of the sample while the sensors at the top and in the middle measured the surface temperature for the top 4 inches (10 cm) and 2 inches (5 cm), respectively. The temperature measurements of the top and middle sensors were used to validate the results from the bottom sensor.

TEMPERATURE RESULTS

The temperature measurements of the three cases presented in Table 7-1 are presented in Figures 7-3 through 7-8.

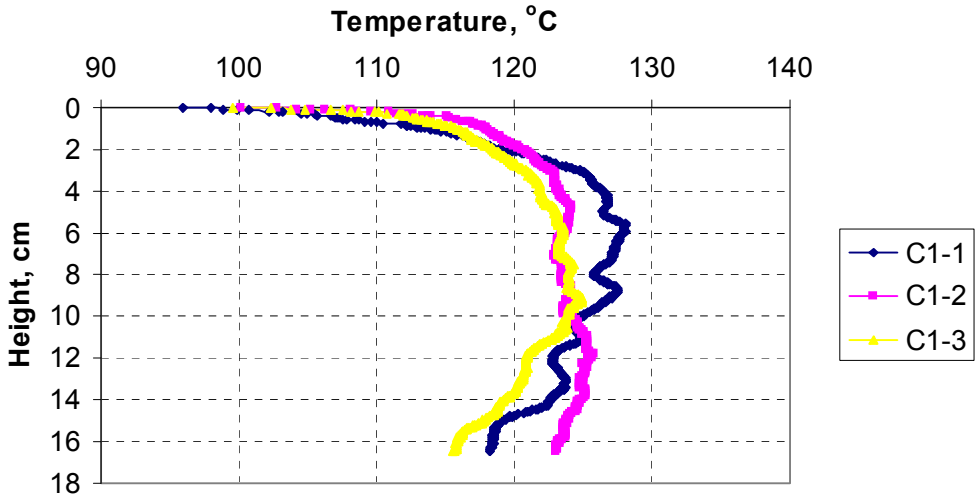

Figure 7-3. The Temperature Profile along the Height of the Specimen for Case 1 (PG 76-22).

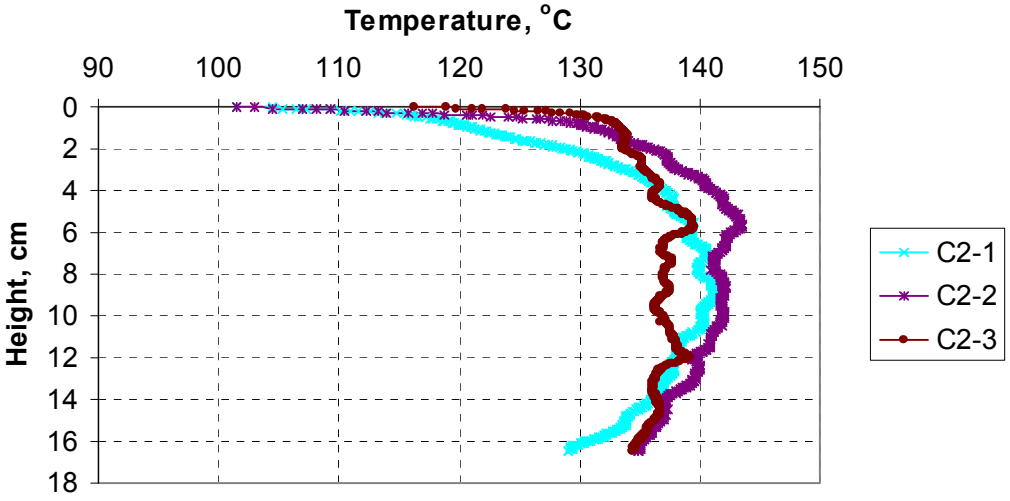

Figure 7-4. The Temperature Profile along the Height of the Specimen for Case 2 (PG 76-22).

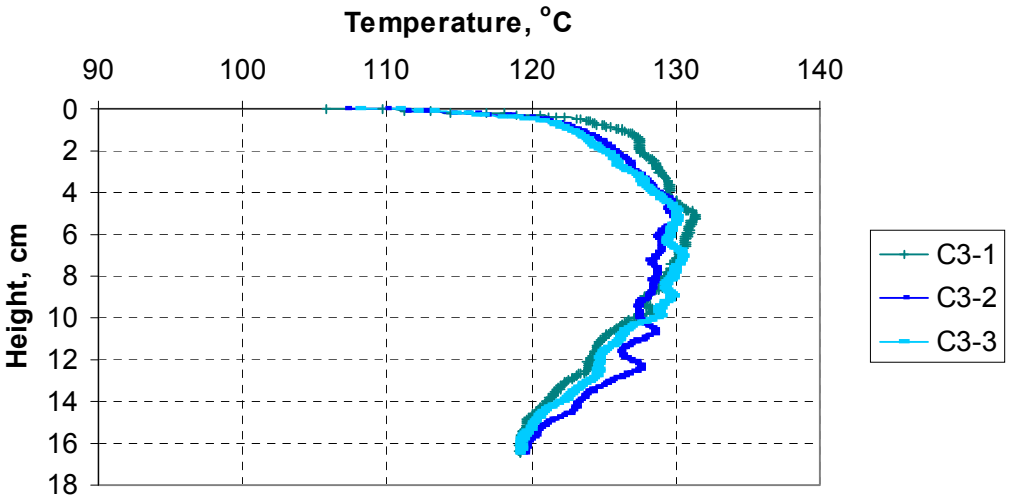

Figure 7-5. The Temperature Profile along the Height of the Specimen for Case 3 (PG 76-22).

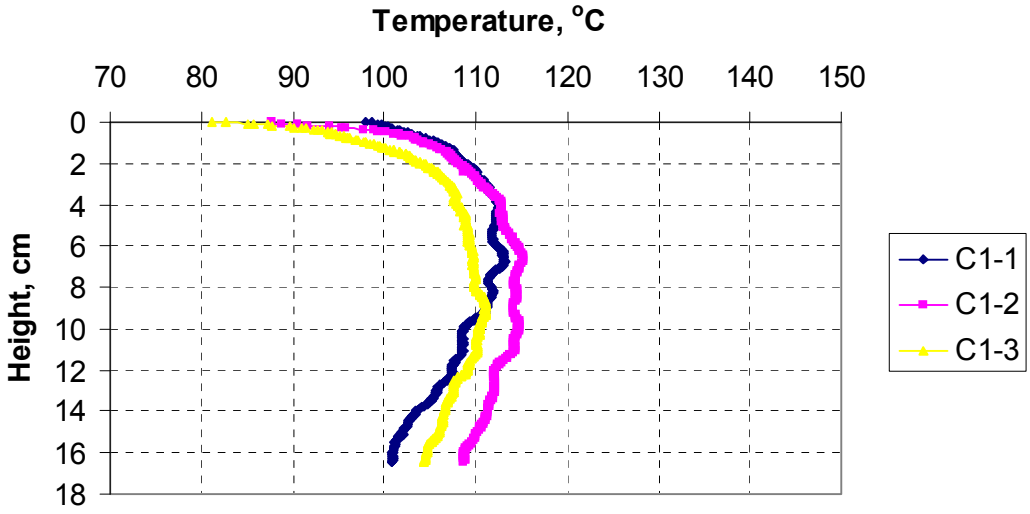

Figure 7-6. The Temperature Profile along the Height of the Specimen for Case 1 (PG 64-22).

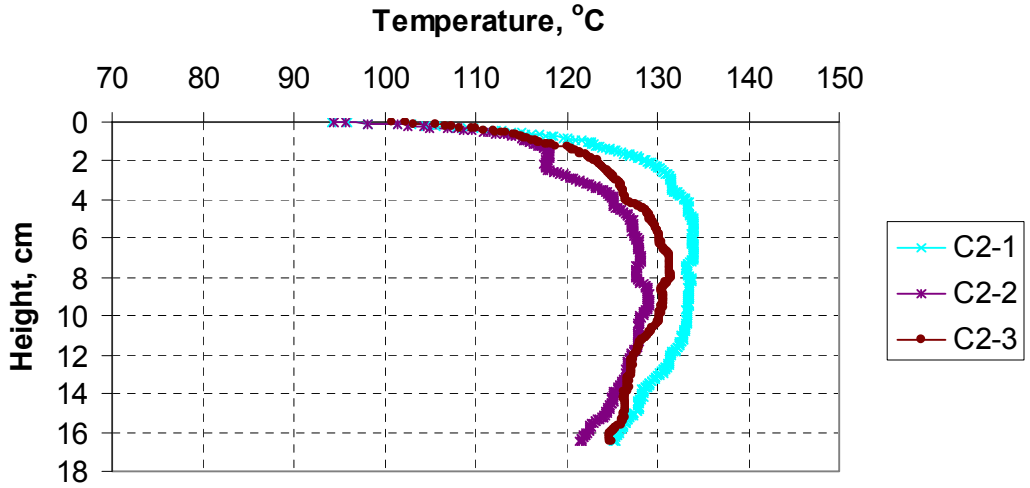

Figure 7-7. The Temperature Profile along the Height of the Specimen for Case 2 (PG 64-22).

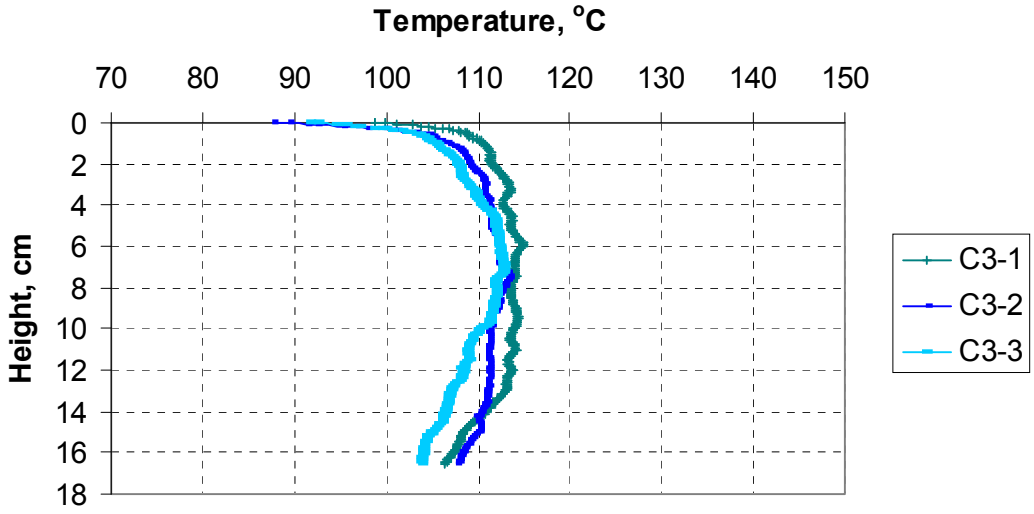

Figure 7-8. The Temperature Profile along the Height of the Specimen for Case 3 (PG 64-22).

It can be seen from Figures 7-3 through 7-8 that different temperature distributions were produced in these cases. The Uniformity Index (UI), which was previously presented in Chapter IV, is calculated for the temperature distribution for different cases. The average UI for each case is presented in Figures 7-9 and 7-10 for binder PG 76-22 and PG 64-22, respectively. It can be seen the temperature distribution is more uniform, or has less UI in case three for both PG 76-22 and PG 64-22 samples. This means that by heating up the upper plate to the mold and mix temperature produces a uniform temperature along the height of the sample. Case 2 produced the highest UI for both PG 76-22 and PG 64-22 samples. The higher UI is the greater nonuniform distribution of the temperature along the height of the samples.

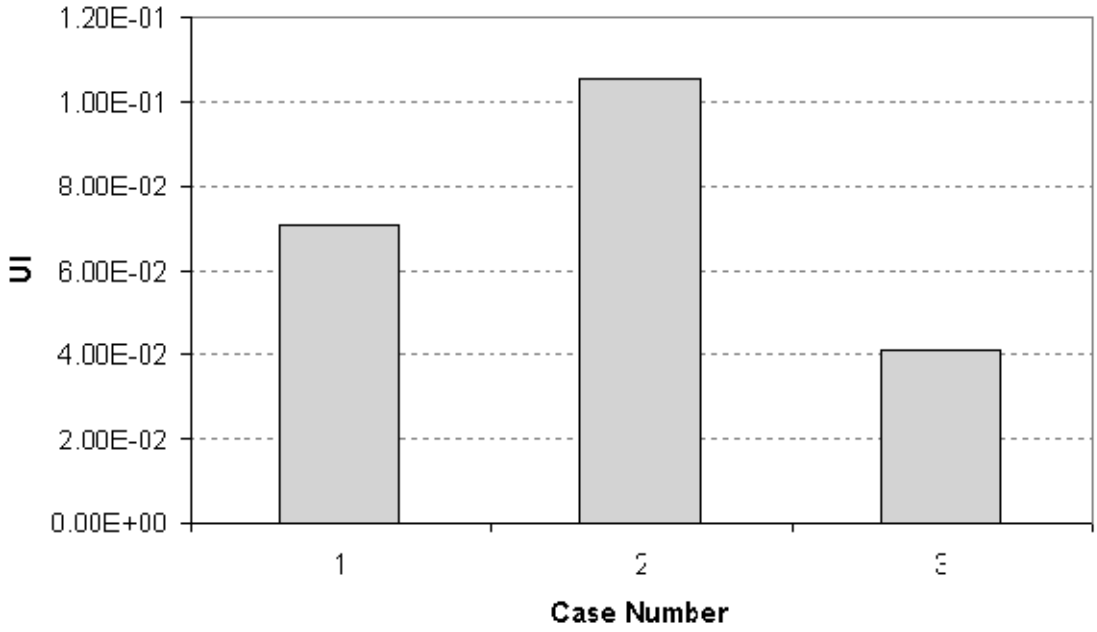

Figure 7-9. Uniformity Index for Temperature Distribution for PG 76-22 Samples.

AIR VOID ANALYSIS

X-ray CT was used to capture the air void distribution along the HMA specimens. An example of air void distribution along the depth is presented in Figure 7-11. The air void distribution was analyzed by dividing the images of a specimen into three regions with equal heights (top, middle or center, and bottom). The percent air voids was calculated for each of the regions using the whole diameter (150 mm diameter) and for a smaller diameter equal to 100 mm. The smaller diameter was used to analyze uniformity across the specimen depth without the influence of air void distribution at the specimen boundary. The average results for the replicates were presented in Figures 7-12 through 7-15. Figures 7-12 and 7-13 show the results for the samples with PG 76-22 binder for the whole diameter (150 mm) and smaller core of 100 mm, respectively.

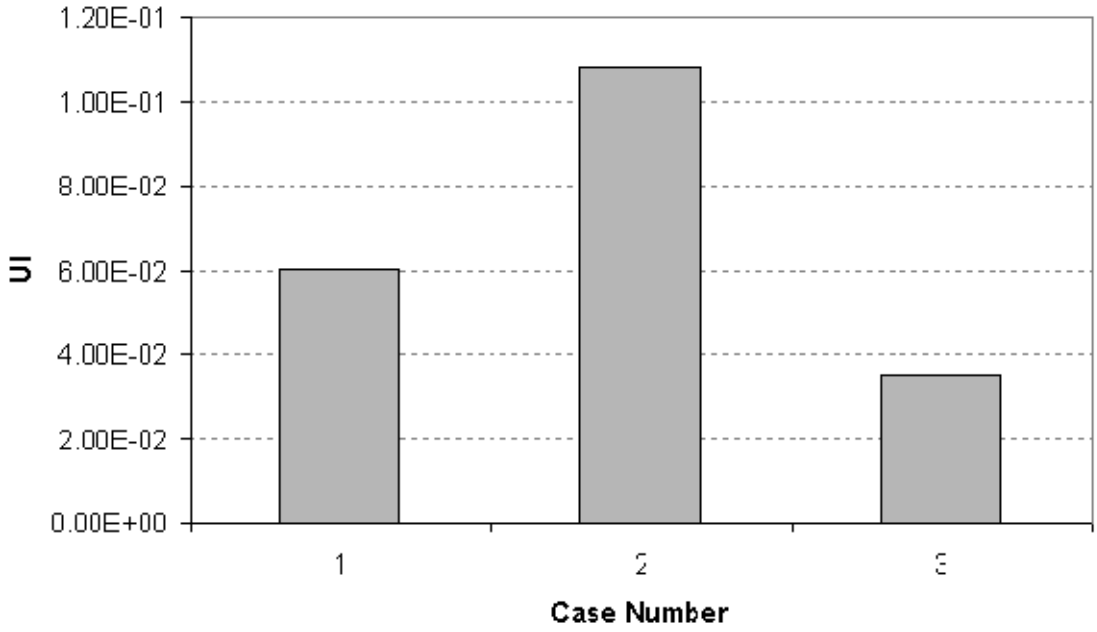

Figure 7-10. Uniformity Index for Temperature Distribution for PG 64-22 Samples.

The results for the samples with PG 64-22 binder were presented in Figures 7-14 and 7-15 for the whole and small diameter, respectively. Specimens for all cases were compacted to similar average percent air voids of about 8.5. These percent air voids values shown in Figures 7-12 through 7-15 did not show trends in terms of the relationships between temperature profiles and percent air voids in different parts of a specimen.

The Uniformity Index (UI) defined in Chapter IV was used to analyze air void distribution. The UI was calculated for 150 mm diameter and 100 mm diameter images. In addition, the analysis was carried out for images of the whole specimen height and for images that belong to the middle third of the specimen height. The average UI for the replicates from each case for mixes with PG 76-22 are shown in Figures 7-16 through 7-19 and the results for mixes with PG 64-22 are shown in Figures 7-20 through 7-23. The first observation is that the middle part has a smaller UI than the full height. This is consistent with previous findings that the air void distribution tends to be nonuniform towards the top and bottom while the middle part of a specimen tends to be more uniform. It is interesting to note that specimens with PG 64-22 have less UI values

than the PG 76-22 specimens. These results indicate that the compaction effort was more uniformly distributed in the unmodified binder compared with the modified binder. The UI for the middle part for both PG 76-22 and PG 64-22 samples in case 3 was lower than the corresponding one in cases 1 and 2. It is believed that the uniformity of the temperature distribution in case 3 produced a more uniform air void distribution in the middle part of the test samples. The UI results for the full height did not show the same relationship between the UI of air void and temperature for both PG 64-22 and PG 76-22 samples.

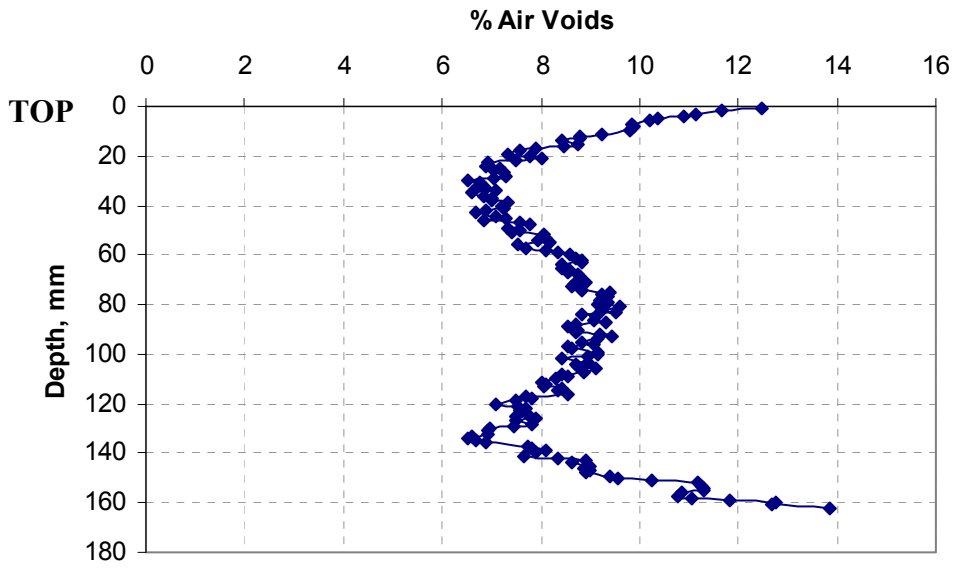

Figure 7-11. The Air Void Distribution along the Height of SGC Specimen.

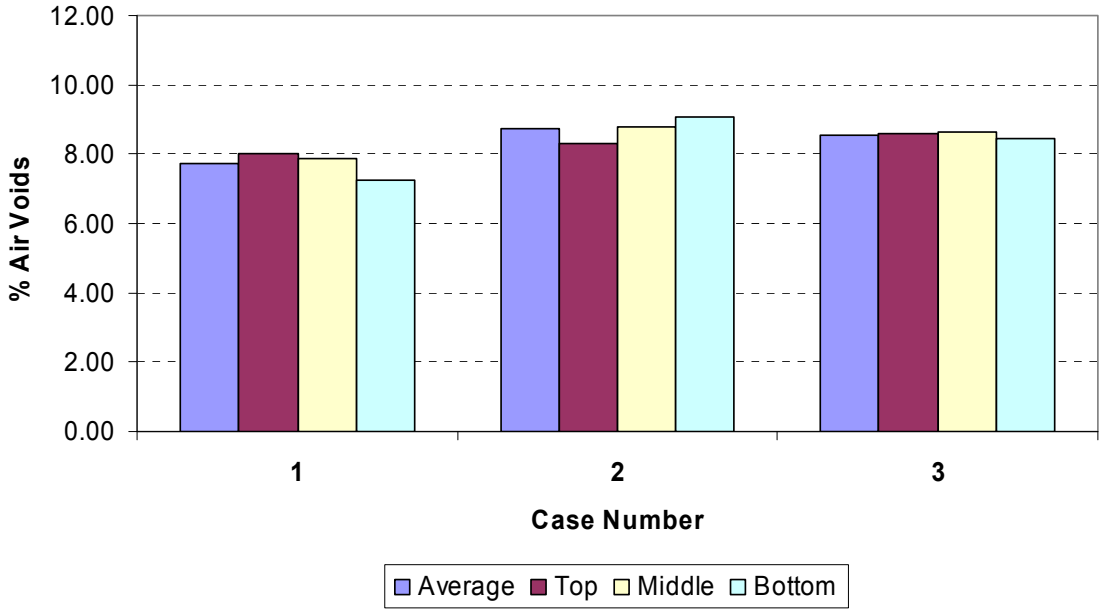

Figure 7-12. Percent Air Voids for 150 mm Diameter Specimens with PG 76-22 Binder.

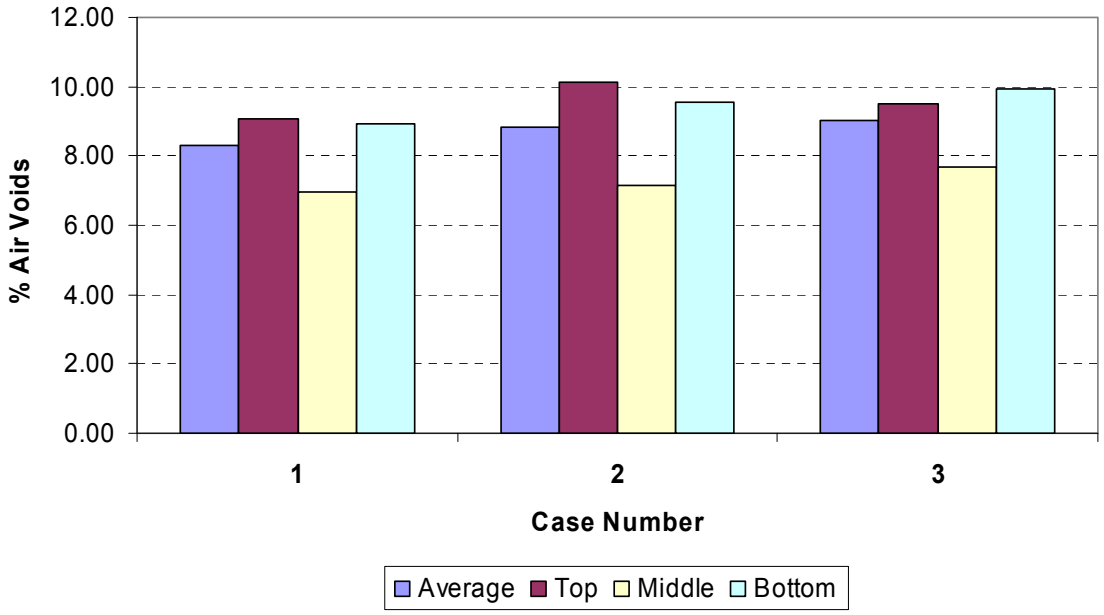

Figure 7-13. Percent Air Voids for 100 mm Diameter Specimens with PG 76-22 Binder.

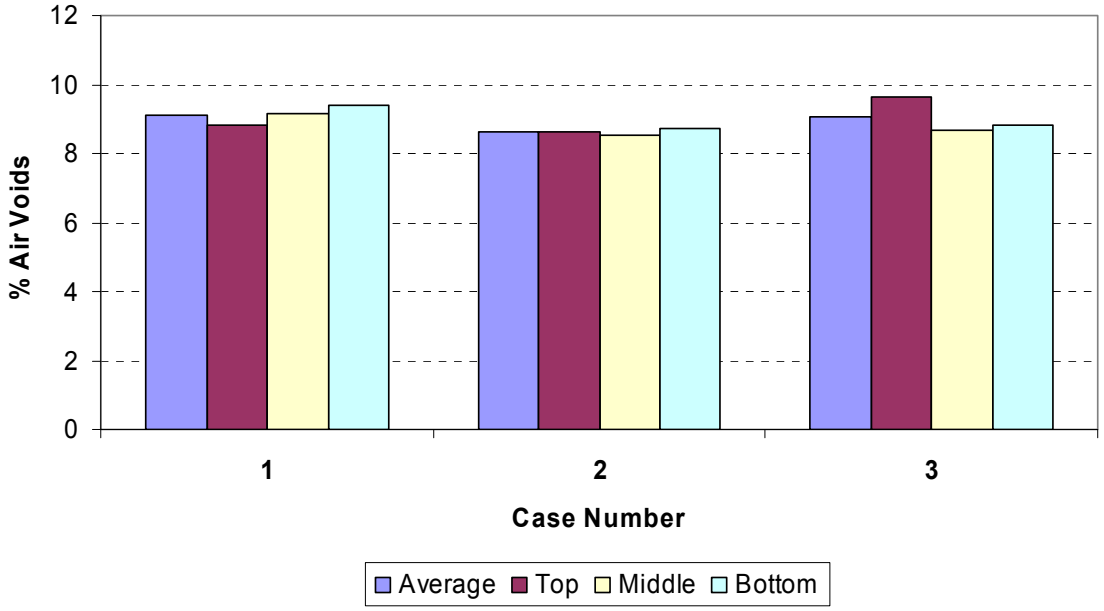

Figure 7-14. Percent Air Voids for 150 mm Diameter Specimens with PG 64-22 Binder.

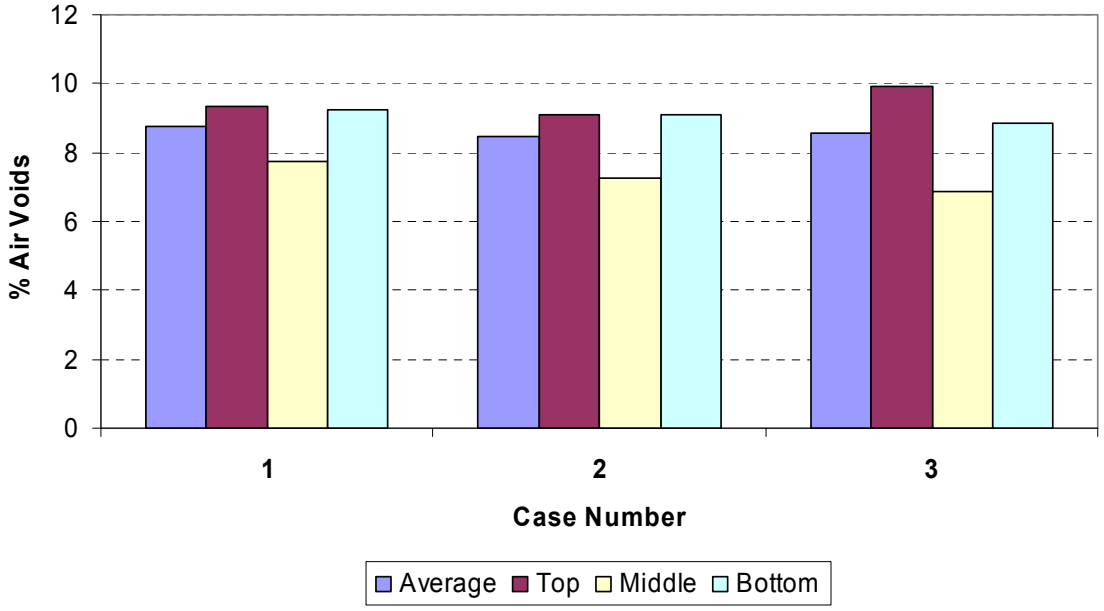

Figure 7-15. Percent Air Voids for 100 mm Diameter Specimens with PG 64-22 Binder.

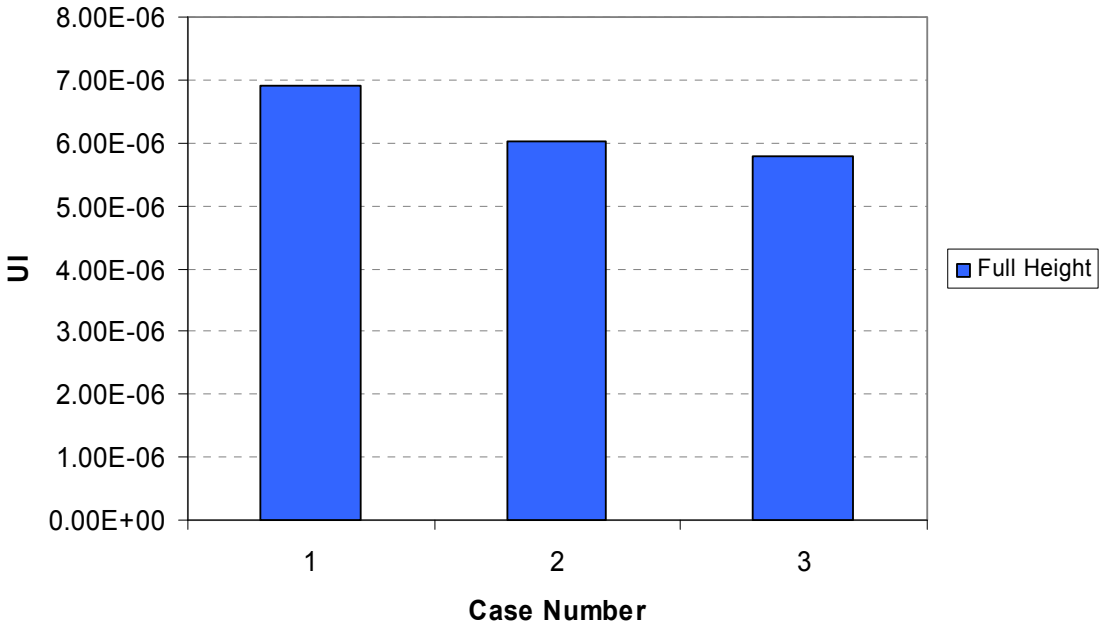

Figure 7-16. Uniformity Index for Full Height of 150 mm Diameter Specimens with PG 76-22 Binder.

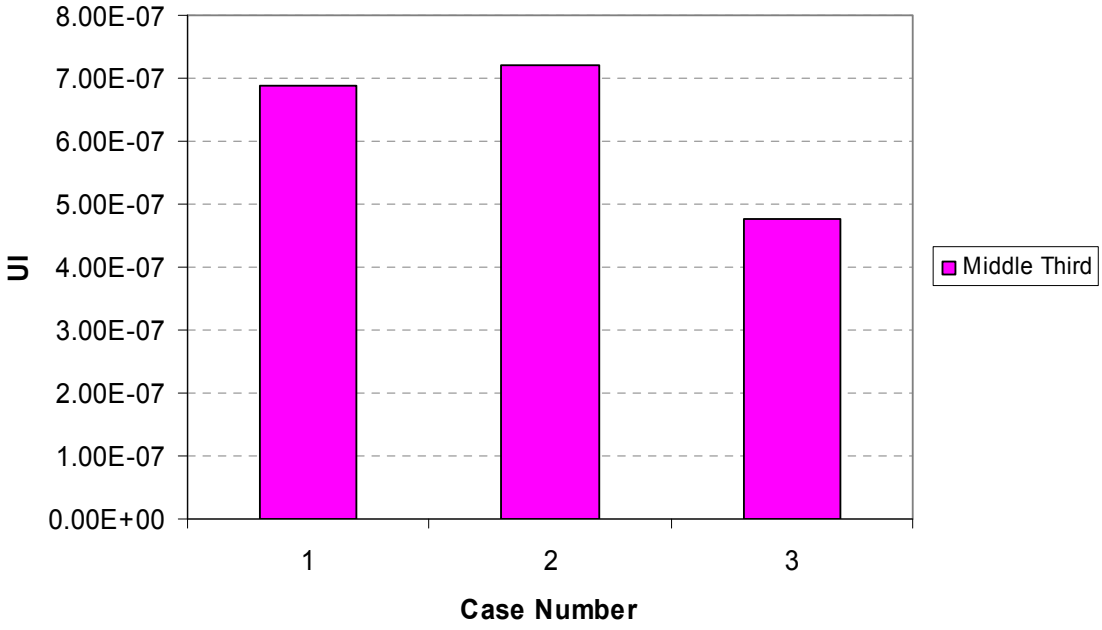

Figure 7-17. Uniformity Index for Middle Third of 150 mm Diameter Specimens with PG 76-22 Binder.

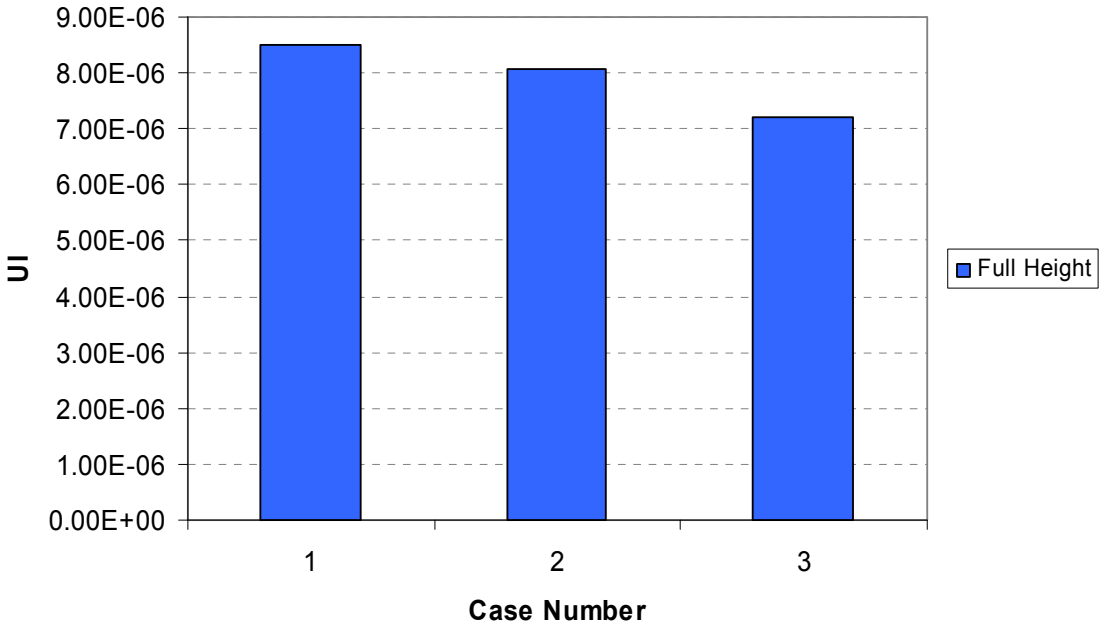

Figure 7-18. Uniformity Index for Full Height of 100 mm Diameter Specimens with PG 76-22 Binder.

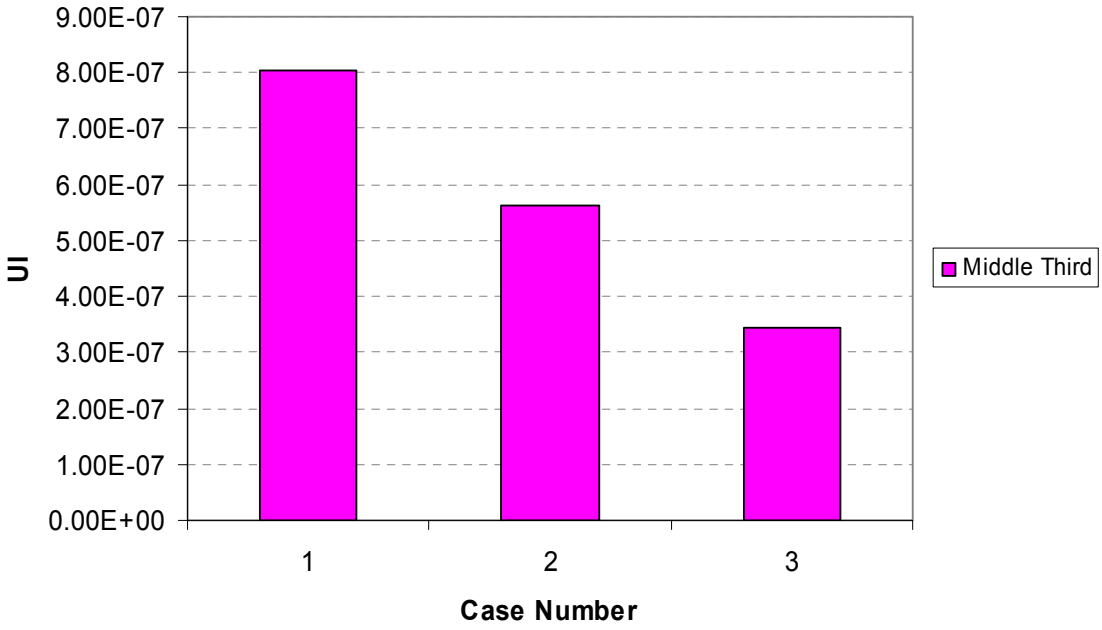

Figure 7-19. Uniformity Index for Middle Third of 100 mm Diameter Specimens with PG 76-22 Binder.

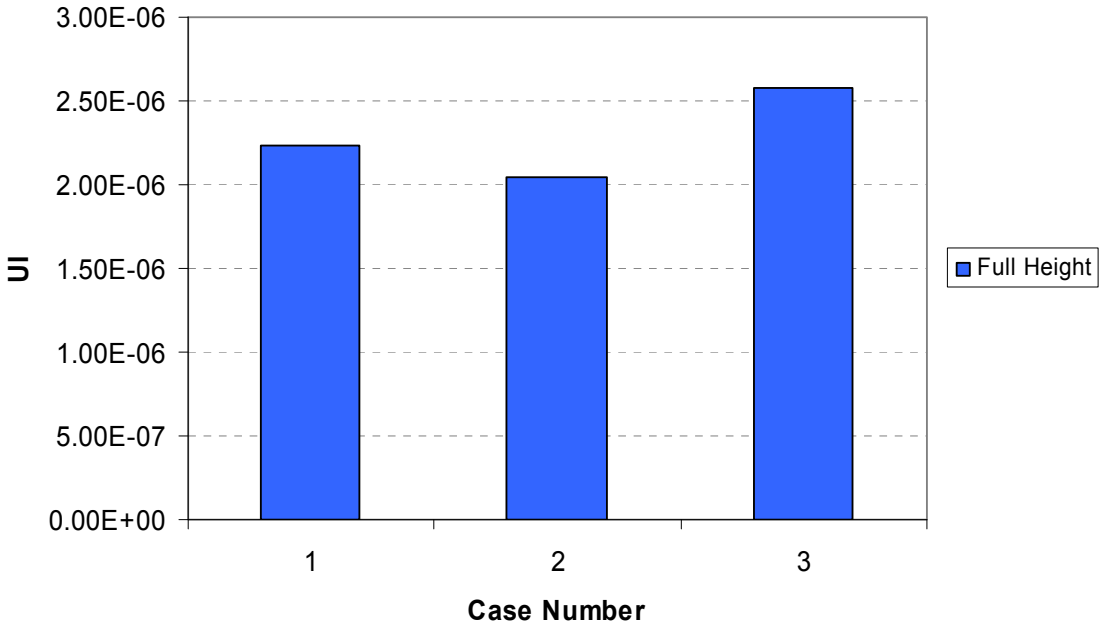

Figure 7-20. Uniformity Index for Full Height of 150 mm Diameter Specimens with PG 64-22 Binder.

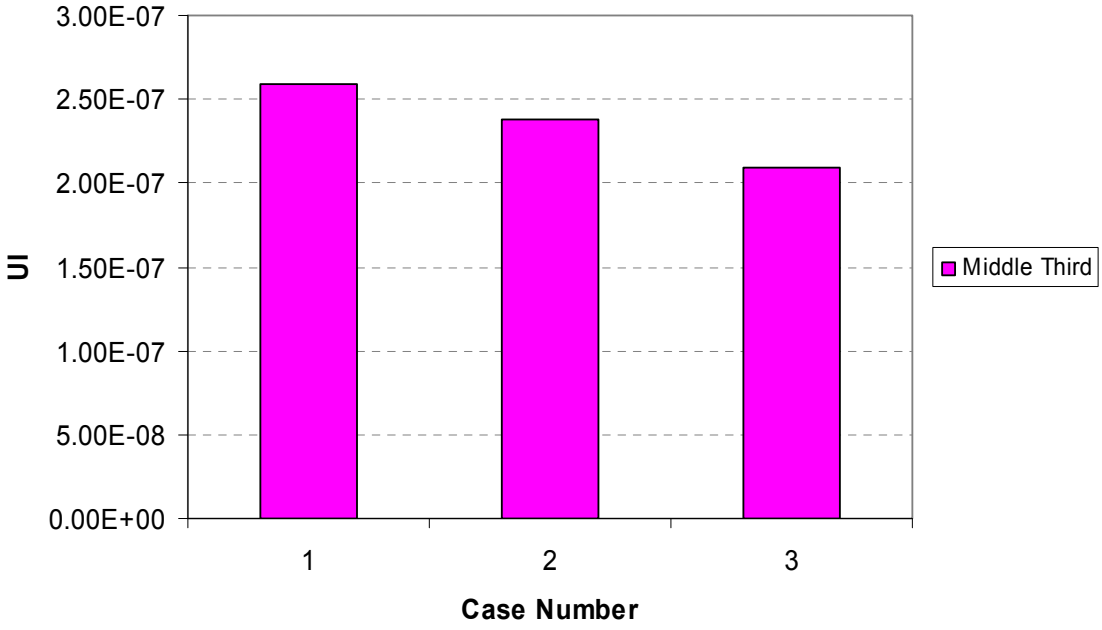

Figure 7-21. Uniformity Index for Middle Third of 150 mm Diameter Specimens with PG 64-22 Binder.

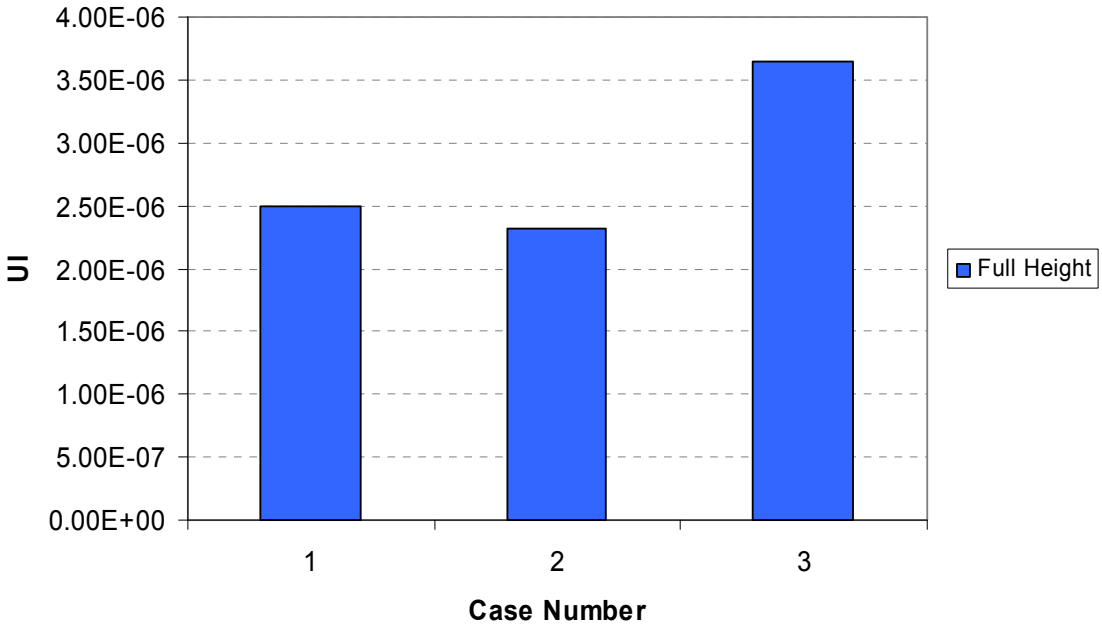

Figure 7-22. Uniformity Index for Full Height of 100 mm Diameter Specimens with PG 64-22 Binder.

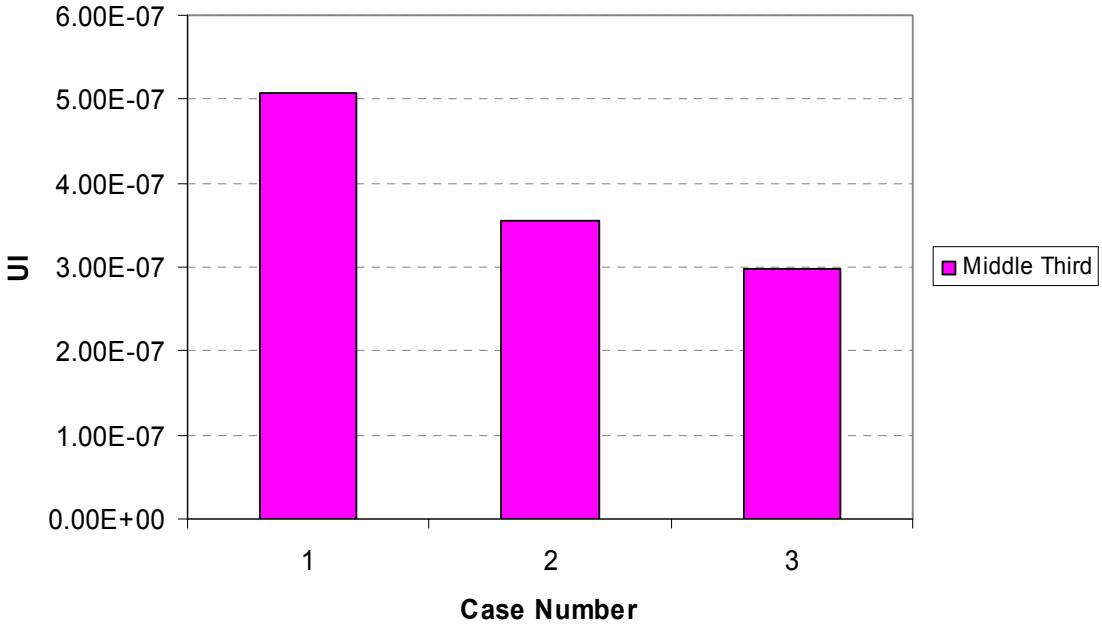

Figure 7-23. Uniformity Index for Middle Third of 100 mm Diameter Specimens with PG 64-22 Binder.

SUMMARY OF FINDINGS

The infrared temperature measurement system was used to measure the temperature profile along the specimen height during extraction of a specimen from the compaction mold. Combinations of top plate, base plate and mold temperatures were used to generate different temperature profiles. The following are the main findings:

- The results demonstrated a relationship between the temperature profile and air void distribution. Improvement of the uniformity of temperature profile is associated with uniformity in air void distribution. Case 3, which has more uniform temperature profile than the other cases, improved the uniformity of the air distribution in the middle third of the samples. However, this relationship is weak and does not warrant changes to the compaction temperature at this point.
- In general, it appears that compaction against the solid boundaries of the plates and mold rather than the temperature profile is the main cause of air void nonuniformity.
- The air void distribution is more uniform for specimens prepared using a modified binder compared with specimens prepared with an unmodified binder.
- The middle third of a specimen is more uniform than the whole specimen. This is consistent with findings from previous studies.

CHAPTER VIII
FORENSIC EVALUATION OF AIR VOID DISTRIBUTION IN ASPHALT PAVEMENT*

INTRODUCTION

Air void distribution is a major factor that affects the performance of asphalt mixture. Quantifying the air void distribution using X-ray CT is a powerful tool for forensic evaluation of HMA compaction related problems. One of the tasks of this research project was to assist TxDOT in conducting forensic evaluations of HMA pavements using X-ray CT. There was no specific objective to test a certain type of HMA mixture or pavements. Construction projects were selected for forensic evaluation based on requests from TxDOT engineers or other researchers. The following projects were included for this specific part of the study:

- SL 368 in San Antonio (Warm Mix)
- US 290 in Houston District
- FM 529 in Houston
- SH 114 in Fort Worth

The results for the first three projects (SL 358, US 290, and FM 529) of the forensic evaluation are given in Appendix B. The main task in these projects was to analyze the air void distribution in order to identify and help to eliminate some problems associated with these projects. This chapter reports on a comprehensive forensic evaluation that was conducted in SH 114 in collaboration with TxDOT Project 0-4822.

---

*Reprinted with the permission from "Evaluation of Full Depth Asphalt Pavement Construction using X-ray Computed Tomography and Ground Penetrating Radar" by Kassem, E., Walubita L., Scullion, T., Masad, E., and Wimsatt A., 2008, *Journal of Performance of Constructed Facilities,* ASCE, in press.

SH 114 IN FORT WORTH

Overview

In 2001, the Texas Department of Transportation developed guidelines for the design of full depth or perpetual pavements with more than 30 million Equivalent Single Axle Loads (ESALs) (TxDOT, 2001). These guidelines were developed by the Flexible Pavement Design Task Force, which consisted of senior TxDOT engineers and representatives from the Asphalt Institute, Texas Asphalt Pavement Association, and various industry groups. The objectives of the task force were to develop new asphalt mix specifications and pavement designs that could meet the demands of heavy truck traffic.

TxDOT has a long history of successfully constructing full depth hot mix asphalt (HMA) pavements as many of them were constructed in the 1960s and 1970s. The new guidelines recommended constructing pavement structures similar to the perpetual pavement concept developed by the Asphalt Institute (Newcomb et al., 2001). Figure 8-1 shows the proposed pavement structure for the Texas full depth pavements. The top layer is porous friction course (PFC), which has an open-graded structure to provide a good ride quality in terms of reduction in splash, spray and noise. The second layer is stone matrix asphalt (SMA) mix which is designed to have very good stone-on-stone contacts and very good resistance to permanent deformation. The next two layers are referred to as stone filled (SF) mixes that were designed to have good resistance to permanent deformation. The bottom asphalt layer, which is referred to as rich bottom layer (RBL), included a high asphalt content to resist fatigue cracking and to have low permeability. The SF and RBL mixes were designed according to the Superpave criteria and special TxDOT specifications (Scullion, 2006). The labels starting with "SS" and shown in parentheses in Figure 8-1 give the numbers for these special specifications.

In total eight full depth pavements were approved for construction in Texas starting in 2002. In 2005 a research study was initiated to evaluate the design, construction, and performance aspects of these new pavement structures (Scullion, 2006). The evaluation included a Ground Penetrating Radar (GPR) survey, field coring and laboratory testing. Details about the experimental evaluation can be found in Scullion (2006) and Walubita and Scullion (2007). In addition, some field cores were extracted

and analyzed using X-ray Computed Tomography (CT) in order to verify the GPR measurements. This section reports the findings from the field and laboratory evaluations of full depth pavement sections constructed in SH 114.

PFC (SS3231)	**1.0″-1.5″ Porous Friction Course**	**Sacrificial Layer**
HDSMA (SS3248)	**2.0″-3.0″ Heavy Duty SMA ½″ Aggregate with PG76-XX**	**Impermeable Load Carrying**
SFHMAC (SS3249)	**2.0″-3.0″ Stone-Filled HMAC ¾″ Aggregate with PG76-XX**	**Transitional Layer**
SFHMAC (SS3248)	**8.0″-'variable' Stone Filled HMAC, 1.0″-1.5″ Aggregate with PG76-XX**	**Load Carrying Layer**
Superpave (SS3248)	**2.0″-3.0″ Superpave or 3146 ½″ Aggregate with PG64-XX**	**Rich Bottom Layer (RBL) or Stress Relieving Impermeable Layer**
Stabilized foundation	**6.0″-8.0″stiff base or stabilized subgrade. Primarily to serve as construction working table or compaction platform for succeeding layers**	

PFC: Porous Friction Course, HMAC: Hot Mix Asphalt Concrete, HDSMA: Heavy Duty Stone Matrix Asphalt, SFHMAC: Stone Filled Hot Mix Asphalt Concrete, SS: Special Specifications, RBL: Rich Bottom Layer)

Figure 8-1. Texas Typical Full Depth Asphalt Pavement Structural Sections (Scullion, 2006).

Objectives

The objective of this study was to use GPR and X-ray CT to evaluate the quality of constructing full depth pavement sections in Texas. In particular, the primary focus was on the level of compaction and uniformity of the SF mix, which is used in layers 3 and 4 of Figure 8-1. This objective is achieved through the following tasks:

- Utilize GPR in order to assess the density uniformity in full depth pavement sections.

- Employ X-ray CT to analyze air void distribution in cores recovered from these sections.
- Evaluate and compare the findings from the GPR and X-ray CT methods.
- Develop recommendations in order to improve the construction of new full depth pavement structures.

Background

In the next section, an overview about the Ground Penetrating Radar (GPR) and its use in asphalt pavements will be given. An overview about the used X-ray CT system at Texas A&M University was given previously in Chapter IV.

Ground Penetrating Radar

The Ground Penetrating Radar sends discrete pulses of radar energy into the pavement system and captures the reflections from each layer interface within the structure. Radar is an electromagnetic wave, and therefore, obeys the laws governing reflection and transmission of electromagnetic (e-m) waves in layered media. The particular GPR unit used in this study can operate at highway speeds (70 mph), transmit and receive 50 pulses per second, and can effectively penetrate to a depth of 2 feet (60.96 cm). The Texas Transportation Institute's (TTI's) 1-Gigahertz (1-GHz) air-launched GPR unit is shown in Figure 8-2, and a typical plot of captured reflected energy versus time for one pulse is shown in Figure 8-3, as a graph of volts versus arrival time in nanoseconds. The reflection A_1 is the energy reflected from the surface of the pavement, and A_2 and A_3 are reflections from the top of the base and subgrade, respectively. Details on the uses of GPR to compute layer properties and thickness can be found elsewhere (Scullion and Chen, 1999).

Figure 8-2. TTI GPR Equipment (Scullion, 2006).

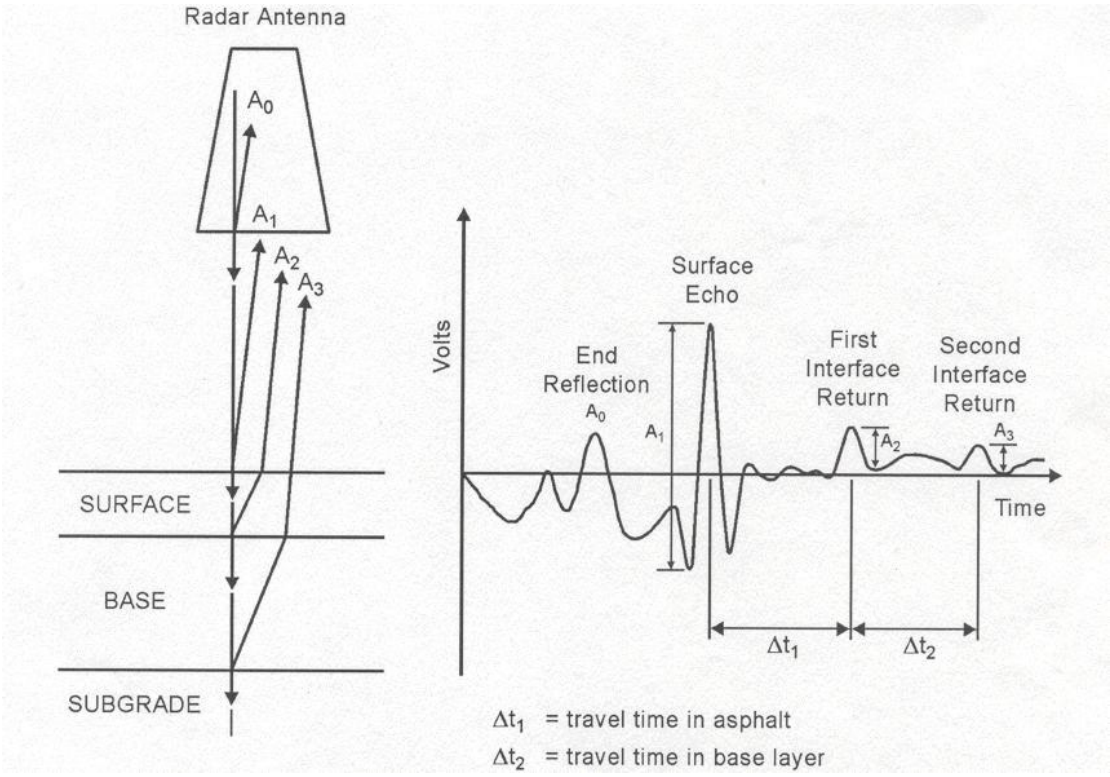

Figure 8-3. Illustration of the Principles of GPR (Scullion, 2006).

In most GPR projects, several thousand GPR traces are collected. A typical display of a GPR trace from a thick asphalt pavement with no defects is shown in Figure 8-4. In this trace there is a clear reflection from the surface and another from the top of the base, with no major reflections between these peaks. This type of reflection is judged as ideal, with no clear subsurface defects.

In order to conveniently display this information, color coding schemes are used to convert the traces into line scans and stack them side-by-side so that a subsurface image of the pavement structure can be obtained. This approach is used extensively in Texas. Color coding consists of converting this trace into a single-line scan of different colors where the high positive volt areas are color coded red, the negatives are blue and the areas around zero volts are green. Using the color coding and stacking scheme, this data are transformed into Figure 8-5, which shows a COLORMAP subsurface image for a 2500 ft section of highway with no defects. The labels on this figure are as follows: A) the surface of the pavement which is plotted as a red line at the top of the figure, B) the top of the base layer, C) the variation in surface reflection (an indication of the top layer uniformity) D) the distance scale in miles and feet, and E) the depth scale in inches. It is noted that zero on the depth scale is the reflection from the surface of the pavement. The pavement is homogeneous, and the layer interfaces are easy to detect.

In contrast to the GPR image shown in Figure 8-5, Figure 8-6 shows data from one of the Texas full depth pavements with some defects. The GPR data in Figure 8-6a were taken after construction of a 1 inch SF layer but before the placement of the surface layer for a section of approximately 500 ft. In these data, there are several strong reflections (red and blue lines) from within the SF layers. The blue areas indicate locations of low density material, while the red areas are locations of trapped moisture.

Figure 8-6b shows a GPR reflection from a single location, the positive reflections from the surface and top of the base are clear. However, between these are two large inverted (negative) peaks. Negative peaks occur with a transition from a layer of high to a layer of much lower dielectric. Within the full depth pavement structure, this can only be caused by a very large localized increase in air voids. The two negative reflections in Figure 8-6b were found to be associated with areas of “honeycombing” at the bottom of the first and second SF layer.

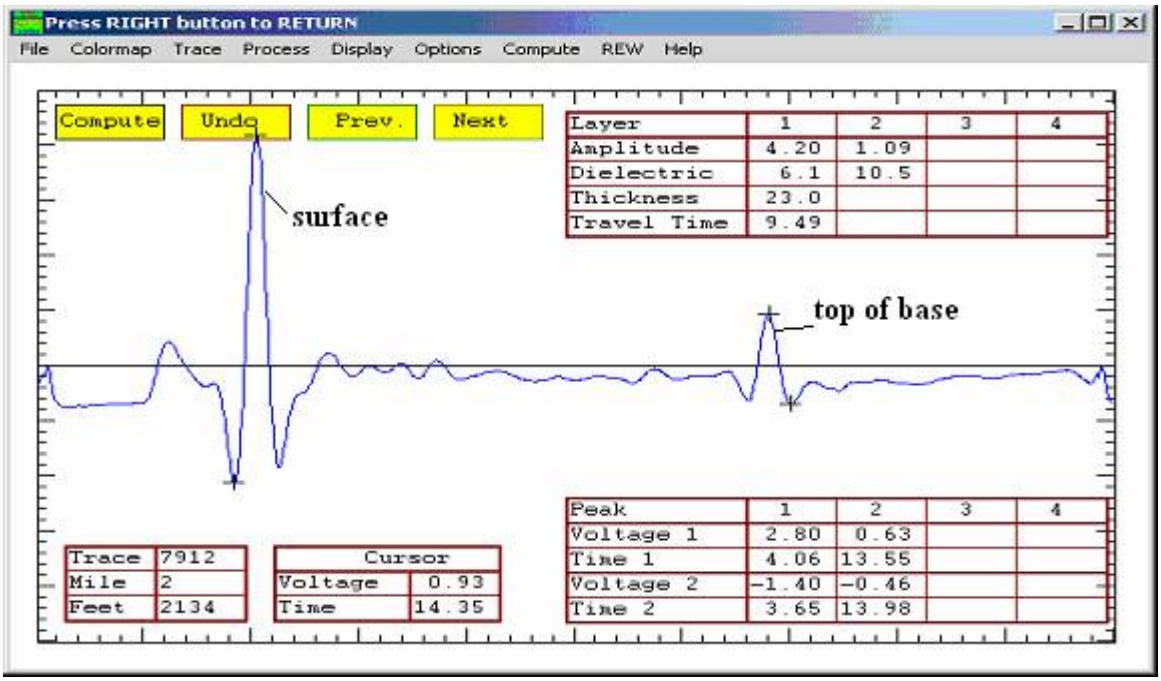

Figure 8-4. One Individual GPR Trace from a Thick Asphalt Pavement (Scullion, 2006).

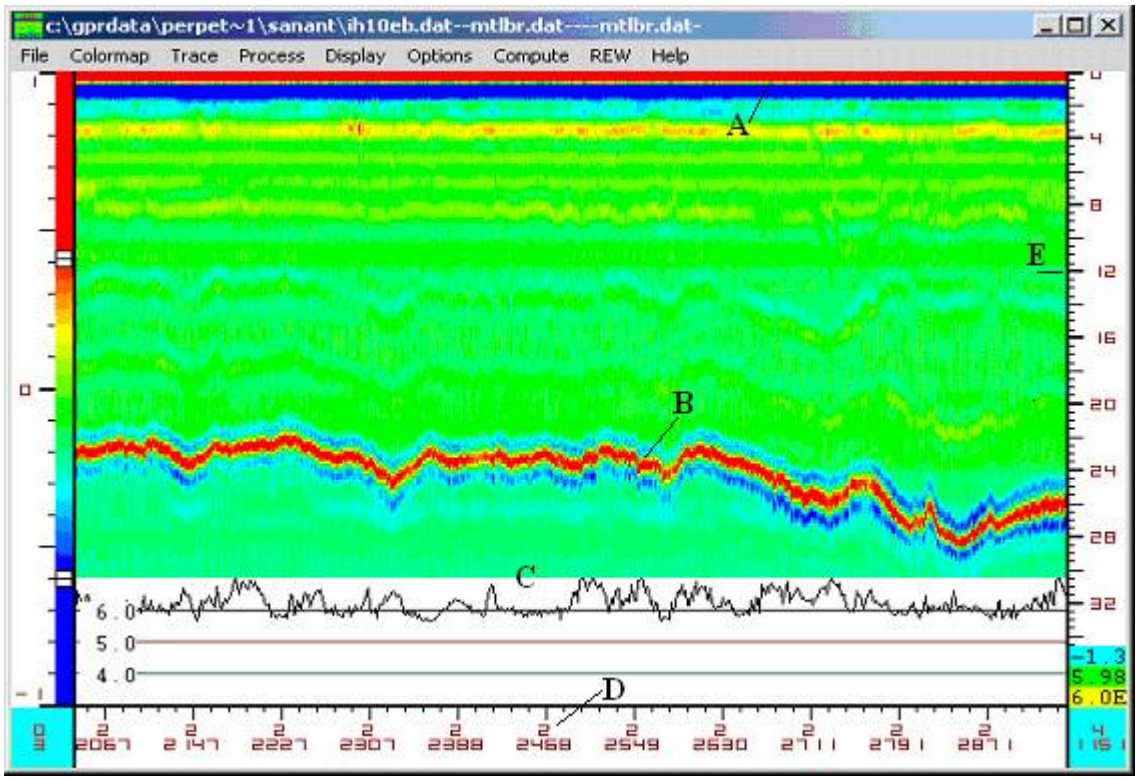

Figure 8-5. Color-Coded GPR Traces for a 1000 ft Section of Thick Asphalt Pavement (Scullion, 2006).

In Figure 8-6c, a different type of GPR pattern is observed. The two positive reflections from the top and bottom of the mix are still present, but this time a very strong positive reflection is observed close to the surface reflection. Very large positive reflections can be caused by the presence of excessive moisture at this interface. This is clearly problematic and will lead to stripping in the mix and premature pavement deterioration.

The GPR data shown in Figure 8-6 indicate that GPR is a good field tool for identifing defects from within HMA layers. The case study presented below is aimed at validating the GPR images with advance laboratory testing on cores extracted from the potential problem areas.

Project Description

The Full Depth Asphalt Pavement (FDAP) project is located in Forth Worth District of Texas on SH 114 in Wise County. It is approximately a 2.2 mile long project consisting of two 12 ft eastbound main-lanes, a 4 ft inside shoulder, and a 10 ft outside shoulder. SH 114 is a heavily trafficked highway with an average daily traffic (ADT) of approximately 18,000.

The SH 114 FDAP project was designed according to TxDOT guidelines for full depth asphalt pavements (TxDOT, 2001). As shown in Figure 8-7 the majority of the FW-01 section included SF mixes in layers 2, 3 and 4. The Texas District also decided to include a short section constructed using conventional dense-graded asphalt mixes as shown in the structure labeled FW-02 in Figure 8-7. The FW-01 and FW-02 sections are approximately 1.7 miles and 0.25 miles in length, respectively. The FW-02 section was constructed after the FW-01 section was placed because FW-01 mixes exhibited compaction problems (Walubita and Scullion, 2007).

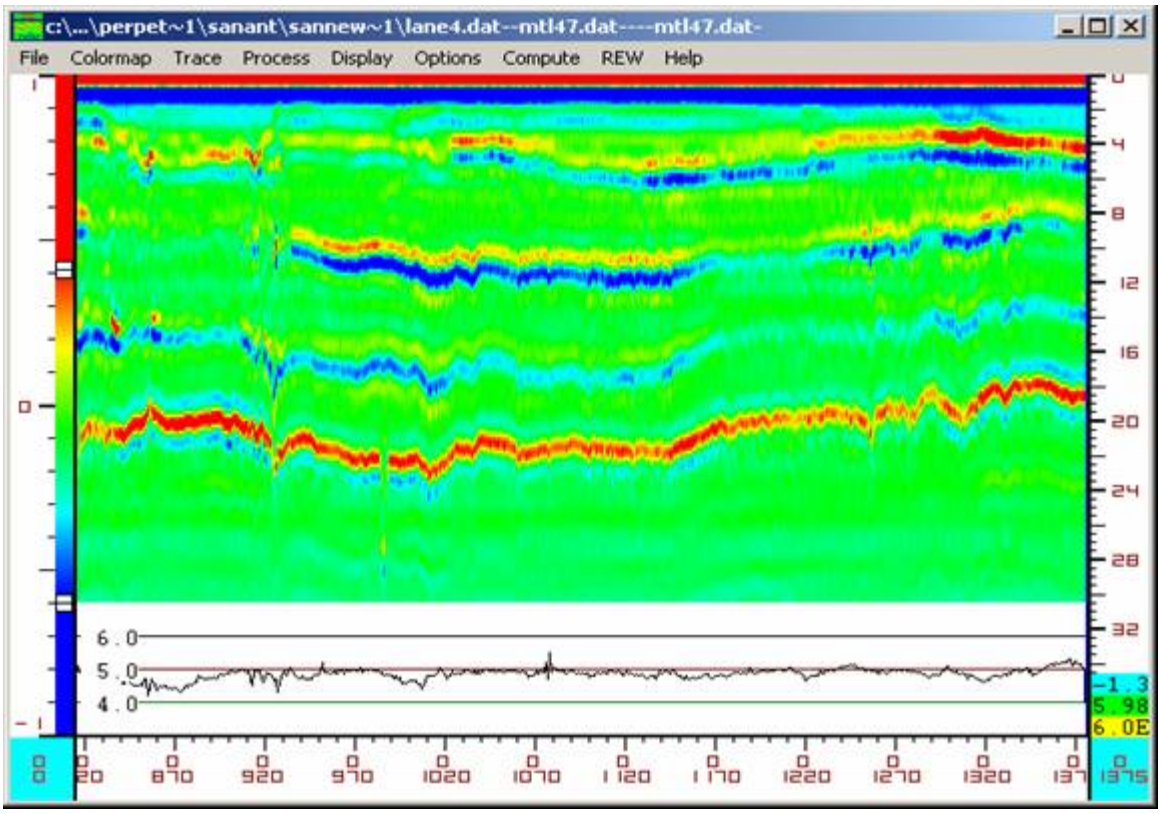

a) Color map with reflections from interfaces

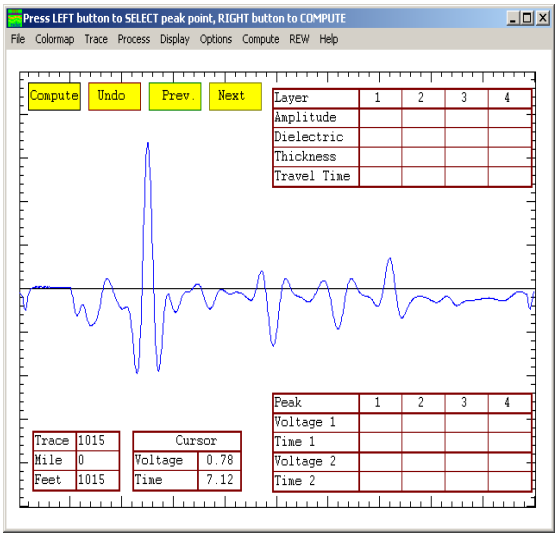

b) Voided areas

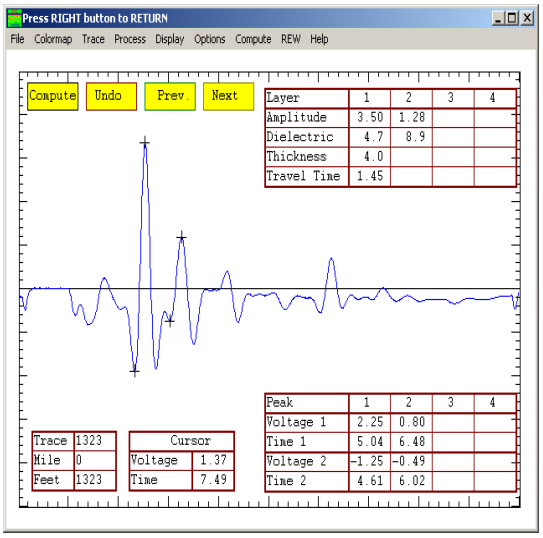

c) Areas with trapped moisture

Note: Major reflections from layer interfaces. Compaction problems with depth, the red subsurface areas indicate areas of trapped moisture. At the far right of the GPR plot, moisture is trapped 4 inches below the Surface.

Figure 8-6. GPR Data from a Full Depth Pavement (Scullion, 2006).

FW-01: Superpave

Layer	Material	Binder + Aggregate	Thickness
Layer 1	HDSMA	6.8% PG 70-28 + Igneous/Granite	2"
Layer 2	3/4" SFHMAC	4.2% PG 76-22 + Limestone	3"
Layer 3	1"SFHMAC	4.0% PG 70-22 + Limestone	13"
Layer 4	3/4" SFHMAC (RBL)	4.2% PG 64-22 + Limestone	4"
Layer 5	Stabilized Subgrade	6% Lime Treated	8"
Subgrade			∞

FW-02: Conventional

Layer	Material	Binder + Aggregate	Thickness
Layer 1	HDSMA	6.8% PG 70-28 + Igneous/Granite	2"
Layer 2	TxDOT Type C	4.4% PG 70-22 + Limestone	3"
Layer 3	TxDOT Type B	4.5% PG 64-22 + Limestone	13"
Layer 4	TxDOT Type C (RBL)	4.3% PG 64-22 + Limestone	4"
Layer 5	Stabilized Subgrade	6% Lime Treated	8"
Subgrade			∞

Figure 8-7. SH 114 Full Depth Asphalt Pavement Structural Sections (Walubita and Scullion, 2007).

The SF mixes in section FW-01 were designed according to the Superpave criteria to achieve 4 percent air voids (i.e., 96 percent density) at 100 gyrations. The rich bottom layer (RBL) was designed to have 97 percent density at 100 gyrations. All asphalt mixes passed the TxDOT requirement of a rut depth less than 12.5 mm (0.5 inch) in the Hamburg wheel tracking test (Walubita and Scullion, 2007). Figure 8-8 shows the aggregate gradations for the rut-resistant layers (1 inch SF in FW-01 section and TxDOT Type B in FW-02 section) according to both mix design and extraction from field cores. The 1 inch SF was designed with a coarse aggregate gradation passing below the Superpave restricted zone. The 1 inch SF was coarser than the TxDOT Type B mix. Based on extracted gradations, the 1 inch SF included more of the coarser aggregate (about 15.1 percent cumulative retained on the ¾ inch sieve instead of the design 10.7 percent) whereas the TxDOT Type B used more of the medium-fine rock (i.e., 74.59 percent cumulative retained on No. 10 versus the design 69.80 percent). Walubita and Scullion (2007) provide more information about the structural design, mix design, field binder content, aggregate gradations, construction details, and the performance of the SH 114 FDAP.

GPR Results

TxDOT construction personnel reported that the 1 inch SF layer was difficult to compact, permeable, and water would flow off the edge of the pavement during periods of heavy rainfall. To evaluate if moisture was trapped within the full depth pavement a GPR survey was conducted and the results are shown in Figure 8-9. These results clearly show trapped moisture in the asphalt mixes. Based on these findings, there was a major concern in TxDOT that the pavement might deteriorate if traffic is allowed with water trapped at the layer interface. To address this, edge drains were installed in this section and a chip seal was placed over the top of the ¾ inch SF layer.

The compaction difficulty in the 1 inch SF mix was attributed to the coarse and large aggregate gradation and the cold weather at the time of placement. Most of the lower layers for this pavement were placed from December 2003 to February 2004. Based on the observed construction problems with the FW-01 section, the Texas District constructed the last 0.25 miles of this project using traditional Texas dense graded mixes, designated at FW-02 in Figure 8-7. GPR measurements were taken on both structures in 2006 after the placement of the surface seal and edge drains in the FW-01 section. At that time no moisture was detected in either section, but some density variations were observed on the FW-01 section as shown in Figure 8-10. Figure 8-11 shows some low density areas that were detected in the FW-01 section. This low density problem was primarily centered around the longitudinal construction joints. Radar measurements indicated no evidence of major surface density and thickness variations or presence of moisture on the FW-02 section. In general, the FW-02 section appears to have been better compacted than the FW-01 section. To verify these interpretations of the GPR data, field cores were taken from the different areas and returned to the laboratory for detailed evaluation.

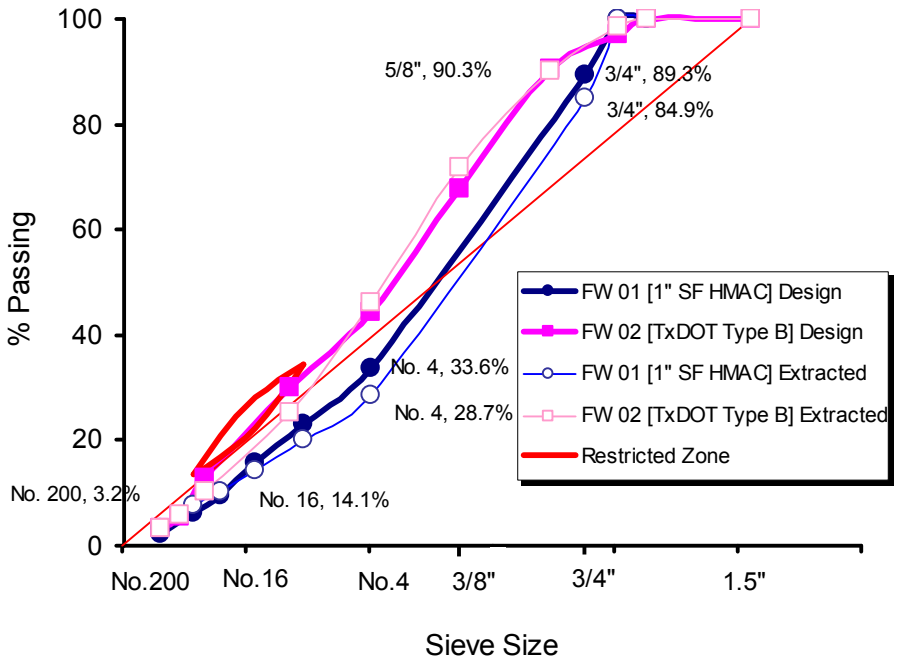

Figure 8-8. Aggregate Gradations (Walubita and Scullion 2007).

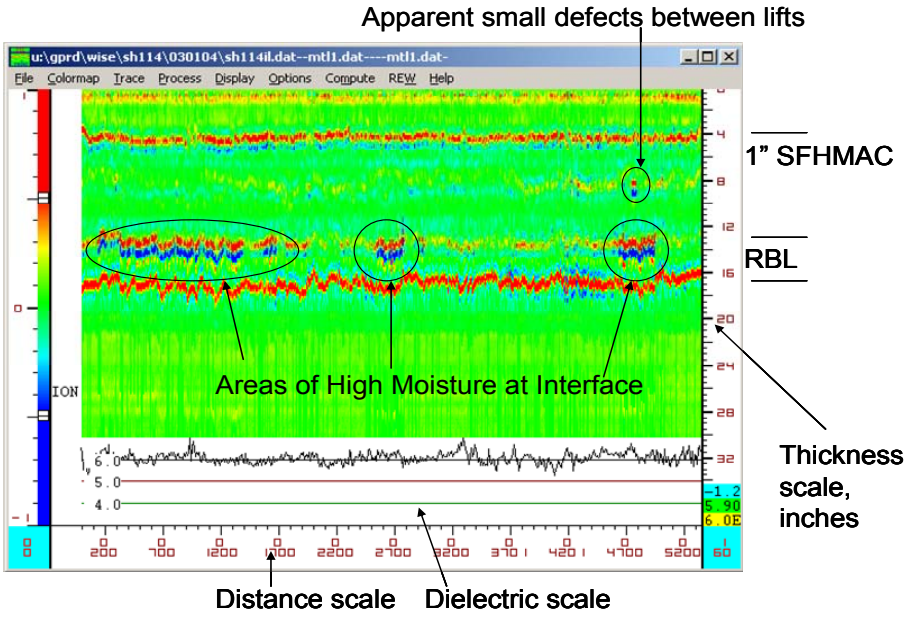

Figure 8-9. GPR Data Collected after Construction of the FW-01 Section (Walubita and Scullion, 2007).

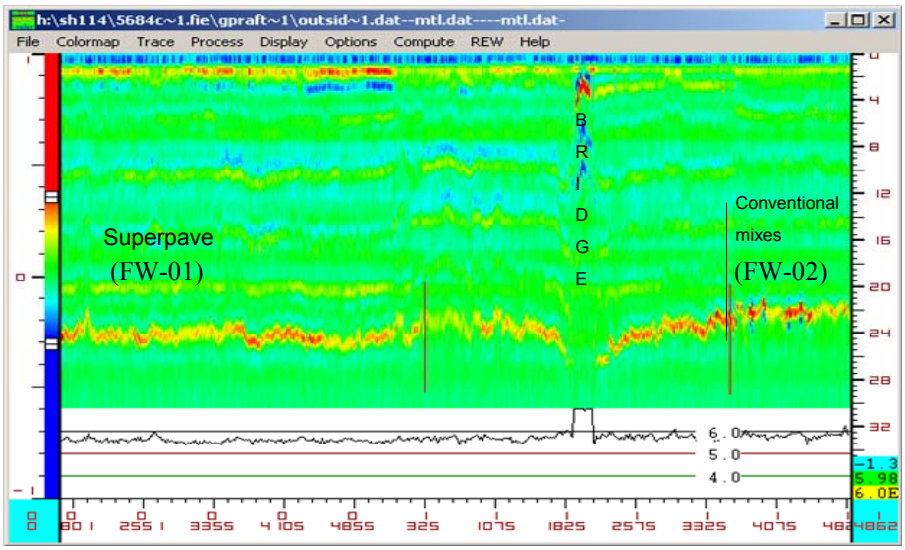

Figure 8-10. GPR Data after Construction of FW-01 and FW-02 (Walubita and Scullion, 2007).

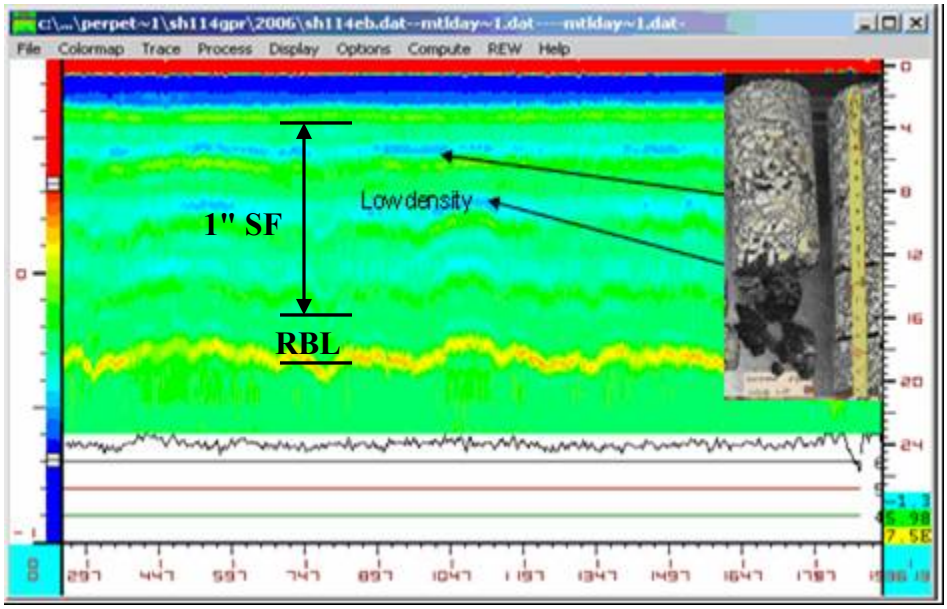

Figure 8-11. GPR Data Showing Low Density Areas within the 1-inch SF Layer of the FW-01 Section (Walubita and Scullion, 2007).

X-ray CT Analysis and Discussion

Four field cores were examined in order to characterize the air void distribution. One field core was taken from the FW-02 section, and three field cores were taken from the FW-01 section at different locations.

The X-ray CT images were thresholded in order to separate air voids from the other mix constituents (aggregate and asphalt). The threshold level represents a boundary value below which pixels in the analyzed image are considered as part of the air voids, whereas pixels that have intensity values above the threshold value are considered to belong to the remaining phases. The thresholded images were analyzed to determine average percent air voids for a specimen (*%AV*), average percent air voids in an image ($\%AV_{image}$), and average air void radius in an image (*r*) using Equations (8-1), (8-2) and (8-3), respectively.

$$\%AV = \frac{1}{N}\sum_{N}^{1}\%AV_{image} \tag{8-1}$$

$$\%AV_{image} = \frac{A_{TV}}{A_T} \tag{8-2}$$

$$r = \sqrt{\frac{A_{TV}}{\pi n}} \tag{8-3}$$

where A_{TV} is the total area of the air voids in a CT image, A_T is the total cross-sectional area of a CT image, N is the number of CT images, and n is the number of the air voids in a CT image. The analysis was conducted using macros that were developed in Image-Pro® Plus software.

The percent air voids and average radius of air voids for the cores from sections FW-01 and FW-02 are shown in Figures 8-12 and 8-13, respectively. The average radius of air voids at a given depth corresponds well with percent air voids at that depth. As shown in Figure 8-12, there were low density (high air void) areas within the FW-01 pavement structure especially within the 1 inch SF layer at depths of 6 inches and 10 inches. These findings confirm those from the GPR measurements presented in Figure 8-

11. In general, the distributions of both percentage of air voids and average radius of air voids for the FW-01 core revealed the poor compaction of this section.

As shown in Figures 8-13a and 8-13b, the percent air voids and air void radius distributions in FW-02 section did not show much nonuniformity indicating that the compaction uniformity of the FW-02 section was better than the compaction of the FW-01 section. The results of the X-ray CT for section FW-02 correlated well with the GPR findings presented in Figure 8-10. The three-dimensional distribution of air voids that correspond to the results in Figures 8-12(a) and 8-13(a) are shown visually in Figures 8-14(a) and 8-14(b), respectively.

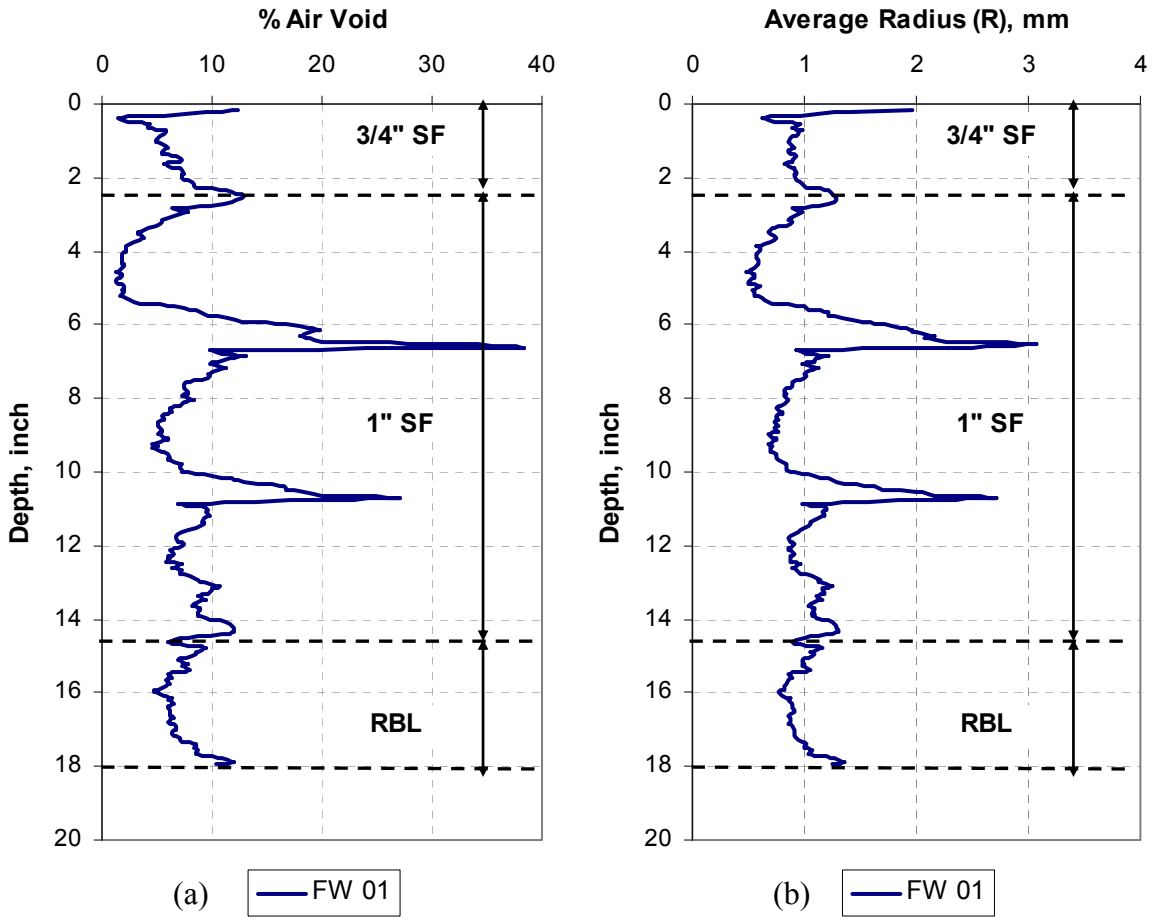

Figure 8-12. Air Void Distribution across the Depth of Core 1 from FW-01 Section (a) Percent Air Voids, (b) Air Void Radius.

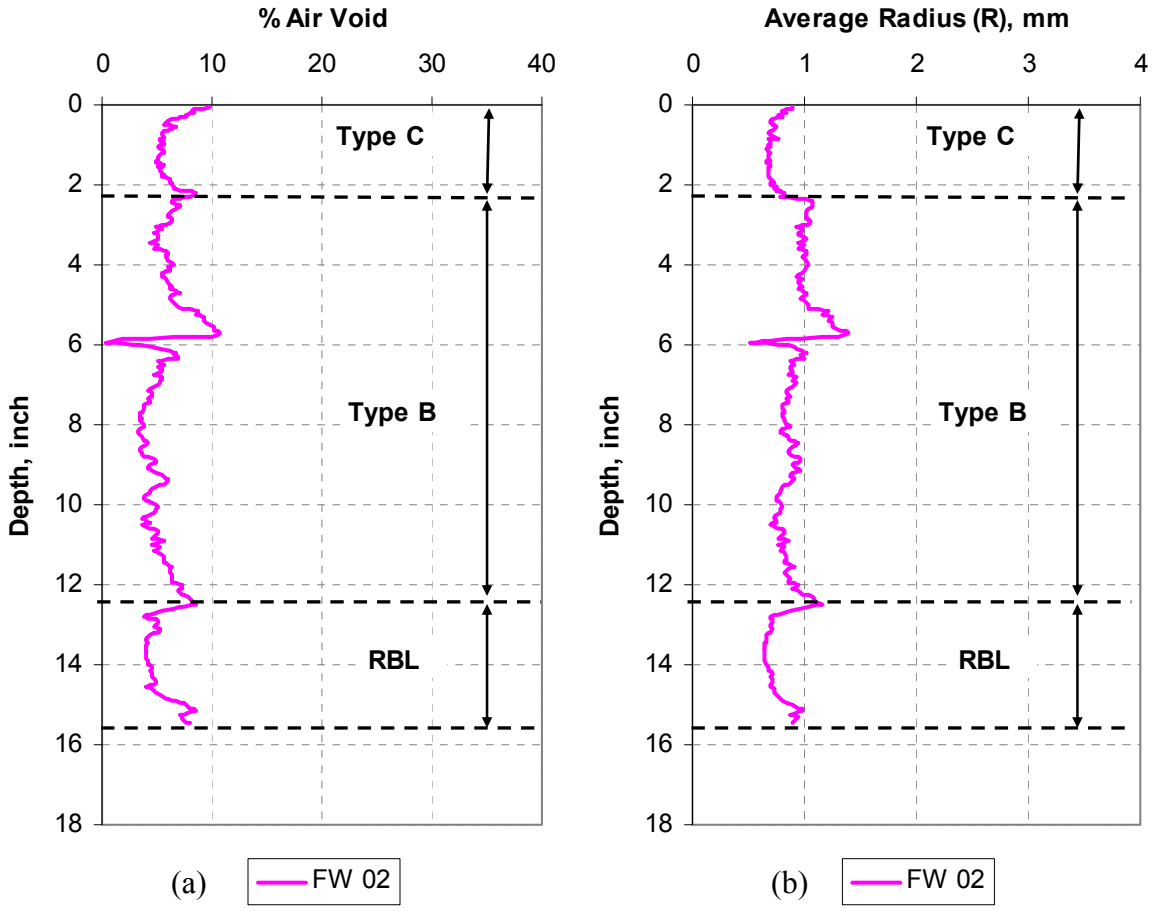

Figure 8-13. Air Void Distribution across the Depth of Core 2 from FW-02 Section (a) Percent Air Voids, (b) Air Void Radius.

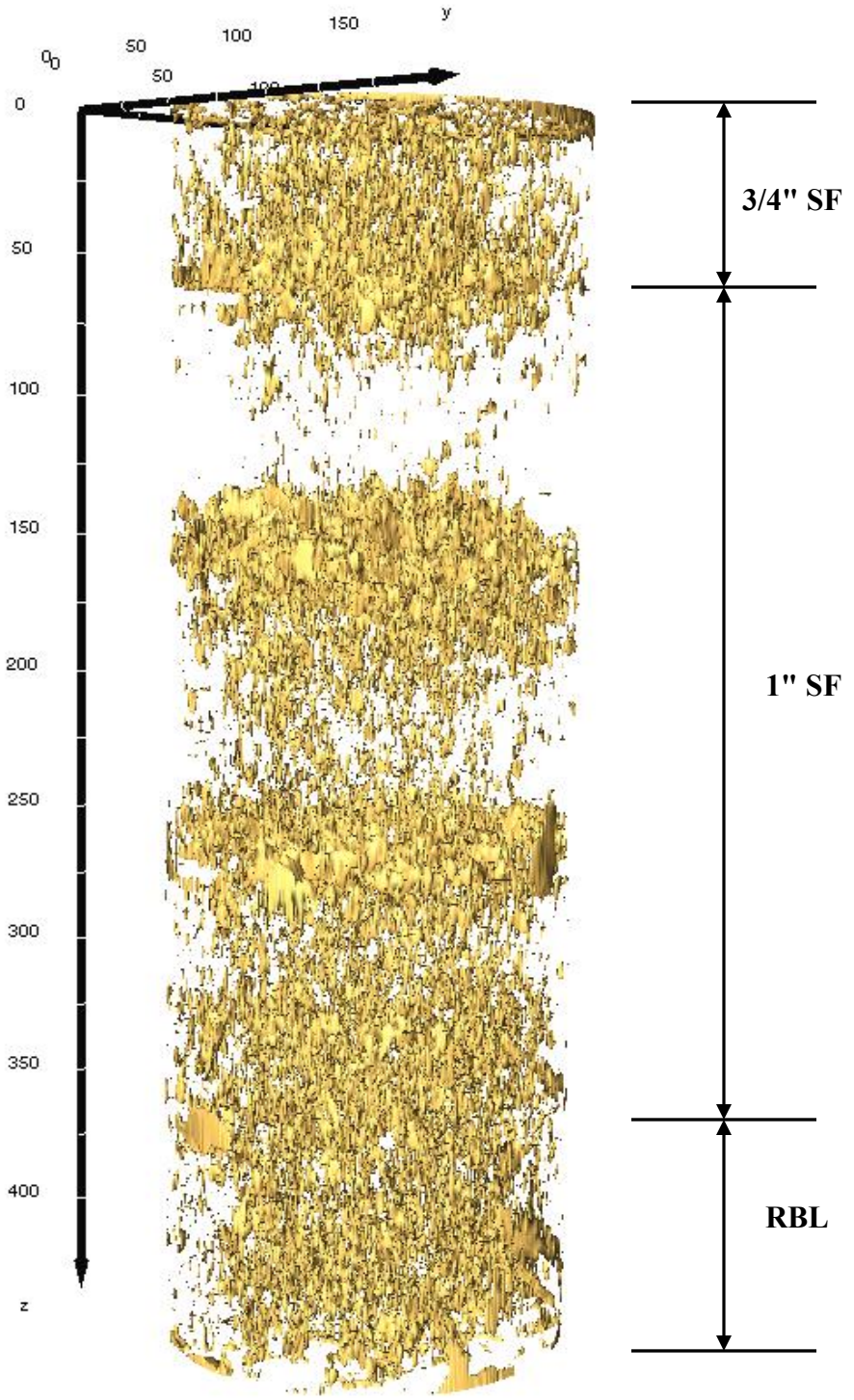

(a)

Figure 8-14. Three-Dimensional of Air Voids across the Depth (a) Core 1 from FW-01 Section, (b) Core 2 from FW-02 Section.

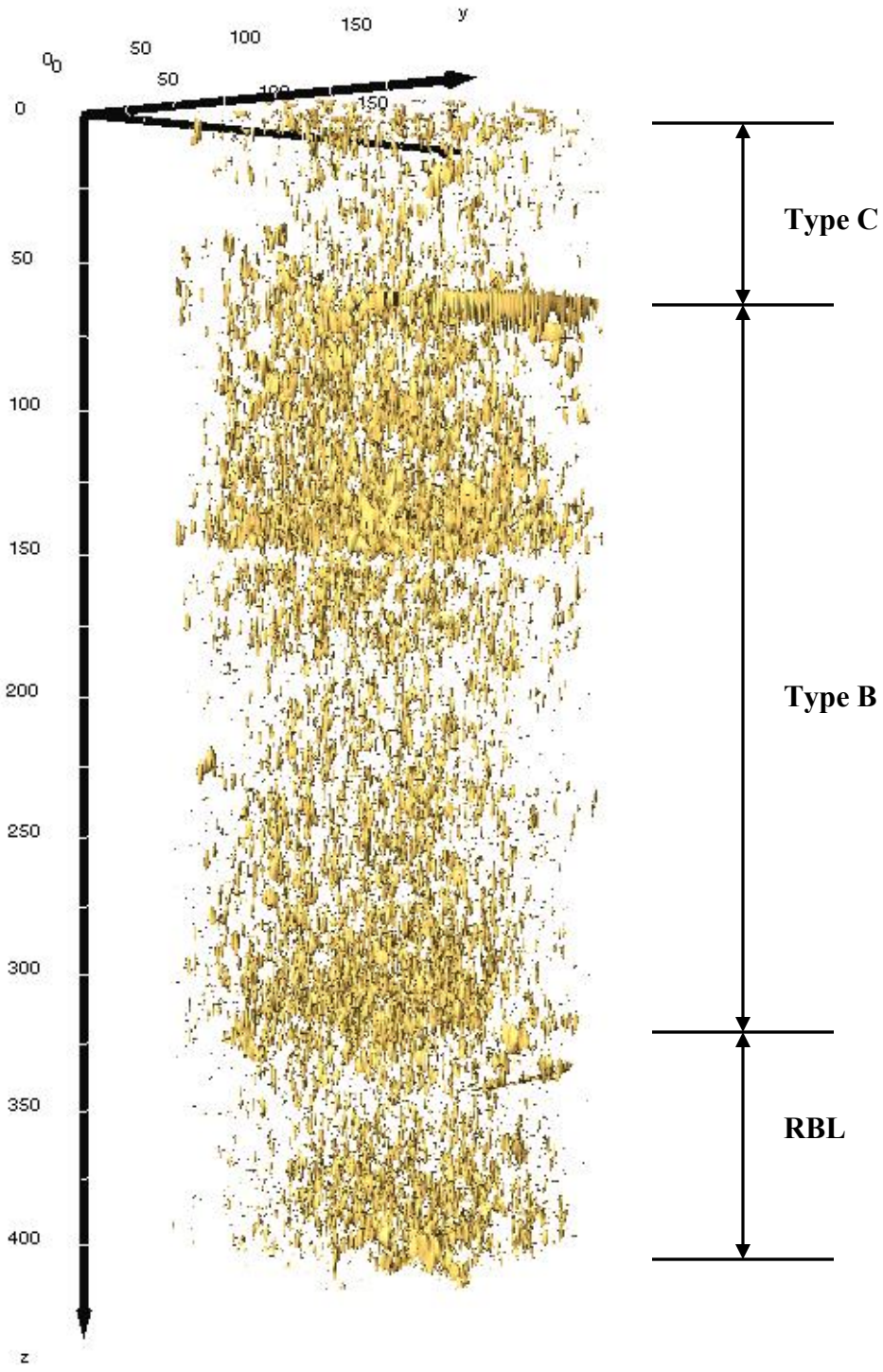

(b)

Figure 8-14. Continued.

Based on the initial findings presented in Figures 8-12 and 8-13, two more cores were taken from the FW-01 sections and evaluated using X-ray CT. The results are shown in Figures 8-15 and 8-16. The scanning for the core in Figure 8-15 focused on only 3 inches above the interface between the 1 inch SF mix and the RBL mix, while the scanning was conducted for about 8.5 inches above the interface for the core in Figure 8-16. As can be seen in Figures 8-15 and 8-16, there were a high percentage of air voids which associated with large air voids at the interface between the 1 inch SF layer and the RBL layer and within the 1 inch SF layer for the FW-01 section. This finding correlates well with the GPR traces, which also demonstrated low density areas at the interface and within the 1 inch SF layer.

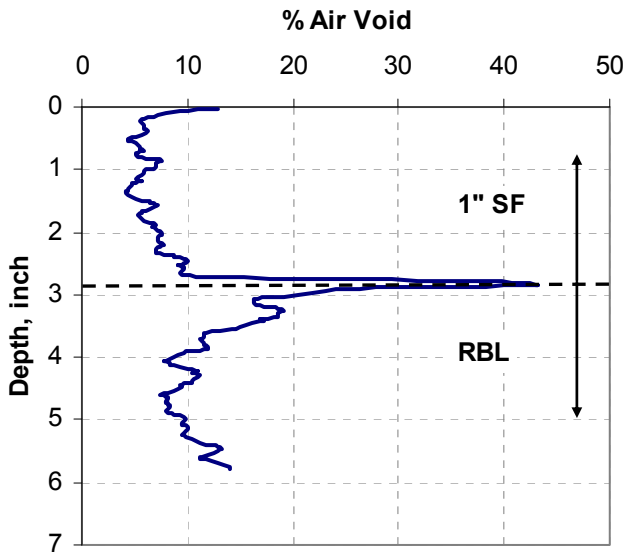

Figure 8-15. Air Void Distribution across the Depth of Core 3 from FW-01 Section.

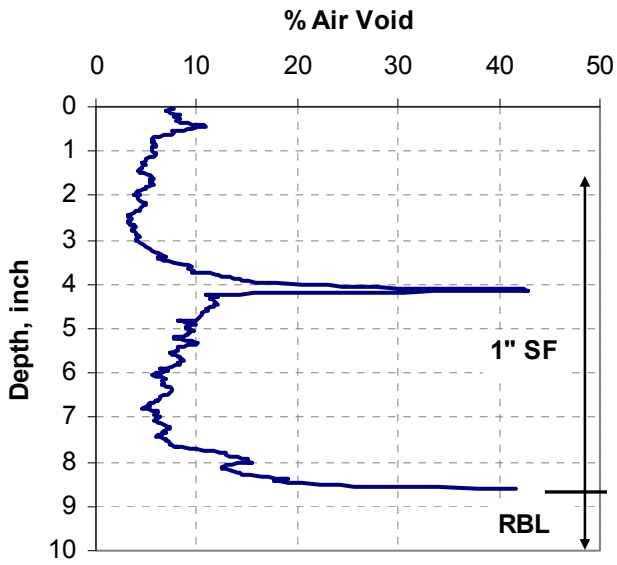

Figure 8-16. Air Void Distribution across the Depth of Core 4 from FW-01 Section.

CONCLUSIONS

The Ground Penetrating Radar and X-ray Computed Tomography were used in order to evaluate the construction of new full depth asphalt pavements. The GPR was able to detect and show the extent of the compaction problem in the new pavement investigated in this study. The GPR detected low density areas typically at the bottom of the stone filled (SF) layers. These layers were placed in 4 inch lifts and it appears that the bottom 1 inch of the lift was poorly compacted. The color coded image display of GPR data were very useful in quantifying the depth and extent of both water filled and air filled voids within the HMA layer. This information was used to generate a strategy to drain trapped moisture from the pavement structure.

X-ray CT was used to provide detailed information about the air void distribution in field cores and verify the GPR findings. The X-ray CT results were in very good agreement with the GPR measurements as it showed that the FW-01 section had less uniformity in air void distribution and larger air voids than the FW-02 section. Based on the results, it is recommended to make adjustments to the design of the SF mixes used in Texas to allow better compaction.

CHAPTER IX
DETERMINATION OF THE MOISTURE DIFFUSION COEFFICIENT OF ASPHALT MIXTURES*

INTRODUCTION

Air void distribution is not uniform through the depth of the mat of asphalt pavements. The findings of Chapter IV showed that the middle part of the mat is more compacted than the top and bottom parts. In this chapter the effect of the nonuniformity of the air void distribution on the moisture diffusion through the asphalt pavements will be evaluated. The presence of the moisture in asphalt pavements causes loss of bond between the aggregate and binder surfaces (adhesive failure) and/or loss of the cohesive bond within the binder (cohesive failure). These two failure modes are manifested in asphalt pavements as loss of binder (stripping), loss of aggregate (raveling), cracking and even permanent deformation. Moisture enters the asphalt pavements through different mechanisms such as infiltration of surface water, capillary rise of subsurface water and diffusion of water vapor. Most of the research has focused on permeability as a measure of the infiltration of water in the mixture (Masad et al., 2006a). A recent study by Masad et al. (2007) provided experimental evidence of water capillary rise in asphalt mixtures. Kassem et al. (2006) developed an experimental method for measuring moisture diffusion coefficients in asphalt mastics (fine aggregate particles mixed with binder). Moisture diffusion is an important mechanism for the cause of moisture damage in areas with low levels of annual rainfall such as New Mexico and Arizona (Caro et al., 2007). Moisture is transported into the mix under diffusion due to the difference in relative humidity between the pavement surface that has low relative humidity and the pavement underlying layer that has high relative humidity. Kassem et al. (2006) showed a good

---

*Reprinted with the permission from "Measurements of the Moisture Diffusion Coefficient of Asphalt Mixtures and its Relationship to Mixture Composition." by Kassem, E., Masad, E., Lytton, R., and Bulut, R., 2008., *International Journal of Pavement Engineering*, IJPE, in press, Copyright Taylor & Francis, International Journal of Pavement Engineering is available online at http://www.informaworld.com

correlation between the measured diffusion coefficients in the lab and the reported moisture damage from the field.

Kringos and Scarpas (2005a, 2005b) developed a finite element analysis tool to simulate the gradual development of moisture damage in asphalt mixtures as a result of water diffusion. The moisture diffusion coefficients are required inputs for these models. The study herein complements the findings from an earlier study (Kassem et al. 2006) in which they reported the diffusion coefficients for asphalt mastics. This study aims at developing an experimental procedure for measuring the diffusion coefficient of full asphalt mixtures and evaluating the effect of the nonuniformity of air void distribution on the moisture diffusion.

OBJECTIVES

The objective of this study was to develop an experimental procedure for measuring the diffusion coefficient of full asphalt mixtures and to evaluate the effect of air voids on moisture diffusion. Using thermocouple psychrometers to measure the relative humidity in asphalt mixtures under well-defined boundary conditions achieved this objective. The moisture diffusion equation was solved numerically using the specified boundary conditions to determine moisture diffusion coefficients. These coefficients were related to the percent air voids in asphalt mixtures.

MEASUREMENTS OF SUCTION USING THERMOCOUPLE PSYCHROMETERS

Suction can be defined as a free energy state of water in a porous medium (Bulut and Wray 2005, Edlefsen and Anderson 1943). Asphalt mixtures are porous media that have the ability to attract and retain water (Kassem et al., 2006). Equation 9-1 (Fredlund and Rahardjo, 1993) below measures the total suction.

$$h = -\frac{RT}{v_{w0}\omega_v}\ln\left(\frac{\bar{u}_v}{\bar{u}_{v0}}\right) \tag{9-1}$$

where h = total suction, $\bar{u}_v$ = partial pressure of pore-water vapor, $\bar{u}_{v0}$ = saturation pressure of water vapor over a flat surface of pure water at the same temperature, ($\bar{u}_v / \bar{u}_{v0}$)

= relative humidity, R = universal gas constant, T = absolute temperature, v_{w0} = specific volume of water, ω_v = molecular mass of water vapor. Total suction, as can be seen in Equation 9-1, is a function of relative humidity at a given temperature.

The thermocouple psychrometers were utilized herein in order to measure the total suction. Thermocouple psychrometers measure total suction by measuring the relative humidity in a confined space. Psychrometers operate based on the temperature difference between two surfaces, the evaporating surface (wet bulb), and the non-evaporating surface (dry bulb). The operation of thermocouple psychrometers depends on two principles—the Seebeck effect and the Peltier effect (Fredlund and Rahardjo, 1993). In a closed circuit of two different metals, an electromotive force is generated when the two junctions of the circuit have a temperature difference (Figure 9-1a). This principle is known as the Seebeck effect (Fredlund and Rahardjo 1993). The induced electromotive force is a function of the temperature difference between the two junctions. Inducing a current through a closed circuit that consists of two different metals generates different thermal conditions at both junctions (Figure 9-1b). One junction gets cooler while the other gets warmer, which is known as the Peltier effect (Fredlund and Rahardjo, 1993).

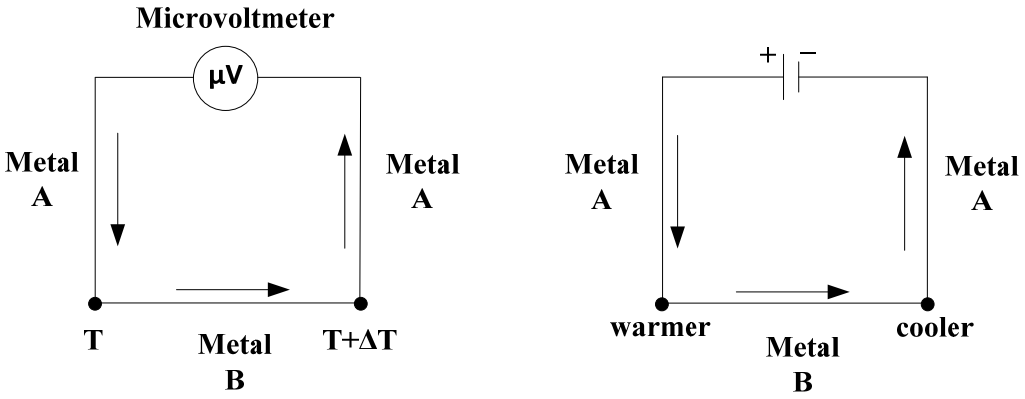

Figure 9-1 (a) Seebeck Effect, (b) Peltier Effect (Fredlund and Rahardjo, 1993).

The thermocouple psychrometer uses the Peltier effect to cool its junction until it reaches the dewpoint. Therefore, water vapor condenses on this junction. The condensed water starts to evaporate once the cooling current stops, leaving a temperature difference between the junction and the surrounding atmosphere. The temperature reduction of the junction depends on the evaporation rate, which is influenced by water vapor pressure or suction in the atmosphere. The difference in the temperature of both junctions generates an electromotive force in the circuit, according to the Seebeck effect. A microvoltmeter measures the generated electromotive force, or microvolts, in the circuit.

Calibration reveals the relationship between different suction levels and microvolts in the circuit of thermocouple psychrometer. In the calibration process, salt solutions with different concentrations, which correspond to different suction levels, are used to generate the relationship between total suction and recorded microvolts (Figure 9-2). The recorded microvolts increase proportionally with an increase in the suction level over a certain range. This range differs slightly from one psychrometer to another. For most of the psychrometers, this range is from about 3.67 *pF* (4.5 bar) to about 4.68 *pF* (47 bar) where $pF=Log(1019.8h)$; h with bar. If the suction level is below the lower limit of this range, the recorded microvolts are either negative values or equal to zero as shown in Stage I of Figure 9-3. Stage II in Figure 9-3 shows the measurements within the psychrometer's range, where the psychrometers function properly. In Stage III of Figure 9-3, the suction levels increase beyond the upper limit of psychrometer's range causing the microvolt reading to decrease until it reaches zero or negative values. Stage II of Figure 9-3 generates the calibration curve of a thermocouple psychrometer as shown in Figure 9-2. See Fredlund and Rahardjo (1993), Kassem (2005), and Bulut and Leong (2008) for more information about operational principles for psychrometers.

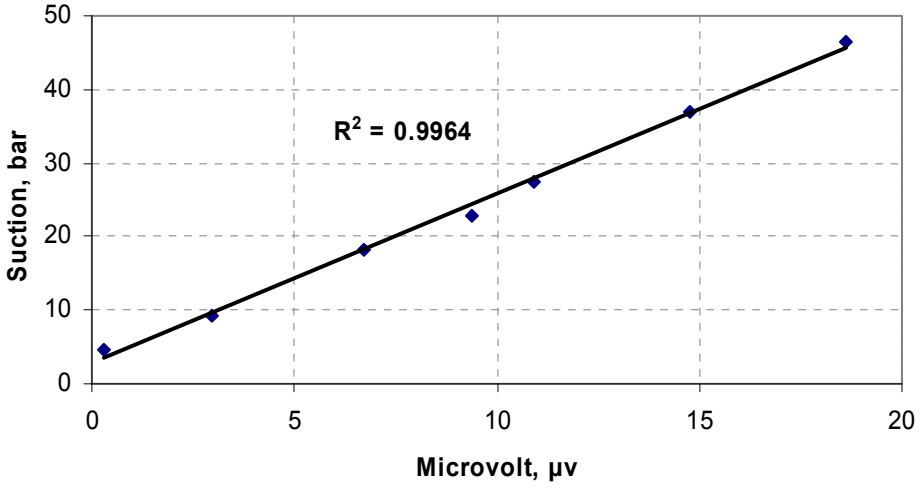

Figure 9-2. Calibration Curve of Thermocouple Psychrometer.

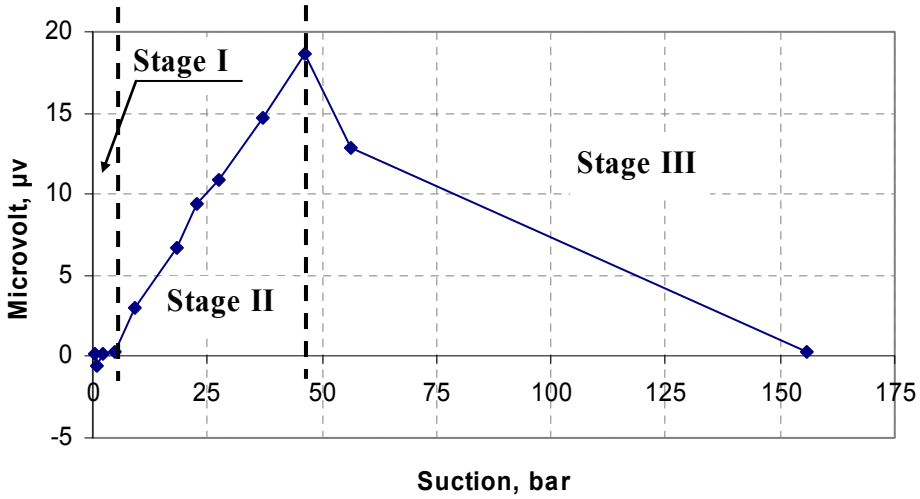

Figure 9-3. Relationship between Microvolt Outputs and Total Suction.

ANALYSIS OF DIFFUSION COEFFICIENTS

Mitchell (1979) proposed a simplified approach for solving the general mass-transport diffusion equation. He utilized Laliberte and Corey's (1967) permeability equation given by Equation 9-2 and the mass balance equation for unsteady fluid flow to develop a simplified formulation of moisture diffusion.

$$k(h) = k_0 \left(\frac{h_0}{h} \right)^n \tag{9-2}$$

where, $k(h)$ = permeability as a function of total suction (unsaturated permeability), k_0 = saturated reference permeability, h_0 = a reference value of total suction, h = total suction, n = positive constant depending on material's type.

Mitchell (1979) assumed the n value in Equation 9-2 to be 1, which is valid for low permeability and tight materials, such as very high plastic clays. The permeability value k from Equation 9-2 is then substituted into Darcy's law given in Equation 9-3 to get Equation 9-4. Darcy's equation describing one-dimensional unsaturated flow is given by:

$$v = -k(h) \left(\frac{dh}{dx} \right) \tag{9-3}$$

where, v = flow velocity, $\frac{dh}{dx}$ = head (suction) gradient.

Combination of Equations 9-2 and 9-3 leads to the following non-linear relationship:

$$v = -k_0 \left(\frac{h_0}{h} \right) \left(\frac{dh}{dx} \right) \tag{9-4}$$

Mitchell (1979) took the following steps to reduce the non-linear relationship presented in Equation 9-4 into a linear one. Equation 9-4 can be rearranged to become:

$$v = -k_0 h_0 \left(\frac{dh/h}{dx} \right) \tag{9-5}$$

The dh/h term in Equation 9-5 can be represented as follows:

$$\frac{dh}{h} = d(\log_e h) = \frac{1}{0.434} d \log_{10} h \tag{9-6}$$

Substituting Equation 9-6 into Equation 9-5 gives:

$$v = -\frac{k_0 h_0}{0.434} \frac{d \log_{10} h}{dx} \tag{9-7}$$

where $\log_{10} h$ = the total suction in pF units, which is termed u. Therefore, Equation 9-7 can be written as:

$$v = -\frac{k_0 h_0}{0.434} \frac{du}{dx} = -p \frac{du}{dx} \tag{9-8}$$

where $p = \frac{k_0 h_0}{0.434}$ is a constant.

In Figure 9-4, Mitchell (1979) considered an incremental section of the porous material with the dimensions Δx, Δy, and Δz for using the conservation of mass principle. The section proposed by Mitchell has a source of moisture generated in the material at a rate per unit volume defined by $f(x,t)$.

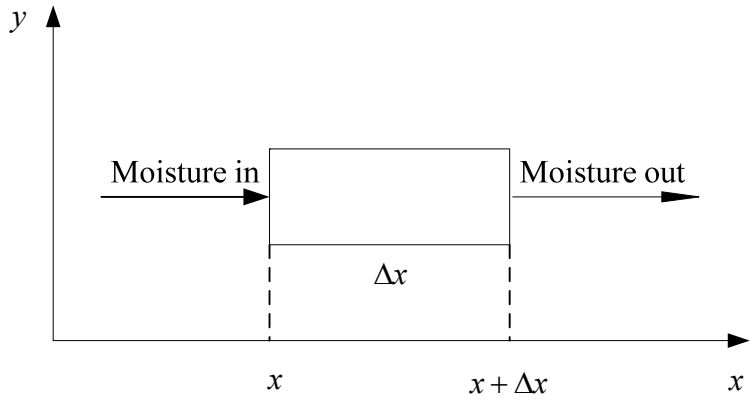

Figure 9-4. Incremental Section with Dimensions Δ*x*, Δ*y*, and Δ*z*.

Equation 9-9 represents the net flow into the body for the case of one-dimensional flow in the *x* direction:

$$\Delta Q = v_x \Delta y \Delta z \Delta t\big|_x - v_x \Delta y \Delta z \Delta t\big|_{x+\Delta x} + f(x,t)\Delta x \Delta y \Delta z \Delta t \tag{9-9}$$

Substituting v_x from Equation 9-8 into Equation 9-9 gives:

$$\Delta Q = -p\,\Delta y\,\Delta z \left(\frac{\partial u}{\partial x}\right)_x \Delta t - \left\{-p\,\Delta y\,\Delta z \left(\frac{\partial u}{\partial x}\right)_{x+\Delta x} \Delta t\right\} + f\,(x,t)\Delta x\,\Delta y\,\Delta z\,\Delta t \tag{9-10}$$

$$= p\,\Delta x\,\Delta y\,\Delta z\,\frac{\left(\frac{\partial u}{\partial x}\right)_{x+\Delta x} - \left(\frac{\partial u}{\partial x}\right)_x}{\Delta x}\Delta t + f\,(x,t)\Delta x\,\Delta y\,\Delta z\,\Delta t \tag{9-11}$$

$$\Delta Q_{\Delta x \to 0} = p\Delta x \Delta y \Delta z \frac{\partial^2 u}{\partial x^2}\Delta t + f(x,t)\Delta x \Delta y \Delta z \Delta t \tag{9-12}$$

Mitchell (1979) defined the relationship between moisture content and suction as shown in Equation 9-13:

$$c = \frac{dw}{du} \tag{9-13}$$

where, c = the slope of the suction-moisture characteristic curve, w = gravimetric water content , u = suction in pF.

The water content is defined as:

$$w = \frac{W_w}{W_s} \tag{9-14}$$

where, W_w= weight of water, W_s = weight of solids. The amount of stored moisture can be expressed by Equation 9-15:

$$\Delta Q = \frac{\Delta W_w}{\gamma_w} = \frac{\Delta w W_s}{\gamma_w} = \Delta x\, \Delta y\, \Delta z\, (\Delta uc\, \frac{\gamma_d}{\gamma_w}) \tag{9-15}$$

where, γ_d = dry density, γ_w = water density

The amount of stored moisture given in Equation 9-15 equals the net flow into the body given by Equation 9-12. Hence, combining Equations 9-12 and 9-15 gives:

$$p\,\Delta x\, \Delta y\, \Delta z\, \Delta t\, \frac{\partial^2 u}{\partial x^2} + f\,(x,t)\Delta x\, \Delta y\, \Delta z\, \Delta t = \Delta x\, \Delta y\, \Delta z\, (\Delta uc\, \frac{\gamma_d}{\gamma_w}) \tag{9-16}$$

$$p\, \frac{\partial^2 u}{\partial x^2} + f\,(x,t) \underset{\substack{\Delta x \to 0 \\ \Delta y \to 0 \\ \Delta z \to 0}}{=\!=} \frac{\gamma_d c}{\gamma_w} \frac{\partial u}{\partial t} \tag{9-17}$$

Equation 9-17 can be rewritten as:

$$\frac{\partial^2 u}{\partial x^2}+\frac{f(x,t)}{p}=\frac{\gamma_d c}{\gamma_w p}\frac{\partial u}{\partial t} \tag{9-18}$$

or

$$\frac{\partial^2 u}{\partial x^2}+\frac{f(x,t)}{p}=\frac{1}{\alpha}\frac{\partial u}{\partial t} \tag{9-19}$$

Equation 9-19 is the diffusion equation, where $\alpha=\frac{\gamma_w p}{\gamma_d c}$ is the diffusion coefficient.

Diffusion coefficient is assumed to be constant over small changes in suction. The one-dimensional diffusion equation can easily be extended into a three-dimensional flow as follows (Mitchell, 1979):

$$\frac{\partial^2 u}{\partial x^2}+\frac{\partial^2 u}{\partial y^2}+\frac{\partial^2 u}{\partial z^2}+\frac{f(x,y,z,t)}{p}=\frac{1}{\alpha}\frac{\partial u}{\partial t} \tag{9-20}$$

DRYING TEST PROCEDURE FOR DETERMINATION OF *α*

The diffusion coefficient can be measured using the drying (evaporation) test in which the change of the total suction of an asphalt mixture specimen is monitored as moisture leaves the specimen as a function of time. In this test, an impermeable membrane encloses a cylindrical asphalt mixture specimen from all sides except the top. The moisture flows out of the sample through the top surface, which is exposed to a known atmospheric suction. Figure 9-5 presents a schematic view of the test setup.

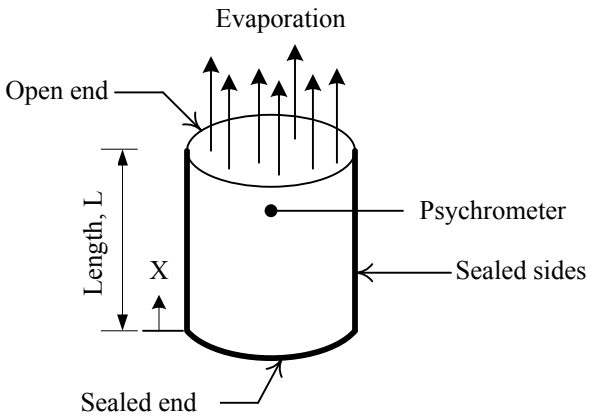

Figure 9-5. Schematic View of the Drying Test Sample.

Mitchell (1979) developed a solution for Equation 9-20 using the boundary conditions of the experiment. Substituting $f\,(x\,,y\,,z\,,t\,)$ as zero simplifies Equation 9-20 to Equation 9-21:

$$\alpha \frac{\partial^2 u}{\partial x^{\,2}} = \frac{\partial u}{\partial t} \tag{9-21}$$

The boundary conditions for this problem are as follows.

Sealed boundary:

$$\frac{\partial u\,(0,t\,)}{\partial x} = 0 \tag{9-22}$$

Open boundary:

$$\frac{\partial u(L,t)}{\partial X} = -\,h_e\left[u(L,t) - u_a\right] \tag{9-23}$$

Initial suction:

$$u(X,0) = u_0 \tag{9-24}$$

Using the Laplace Transform method, Equation 9-25 provides the solution to Equation 9-21:

$$u = u_a + \sum_{n=1}^{\infty} \frac{2(u_0 - u_a)\sin z_n}{z_n + \sin z_n \cos z_n} \exp\left(-\frac{z_n^2 \alpha t}{L^2}\right) \cos(z_n \frac{X}{L}) \quad (9\text{-}25)$$

where: u = suction (pF) as a function of the position and the time, u_a = atmospheric suction in (pF), u_0 = initial suction (pF), t = time, x = distance from closed end, L = the total length of the sample, h_e = evaporation coefficient cm^{-1}, z_n is the solution of $cot\ z = z_n / h_e L$. Matching the measured suction values at various times with Equation 9-25 determines the diffusion coefficient.

MATERIALS AND TEST PROCEDURE

This study used ten asphalt mix specimens (4 inch diameter and 4 inch height). Six samples were prepared using Florida limestone aggregate (WR) and four samples were prepared using Georgia granite (GA) aggregate. These specimens were tested previously to investigate the effect of material properties and air void structure on moisture damage (Birgisson et al., 2003. Birgisson et al., 2004) and investigate the relationship between water content and total suction (Kassem et al., 2006). Tables 9-1 and 9-2 present the properties of the tested samples and the gradation, respectively. In Tables 9-1 and 9-2, the letter C stands for coarse-graded mixture, and the letter F stands for fine-graded mixture (Birgisson et al., 2003). All test samples were compacted at 7 percent air voids. A summary of the procedure for the test set up and suction measurements follows:

1. Drilled hole in a specimen using a bit with a diameter of 0.95 cm (3/8 in) diameter—depth of the hole half of the diameter of a specimen (5 cm); distance between the top of a specimen and top of the hole approximately 1 cm (Figure 9-5).
2. Saturated specimen with water using vacuum saturation; kept specimen in a room at a temperature of 25^{o}C for one hour.
3. Cleaned hole from standing free water; inserted head of thermocouple psychrometer all the way into the hole.
4. Sealed hole with plastic tape to prevent loss of moisture.

5. Enclosed test specimen in clear wrap, aluminum foil, and heavy plastic tape from all sides except the top to allow evaporation (Figure 9-5).
6. Placed specimens under isothermal conditions at 25°C (Figure 9-6); used water bath to provide the test specimens with an isothermal condition throughout the test; used temperature control unit to maintain water temperature at 25°C; test specimens kept in empty plastic tubes (Figure 9-6).
7. Connected psychrometers to CR-7 datalogger which has the capability of recording the microvolts for 40 psychrometers at the same time every ten minutes; connected CR-7 datalogger to a computer to retrieve the measurements (Figure 9-6).

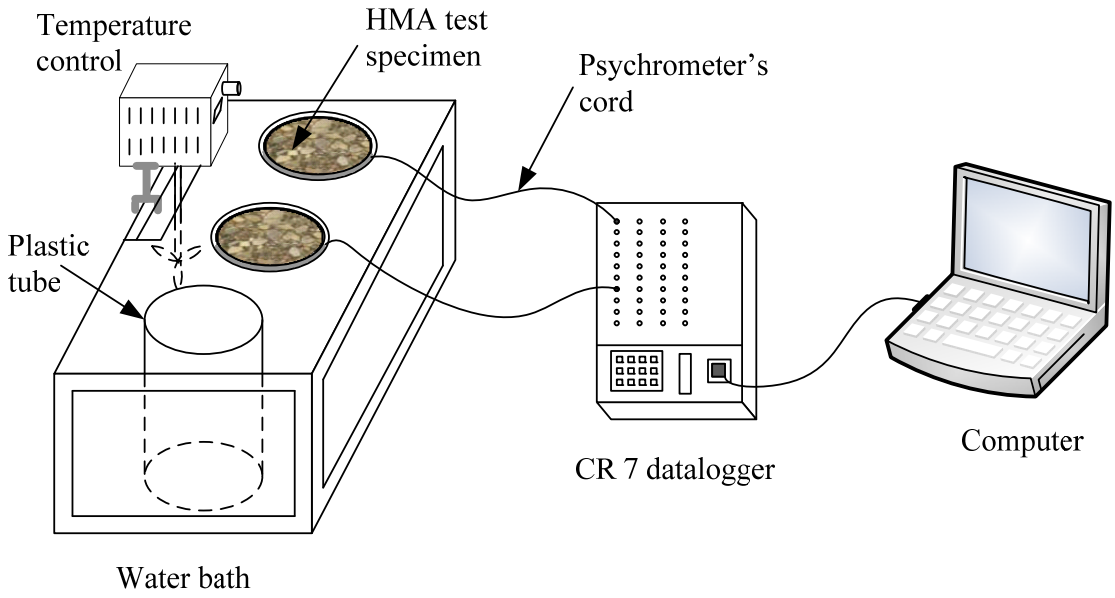

Figure 9-6. Schematic View of Test Setup.

Table 9-1. Volumetrics for Limestone and Granite Mixtures (Kassem et al., 2006).

Volumetric Property	Limestone						Granite			
	WR-C1	WR-C2	WR-C3	WR-F1	WR-F2	WR-F3/C4	GA-C2	GA-C3	GA-F1	GA-F2
Max. Specific Gravity (G_{mm})	2.328	2.347	2.349	2.338	2.375	2.347	2.500	2.492	2.473	2.532
Binder Specific Gravity (G_b)	1.035	1.035	1.035	1.035	1.035	1.035	1.035	1.035	1.035	1.035
Bulk Specific Gravity (G_{mb})	2.235	2.255	2.254	2.244	2.281	2.254	2.399	2.391	2.473	2.433
Percent Binder (P_b)	6.5	5.8	5.3	6.3	5.4	5.6	5.26	5.25	5.68	4.56
Aggregate Specific Gravity (G_{sb})	2.469	2.465	2.474	2.488	2.489	2.468	2.687	2.686	2.686	2.687
Aggregate Effective Specific Gravity (G_{se})	2.549	2.545	2.528	2.554	2.565	2.537	2.719	2.709	2.706	2.725
Absorbed Percent Binder P_{ba}	1.1	1.3	0.9	1.1	1.2	1.1	0.43	0.31	0.28	0.53
Effective Percent Binder P_{be}	5.3	4.6	4.5	5.3	4.2	4.5	4.85	4.96	5.42	4.06
Voids in Mineral Aggregates VMA (%)	15.4	13.8	13.6	15.6	13.2	14.0	15.4	15.7	16.6	13.6
Design Percent Air Voids Va (%)	4.0	3.9	4.0	4.0	3.9	3.9	4.0	4.1	4.0	3.9
Voids Filled with Asphalt VFA (%)	74.0	71.6	70.2	74.2	70.1	71.8	73.8	74.2	75.9	71.2
Dust to Asphalt Ratio D/A	1.0	0.8	1.2	0.8	1.4	1.0	0.8	0.9	0.6	1.2

Table 9-2. Granite and Limestone Mixture Gradations.

Sieve Size (mm)	Granite: Percent Passing			
	GA-C2	GA-C3	GA-F1	GA-F2
19	100	100	100	100
12.5	90.9	97.3	94.7	90.5
9.5	72.9	89.5	84	77.4
4.75	45.9	55.4	66.4	60.3
2.36	28.1	33.9	49.2	43.2
1.18	18.9	23	32.7	34
0.6	13.2	16	21	23
0.3	9.2	11.2	12.9	15.3
0.15	5.6	6.8	5.9	8.7
0.75	3.9	4.7	3.3	5.4

Sieve Size (mm)	Limestone: Percent Passing					
	WR-C1	WR-C2	WR-C3	WR-F1	WR-F2	WR-F3/C4
19	100	100	100	100	100	100
12.5	97	91	98	96	91	95
9.5	90	74	89	85	78	85
4.75	60	47	57	69	61	67
2.36	33	30	36	53	44	37
1.18	20	20	24	34	35	26
0.6	15	14	18	23	24	20
0.3	11	10	13	15	16	14
0.15	7.6	6.7	9.2	9.6	9.1	8.6
0.75	4.8	4.8	6.3	4.8	6.3	5.8

X-RAY COMPUTED TOMOGRAPHY

The experiment used X-ray Computed Tomography, which is a nondestructive technique, to capture the percentage of air voids distribution in test specimens under dry conditions (Masad, 2004). The test asphalt specimen is placed between an X-ray source and a detector. X-rays pass through the test specimen, and the intensity of X-rays is measured before entering the specimen and after it penetrates the specimen. The loss of X-ray intensities determines the linear attenuation coefficients of the materials in the test samples. The density distribution within the test sample is determined as a function of the attenuation coefficients.

The X-ray CT images were captured in one millimeter increments in the vertical direction. The captured image consists of 256 levels of gray intensity that correspond to different densities within the specimen, as shown in Figure 9-7. The black areas represent air voids (low density). Using a suitable gray intensity threshold value, air voids can be separated from other mix constituents (aggregate and mastic). The threshold level represents a boundary value below which pixels belong to the air void and above which the pixels belong to remaining constituents. Equations 9-26, 9-27, and 9-28 compute the average percent air voids for a specimen ($\%AV$), average percent air voids in an image ($\%AV_{image}$), and average air void radius in an image (r), respectively.

$$\%AV = \frac{1}{N}\sum_{1}^{N} \%AV_{image} \tag{9-26}$$

$$\%AV_{image} = \frac{A_{TV}}{A_T} \tag{9-27}$$

$$r = \sqrt{\frac{A_{TV}}{\pi n}} \tag{9-28}$$

where A_{TV} is the total area of the air voids in a CT image, A_T is the total cross-sectional area of a CT image, N *is* the number of CT images, and n is the number of the air voids in a CT image.

The analysis was carried out with macros that were developed in Image-Pro® Plus software (1999). Figure 9-8 presents an example of typical air void distribution along the depth of a test specimen. Some of the test specimens were trimmed from the top to produce different percents of air voids above the psychrometer's level.

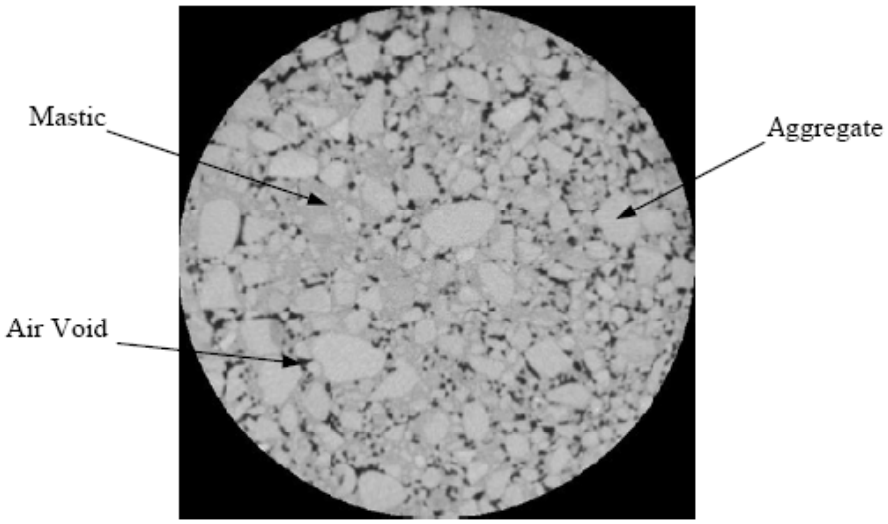

Figure 9-7. X-Ray CT Image.

DIFFUSION COEFFICIENTS RESULTS

The CR-7 datalogger recorded the microvolts measured by the psychrometers. Figure 9-9 shows an example of the change of the recorded microvolts over time for a test specimen. This pattern was similar for all test specimens. Because of water evaporation from the open end to the surrounding environment, the suction increased and hence the recorded microvolts increased as well. The three stages shown in Figure 9-9 correspond to those discussed earlier in Figure 9-2. In Stage I and Stage III the suction values were out of the psychrometer's range, and only microvolt values recorded in Stage II were considered in determining the diffusion coefficient. Calibration curves similar to the one shown in Figure 9-3 were used to convert microvolt values in Stage II

to suction values as shown in Figure 9-10. All psychrometers operated successfully within the range of 3.75 *pF* to 4.5 *pF*.

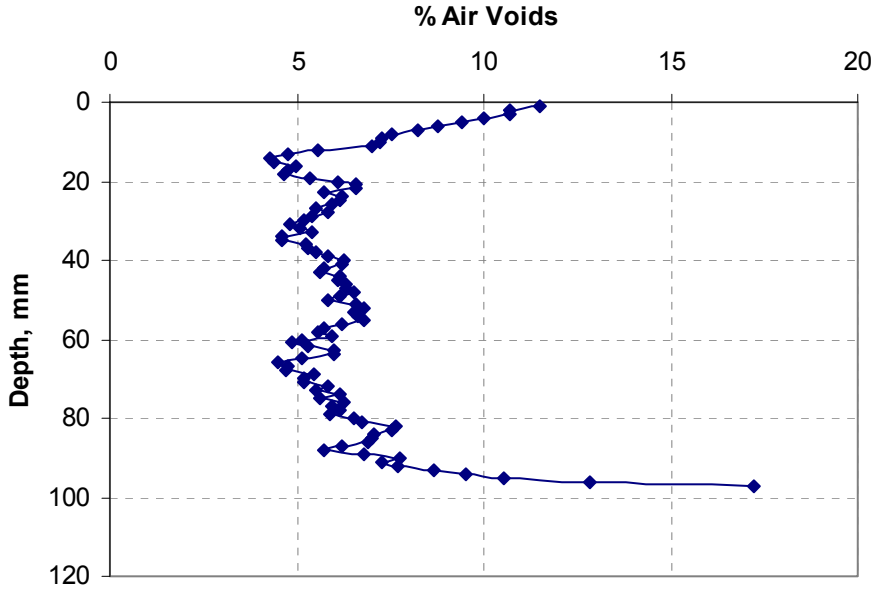

(a)

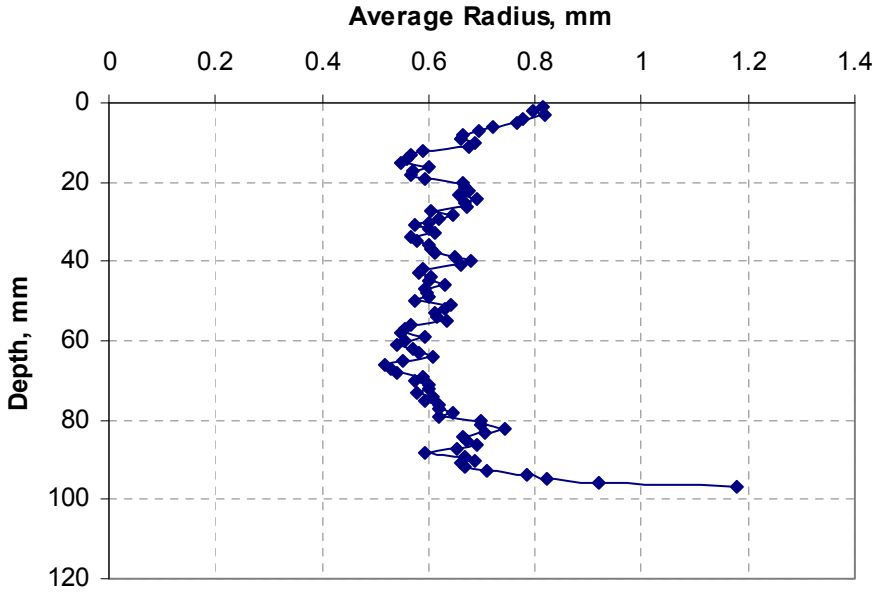

(b)

Figure 9-8. (a) Distribution of Percent Air Voids Distribution along Depth, (b) Distribution of Average Air Void Radius along Depth.

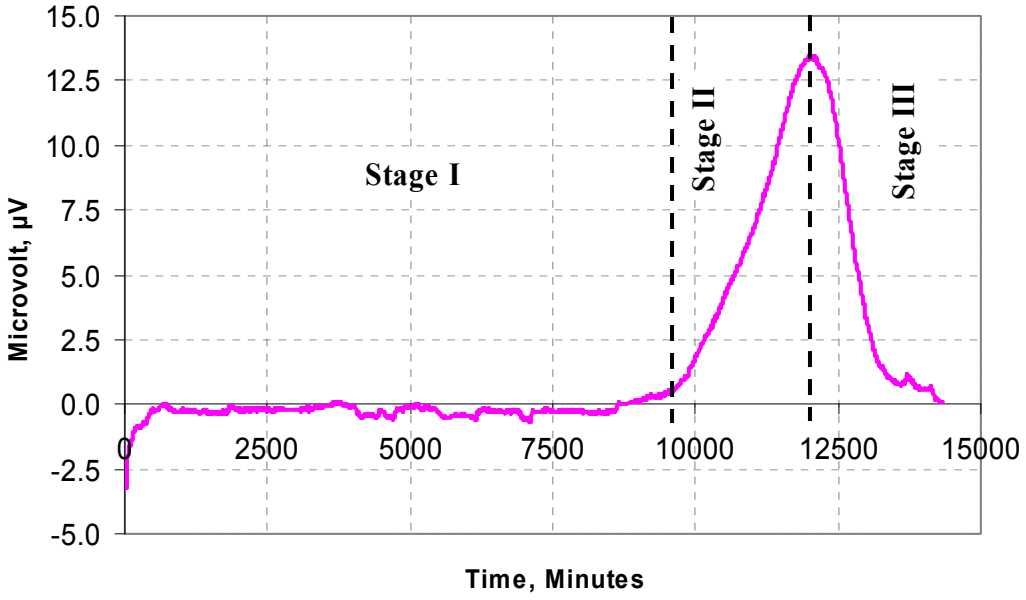

Figure 9-9. Change of Recorded Microvolts over Time.

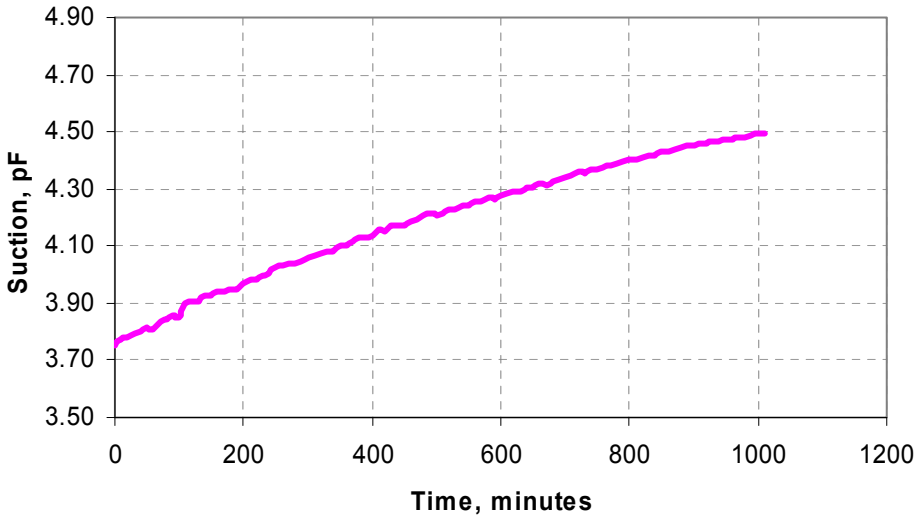

Figure 9-10. Change of Suction over Time (Stage II).

The atmospheric suction is required for the solution of Equation 9-25. The atmospheric suction of the air in the laboratory was determined by measuring the relative humidity in the air with a sling psychrometer. A Sling psychrometer consists of two thermometers (wet-bulb thermometer and dry-bulb thermometer). The wet-bulb

thermometer measures the saturation temperature, (T_{wb}) while a dry-bulb thermometer measures the air temperature (T_{db}). The wet bulb has a cloth wick over its bulb. Before taking readings the cloth wick was dipped in water and the instrument was rotated or whirled. The water evaporates from the cloth wick and cools the wet bulb. The degree of cooling depends on the evaporation rate, which depends on the relative humidity in the surroundings. The measured T_{wb} and T_{db} are employed to determine the relative humidity using psychrometric charts (Sood, 2005). The measured relative humidity was around 66 percent, which corresponds to an atmospheric suction of 5.76 pF at 25^{o}C using Equation 9-1. The diffusion coefficients of test specimens were determined as follows:

- Assumed an initial value of diffusion coefficient and refined by iteration; used this value to calculate the theoretical suction value in Equation 9-25.
- Determined the square difference or error (E^2) between the theoretical suction using Equation 9-25, and the suction measured using the psychrometer over time as follows:

$$E^2 = \sum (u_{Theortetical} - u_{measured})^2 \tag{9-29}$$

- Determined the diffusion coefficient which minimized the square error.

The calculated diffusion coefficient was used to generate the theoretical change of suction over time using Equation 9-25. Figure 9-11 presents an example of change of theoretical suction and measured suction over time. It can be seen that there is very good correlation between the laboratory suction measurements and the theoretical curve.

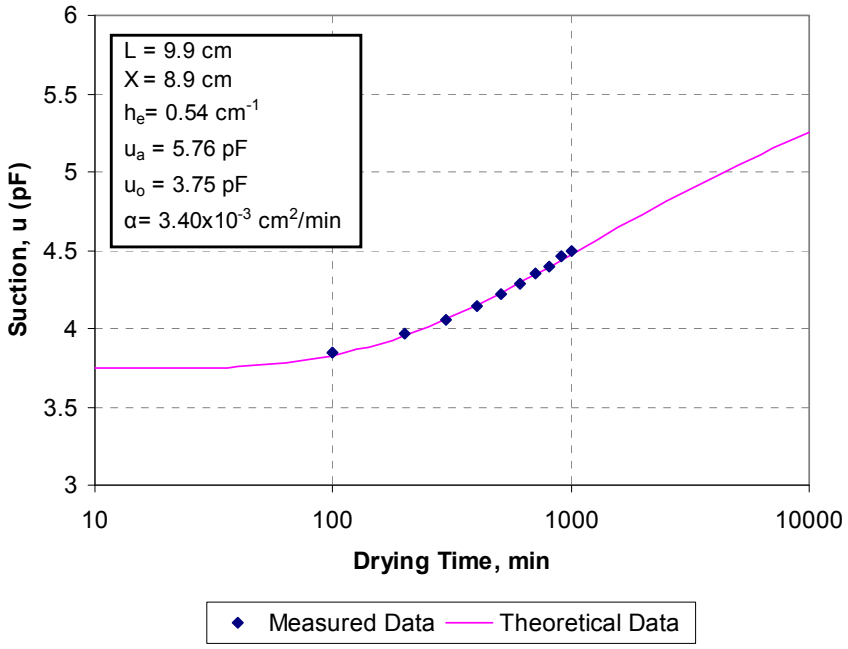

(a)

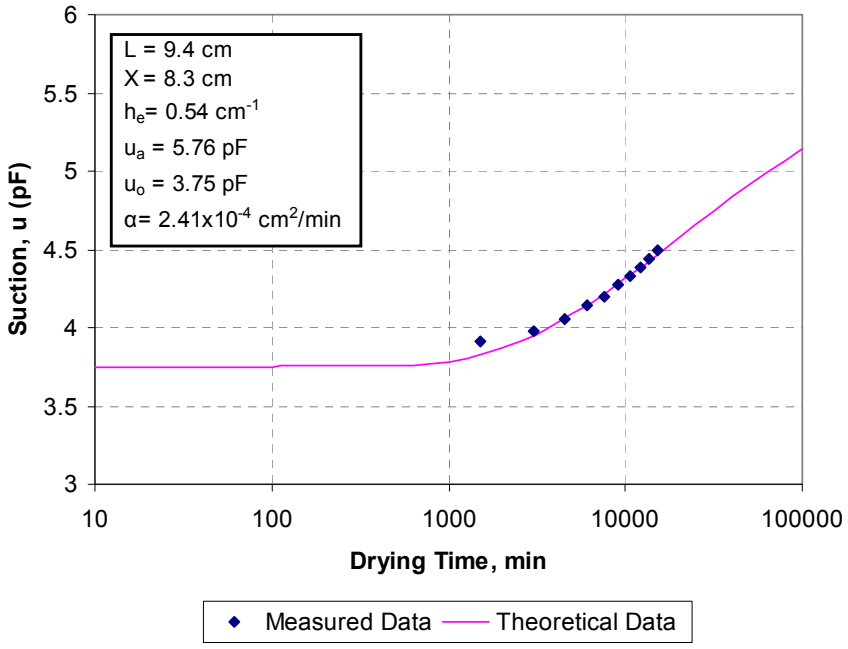

(b)

Figure 9-11. Change in Measured and Theoretical Suction over Time with (a) Higher Percent Air Void above Psychrometers, (b) Less Percent Air Void above Psychrometers.

Table 9-3 presents the diffusion coefficient values measured in the laboratory in this research study. Table 9-3 also gives the percent of total air voids, average radius of percent air voids, percent of connected air voids, and average radius of percent connected air voids within the asphalt mixture from the location of the psychrometer to the open-end of the specimen where the moisture evaporation takes place. These air void characteristics were determined by analyzing the X-ray CT images that belong to the region above the psychrometer. A wide range of diffusion coefficients (from $5.67\times10\text{-}^{5}$ cm^2/sec to 2.92×10^{-6} cm^2/sec) were obtained for the given asphalt concrete samples.

Table 9-3. Summary of Test Results.

Sample	Length of specimens	Distance from closed end	α	Total Air Voids		Connected Air Voids	
ID	L, cm	X, cm	cm^2/sec	% Air Voids	R, mm	% Air Voids	R, mm
WR-C1	9.90	8.90	5.12E-05	11.86	0.962	9.75	1.120
WR-C2	9.90	8.90	5.67E-05	12.88	1.018	10.53	1.274
WR-C3	9.90	9.00	3.47E-05	10.13	0.739	7.72	0.894
WR-C1(2)	9.10	8.00	4.02E-06	6.03	0.623	2.17	0.576
WR-C3(2)	9.00	7.80	3.47E-06	7.30	0.606	3.85	0.634
WR-F1	6.50	5.60	4.57E-06	6.37	0.528	4.28	0.604
WR-F2	6.40	5.40	9.52E-06	4.69	0.568	2.98	0.720
WR-F3	9.40	8.20	6.22E-06	7.57	0.623	3.48	0.662
WR-F3(2)	10.00	8.60	6.77E-06	7.90	0.590	4.00	0.644
GA-C2	8.90	7.95	5.12E-06	4.91	0.607	2.54	0.563
GA-C3	8.40	7.30	2.92E-06	4.81	0.559	1.73	0.486
GA-F1	9.30	8.40	2.92E-06	6.23	0.529	1.74	0.730
GA-F2	8.80	7.60	3.47E-06	5.72	0.522	3.28	0.584

The measured diffusion coefficients varied among the different specimens although all specimens were prepared with approximately 7 percent air voids. In the region of the asphalt mixture specimen above the psychrometer, however, the diffusion coefficient values were related to the percent air voids. This can be attributed to the fact that moisture loss and change in suction occur more rapidly toward the open side of the specimen (top side), where the psychrometer was placed. Initially, three psychrometers were employed in the test specimen— one at the top (one centimeter below the top surface), one in the middle of the test samples, and one near to the sealed end. The psychrometers placed in the middle and close to the bottom of a specimen experienced no change in suction measurements. This can be attributed to the fact that the diffusion coefficient of HMA is small, and it might need more time for the middle and end psychrometers to detect the change in suction. Therefore, it was concluded that the measurements conducted by the psychrometer represent the suction level and moisture diffusion in the region above the psychrometer's level.

Figure 9-12 shows the relationship between the measured diffusion coefficients and total percent air voids and connected percent air voids above the psychrometers. Figure 9-13 presents the relationship between the average air void size for total and connected air voids and the measured diffusion coefficients. It is interesting to note that the average air void size of connected air voids is higher than the average size of total air voids, which indicates that the connected air voids are larger than the unconnected air voids. The diffusion coefficient strongly correlates to the average percent of air voids and the average radius of the air voids above the psychrometers. However, better correlation exists between the diffusion coefficients and connected air voids. The results show that moisture diffusion is controlled by air void percent and size. This is caused by the fact that moisture diffusion in air voids is much higher than in the other phases (aggregates and mastic) as shown in the diffusion values in Table 9-4.

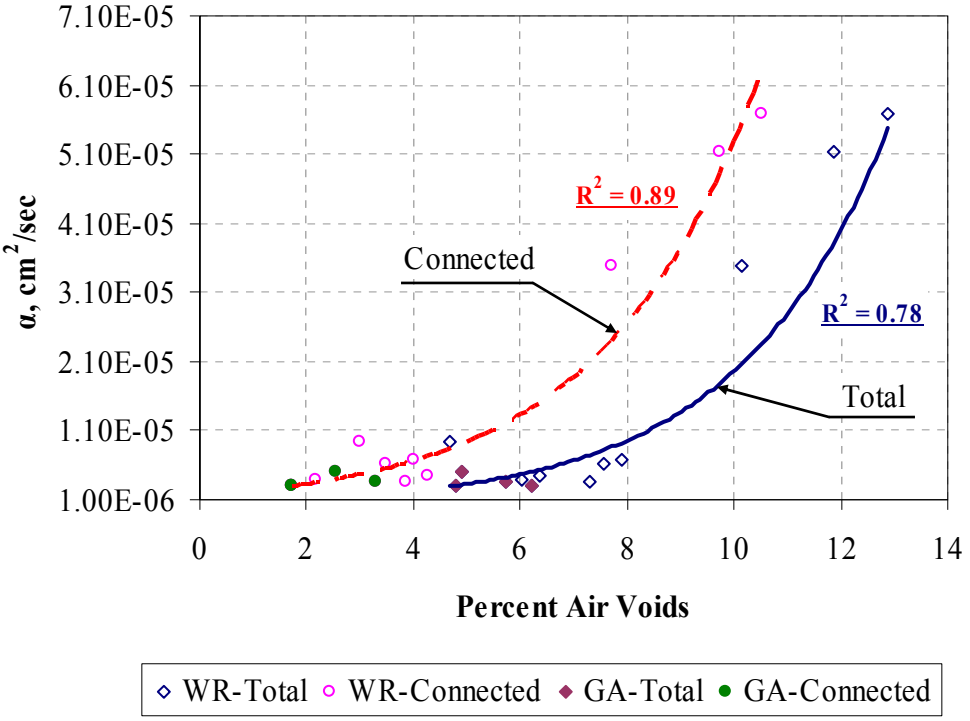

Figure 9-12. Relationship between Diffusion Coefficients and Percent of Air Voids above Psychrometers.

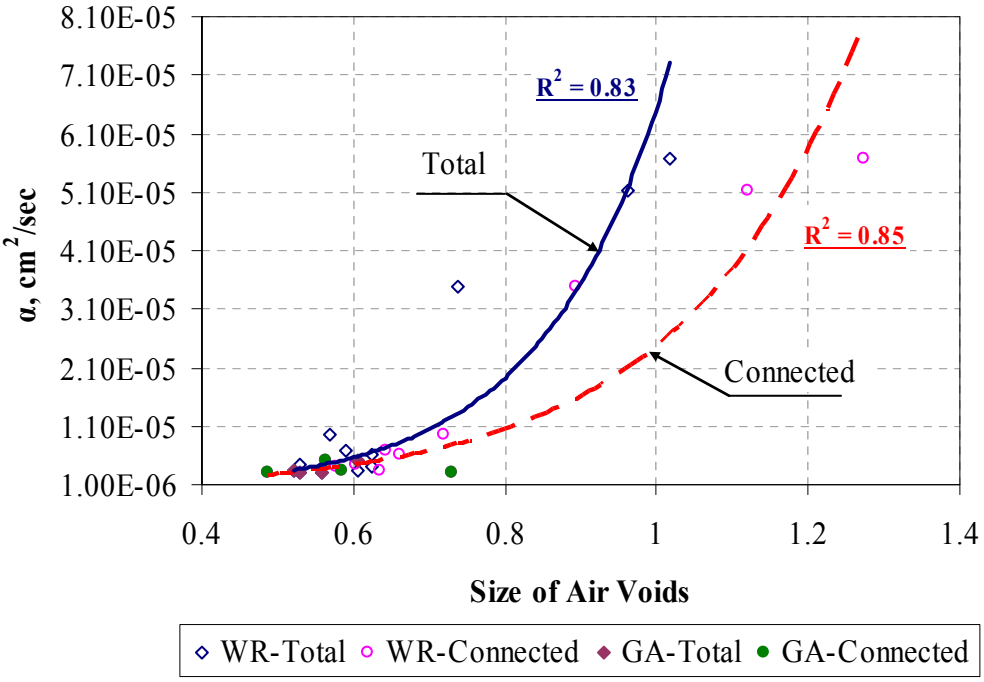

Figure 9-13. Relationship between Diffusion Coefficients and Air Void Size above Psychrometers.

Table 9-4. Diffusion Coefficients of Different Phases within HMA.

Phase	Range of Diffusion Coefficient cm^2/sec	Reference
Air Void	0.264	Montgomery (1947)
	0.260	Geankoplis (1993)
Mastic	$6.43x10^{-8}$ to $3.5x10^{-7}$	Kassem et al. (2006)
Aggregates	Limestone: $3.33x10^{-7}$ to $2.42x10^{-6}$ Granite: $8.06x10^{-7}$ to $1.94x10^{-6}$	Kringos et al. (2007)

CONCLUSIONS

Moisture diffusion is one mechanism by which the water can get into an asphalt mixture causing moisture damage. In a previous study (Kassem et al. 2006), the diffusion coefficient of asphalt mastic was measured. In this study, an experimental procedure was developed to measure the diffusion coefficient of full asphalt mixtures. To the best knowledge of the authors, the diffusion coefficient for asphalt mixtures was not measured in the past.

The experimental procedure relies on measuring the change in suction during moisture evaporation in asphalt mixtures. The range of the diffusion coefficients of asphalt mixtures was determined to be in between $5.67\times10^{-5}$and 2.92×10^{-6} cm^2/sec.

The air void phase within asphalt mixtures was found to control the rate of moisture diffusion in asphalt mixtures. The correlation of the diffusion coefficient value with connected air voids was better than the correlation with total percent air voids. The measured diffusion coefficient is a necessary input for modeling moisture transport and predicting moisture damage in asphalt mixtures.

CHAPTER X
FRACTURE-BASED ANALYSIS OF INFLUENCE OF AIR VOIDS ON MOISTURE DAMAGE

INTRODUCTION AND OBJECTIVES

As discussed earlier in this dissertation, percent and size of air voids is an important factor that influences asphalt pavement performance. In this chapter, experimental methods and a fracture mechanics approach that accounts for fundamental material properties are used to evaluate the resistance of asphalt mixtures with different percent air voids to moisture damage. Asphalt mixture specimens with different percent air voids were prepared. Test specimens were subjected to dynamic loading under two different conditions: dry (unconditioned) and wet (moisture-conditioned). The moisture conditioning was conducted such that specimens with different percent air voids had the same amount of moisture by varying the moisture conditioning time.

The crack growth index developed originally by Lytton (1993) and later modified and implemented by Masad et al (2006b) and Arambula (2007) was employed in order to assess resistance to moisture damage. The inputs of the fracture model include the viscoelastic properties, pseudo strain dissipated energy, tensile strength, and the adhesive bond surface energy of asphalt mixture.

ASPHALT MIXTURES TEST SPECIMENS

This mixture was used in the construction of the overlay of the State Highway 87 in Yoakum district. The mixture was Type C (TxDOT 1993 Specifications) and designed with Fordyce Gravel and Colorado Materials limestone screening with a PG 76-22 binder. The aggregate gradation is given in Table 10-1 and shown in Figure 10-1.

The Superpave gyratory compactor was used to compact laboratory cylindrical asphalt mixture specimens. The specimens were prepared according to AASHTO standards (2002b). The mixing and compaction temperatures were determined according to TxDOT 2005 specifications based on the binder grade. The mixing and compaction temperature for the PG 76-22s binder are 325^{o}F and 300^{o}F, respectively. The laboratory SGC specimens were 7 inches in height and 6 inches in diameter. The test specimens

were cored from the SGC specimens and trimmed from the top and the bottom to the size of 6 inches in height and 4 inches in diameter. A total of thirty asphalt mixture specimens were compacted such that the final percent air voids after cutting and trimming were 4±0.5, 7±0.5, or 10±0.5 percent.

Table 10-1. Aggregate Gradation of SH 87 Type C Asphalt Mixtures.

	Type C		Type D/F		Man Sand		Field Sand		Limestone		Lime		Combined
Individual %	18		46		10		15		10		1		100
Sieve Size: (mm)	Pass %	Total %	Pass %	Total %	Pass %	Total %	Pass %	Total %	Pass %	Total %	Pass %	Total %	Total %
22.4	100	18	100	46	100	10	100	15	100	10	100	1	100
16	99.5	17.9	100	46	100	10	100	15	100	10	100	1	99.9
9.5	8.3	1.5	97.1	44.7	100	10	100	15	100	10	100	1	82.2
4.75	0.1	0	49.1	22.6	99.8	10	100	15	99.7	10	100	1	58.6
2	0	0	11.2	5.2	97.2	9.7	98.9	14.8	88.1	8.8	100	1	39.5
0.425	0	0	2	0.9	35.7	3.6	46.2	6.9	44.2	4.4	100	1	16.8
0.18	0	0	1	0.5	11	1.1	5.3	0.8	32.1	3.2	100	1	6.6
0.075	0	0	0.5	0.2	2.2	0.2	0.5	0.1	24.6	2.5	99	1	4

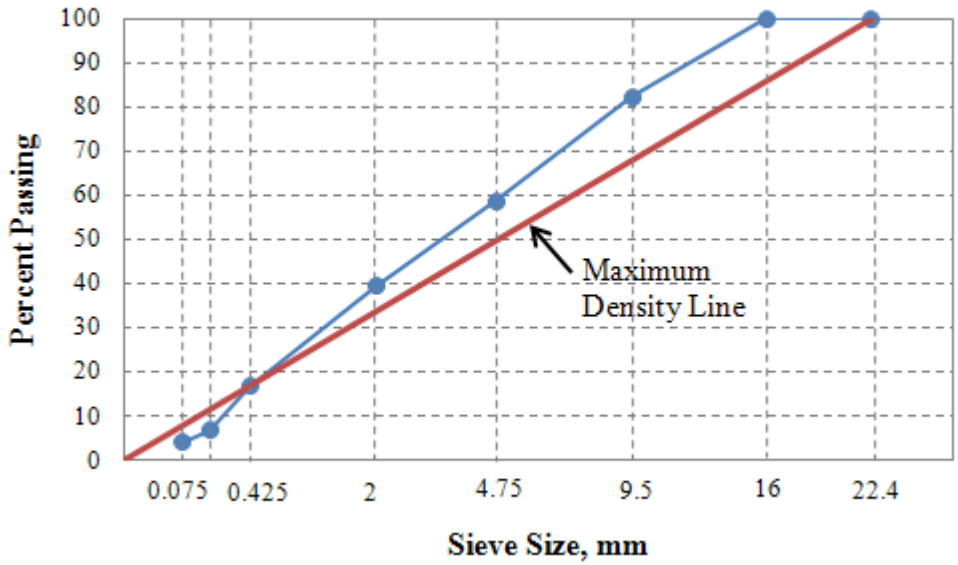

Figure 10-1. 0.45 Power Aggregate Gradation Chart.

MOISTURE CONDITIONING

Half of the test specimens (five specimens at each percent air voids) were subjected to moisture conditioning. The modified Lottman procedure, without the freezing stage, was followed for moisture conditioning (AASHTO 2002c). Vacuum saturation was used in order to achieve a target saturation level in between 70 to 80 percent. However, in order to determine the time at which specimens with different percent air voids achieve this target saturation level, additional specimens were prepared and conditioned for different times. A partial vacuum between 650 mm to 700 mm Hg was used in moisture conditioning. The time required to achieve the target saturation level for specimens with different percent is presented in Table 10-2. The vacuum saturation time durations in Table 10-2 were used in conditioning the test specimens. Consequently, the test specimens were placed in a 60^{o}C water bath for 24 hours. Then, the test specimens were taken to another 20^{o}C water bath to cool down before testing.

Table 10-2. Vacuum Saturation Time

Percent Air Voids	Time, Sec
4	90
7	45
10	25

EXPERIMENTAL TESTS

The following section will cover the experimental tests by which the model's inputs were determined.

Relaxation Test

This test was used to determine the viscoelastic properties which include the initial relaxation modulus (E_o) and the modulus relaxation rate (m). A constant axial tension strain of 80 microstrain was applied to the test specimens for 60 sec followed by 600 sec rest period. Then, a constant compressive strain of 80 microstrain was applied for

60 sec. The time interval used to increase the load from 0 to a constant value of 80 microstrain was 6 sec. The applied load is shown in Figure 10-2. The test was performed at a temperature of 20°C. The test specimens kept at this temperature for 2 hours before testing. The loading was applied by using an MTS machine where the data (time, load, and deformation) were recorded. The deformation was measured by Linear Variable Differential Transformers (LVDTs). Six LVDTs were used to measure the deformation; three LVDTs were used to measure the axial deformation and the other three were used to measure the radial deformation. The LVDTs were placed at 120° along the circumference of the test sample, and three radial LVDTs were placed at the middle of the test specimens. The LVDTs configuration is shown in Figures 10-3 and 10-4. The gauge length between the axial LVDT holders was 4 inch.

The time-dependent relaxation modulus is calculated according to Equation 10-1 (Arambula 2007).

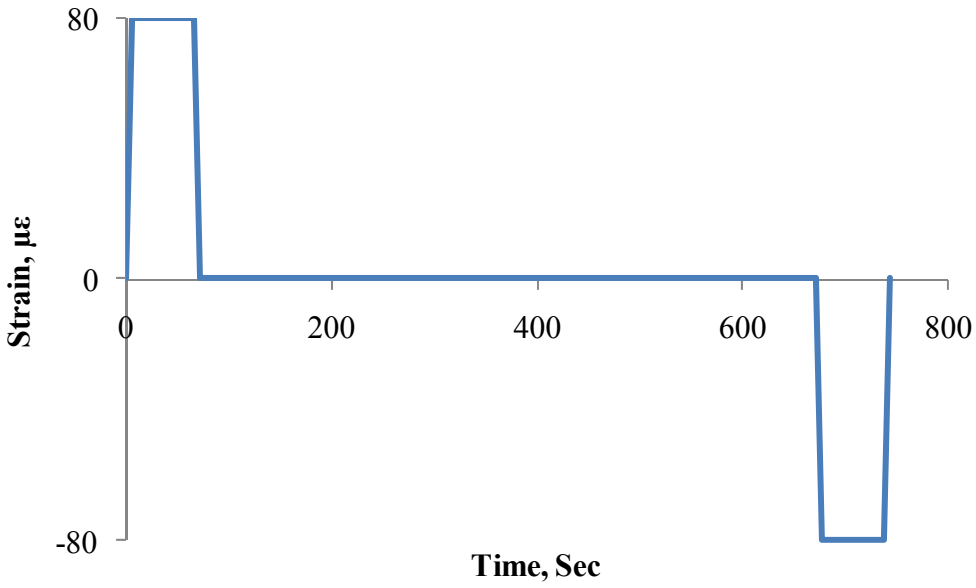

Figure 10-2. Applied Load during the Relaxation Test.

$$E(t) = \frac{P(t)}{\pi r^2 \varepsilon} \tag{10-1}$$

where: $E(t)$ = time-dependent relaxation modulus, $P(t)$ = measured load, r = specimen radius, ε = applied strain.

A power law equation was fitted to the test data to determine the viscoelastic parameter as described in Equation 10-2.

$$E(t) = E_o t^{-m} \tag{10-2}$$

where E_o = the initial relaxation modulus and m = the modulus relaxation rate.

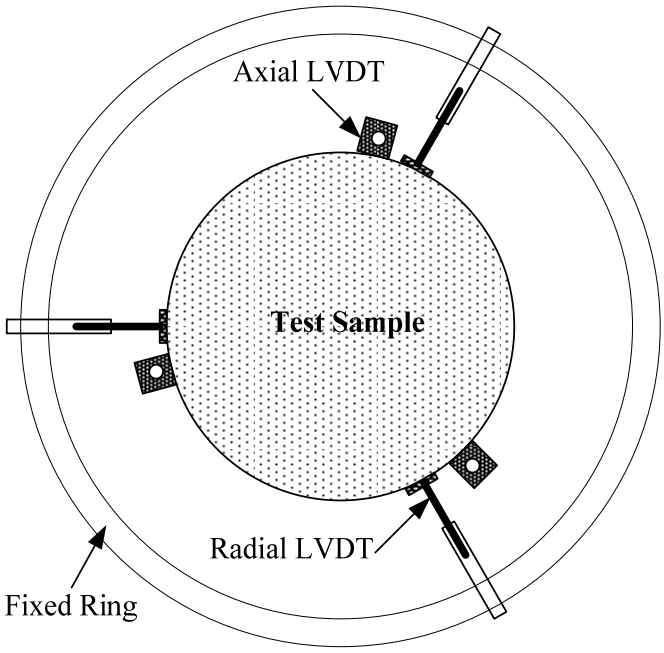

Figure 10-3. Schematic View of LVDTs Configurations.

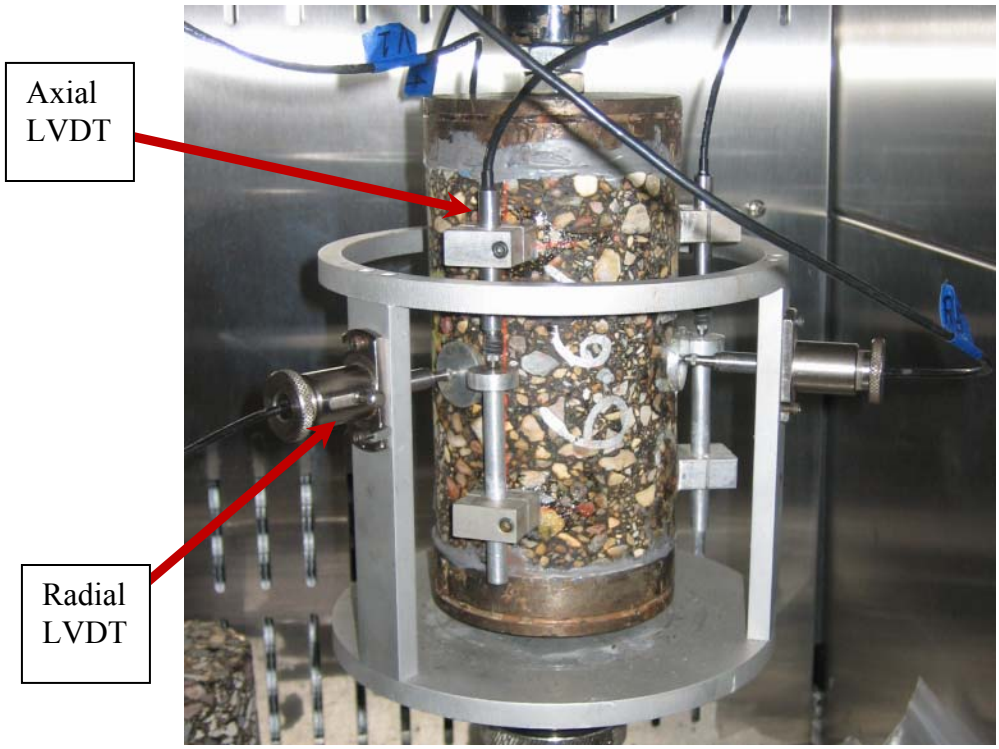

Figure 10-4. LVDTs Configuration.

Dynamic Direct Tension Test

The dynamic direct tension test applied a haversine strain shape with a maximum of 140 microstrain for 0.1 sec followed by a rest period of 0.9 sec as shown in Figure 10-5. A total number of 1000 loading cycles were applied on each specimen. The haversine strain waveform simulates the shape of field pulse developed under moving wheel loads of the commercial vehicles on the highways (Si, 2001).

Several criteria were established to select the strain level for the dynamic direct tension test. The strain level should be high enough to induce cumulative fatigue damage in all specimens with different percent air voids without failing the test specimens. As discussed later, damage is quantified by the area of the stress-pseudo strain hysteresis loop. From previous experience, it is known that test variability and problems in measuring devices increases significantly when specimens start to show disintegration and are close to the failure point. Different strain levels were evaluated and 140 microstrain was found to meet the test criteria. The data were recorded every 50 cycles.

The recorded data points within a single loading cycle should be sufficient to study the dissipated pseudostrain energy. In this test, for every single recorded loading cycle, the data were captured every 0.005 sec. The LVDTs configurations were the exact same used in relaxation modulus test. The test was conducted at a constant temperature of 20°C. Test specimens were conditioned at this temperature for about two hours before conducting the test.

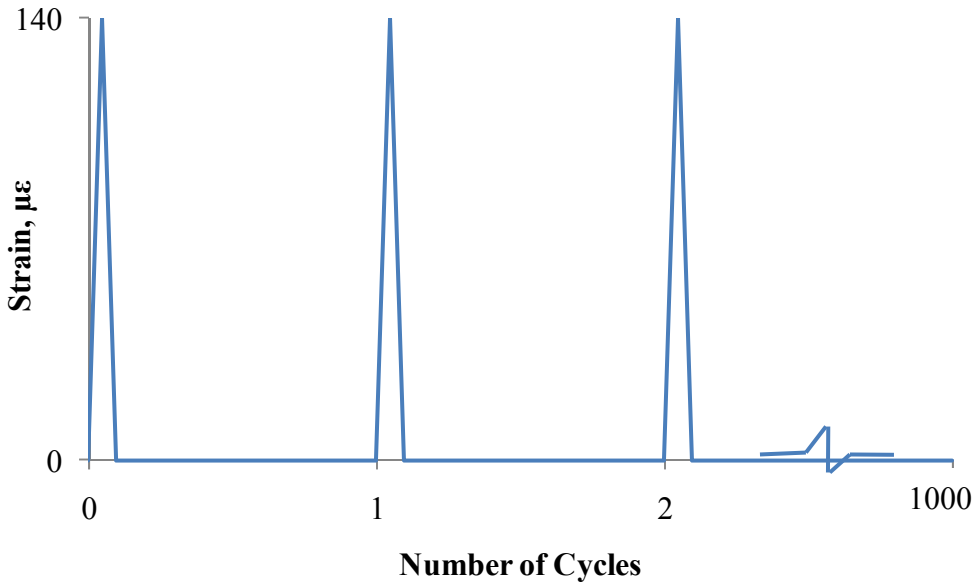

Figure 10-5 Applied Loading Configurations for Dynamic Direct Tension Test.

The viscoelastic stress (σ_V) was computed using the Boltzman superposition for every loading cycle as follows (Arambula 2007):

$$\sigma_V(\tau_k) = \sum_{i=1}^{k} E_o(\tau_k - t_i)^{-m} C_i dt \qquad (10\text{-}3)$$

where: E_o = initial relaxation modulus determined using the relaxation test, τ_{i+1} and t_i = the present and previous time, m = the modulus relaxation rate determined using the relaxation test, $C_i = (d\varepsilon/dt)$ the change in strain for every load increment, dt = time increment, k = number of data points

The measured time-dependent tensile stress was calculated in Equation 10-4.

$$\sigma_m(t) = \frac{P(t)}{\pi r^2} \tag{10-4}$$

where: $P(t)$ = the measured load, r = the radius of the sample

The reference modulus (E_R) was estimated according to Equation 10-5.

$$E_R = \frac{\sigma_m(t)\max}{\varepsilon(t)\max} \tag{10-5}$$

where: $\sigma_m(t)max$ = the maximum measured time-dependent tensile stress at the first load cycle, $\varepsilon(t)max$ = the maximum measured time-dependent tensile strain at the corresponding cycle.

The pseudostrain (ε_R) is the ratio between the viscoelastic stress (σ_V) and the reference modulus (E_R) as given in Equation 10-6.

$$\varepsilon_R(t) = \frac{\sigma_V(t)}{E_R} \tag{10-6}$$

The dissipated pseudostrain energy (DPSE) is the area of hysteresis loop of the measured tensile stress $\sigma_m(t)$ against the calculated pseudostrain (ε_R) as shown in Figure 10-6. The area was computed using the double meridian distance method (Wolf and Ghilani 2002). To account for the reduction in the matter that is able to dissipate the energy, the DPSE was normalized by the ratio of (PS_i/PS_o) as follows:

$$W_R = \frac{DPSE}{(PS_i / PS_o)} \tag{10-7}$$

where, W_R= normalized DPSE, PS_i = pseudostiffness at each load cycle, and PS_o = the maximum pseudostiffness at the first load cycle, the pseudostiffness is the ratio of maximum measured stress to maximum computed pseudostrain. The normalized DPSE quantifies the real damage during the dynamic direct tension test.

The relationship between the normalized DPSE (W_R) and the number of load cycles is presented in a semi-log graph in Figure 10-7. This relationship yields a trend line which has the following form:

$$W_R = a + b\ln(N) \tag{10-8}$$

where, b = the rate of fracture damage accumulation, a = the energy associated with the initial damage which corresponds to the first load cycle.

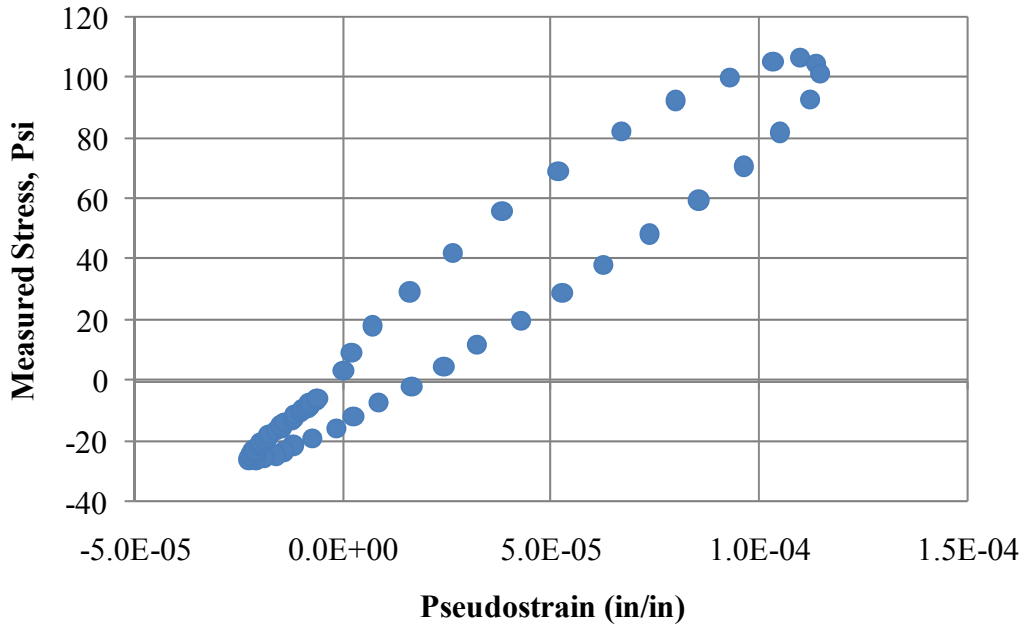

Figure 10-6 An Example of Measured Stress vs. Pseudostrain.

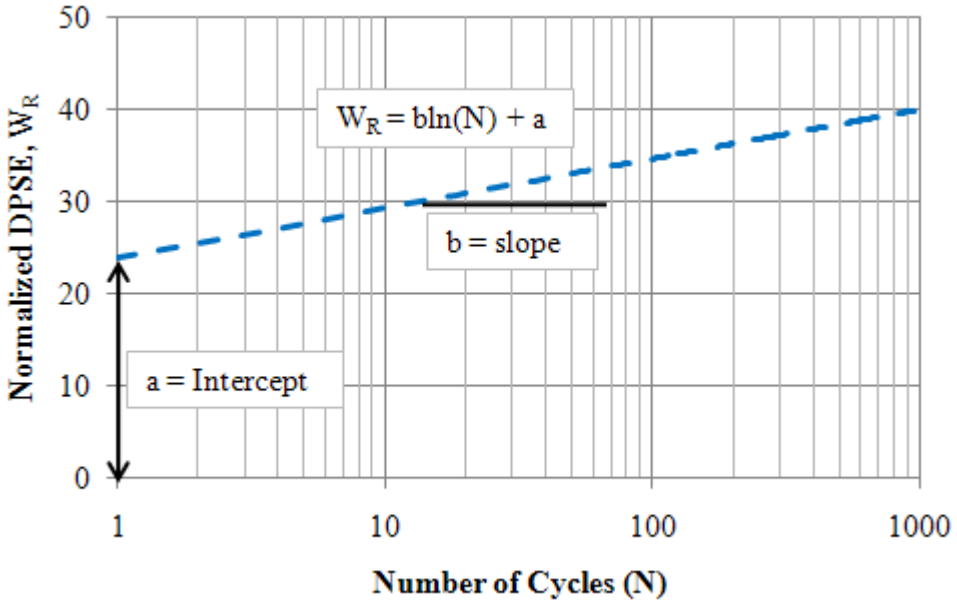

Figure 10-7. Normalized DPSE, W_R vs Number of Cycles.

Tensile Strength Test

This test was used to determine the tensile strength of the test specimens. The tensile strength is a required input in the fracture model. This test was conducted at 20^{o}C after 10 min of the completion of the RDT test. A test sample was continuously pulled at a constant rate of 0.05 in/min until the failure occurs.

Figure 10-8 shows a test specimen after failure inside the MTS machine, while Figure 10-9 shows the failure for the test specimens in dry and wet conditions. Figure 10-9(a) displays the failure in wet condition where the aggregates were stripped from the binder. Figure 10-9(b) shows the failure in dry condition where the aggregates were still coated very well with the binder.

Figure 10-8. Test Sample after Failure inside the MTS Machine.

(a) (b)

Figure 10-9. Test Specimens after Failure (a) Wet Condition, (b) Dry Condition.

Surface Energy Measurements

The surface energy was used to estimate the adhesive bond surface energy between asphalt binder and aggregate and the cohesive bond energy of asphalt binder (Arambula, 2007; Howson et al., 2007). The surface energy can be defined as the required work to create a unit surface area. The surface free energy has three separate components (Howson et al., 2007); monopolar acidic (Γ^{+},), monopolar basic (Γ^{-}) and apolar or Lifshitz-van der Waals (Γ^{LW}). The total surface free energy is calculated according to Equation 10-9.

$$\Gamma = \Gamma^{LW} + 2\sqrt{\Gamma^{+}\Gamma^{-}} \tag{10-9}$$

The adhesive bond energy (ΔG_f) is a required parameter in the proposed model. The Wilhelmy plate (WP) test and the Universal sorption device (USD) are used to determine the surface energy components of asphalt binder and aggregates, respectively. Table 10-3 present the surface energy components for asphalt binder and aggregates.

The adhesive bond energy between the binder (subscript *A*) and aggregate (subscript *S*) was calculated using Equation 10-10. The adhesive bond energy when the water (subscript *W*) displaces asphalt binder from its interface with the aggregate is presented in Equation 10-11.

$$\Delta G_{AS}^{a} = 2\sqrt{\Gamma_{A}^{LW}\Gamma_{S}^{LW}} + 2\sqrt{\Gamma_{A}^{+}\Gamma_{S}^{-}} + 2\sqrt{\Gamma_{A}^{-}\Gamma_{S}^{+}} \tag{10-10}$$

$$\Delta G_{ASW}^{wet} = \Gamma_{AW} + \Gamma_{SW} - \Gamma_{AS} \tag{10-11}$$

Equation 10-12 represents the energy of the interface between any two materials (*i and j*).

$$\Gamma_{ij} = \Gamma_i + \Gamma_j - 2\sqrt{\Gamma_i^{LW}\Gamma_j^{LW}} - 2\sqrt{\Gamma_i^{+}\Gamma_j^{-}} - 2\sqrt{\Gamma_i^{-}\Gamma_j^{+}} \quad (10\text{-}12)$$

Table 10-3. Surface Energy Components.

Materials	Wetting or Dewetting	Γ	Γ^{LW}	Γ^{+}	Γ^{-}
Asphalt Binder (PG 76-22)	Wetting	22.03	21.36	0.05	2.12
	Dewetting	43.56	43.56	0.00	13.11
Aggregates	N/A	111.34	44.37	1.63	687.89
Water	N/A	72.80	21.80	25.50	25.50

CRACK GROWTH FRACTURE MODEL

A crack growth index was used to evaluate the performance and moisture sensitivity of asphalt mixtures. The crack growth index was developed originally by Lytton (1993) and later modified by Masad et al. (2006) and Arambula (2007). Herein, the crack growth index was employed in order to assess the performance and the resistance to moisture damage of asphalt mixtures with different percent air voids. This section includes a brief description of the crack growth model and the reader is referred to Arambula (2007) for more details and the complete derivation. The crack growth was derived from Paris's law (Equation 10-13).

$$\frac{dr}{dN} = A(J_R)^n \quad (10\text{-}13)$$

where: r = average crack radius, N = number of load cycles, A and n = material constants, and J_R = J-integral or the change in pseudostrain energy per unit volume to the change in crack surface area.

$$J_R = \frac{\frac{\partial W_R}{\partial N}}{\frac{\partial (c.s.a)}{\partial N}} \quad (10\text{-}14)$$

where: W_R = DPSE per unit volume, c.s.a = crack surface area. The equation used to estimate the crack growth parameter (r) is presented in Equation 10-15 (Arambula (2007).

$$r = \left[r_o^{\frac{2n+1}{1+n}} + (2n+1)\left(\frac{bE_R}{4\pi E_1 \Delta G_f \sigma_t^2} \right)^{\frac{n}{1+n}} \left(N^{\frac{1}{1+n}} - 1^{\frac{1}{1+n}} \right) \right]^{\frac{1+n}{2n+1}} \quad (10\text{-}15)$$

The initial damage is caused by the presence of initial cracks and voids (r_o). Due to the material nonlinearity at higher strain levels, it is difficult to separate the initial energy into nonlinear and initial damage fractions. Consequently, the initial energy was subtracted from the pseudostrain energy. Test specimens were compared based on the crack growth behavior which represented by the second part of Equation 10-15. The crack growth index (CGI) is presented in Equation 10-16 (Arambula 2007).

$$CGI = \left[(2n+1)^{\frac{1+n}{2n+1}} \left(\frac{bE_R}{4\pi E_1 \Delta G_f \sigma_t^2} \right)^{\frac{n}{2n+1}} \left(N^{\frac{1}{1+n}} - 1^{\frac{1}{1+n}} \right)^{\frac{1+n}{2n+1}} \right] \quad (10\text{-}16)$$

where: CGI = crack growth index, N = number of load cycles, n = material constant equals to reciprocal of the modulus relaxation rate (m), E_o= initial relaxation modulus, ΔG_f= adhesive bond surface energy between asphalt binder and aggregate, σ_t= tensile strength, E_R= reference modulus, $b = \partial WR / \partial \ln(N)$, W_R= pseudostrain energy per unit volume of the intact material.

EXPERIMENTAL TESTS RESULTS

In the following section the results of the experimental tests will be presented and discussed.

Results of Tensile Relaxation Test

Figure 10-10 shows the change of the tensile relaxation modulus over the time for tested specimens at different percent air voids. Figure 10-11 shows the ratio of the initial tensile relaxation modulus in wet condition to the one in dry condition. The results show that the tensile relaxation modulus decreased with the increase in percent air voids. In addition, the ratio of tensile relaxation modulus in wet condition to the one in dry condition decreased with an increase in percent air voids. It is interesting to note from Figure 10-10 that the percent air voids cause a shift in the relaxation modulus curve. This

indicates that a relaxation modulus – percent air voids shift function can be introduced to predict the change in modulus with changes in air voids.

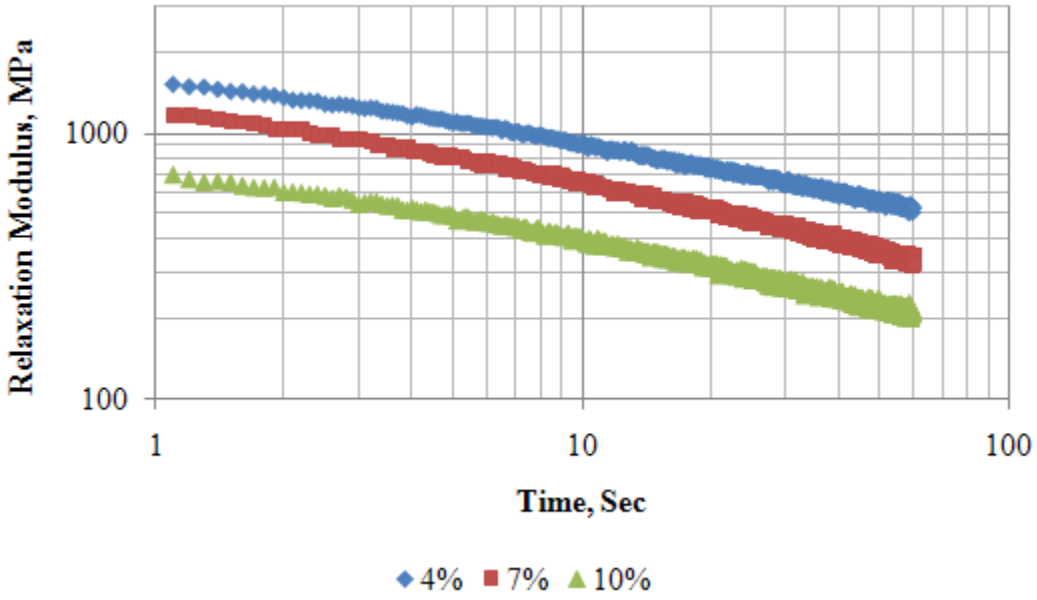

Figure 10-10. Examples of Tensile Relaxation Test Results at Different Percent Air Voids in Dry Condition.

Results of Dynamic Direct Tension Test

Figure 10-12 shows the change of the normalized DPSE (W_R) with the load cycles for tested specimens at different percent air voids. Figures 10-13 and 10-14 show the average intercept (a) at different percent air voids in dry and wet conditions, respectively. The average slope (b) plotted versus percent air voids in dry and wet conditions as shown in Figures 10-15 and 10-16, respectively. By examining the results, the following observations can be made:

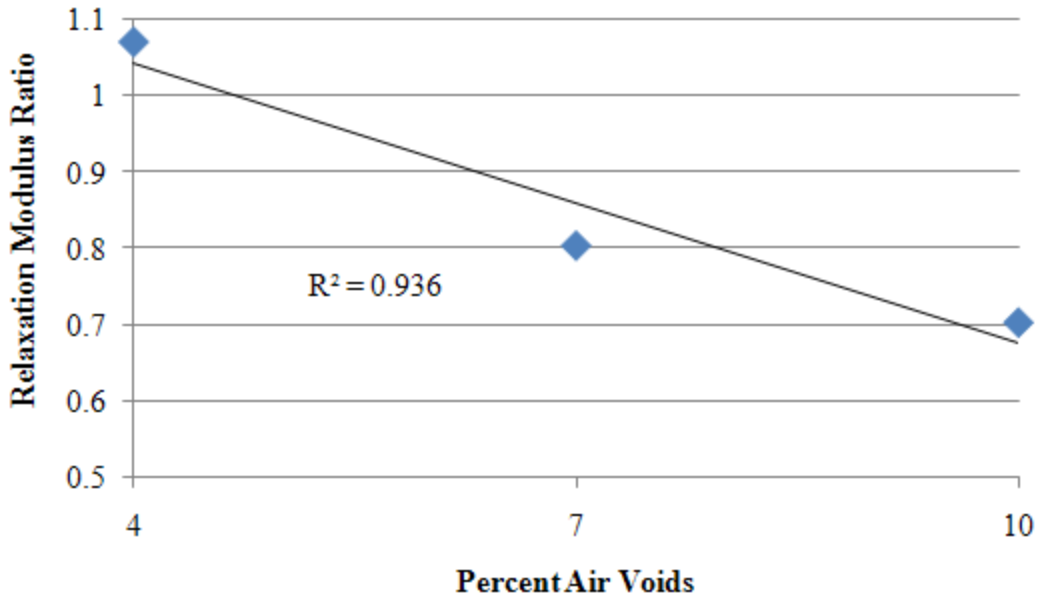

Figure 10-11. Initial Tensile Relaxation Modulus Ratio versus Percent Air Voids.

- The normalized DPSE (W_R) correlated very well with the number of cycles in a semi-log scale.
- The initial W_R or the intercept (a) decreases with the increase in percent air voids.
- The rate of fracture damage accumulation or slope (b) increases with the increase in the initial W_R.

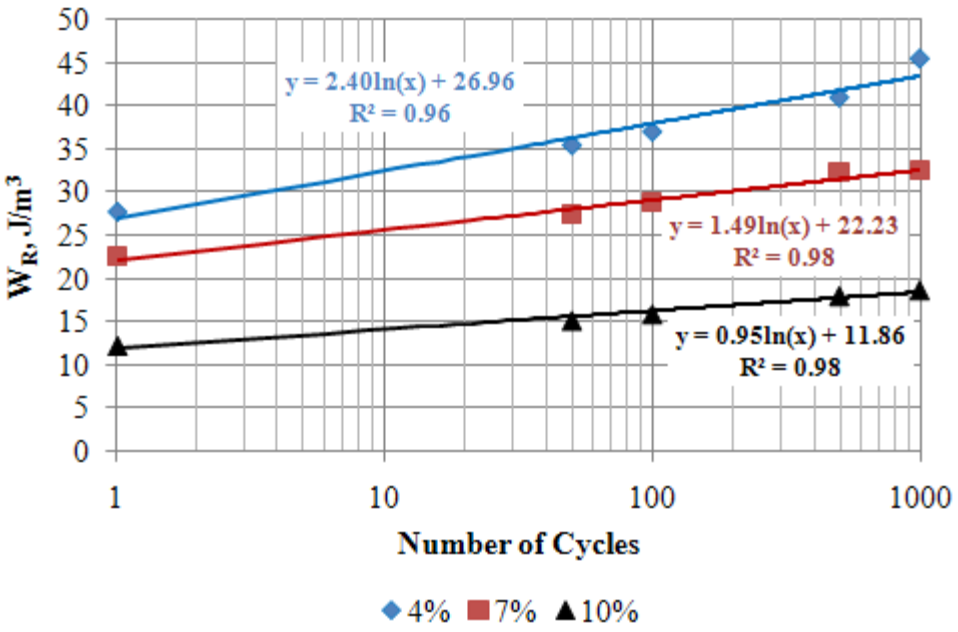

Figure 10-12. Normalized DPSE (W_R) versus Number of Cycles at Different Percent Air Voids.

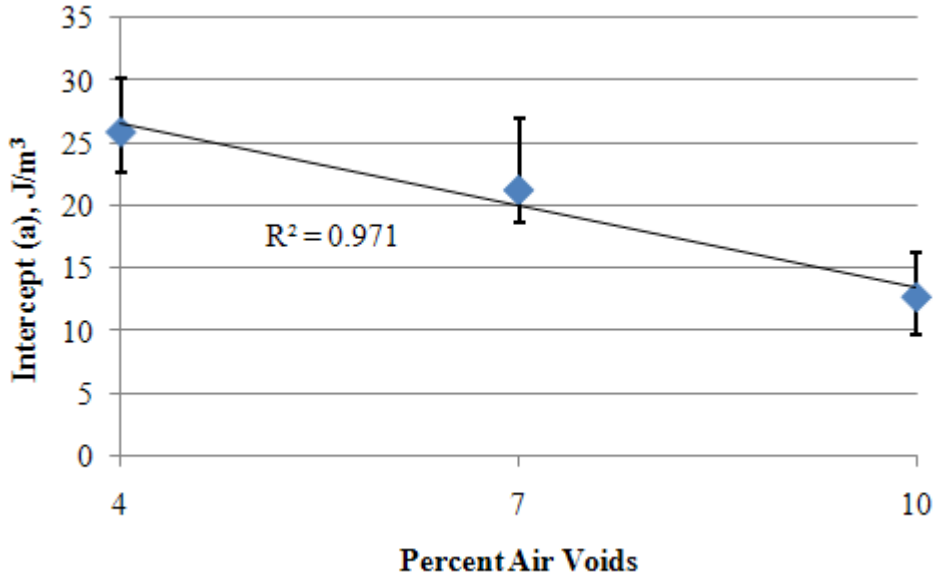

Figure 10-13. Intercept (a) versus Percent Air Voids in Dry Conditions.

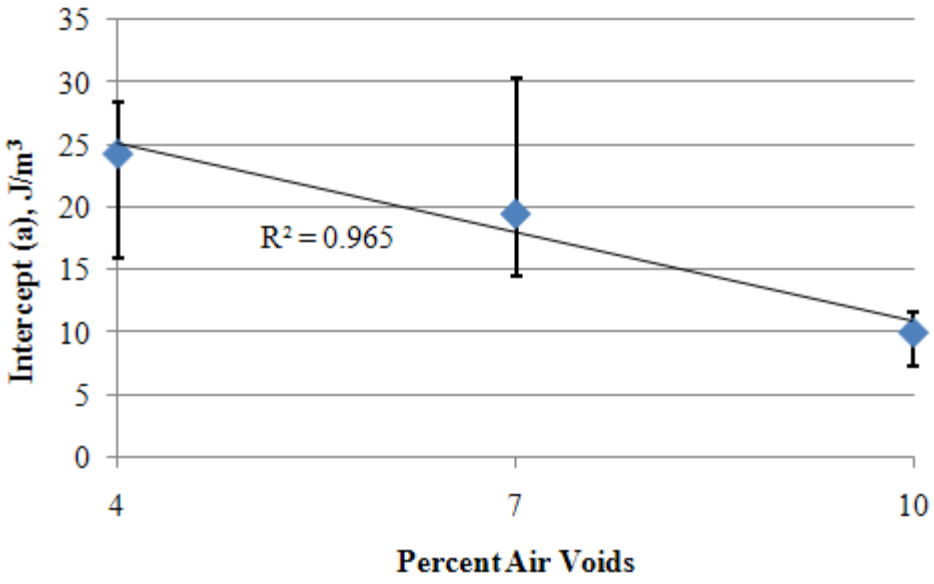

Figure 10-14. Intercept (a) versus Percent Air Voids in Wet Conditions.

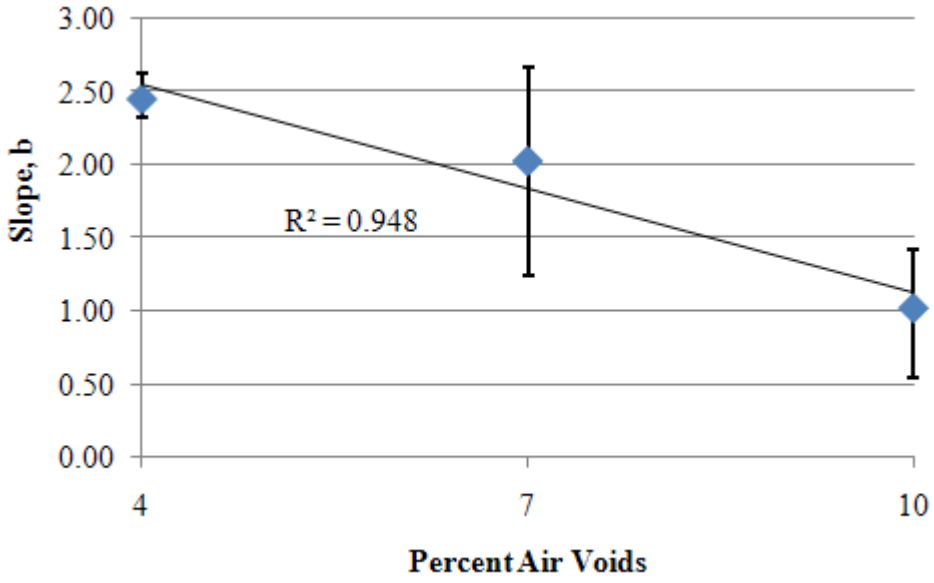

Figure 10-15. Percent Air Voids versus Slope (b) in Dry Conditions.

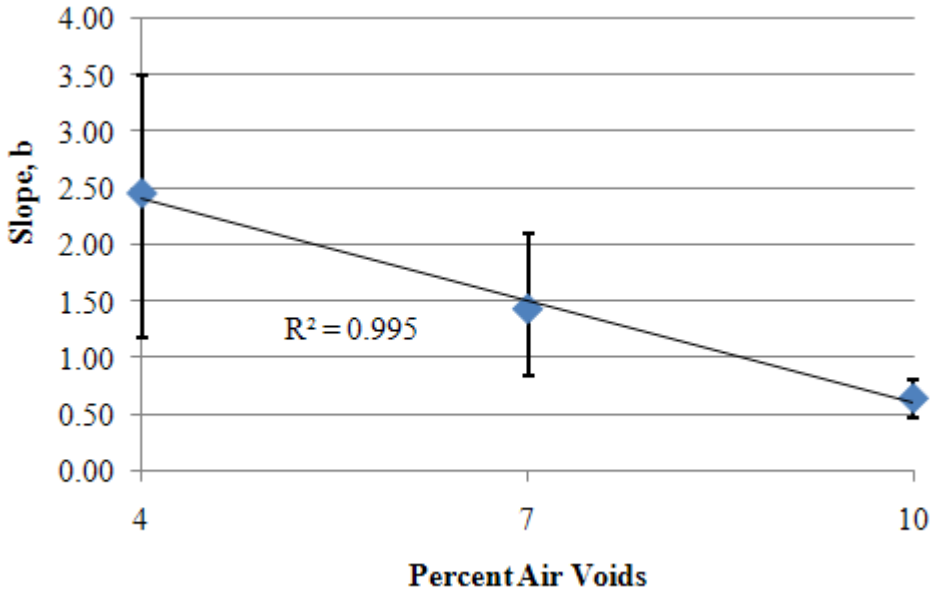

Figure 10-16. Percent Air Voids versus Slope (b) in Wet Conditions.

Results of Tensile Strength Test

Figures 10-17 and 10-18 present the average tensile strength for test specimens with different percent air voids in dry and wet conditions, respectively. The ratio of tensile strength in wet condition to the tensile strength in dry condition at different percent air voids is shown in Figure 10-19. The results show the following:

- The tensile strength decreased with the increase in percent air voids
- The ratio of tensile strength in wet condition to the one in dry condition decreased with the increase in percent air voids.

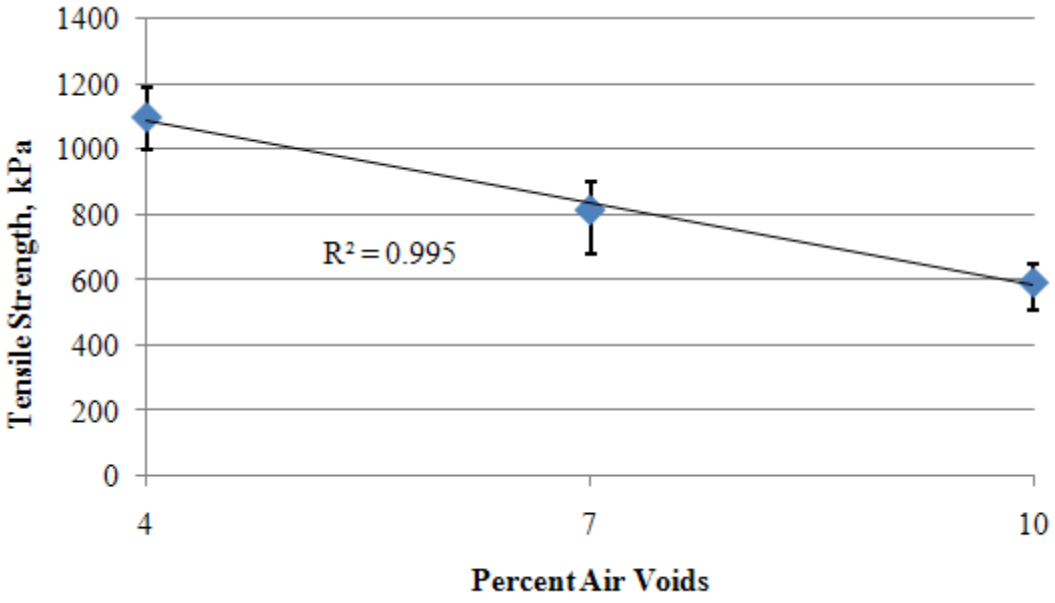

Figure 10-17 Average Tensile Strength versus Percent Air Voids in Dry Conditions.

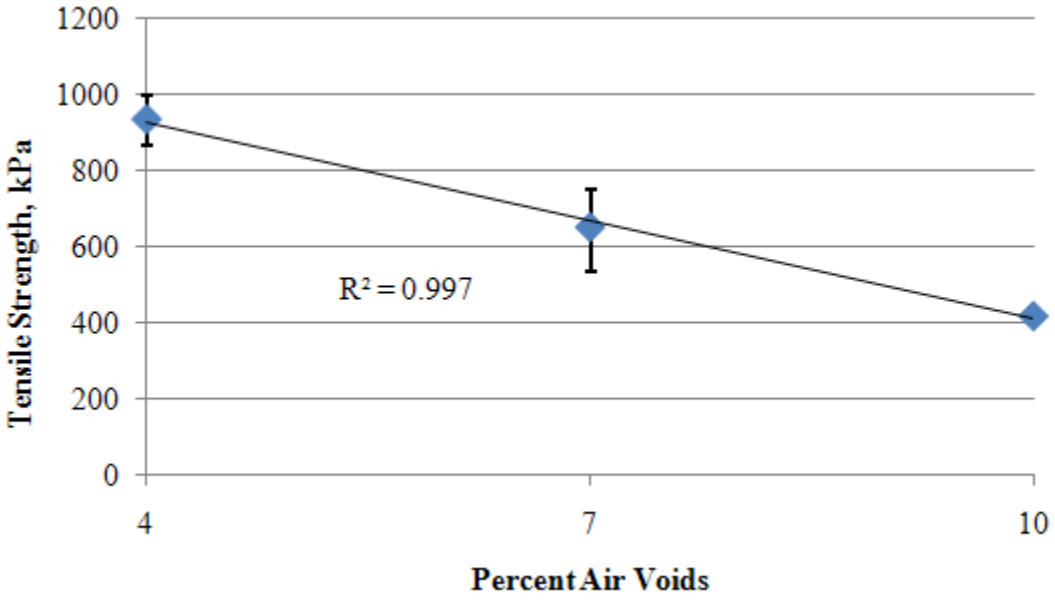

Figure 10-18. Average Tensile Strength versus Percent Air Voids in Wet Conditions.

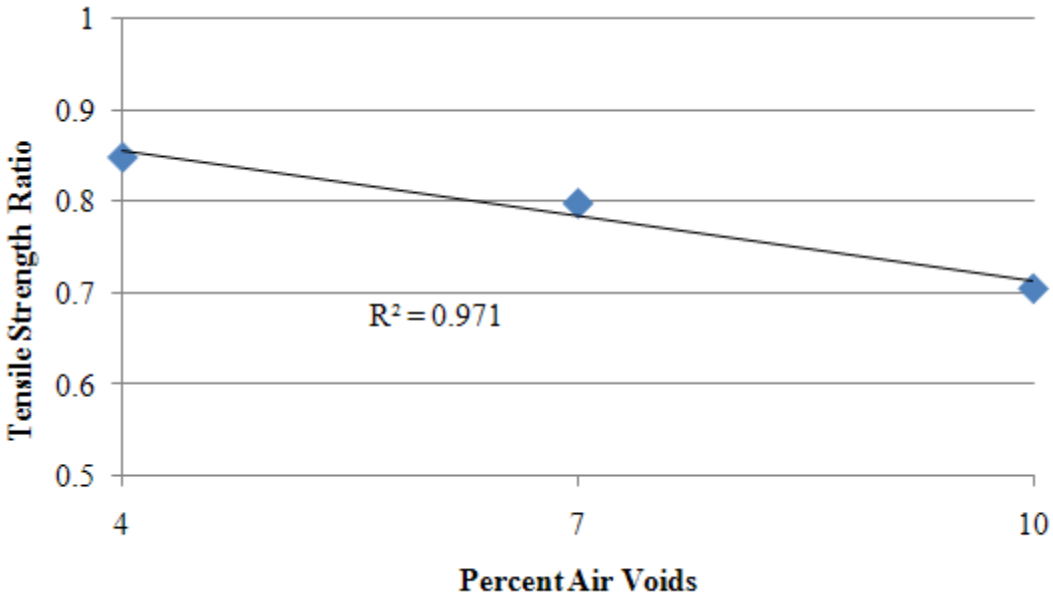

Figure 10-19. Tensile Strength Ratio versus Percent Air Voids.

Results of Adhesive Bond Energy

Surface energy components of the asphalt binder and aggregates given in Table 10-3 were used to determine the adhesive bond energy between asphalt and aggregates. Equations 10-10 and 10-11 were used to calculate the adhesive bond energy between the aggregates and asphalt binder in dry and wet conditions, respectively. The adhesive bond energy of the fracture components in Equation 10-16 was determined to be 97.71 erg/cm^2 in dry condition and -195.41 erg/cm^2 in wet condition. However; the test specimens were not fully saturated of water in the wet conditions. The adhesive bond energy in wet condition was assumed to proportional to the ratio of the reference modulus in wet condition to the one under the dry condition as given in Equation 10-17.

$$\Delta G_f = \frac{E_R(Wet)}{E_R(Dry)} \Delta G_{AS}^a \qquad (10\text{-}17)$$

Table 10-4 summarizes the required parameters in the crack growth index model.

Table 10-4. Average Parameters for the Fracture Model.

Percent Air Voids	Condition	E_0 Mpa	m	E_R Mpa	a J/m^3	b	σ_t kPa	ΔG_f J/m^2
	Dry	1843.38	0.316	5469.36	25.97	2.45	1100.69	0.09717
4	Wet	1974.2	0.341	5375.76	24.35	2.46	935.17	0.09551
	Dry	1394.34	0.318	4437.34	21.43	2.03	816.55	0.09717
7	Wet	1122.37	0.334	3983.1	19.56	1.44	652.41	0.08722
	Dry	808.05	0.298	4094.03	12.79	1.03	594.48	0.09717
10	Wet	594.38	0.316	3436.79	10.09	0.65	419.31	0.08456

RESULTS AND ANALYSIS

The results show that the relaxation modulus decreases with the increase in percent air voids. Specimens with higher percent air voids accumulate damage at lower rate than specimens with low percent air voids. This is an evident in the lower (a) and (b) values at high percent air voids. However, specimens with high percent air voids have lower strength as shown in the tensile strength values reported in the last column of Table 10-4. Figure 10-20 show the crack growth index (CGI) against the number of load cycles for the test specimens. Specimens with less percent air voids had less CGI than the ones with high percent air voids in dry and wet conditions, which means better performance or more resistance to the fracture damage. The dry specimens had less CGI than the wet ones at each percent air voids. The CGI ratio, which is the CGI in wet condition to the one in dry conditions, at each percent air voids is shown in Figure 10-21. It is interesting to notice that the CGI ratio at 7 percent air voids was less than the one at 4 and 10 percent air voids. It means that the detrimental effect of the moisture was minimal at 7 percent air voids. However, it showed be pointed out that samples with less percent air voids performed better.

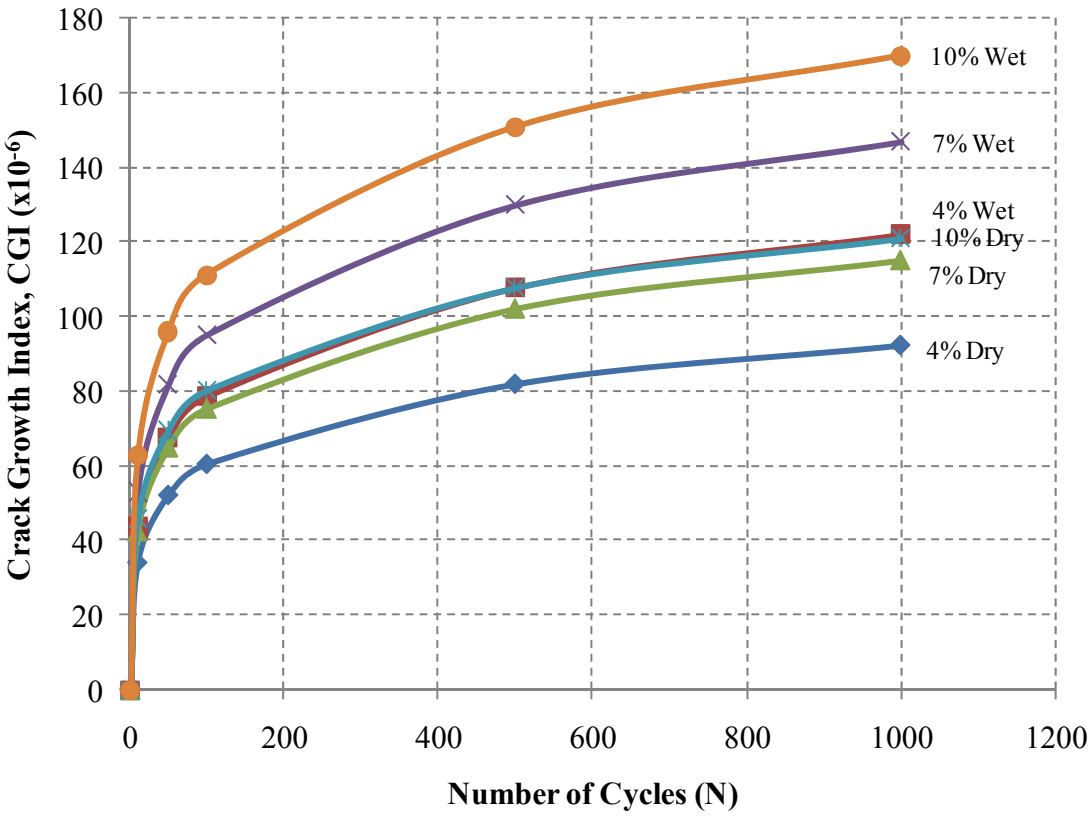

Figure 10-20. Crack Growth Index at Different Percent Air Voids in Dry and Wet Conditions.

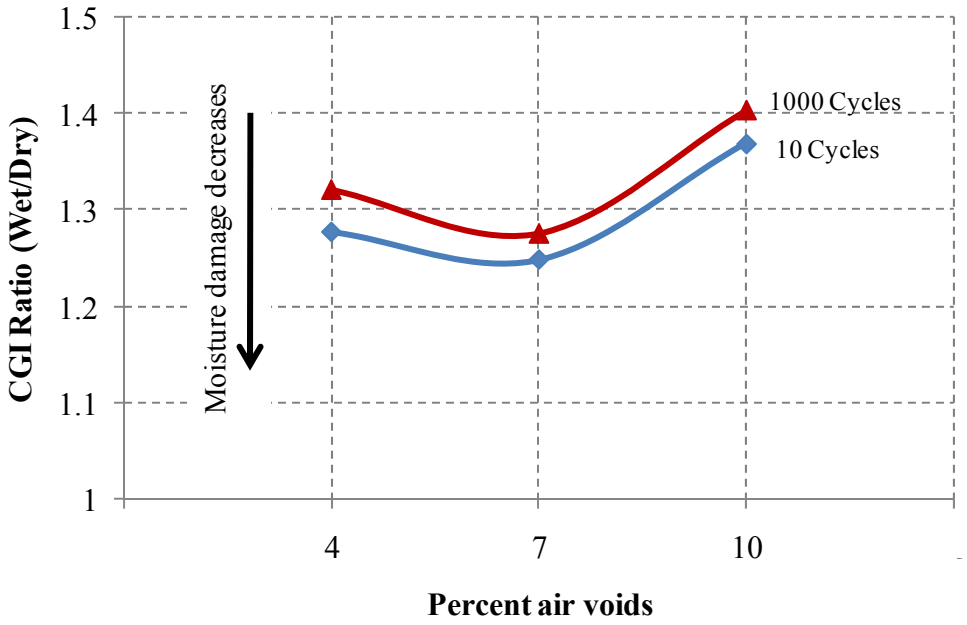

Figure 10-21. Crack Growth Index (Wet/Dry) versus Percent Air Voids.

SUMMARY

In this chapter, the resistance of asphalt mixtures with different percent air voids to moisture damage was evaluated by using a fracture mechanics approach. This approach accounts for the fundamental material properties which include the viscoelastic properties, pseudo strain dissipated energy, tensile strength, and the adhesive bond surface energy of asphalt mixture. Dry and wet test asphalt mixtures specimens were evaluated. A crack growth index was used to quantify the damage of the test specimens. The dry samples performed better than the wet one at each percent air voids. The test specimens with less percent air voids performed better than the ones with higher percent air voids. The detrimental effect of moisture at 7 percent air voids specimens was the least compared to 4 and 10 percent air voids specimens.

CHAPTER XI
CONCLUSIONS

This study focused on evaluating the influence of different field compaction patterns on uniformity of air void distribution in asphalt pavements. It also examined the influence of changing some parameters in the laboratory compaction process on mechanical properties and resemblance of laboratory compaction to field compaction. Research team has also conducted forensic evaluation in which the air void distribution measured using X-ray CT was compared with the results of Ground Penetrating Radar. The effect of nonuniformity of the air void distribution on the moisture diffusion through the asphalt pavements was evaluated by measuring diffusion coefficients of asphalt mixtures. The resistance of asphalt mixtures to moisture damages was evaluated using a fracture mechanics approach. The following points summarize the main findings from this study.

EVALUATION OF FIELD COMPACTION

- The analysis results of various pavement sections compacted using different patterns provided experimental evaluation of the influence of the field compaction pattern on the uniformity of air void distribution in asphalt pavements. The X-ray CT images along with the locations of the cores were used to generate air void maps in the pavement. These maps are useful to relate air void distributions to the compaction pattern.
- The efficiency of compaction at a given point is a function of the location of this point with respect to the roller width. Therefore, a new index referred to as the Compaction Index (CI) is proposed to quantify the compaction effort at any point in the pavement. This index is the summation of the multiplication of each pass with an effectiveness factor. The effectiveness factor at a point is a function of the location of the point with respect to the roller width. A point on the mat closer to the center of the roller is subjected to more effective compaction than a point closer to the edge of the roller.

- It is demonstrated that the CI is useful to set up the compaction pattern in order to achieve uniform percent air voids; a more uniform CI corresponds to more uniform air voids.
- The use of the pneumatic roller in the breakdown stage was found to be effective in reducing the percent air voids and improving uniformity in the top half of the lift thickness of the mixtures used in this study.
- It has been reported in the past that the mixture near longitudinal joints is usually less compacted than the mixture towards the center of the pavement. This has been attributed to the lower confinement, typically lower number of passes and the faster rate of heat loss at the joint compared with the center of the pavement. Based on the results of this study, the low compaction at the joint is also attributed to the low effectiveness factor due to the relative location of the joint with respect to the roller width.
- The results suggest that the joints need to be compacted to a higher CI compared with the center of the pavement in order to compensate for the other factors that reduce joint compactability. This can be achieved by increasing the number of passes and/or increasing the effectiveness factor. The compaction of a confined joint resulted in lower and more uniform air voids than compaction of an unconfined joint.

EVALUATION OF LABORATORY COMPACTION

- In general, laboratory specimens compacted using a 2.0° gyratory angle performed slightly better in Hamburg tests than specimens compacted using a 1.25^{o} gyratory angle.
- Overlay test results did not show any difference among the lab prepared specimens compacted using 1.25° or 2.0° angles.
- There is no trend indicating that permeability in gyratory specimens is influenced by the angle of gyration.
- Laboratory compacted samples had comparable rut depth to field cores when percent air voids was similar.

- There was a slight influence of compaction pattern on the Hamburg results. However, there was no trend indicating an influence of compaction pattern on the overlay testing results or permeability results. The variability in the overlay testing results might have overshadowed the influence of compaction pattern or resistance to fracture as measured using the overlay tester.
- Hamburg results were found to be more related to the average percent of air void rather than the air void structure. Field cores with less average percent of air void performed better than the ones that had higher percent of air void.
- The overlay test results clearly show that specimens prepared to have uniform air void distribution had less variation in the failure number of cycles than all other cases. Based on this finding, it is recommended to cut the top and the bottom parts of the laboratory samples for the overlay test in order to improve air void uniformity and reduce the test variability.
- There is a relationship between temperature profile and air void distribution. Improvement of the uniformity of temperature profile is associated with uniformity in air void distribution. However, this relationship is weak and does not warrant changes to the compaction temperature at this point.
- The air void distribution is more uniform for specimens prepared using a modified binder compared with specimens prepared with an unmodified binder.
- The middle third of a specimen is more uniform than the whole specimen. This is consistent with findings from previous studies.

COMPARISON OF X-RAY CT WITH GROUND PENETRATING RADAR

- The GPR was able to detect and show the extent of the compaction problem in the new pavement investigated in this study. The GPR detected low density areas typically at the bottom of the stone filled layers. These layers were placed in 4 inch lifts and it appears that the bottom 1 inch of the lift was poorly compacted.
- The color coded image display of GPR data were very useful in quantifying the depth and extent of both water filled and air filled voids within the HMA layer. This information was used to generate a strategy to drain trapped moisture from the pavement structure

- The X-ray CT results were in very good agreement with the GPR measurements as it showed that the section with stone filled mix had more nonuniform air void distribution and larger air voids than the sections with conventional dense graded asphalt mix. Based on the results, it is recommended to make adjustments to the design of the stone filled mixtures used in Texas to allow better compaction.

AIR VOIDS DISTRIBUTION AND MOISTURE DIFFUSION

- The effect of nonuniformity of air void distribution on the moisture diffusion was investigated by measuring the moisture diffusion coefficients of asphalt mixtures.
- The diffusion coefficients of asphalt mixtures were measured in laboratory for the first time. The range of the diffusion coefficients was in between 5.66E-5 to 2.92E-6 cm^2/sec.
- Higher percent of air voids at the top surface of the test samples expedited the moisture flow compared with less percent of air voids at the top.
- The size of air voids were found to be correlated with the percent of air voids. Higher percent of air voids yield larger air void size. The size of air voids at the top surface of the test samples correlated well with the measured diffusion coefficients.

FRACTURE ANALYSIS OF MOISTURE DAMAGE

- The resistance of asphalt mixtures with different percent air voids to moisture damage was evaluated by using a fracture mechanics approach in which a crack growth index was used to quantify the damage of the test specimens.
- The analysis approach confirmed that the dry samples performed better than the wet one at each percent air voids.
- The test specimens with less percent air voids performed better than the ones with higher percent air voids
- The detrimental effect of moisture was the lowest at 7 percent air voids compared with 4 and 10 percent air voids specimens.

REFERENCES

American Association of State Highway and Transportation Officials (AASHTO). (2002a). "Bulk Specific Gravity of Compacted Asphalt Mixtures Using Saturated Surface-Dry Specimens." *T166*. Standard Specifications for Transportation Materials and Methods Sampling and Testing, American Association of State Highway and Transportation Officials, Washington, D.C.

American Association of State Highway and Transportation Officials (AASHTO). (2002b). "Preparing and Determining the Density of Hot-Mix Asphalt (HMA) Specimens by Means of the Superpave Gyratory Compactor." *T312*. Standard Specifications for Transportation Materials and Methods Sampling and Testing, American Association of State Highway and Transportation Officials, Washington, D.C.

American Association of State Highway and Transportation Officials (AASHTO). (2002c). "Standard Method of Test for Resistance of Compacted Asphalt Mixtures to Moisture-Induced Damage." *T283*. Standard Specifications for Transportation Materials and Methods Sampling and Testing, American Association of State Highway and Transportation Officials, Washington, D.C.

Arambula, E. (2007). "Influence of Fundamental Material Properties and Air Void Structure on Moisture Damage of Asphalt Mixes". Ph.D. Dissertation, Texas A&M University, College Station, Texas.

American Society of Testing and Materials (ASTM). (2006). "Standard Test Method for Measurements of Hydraulic Conductivity of Saturated porous Materials Using a Flexible Wall Permeameter." *D5084*. Annual Book of ASTM Standards, American Society of Testing and Materials, West Conshohocken, Pennsylvania.

Birgisson, B., Roque, R., and Page G. (2003). "Evaluation of Water Damage Using Hot Mix Asphalt Fracture Mechanics," *Journal of the Association of the Asphalt Paving Technologists,* 72, 424-462.

Birgisson, B., Roque, R., and Page G. (2004). "The Use of a Performance-Based Fracture Criterion for the Evaluation of Moisture Susceptibility in Hot Mix Asphalt," *Transportation Research Record 3431,* TRB, National Research Council, Washington, D.C., 55-61.

Bulut, R., and Wray, W.K. (2005). "Free Energy of Water – Suction – in Filter Papers," *Geotechnical Testing Journal*, 28(4), 355-364.

Bulut, R., and Leong, E. C. (2008). "Indirect Measurement of Suction," *Journal of Geotechnical and Geological Engineering*, 26, 633-644.

Button, J.W., Little, D.N., Jagadam, V. and Pendleton, O.J. (1994). "Correlation of Selected Laboratory Compaction Methods with Field Compaction," *Transportation Research Record 1454*, TRB, National Research Council, Washington, D.C., 193–201.

Caro, S., Masad, E. Bahsin, A., and Little, D.N. (2007). "Moisture Susceptibility of Asphalt Mixtures, Part 1: Mechanisms," *International Journal of Pavement Engineering*, 8(2), 81-98

Consuegra, A., Little, D.N., Quintus, H.V., and Burati, J. (1989). "Comparative Evaluation of Laboratory Compaction Devices Based on Their Ability to Produce Mixtures with Engineering Properties Similar to those Produced in the Field," *Transportation Research Record 1228*, TRB, National Research Council, Washington, D.C., 80–87.

Corps of Engineers (2000). *Hot-Mix Asphalt Paving Handbook 2000*, AC 150/5370-14A, US Army Corps of Engineers, Washington, D.C.

Edlefsen, N.E, and Anderson, A.B.C. (1943). "Thermodynamics of Soil Moisture," *Hilgardia*, 15, 31-298.

Fredlund, D.G., and Rahardjo, H. (1993). *Soil Mechanics for Unsaturated Soils*, John Wiley & Sons, Inc., New York.

Geankoplis C.J. (1993). *Transport Processes and Unit Operations*, third ed., PTR Prentice Hall Inc., Englewood Cliffs, New Jersey.

Guler, M., Bosscher, P.J., and Plesha M.E. (2002). "A Porous Elasto-Plastic Compaction Model for Asphalt Mixtures with Parameter Estimation Algorithm," *Geotechnical Special Publication no.123,* ASCE, 126-143.

Harvey, J., and Monismith. C.L. (1993). "Effects of Laboratory Asphalt Concrete Specimen Preparation Variables on Fatigue and Permanent Deformation Test Results Using Strategic Highway Research Program A-003A Proposed Testing Equipment," *Transportation Research Record 1417*, TRB, National Research Council, Washington, D.C., 38–57.

Howson, J., Masad, E., Bhasin, A., Branco, V., Arambula, E., Lytton, R., and Dallas, L. (2007). "System for the Evaluation of moisture Damage Using Fundamental Material Properties." *Research Report 0-4524-1*, TTI, College Station, Texas.

Huerne, H.L. (2004). "Compaction of Asphalt Road Pavements: Using Finite Elements and Critical State Theory," Thesis Project, CT&M Dept., University of Twente, Enschede, Netherlands.

Image-Pro® Plus, Version 4.1 (1999). Media Cybernetics, Inc., Bethesda, Maryland.

Izzo, Richard (2008). Email Communications with TxDOT Engineer, Austin, Texas.

Kassem, E.A. (2005). "*Measurements of Moisture Suction in Hot Mix Asphalt Mixes*," M.S. Thesis, Texas A&M University, College Station, Texas.

Kassem, E., Masad, E., Bulut, R., and Lytton, R. (2006). "Measurements of Moisture Suction and Diffusion Coefficient in Hot Mix Asphalt and Their Relationships to Moisture Damage," *Transportation Research Record 1970,* TRB. Washington, D.C., 45-54.

Kringos, N., and Scarpas, A. (2005a). "Raveling of Asphaltic Mixes due to Water Damage: Computational Identification of Controlling Parameters," *Transportation Research Record 1929*, TRB. Washington, D.C., 79-87.

Kringos, N., and Scarpas, A. (2005b). "Simulation of Combined Mechanical-Moisture Induced Damage in Asphaltic Mixes," *First International Workshop on Moisture Damage*, Delft University of Technology, Delft, Netherlands, 2005b (CD-ROM).

Kringos, N., Scarpas, A., and Kasbergern, C. (2007). "Three Dimensional Elasto-Visco-Plastic Finite Element Model for Combined Physical-Mechanical Moisture Induced Damage in Asphaltic Mixes," *Journal of the Association of Asphalt Paving Technologists*, 76, 495-524.

Krishnan J.M., and Rao C.L. (2000). "Mechanics of Air Voids Reduction of Asphalt Concrete Using Mixture Theory," *International Journal of Engineering Science*, 38(12), 1331-1354.

Laliberte, G.E., and Corey, A.T. (1967). "*Hydraulic Properties of Disturbed and Undisturbed Soils. Permeability and Capillary of Soils*," ASTM, Philadelphia, 56-71.

Lytton. R., Uzan, J., Fernando, E., Hiltmen, D., and Stoffels, S. (1993). "Development and Validation of Performance Prediction Models and Specifications for Asphalt Binder and Paving Mixtures," *SHRP A-357*, Strategic Highway Research Program, National Research Council, Washington , D.C.

Masad, E., Muhunthan, B., Shashidhar, N., and Harman T. (1999a). "Internal Structure Characterization of Asphalt Concrete Using Image Analysis," *Journal of Computing in Civil Engineering (Special Issue on Image Processing),* ASCE, 13(2), 88–95.

Masad, E. A., Muhunthan, B., Shashidhar, N., and Harman, T. (1999b). "Quantifying Laboratory Compaction Effects on the Internal Structure of Asphalt Concrete," *Transportation Research Record 1681*, TRB. Washington, D.C., 179–184.

Masad E. (2004). "X-ray Computed Tomography of Aggregates and Asphalt Mixes," *Materials Evaluation Journal*, 62(7), 775-783.

Masad, E., Al-Omari, A., and Lytton, R. (2006a). "Simple Method for Predicting Laboratory and Field Permeability of Hot Mix Asphalt," *Transportation Research Record 1970*, TRB, National Research Council, Washington, D.C., 55-63.

Masad, E., Zollinger, C., Bulut, R., Little, D., and Lytton, R. (2006b). "Characterization of HMA Moisture Damage Using Surface Energy and Fracture Properties," *Journal of the Association of Asphalt Paving Technologists*, 75, 713-748.

Masad, E., Arambula, E., Ketcham, R., Abbas, A., and Epps Martin, A. (2007). "Nondesructive Measurements of Moisture Transport in Asphalt Mixtures," *Journal of the Association of Asphalt Paving Technologists,* 76, 919-952.

Matlab Software, Version 7 (2004). The MathWorks Inc., Natick, Massachusetts.

Mitchell, P.W. (1979). The Structural Analysis of Footings on Expansive Soil, *Report No. 1*, K.W.G. Smith and Associates, Newton, South Australia.

Monismith, C.L. (1992). "Analytically Based Asphalt Pavement Design and Rehabilitation," *Transportation Research Record 1354,* TRB, National Research Council, Washington, D.C., 5–26.

Montgomery R.B., (1947). Viscosity and Thermal Conductivity of Air and Diffusivity of Water Vapor in Air, *Journal of Meteorology*, 4, 193-196.

Newcomb, D.E, Buncher, M., and Huddleston, I.J. (2001). "Concepts of Perpetual Pavements." *Transportation Research Circular on Perpetual Bituminous Pavements, TRB*, Washington D.C., 4-11.

Partl, A., Flisch, A., and Jönsson, M. (2003). "Gyratory Compaction Analysis with Computer Tomography." *International Journal of Road Materials and Pavement Design*, 4(4), 401-422.

Partl, A., Flisch, A., and Jönsson, M. (2007). "Comparison of Laboratory Compaction Methods using X-ray Computer Tomography." *International Journal of Road Materials and Pavement Design*, 8(2), 139-164.

Peterson, B., Mahboub, K., Anderson, M., Masad, E., and Tashman, L. (2004). "Comparing Superpave Gyratory Compactor Data to Field Cores," *Journal of Materials in Civil Engineering, ASCE,* 16(1), 78-83.

Roberts F.L., Kandhal, P.S., Brown, E.R., Lee D., and Kennedy, T.W. (1996). *Hot Mix Asphalt Materials, Mixture Design and Construction*, National Asphalt Pavement Association, Research and Education Foundation, Lanham, Maryland.

Scullion, T., and Chen, Y. (1999). "COLORMAP Version 2, User's Manual with Help Menus," TTI, *1702-4*, College Station, Texas.

Scullion, T. (2006). "Perpetual Pavements in Texas: The State of the Practice," TTI, *4822-1*, College Station, Texas.

Shashidhar, N. (1999). "X-ray Tomography of Asphalt Concrete," *In Transportation Research Record,* TRB, National Research Council, Washington, D.C., 186-191.

Si, Z. (2001). "Characterization of Microdamage and Healing of Asphalt Concrete Mixtures." Ph.D. Dissertation, Texas A&M University, College Station, Texas.

Sood, E. (2005). "Determination of Diffusion Coefficient for Unsaturated Soils," M.S. Thesis, Department of Civil Engineering, Texas A&M University, College Station, Texas.

Sousa, J.B., Harvey, J., Painter, L., Deacon, J.A., and Monismith, C.L. (1991). *Evaluation of Laboratory Procedures for Compacting Asphalt –Aggregate Mixtures*, *Report No. SHRP-A-UWP-91-523*, Strategic Highway Research Program, National Research Council, Washington D.C.

Tashman, L., Masad, E., Peterson, B., and Saleh, H. (2001). "Internal Structure Analysis of Asphalt Mixes to Improve the Simulation of Superpave Gyratory Compaction to Field Conditions," *Journal of the Association of Asphalt Paving Technologists,* 70, 605-645.

TxDOT (2001). "Memorandum on Full-depth Asphalt Pavements, Flexible Pavement Design Task Force Implementation," Texas Department of Transportation (TxDOT), Austin, Texas.

Walubita, L., and Scullion, T. (2007). "Perpetual Pavements in Texas: The Fort Worth SH 114 Project in Wise County," TTI, *4822-2F*, College Station, Texas.

Wolf, P., and Ghilani, C. (2002). *Elementary Surveying: An Introduction to Geomatics*, 10th Ed., Prentice Hall, Upper Saddle River, New Jersey.

Zhou, F., and Scullion, T. (2003). "Upgraded Overlay Tester and its Application to Characterize Reflection Cracking Resistance of Asphalt Mixtures," *Research Report FHWA/TX-04/4467-1*, TTI, College Station, Texas.

APPENDIX A

AIR VOIDS ANALYSIS RESULTS

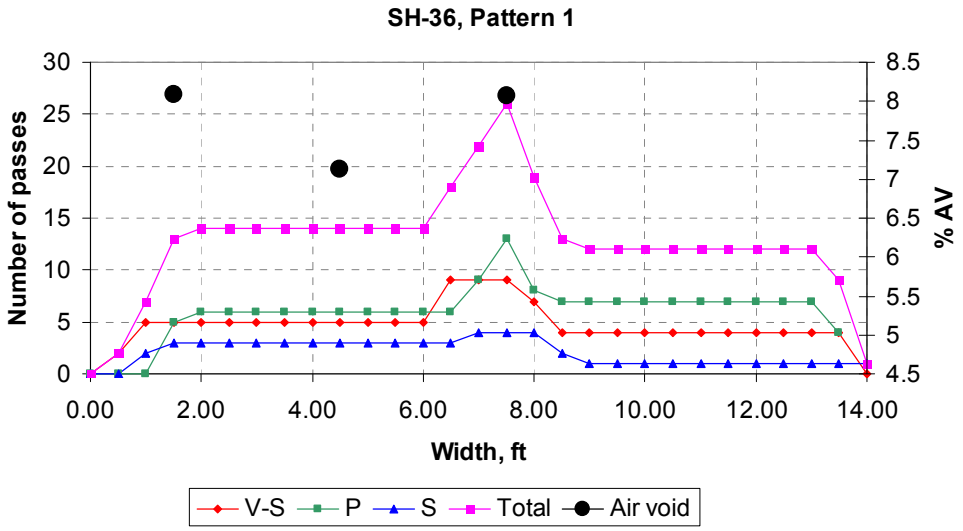

Note: Breakdown roller: vibratory and static (V-S), intermediate roller: pneumatic (P), finish roller: static (S).

Figure A-1. Number of Passes and the Percent of Air Voids across the Mat in SH-36 Test Section (Pattern 1).

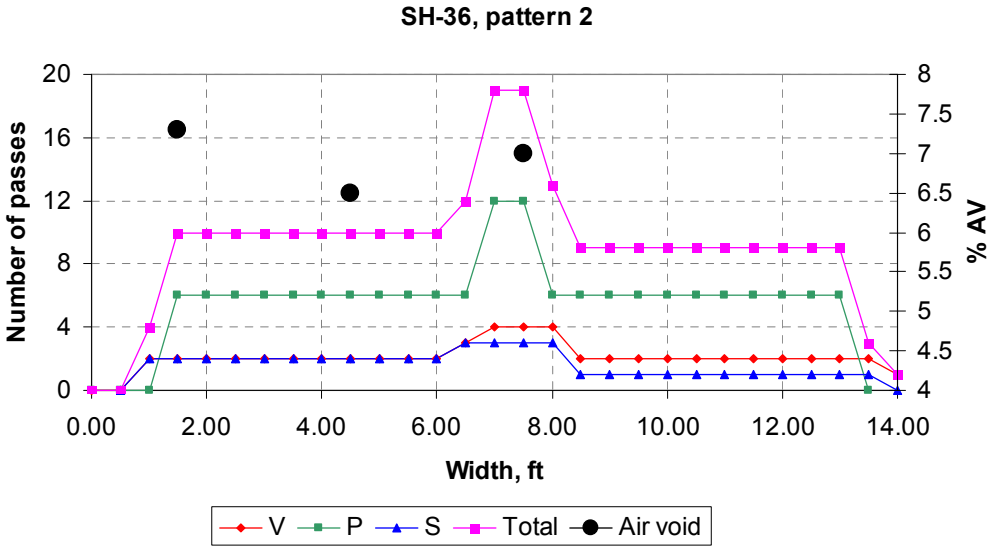

Note: Breakdown roller: vibratory (V), intermediate roller: pneumatic (P), finish roller: static (S).

Figure A-2. Number of Passes and the Percent of Air Voids across the Mat in SH-36 Test Section (Pattern 2).

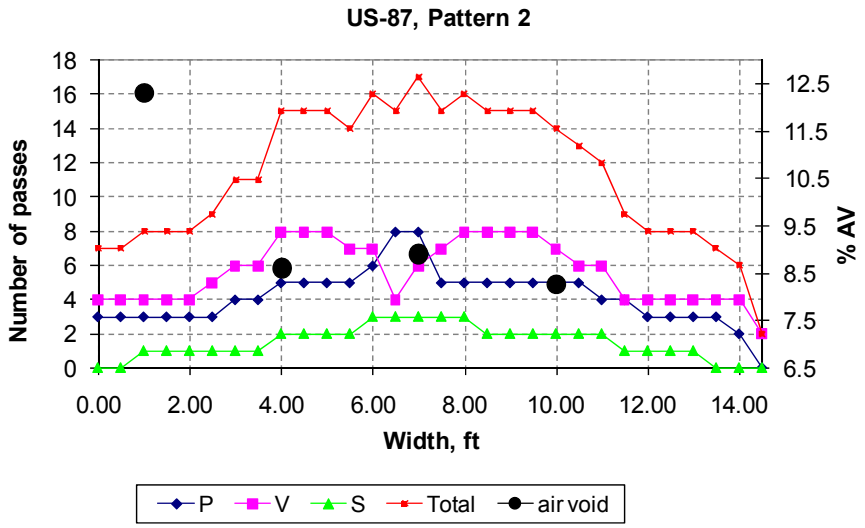

Note: Breakdown roller: pneumatic (P), intermediate roller: vibratory (V), finish roller: static (S).

Figure A-3. Number of Passes and the Percent of Air Voids across the Mat in US 87 Test Section (Pattern 2).

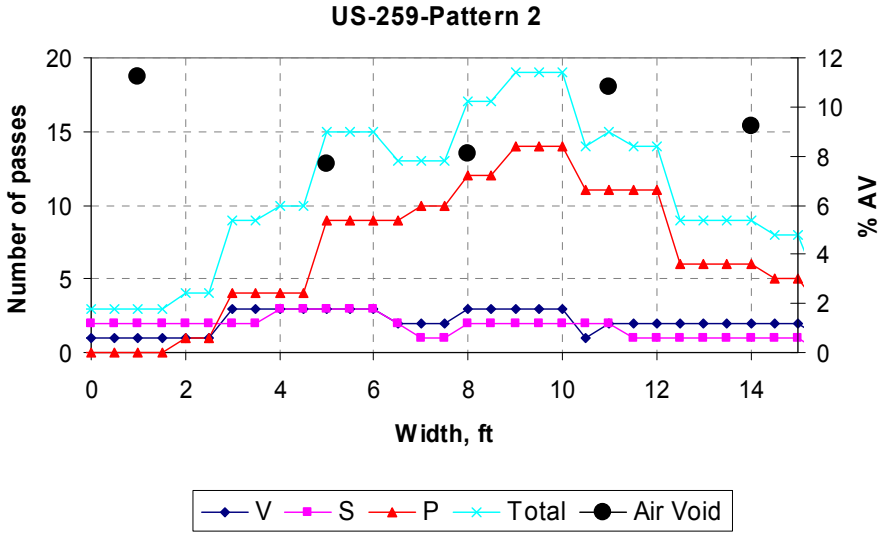

Note: Breakdown roller: vibratory (V), intermediate roller: static (S), finish roller: pneumatic (P).

Figure A-4. Number of Passes and the Percent of Air Voids across the Mat in US-259 Test Section (Pattern 2).

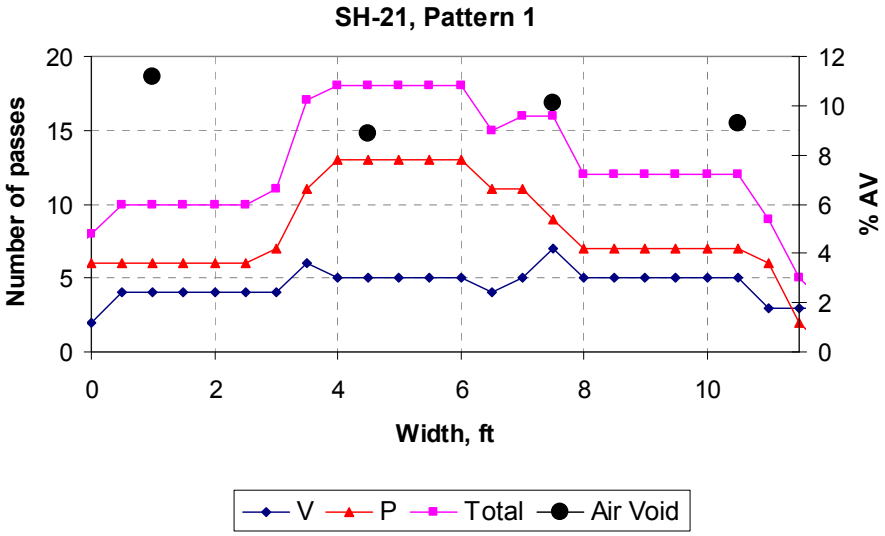

Note: Breakdown roller: vibratory (V), intermediate roller: pneumatic (P), finish roller: static (S). The static roller was applied after the mat cooled down and not included herein.

Figure A-5 Number of Passes and the Percent of Air Voids across the Mat in SH-21 Test Section (Pattern 1).

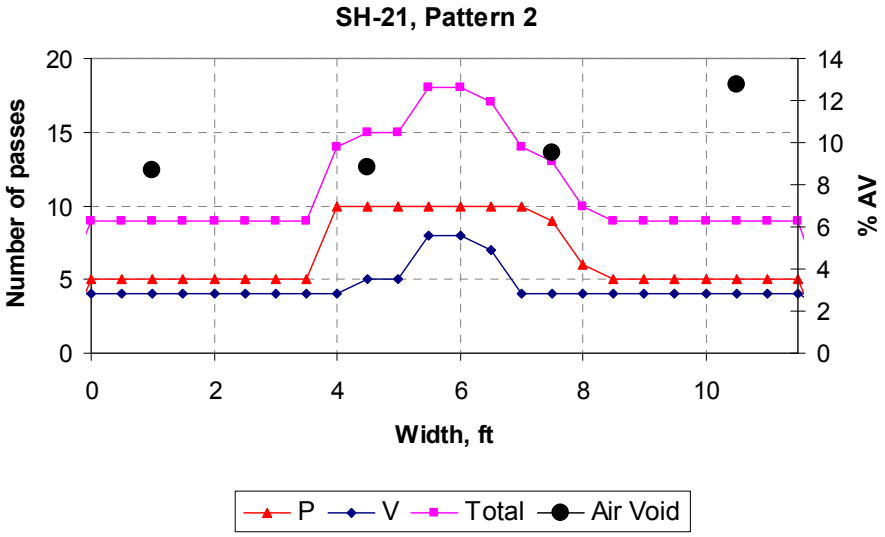

Note: Breakdown roller: pneumatic (P), intermediate roller: vibratory (V), finish roller: static (S). The static rollers were applied after the mat cooled down and not included herein.

Figure A-6. Number of Passes and the Percent of Air Voids across the Mat in SH-21 Test Section (Pattern 2).

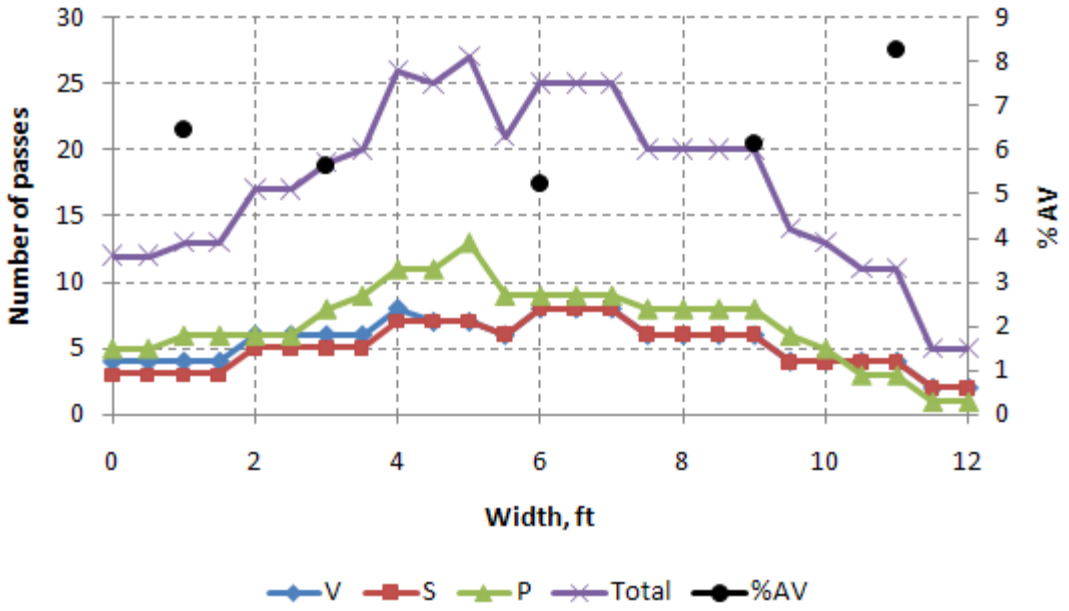

Note: Breakdown roller: vibratory (V), intermediate roller: static (S), finish roller: pneumatic (P).

Figure A-7. Number of Passes and the Percent of Air Voids across the Mat in SH-44 Test Section.

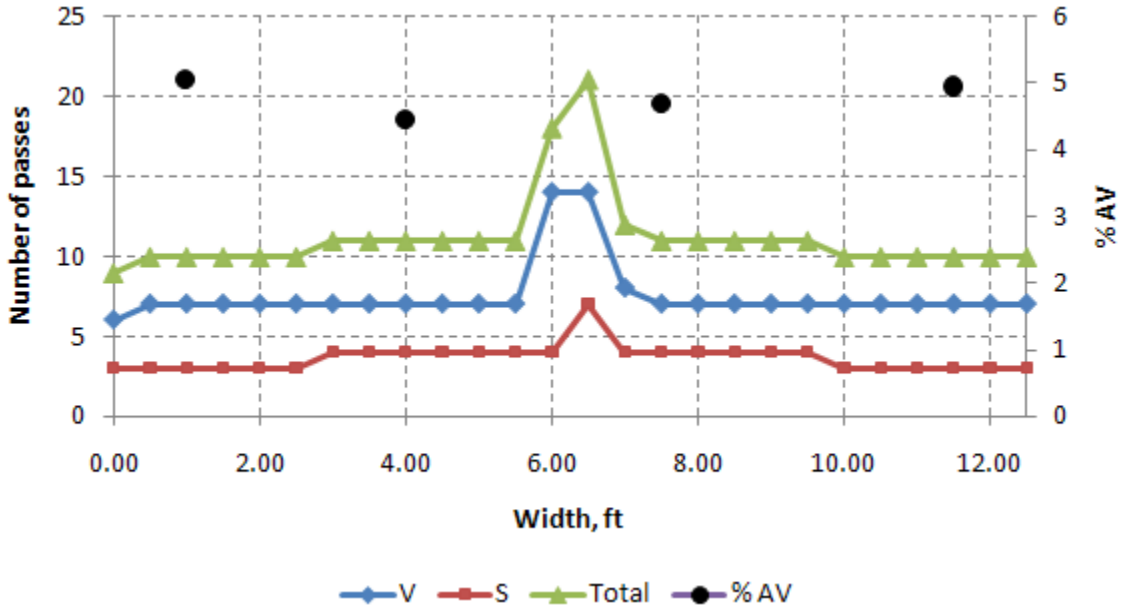

Note: Breakdown roller: vibratory (V), finish roller: static (S).

Figure A-8. Number of Passes and the Percent of Air Voids across the Mat in SL-1 Test Section.

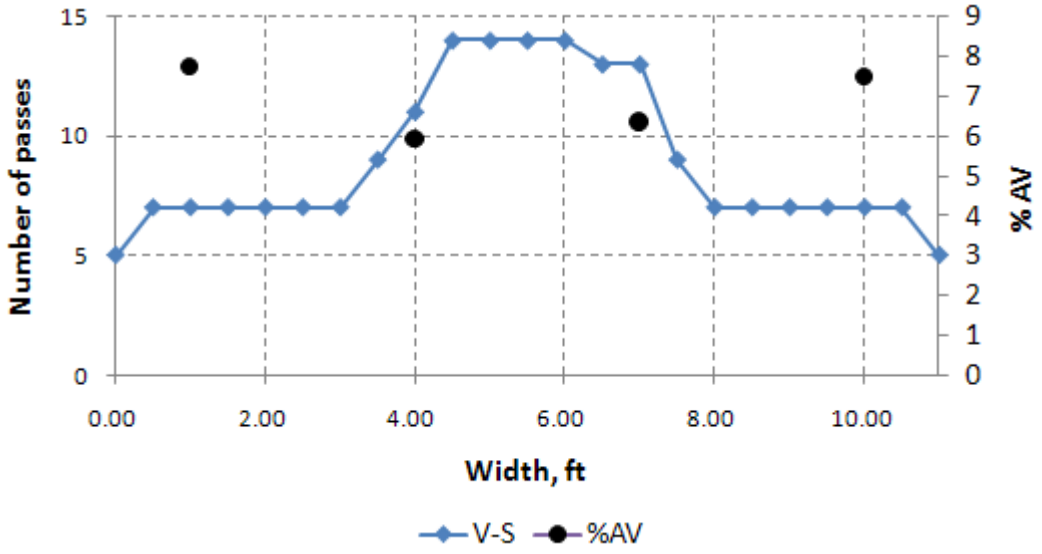

Note: Breakdown roller: vibratory and static (V-S), finish roller: static (S). The static roller was applied after the mat cooled down and not included herein.

Figure A-9. Number of Passes and the Percent of Air Voids across the Mat in SH-6 Test Section.

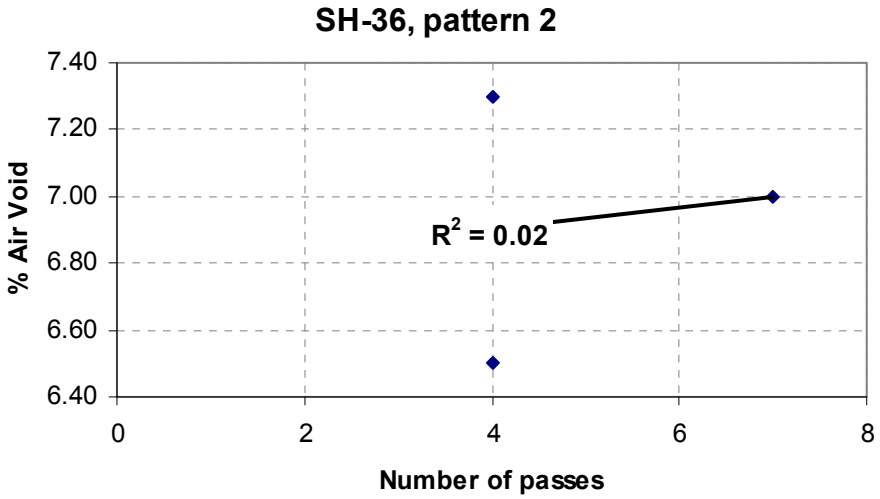

(a)

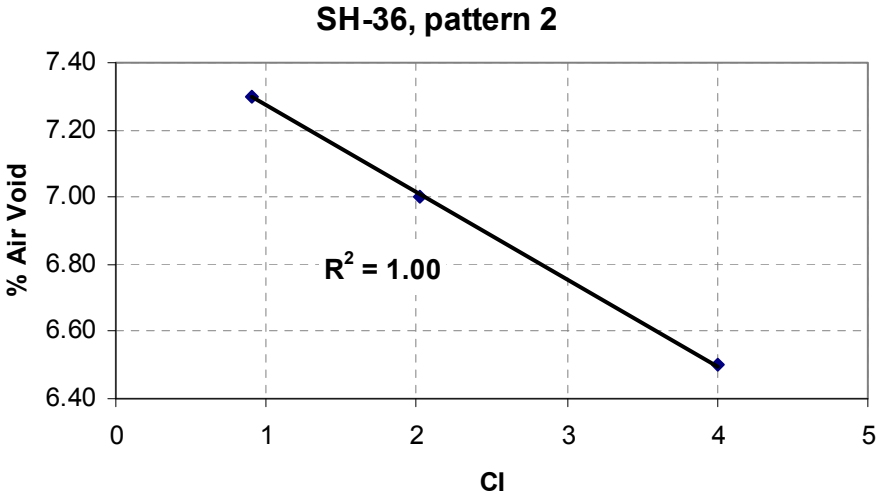

(b)

Figure A-10. (a) Number of Passes versus the Percent of Air Voids in SH-36 Test Section, (b) Compaction Index versus the Percent of Air Voids in SH-36 Test Section.

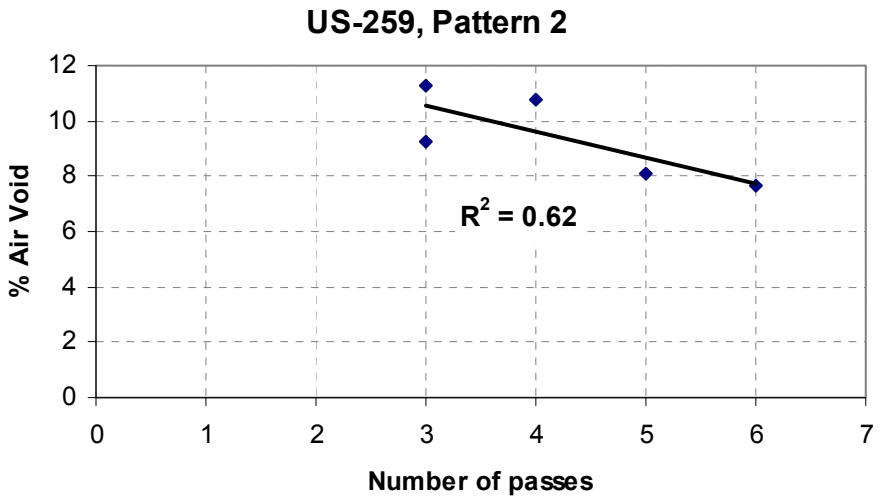

(a)

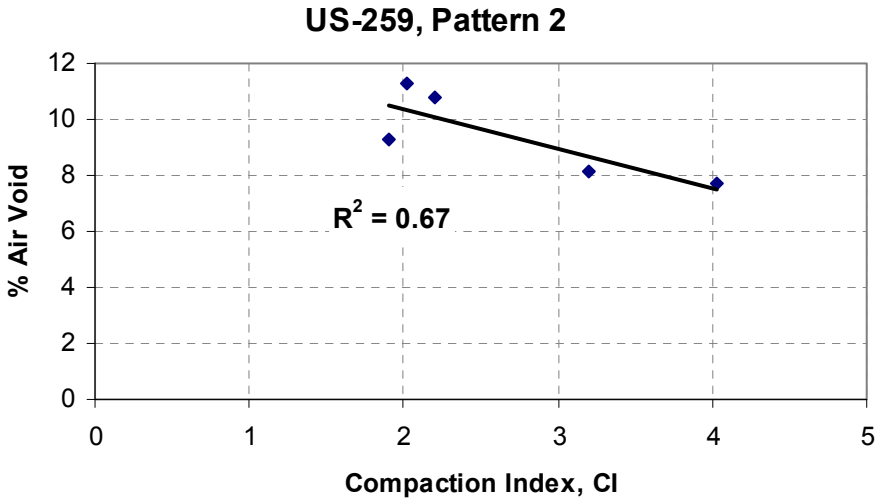

(b)

Figure A-11. (a) Number of Passes versus the Percent of Air Voids in US-259 Test Section, (b) Compaction Index versus the Percent of Air Voids in US-259 Test Section.

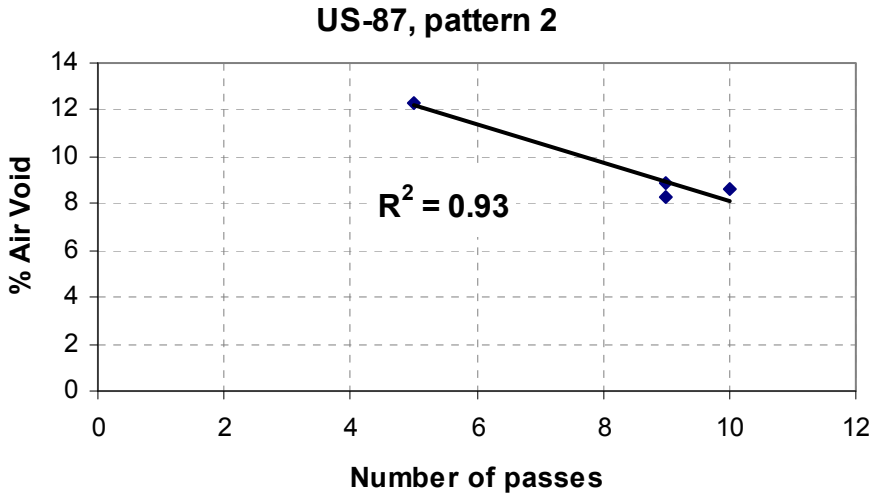

(a)

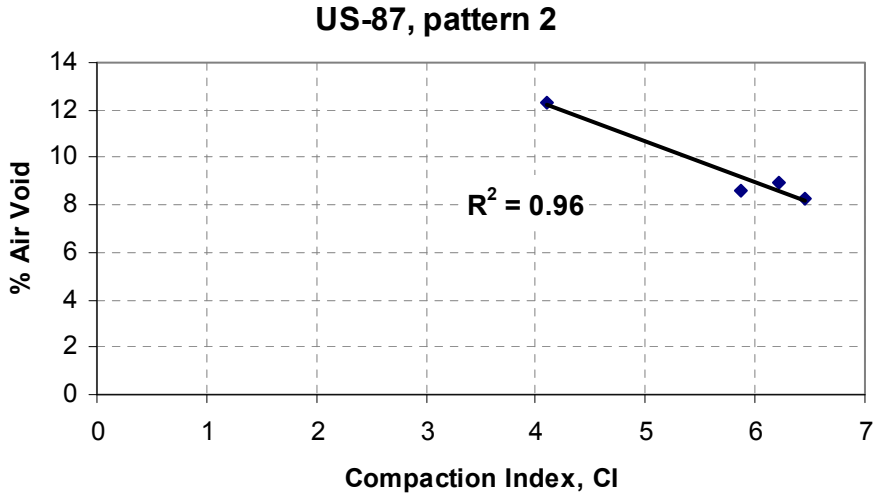

(b)

Figure A-12. (a) Number of Passes versus the Percent of Air Voids in US-87 Test Section, (b) Compaction Index versus the Percent of Air Voids in US-87 Test Section.

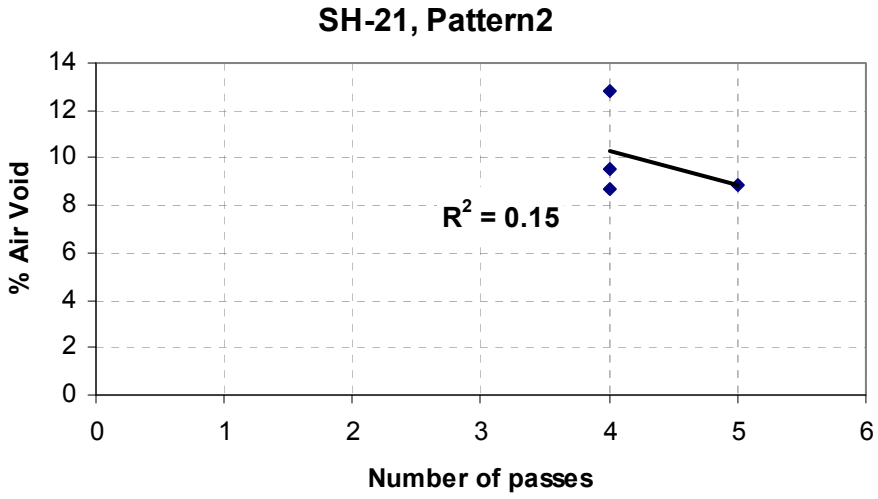

(a)

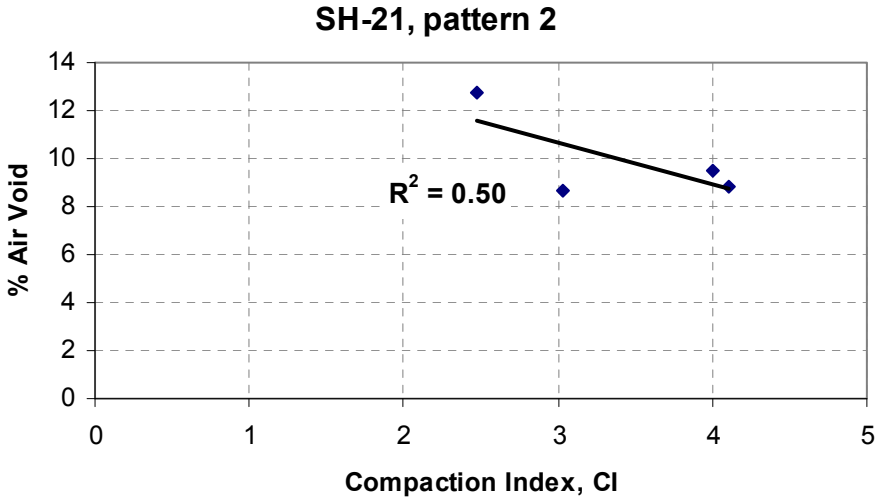

(b)

Figure A-13. (a) Number of Passes versus the Percent of Air Voids in SH-21 Test Section, (b) Compaction Index versus the Percent of Air Voids in SH-21 Test Section.

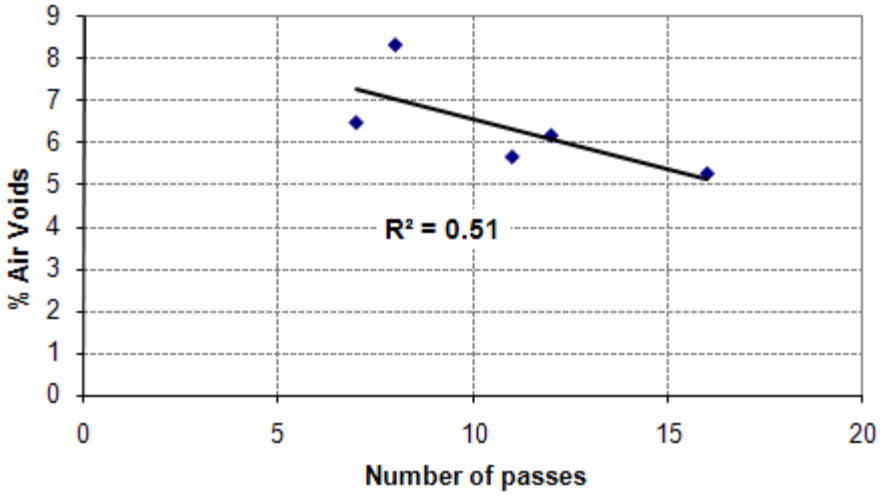

(a)

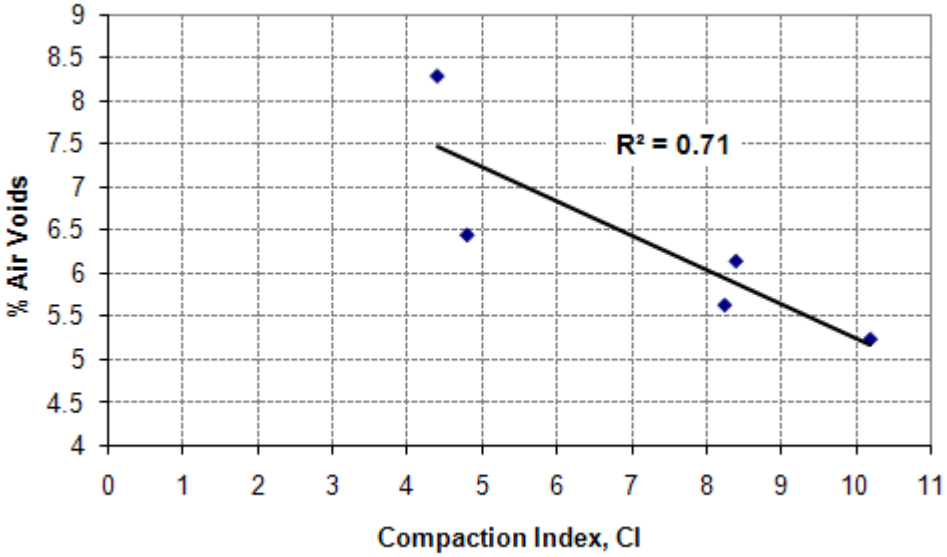

(b)

Figure A-14. (a) Number of Passes versus the Percent of Air Voids in SH-44 Test Section, (b) Compaction Index versus the Percent of Air Voids in SH-44 Test Section.

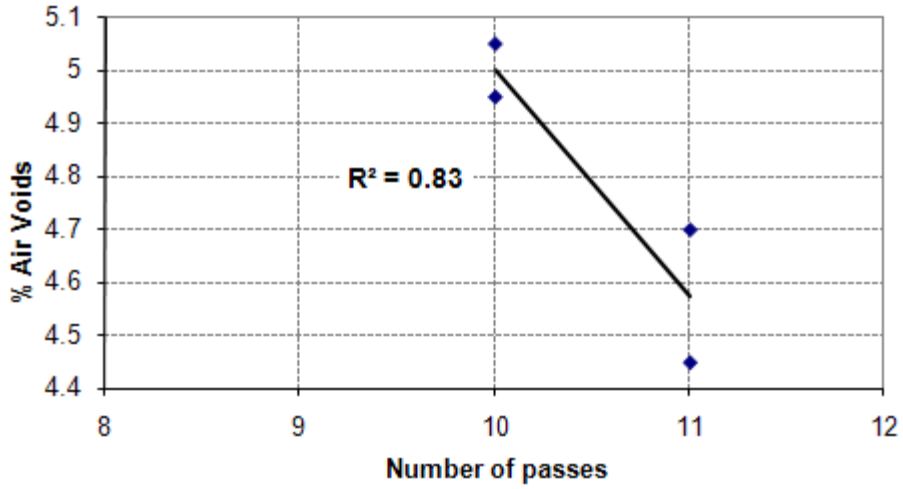

(a)

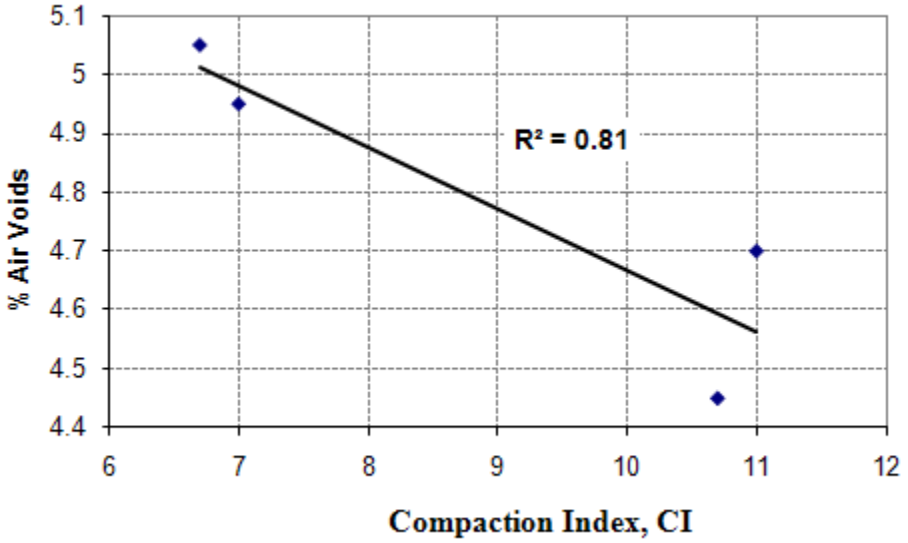

(b)

Figure A-15. (a) Number of Passes versus the Percent of Air Voids in SL-1 Test Section, (b) Compaction Index versus the Percent of Air Voids in SL-1 Test Section.

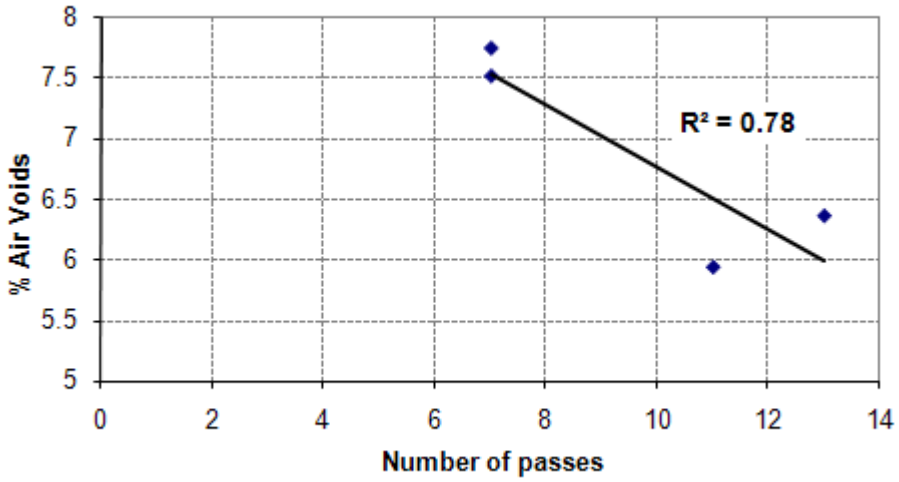

(a)

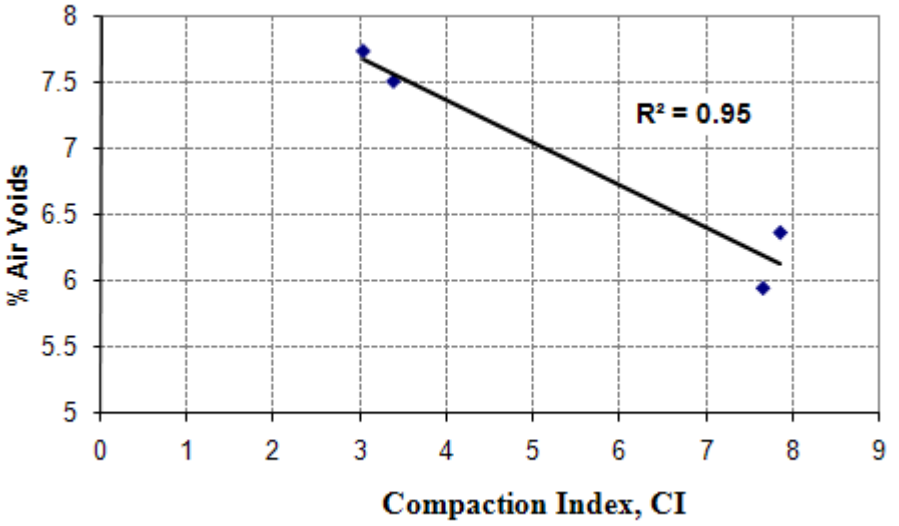

(b)

Figure A-16. (a) Number of Passes versus the Percent of Air Voids in SH-6 Test Section, (b) Compaction Index versus the Percent of Air Voids in SH-6 Test Section.

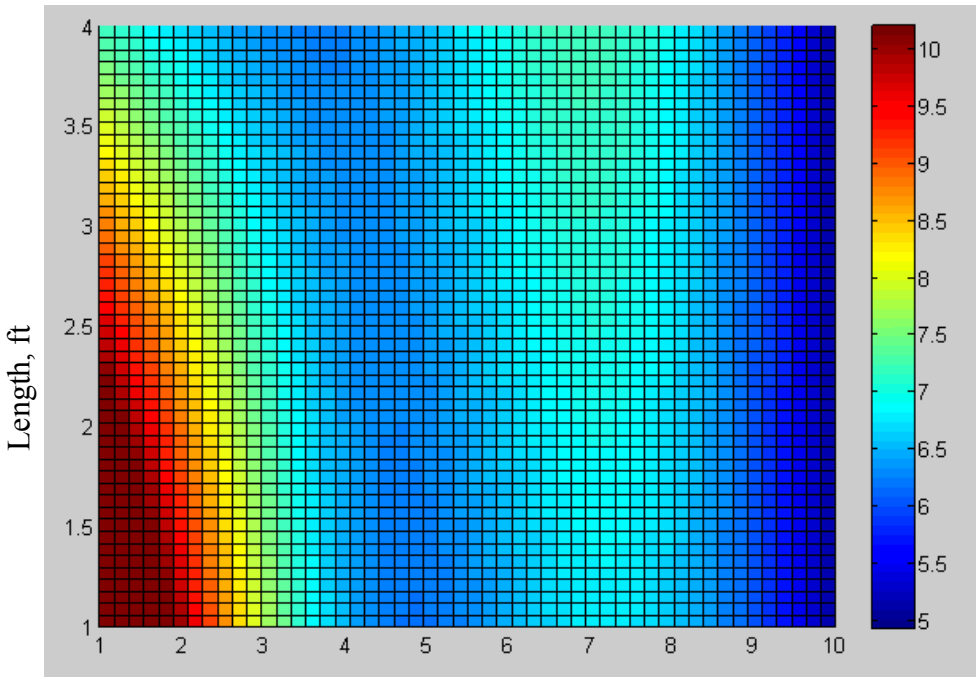

(a)

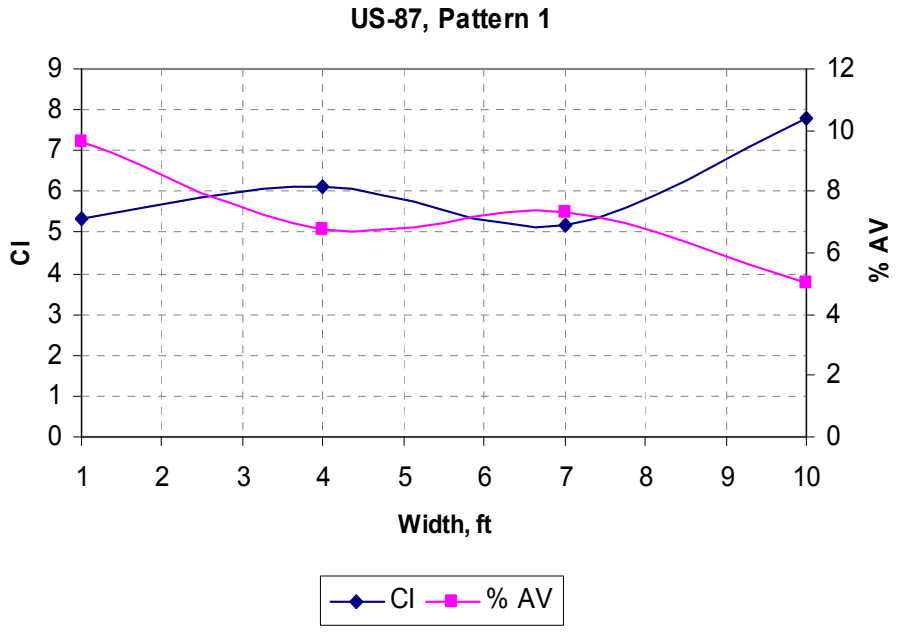

(b)

Note: The total width of the mat is 15 ft.

Figure A-17. (a) Air Void Distribution (%) across the Mat for US-87 Test Section Pattern 1, (b) The CI and Average Percent of Air Voids across the Mat for US-87 Test Section Pattern 1.

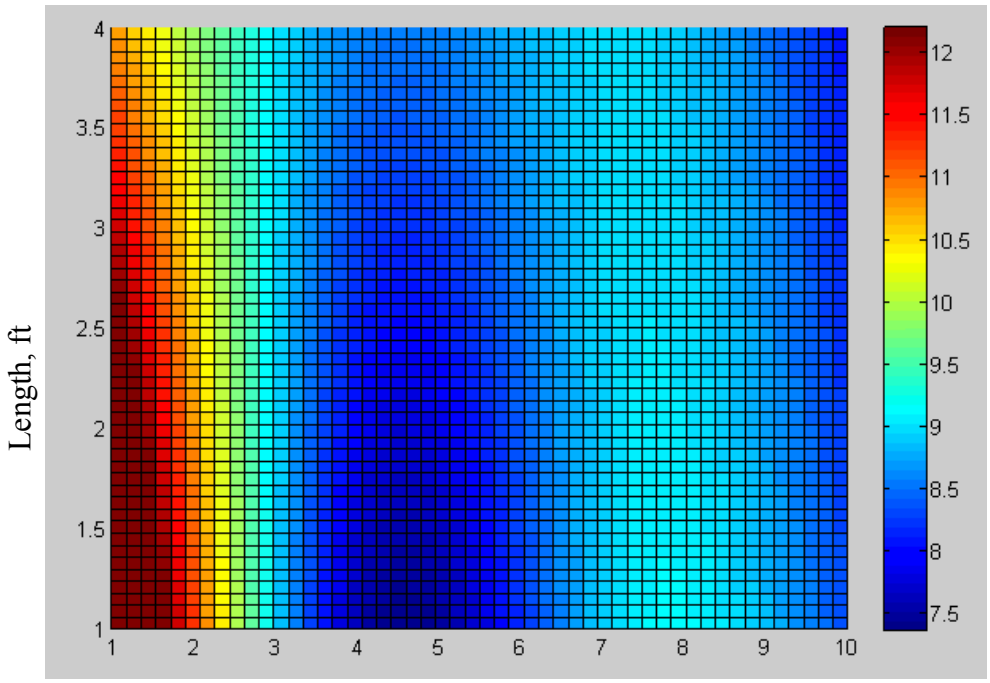

(a)

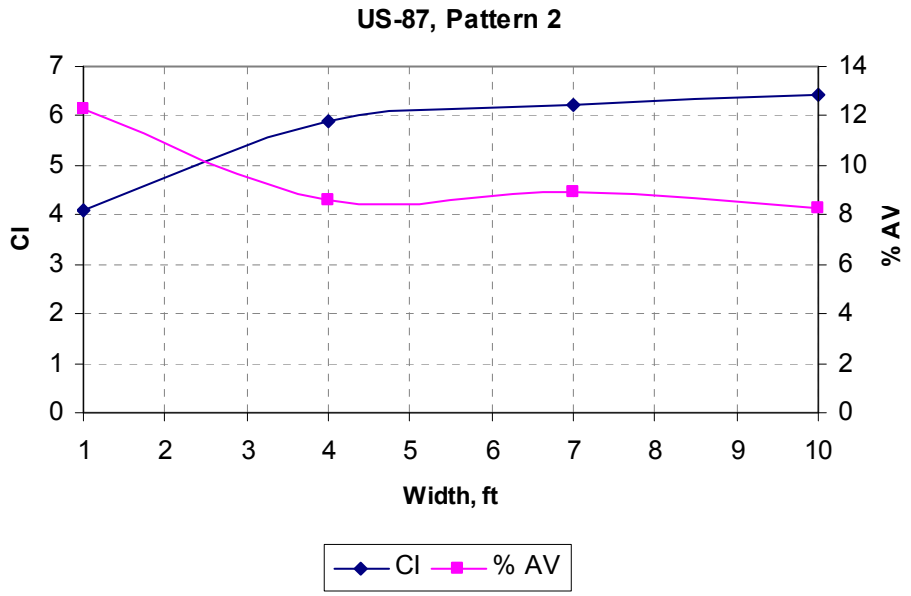

(b)

Note: The total width of the mat is 14.5 ft.

Figure A-18. (a) Air Void Distribution (%) across the Mat for US-87 Test Section Pattern 2, (b) The CI and Average Percent of Air Voids across the Mat for US-87 Test Section Pattern 2.

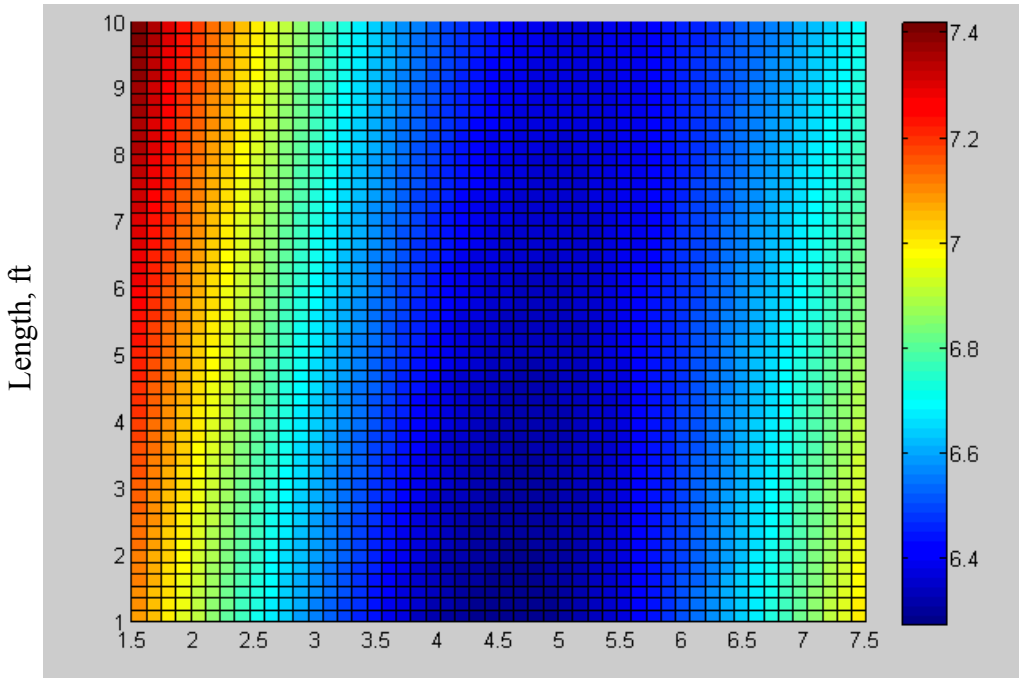

(a)

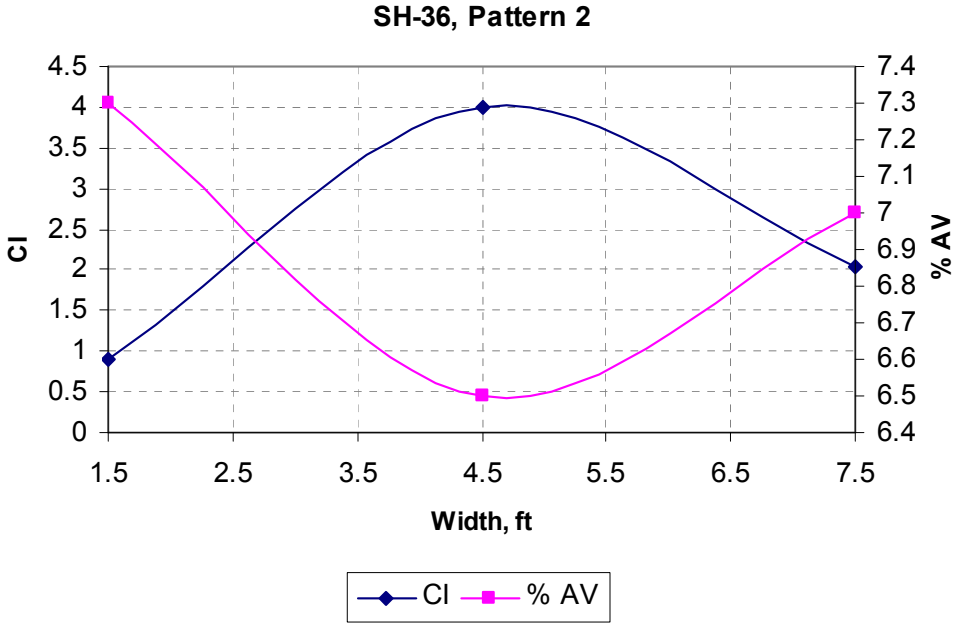

(b)

Note: The total width of the mat is 14 ft.

Figure A-19. (a) Air Void Distribution (%) across the Mat for SH-36 Test Section Pattern 2 (b) The CI and Average Percent of Air Voids across the Mat for SH-36 Test Section Pattern 2.

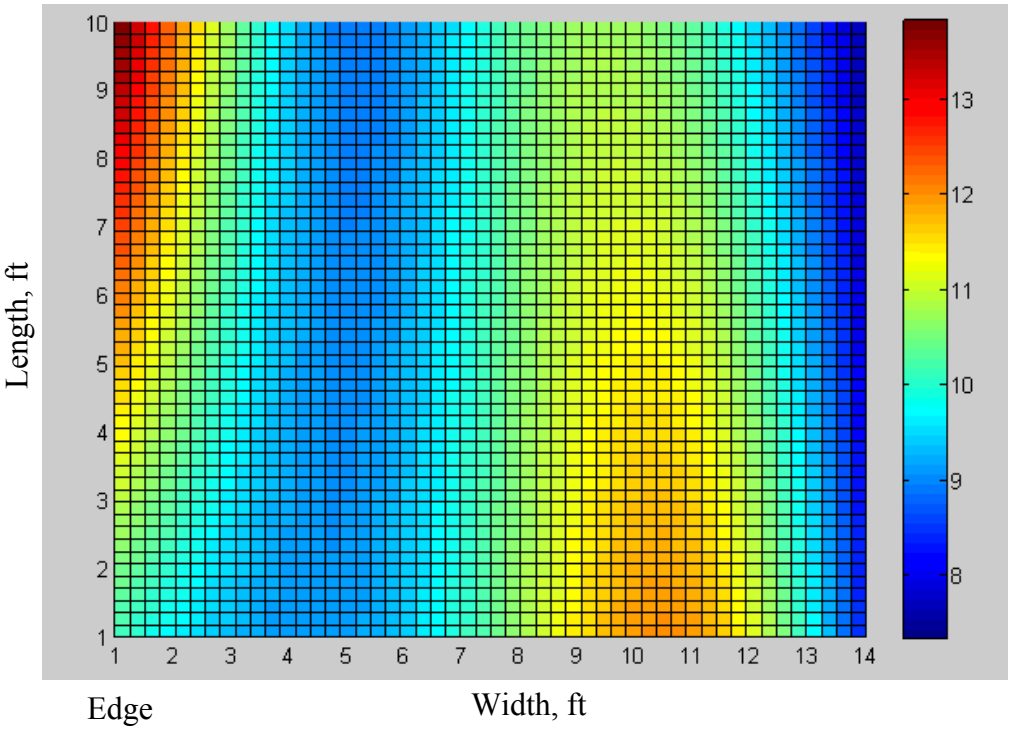

(a)

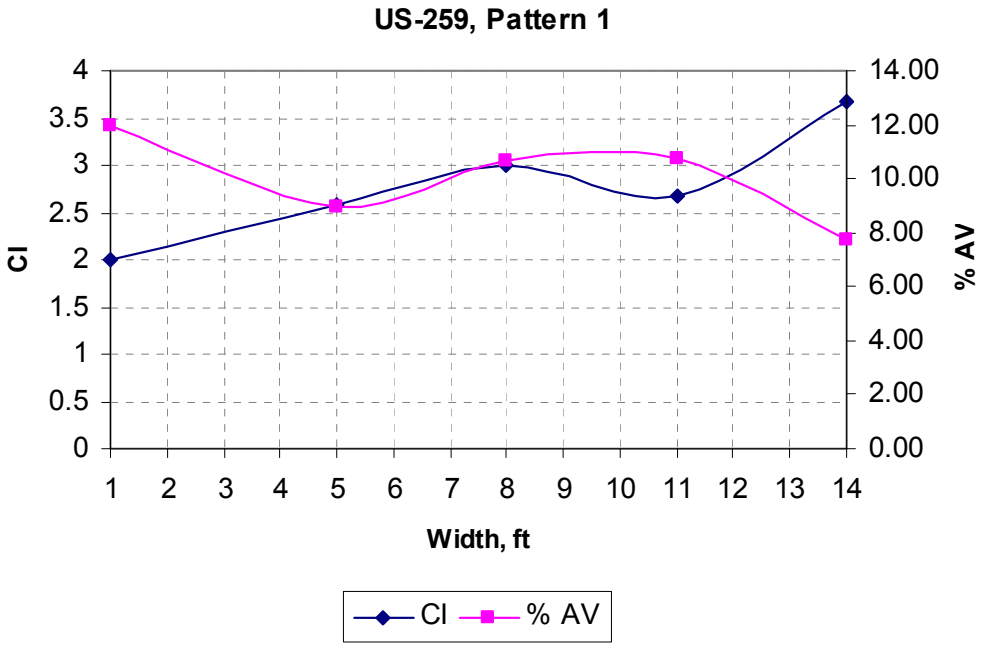

(b)

Note: The total width of the mat is 15 ft.

Figure A-20. (a) Air Void Distribution (%) across the Mat for US-259 Test Section Pattern 1 (b) The CI and Average Percent of Air Voids across the Mat for US-259 Test Section Pattern 1.

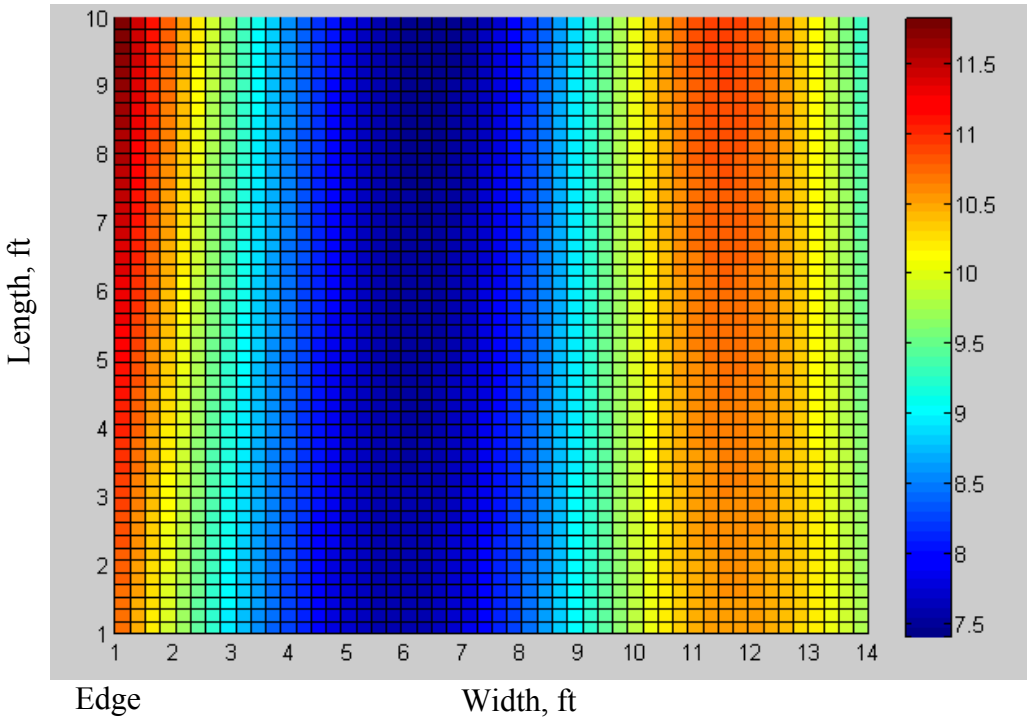

(a)

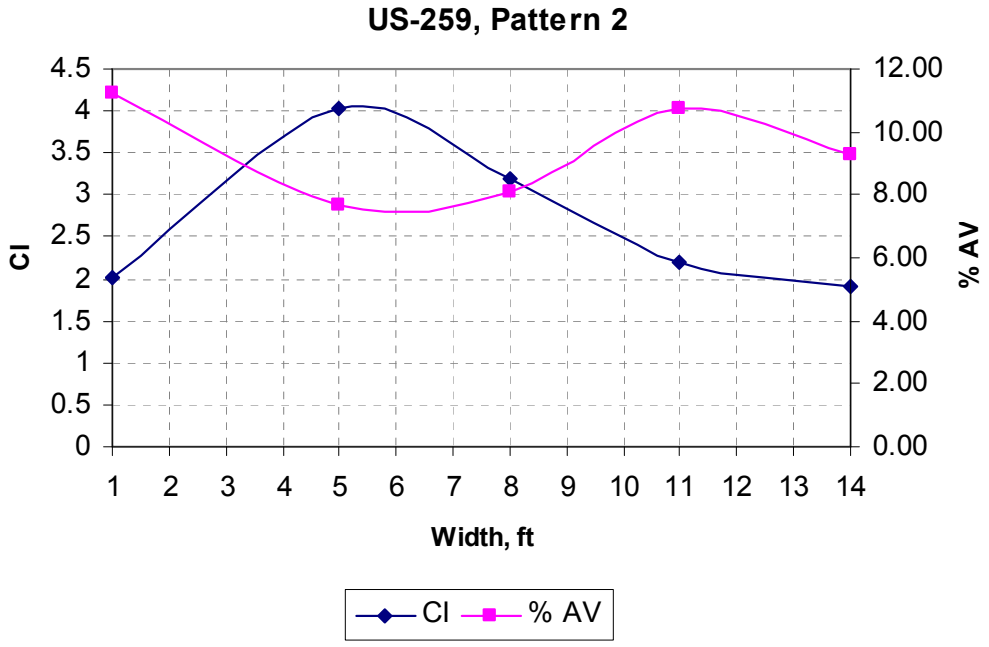

(b)

Note: The total width of the mat is 15 ft.

Figure A-21. (a) Air Void Distribution (%) across the Mat for US-259 Test Section Pattern 2 (b) The CI and Average Percent of Air Voids across the Mat for US-259 Test Section Pattern 2.

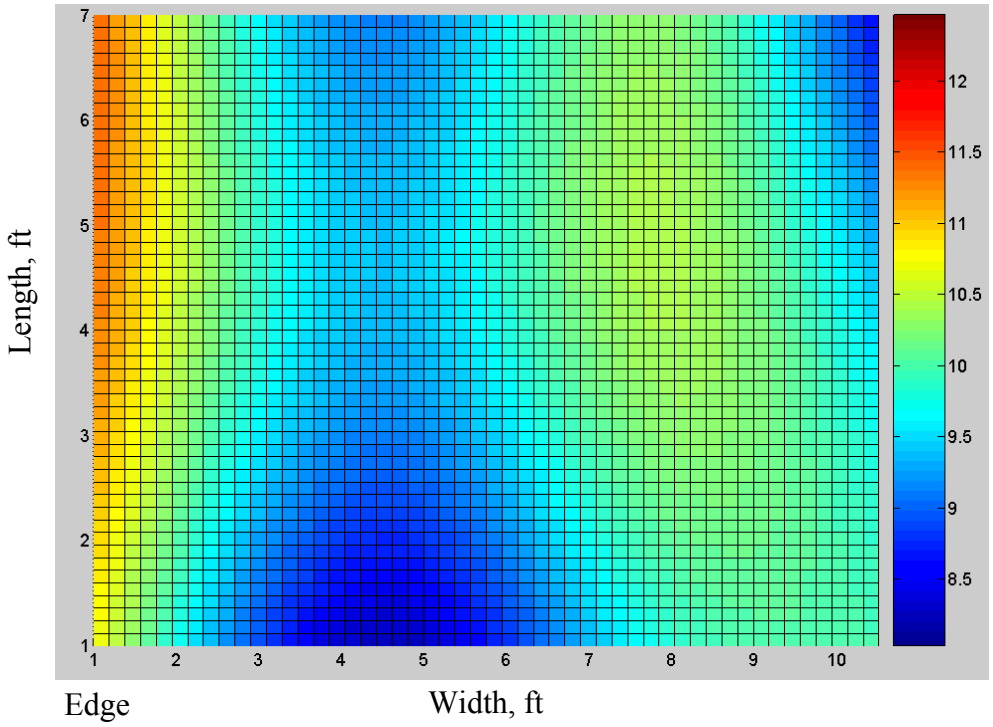

(a)

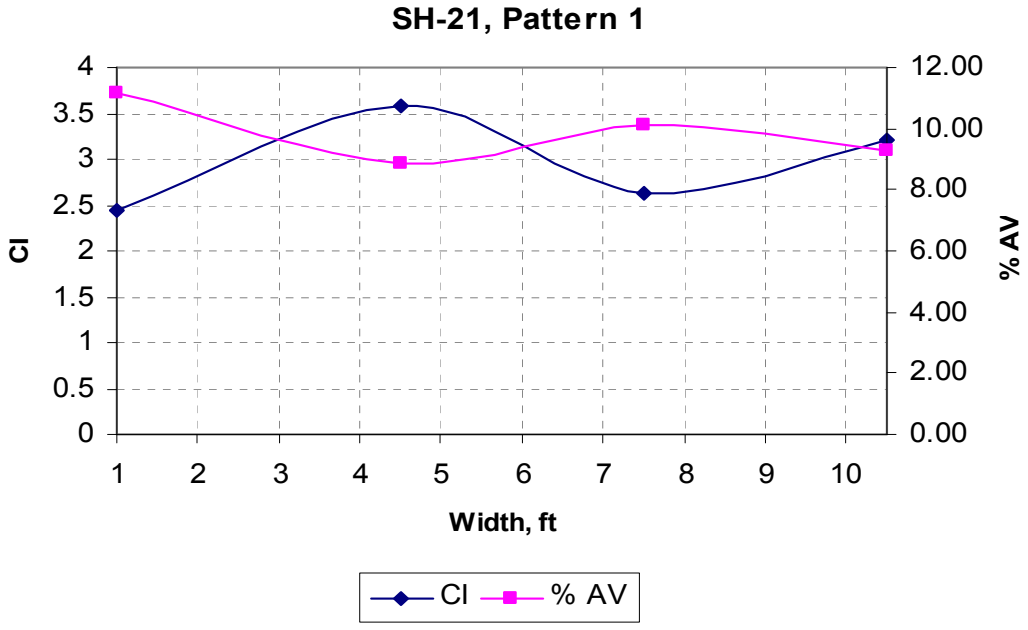

(b)

Note: The total width of the mat is 11.5 ft.

Figure A-22. (a) Air Void Distribution (%) across the Mat for SH-21 Test Section Pattern 1 (b) The CI and Average Percent of Air Voids across the Mat for SH-21 Test Section Pattern 1.

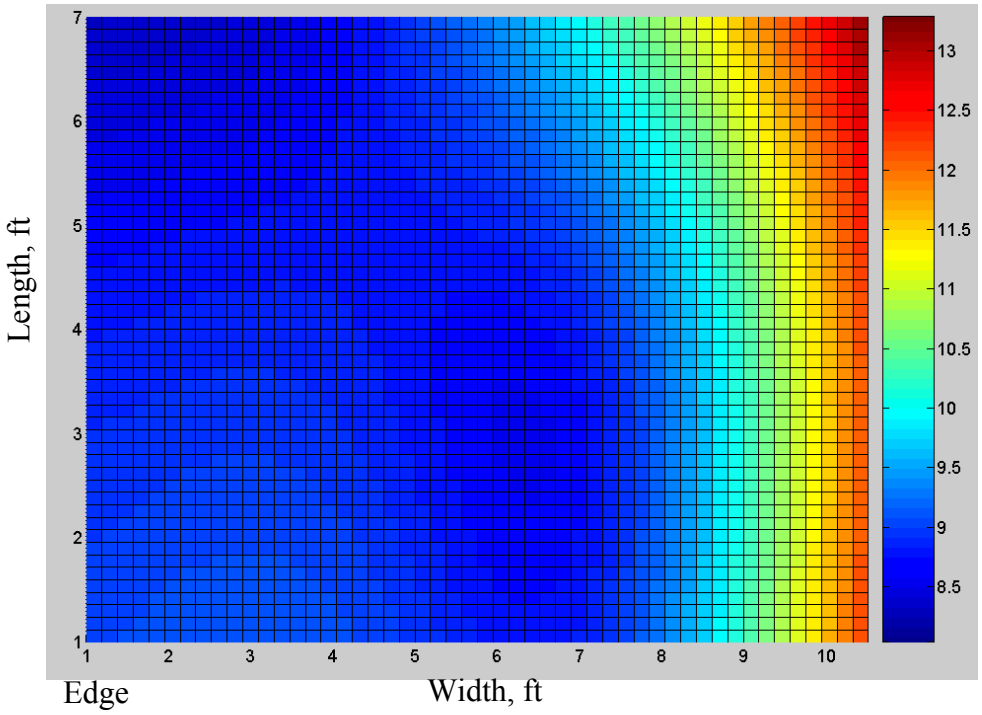

(a)

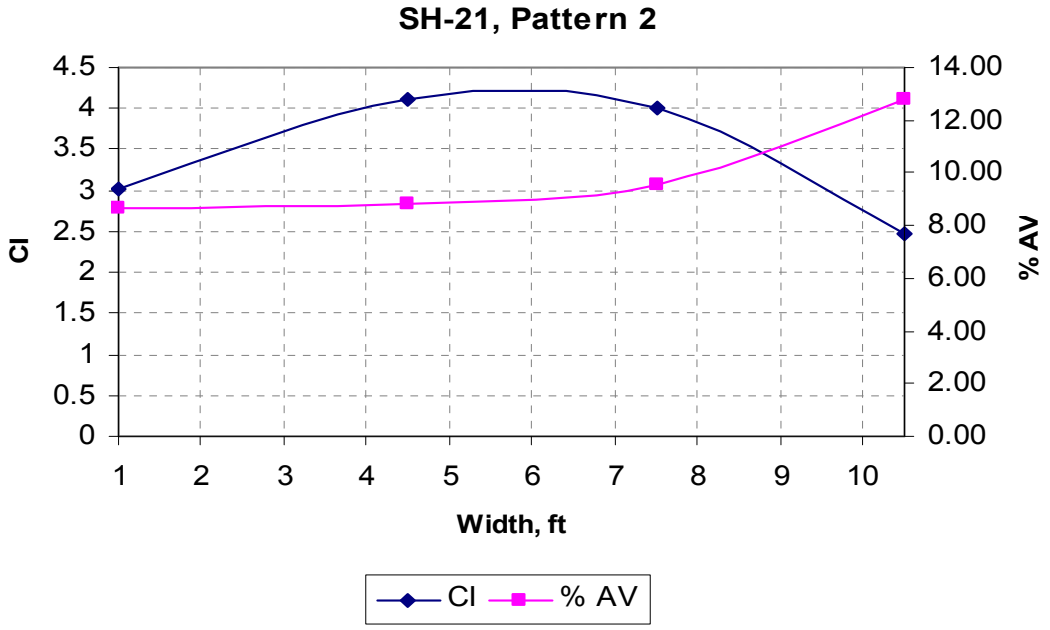

(b)

Note: The total width of the mat is 11.5 ft.

Figure A-23. (a) Air Void Distribution (%) across the Mat for SH-21 Test Section 2 (b) The CI and Average Percent of Air Voids across the Mat for SH-21 Test Section 2.

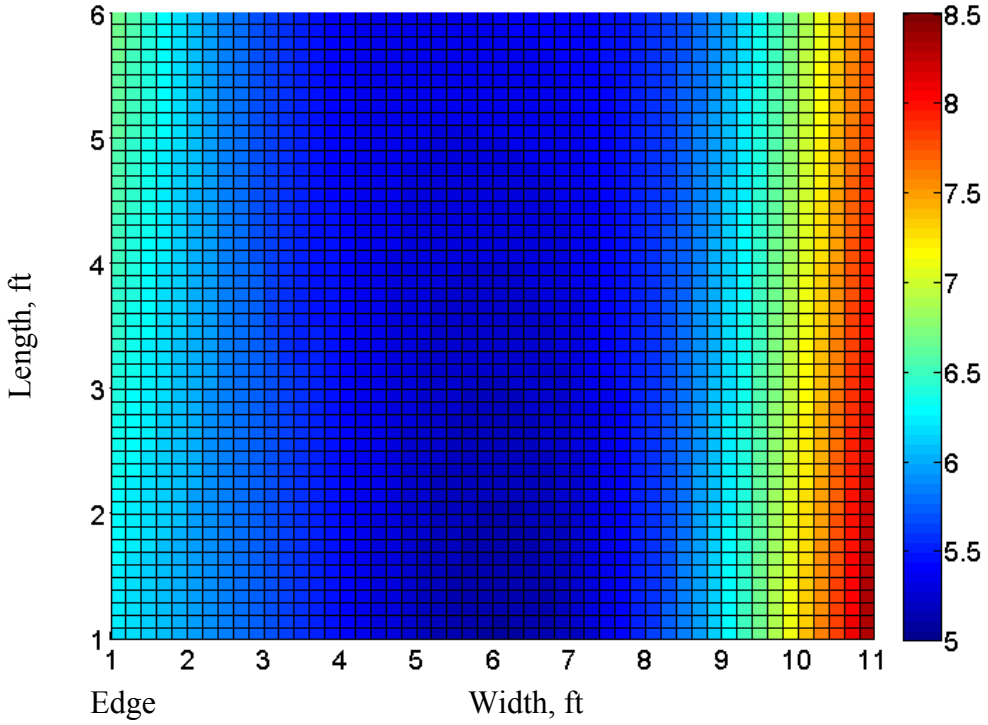

(a)

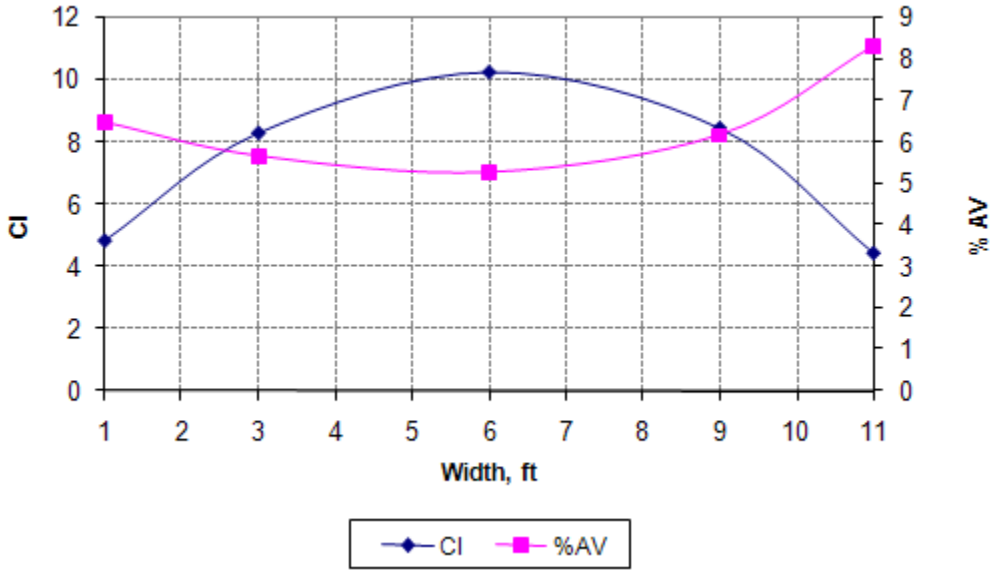

(b)

Note: The total width of the mat is 12.0 ft.

Figure A-24. (a) Air Void Distribution (%) across the Mat for SH-44 Test Section (b) The CI and Average Percent of Air Voids across the Mat for SH-44 Test Section.

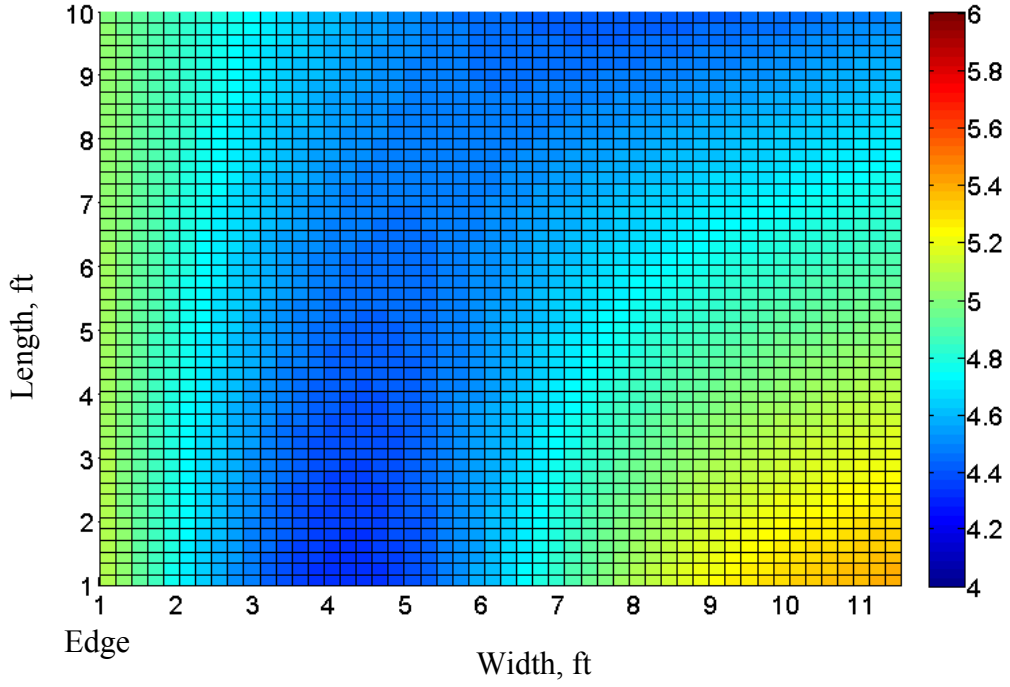

(a)

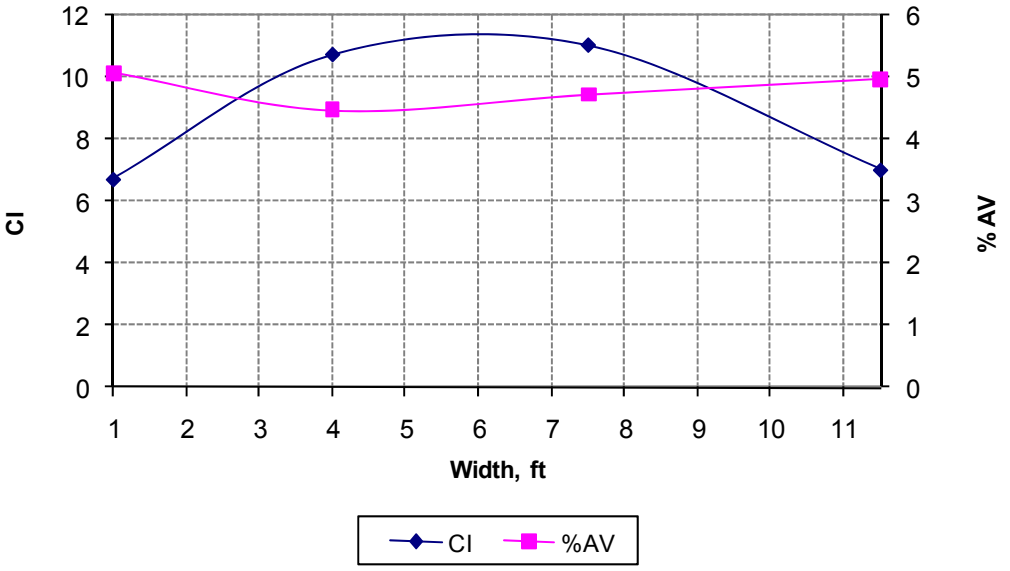

(b)

Note: The total width of the mat is 12.5 ft.

Figure A-25. (a) Air Void Distribution (%) across the Mat for SL 1 Test Section (b) The CI and Average Percent of Air Voids across the Mat for SL 1 Test Section.

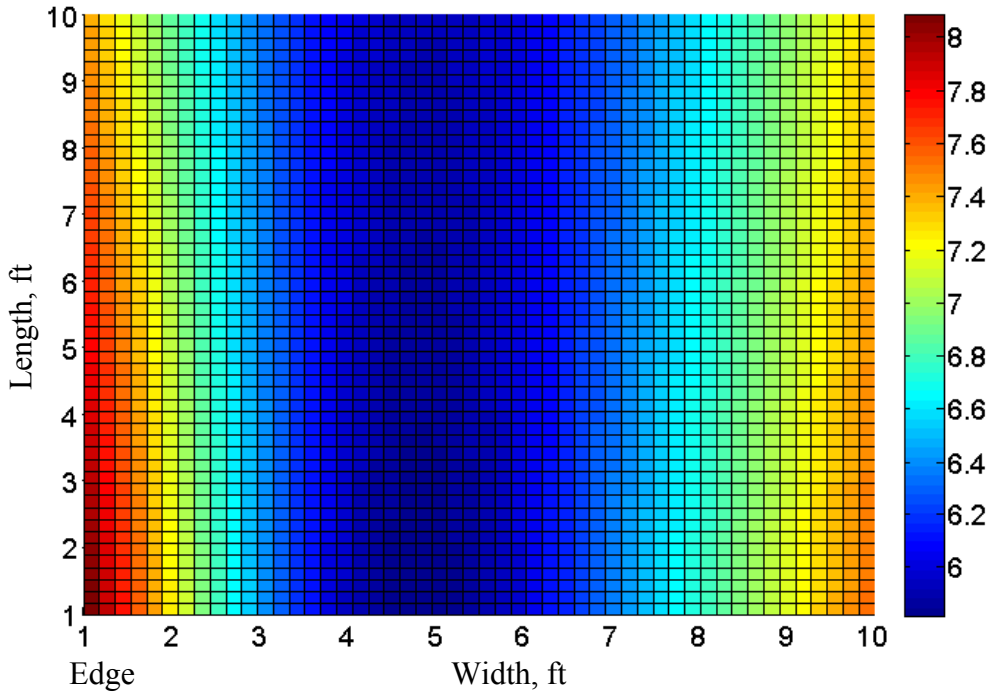

(a)

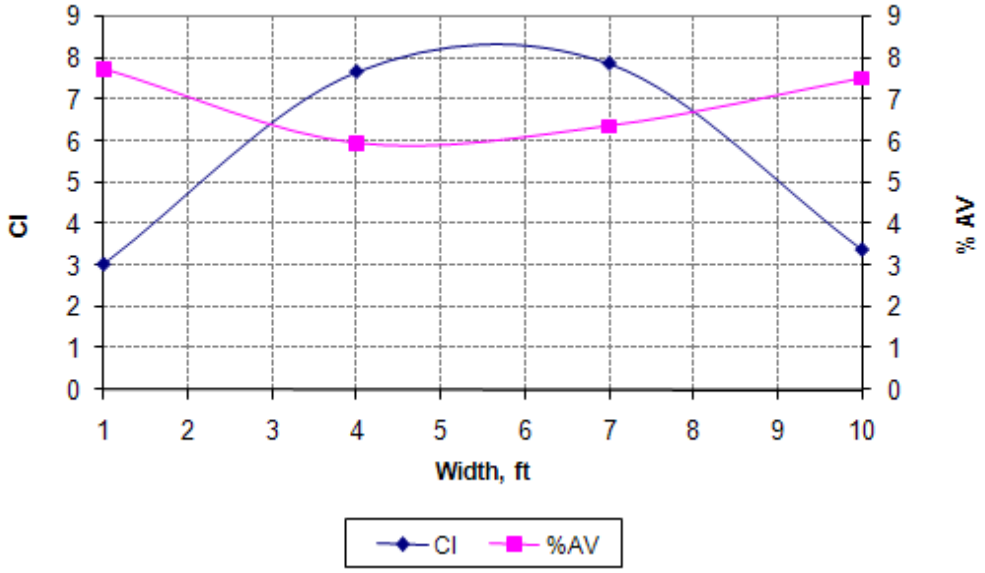

(b)

Note: The total width of the mat is 11 ft.

Figure A-26. (a) Air Void Distribution (%) across the Mat for SH-6 Test Section (b) The CI and Average Percent of Air Voids across the Mat for SH-6 Test Section.

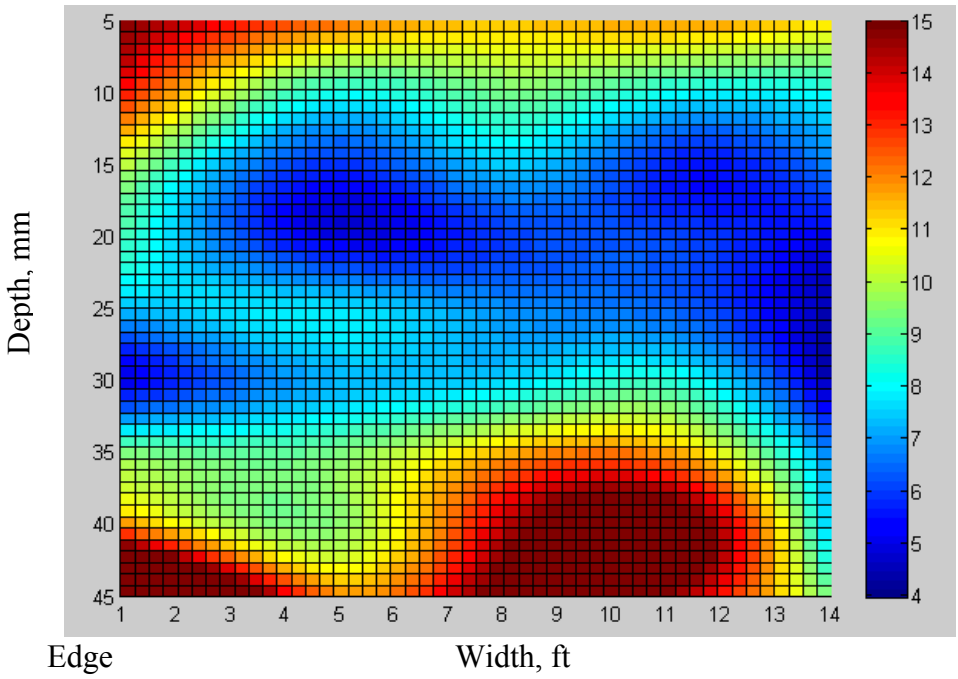

Note: The total width of the mat is 15 ft.

Figure A-27. Air Void Distribution (%) along the Depth of the Mat for US-259 Test Section (Pattern 1).

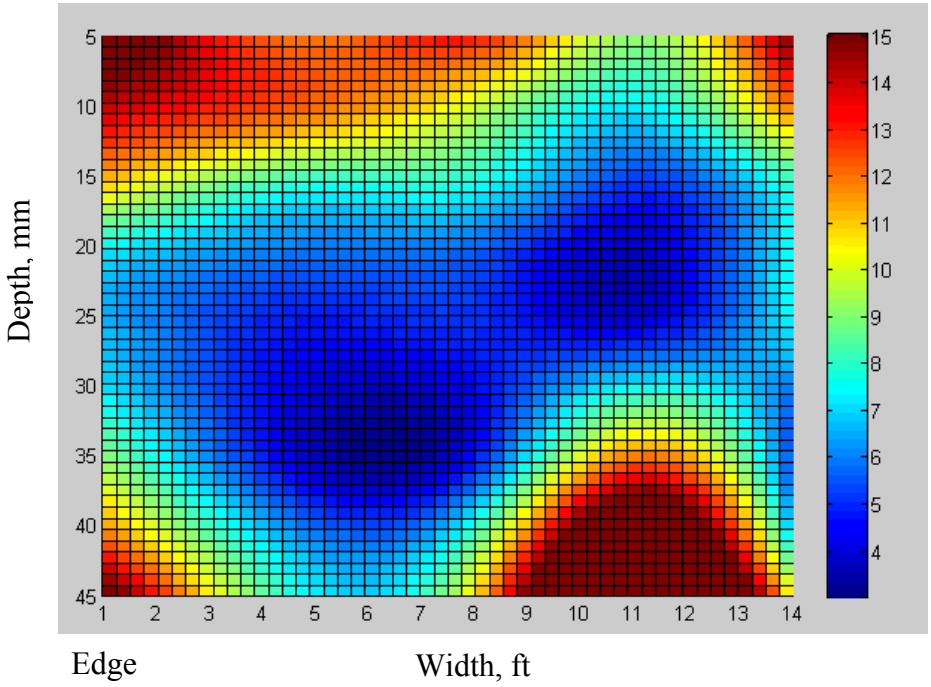

Note: The total width of the mat is 15 ft.

Figure A-28. Air Void Distribution (%) along the Depth of the Mat for US-259 Test Section (Pattern 2).

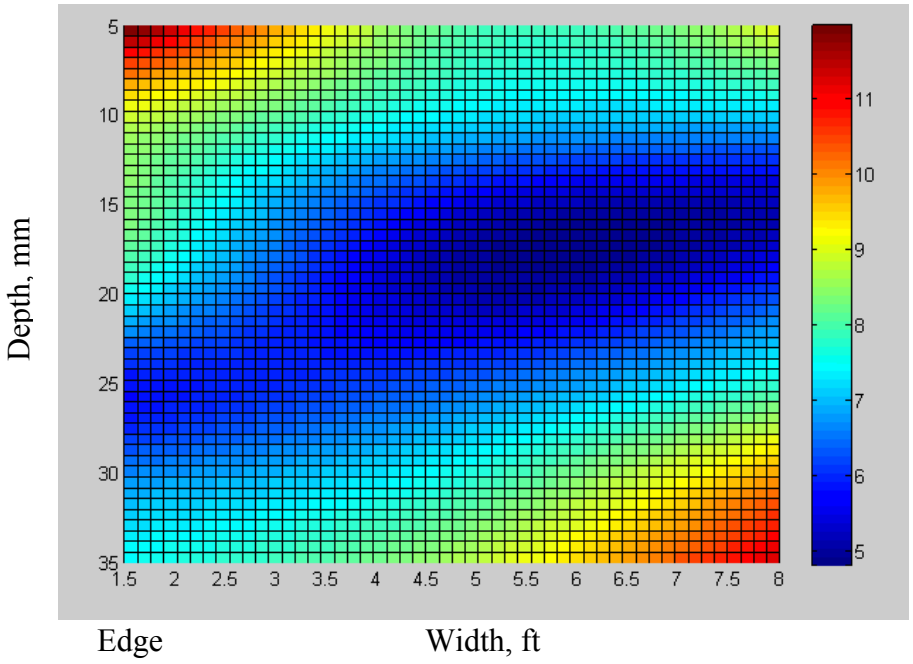

Note: The total width of the mat is 14 ft.

Figure A-29. Air Void Distribution (%) along the Depth of the Mat for SH-36 Test Section (Pattern 1).

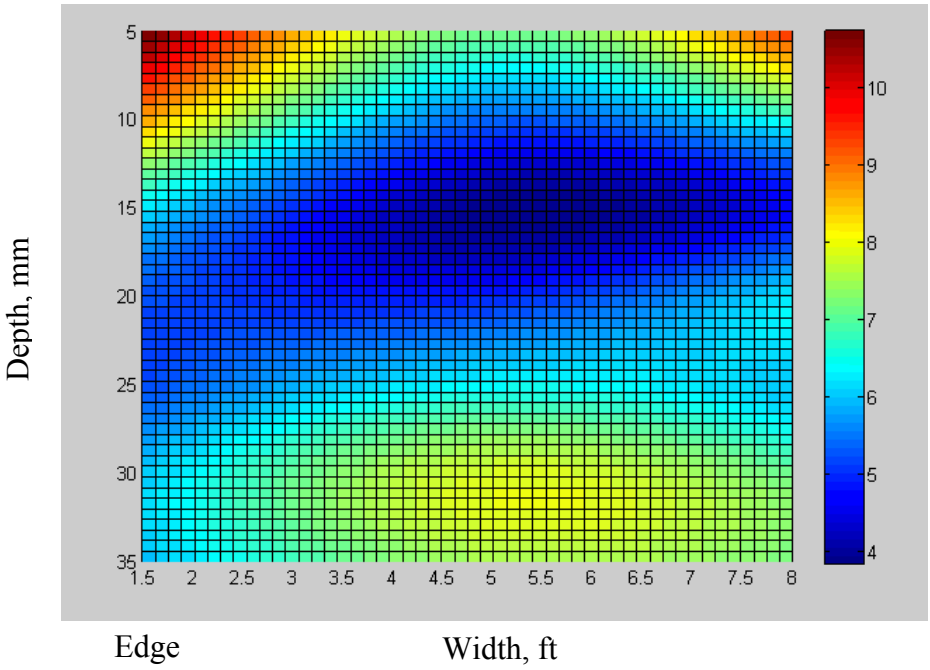

Note: the Total Width of the Mat is 14 ft.

Figure A-30. Air Void Distribution (%) along the Depth of the Mat for SH-36 Test Section (Pattern 2).

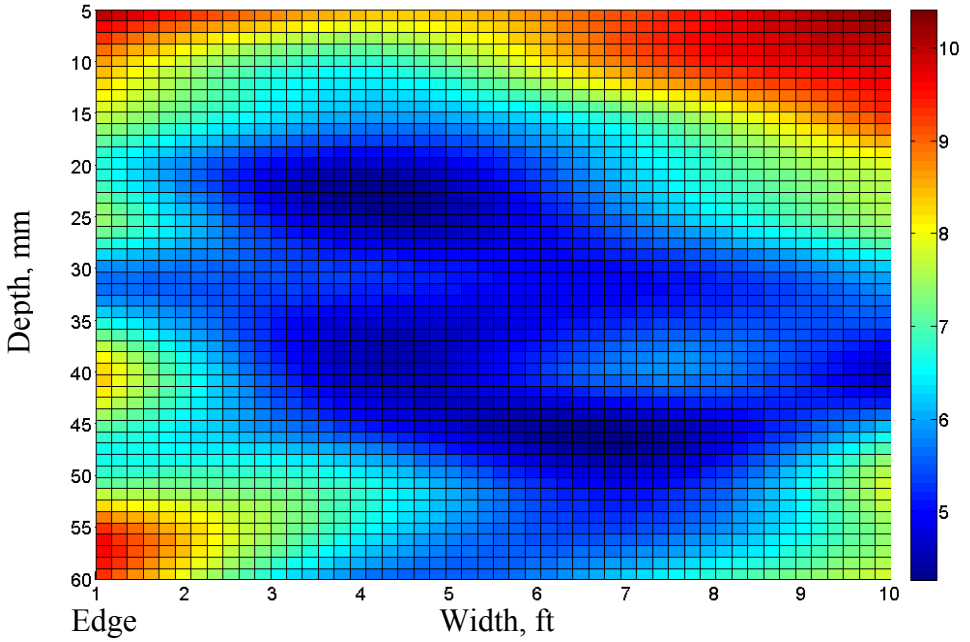

Note: the Total Width of the Mat is 11 ft.

Figure A-31. Air Void Distribution (%) along the Depth of the Mat for SH-6 Test Section.

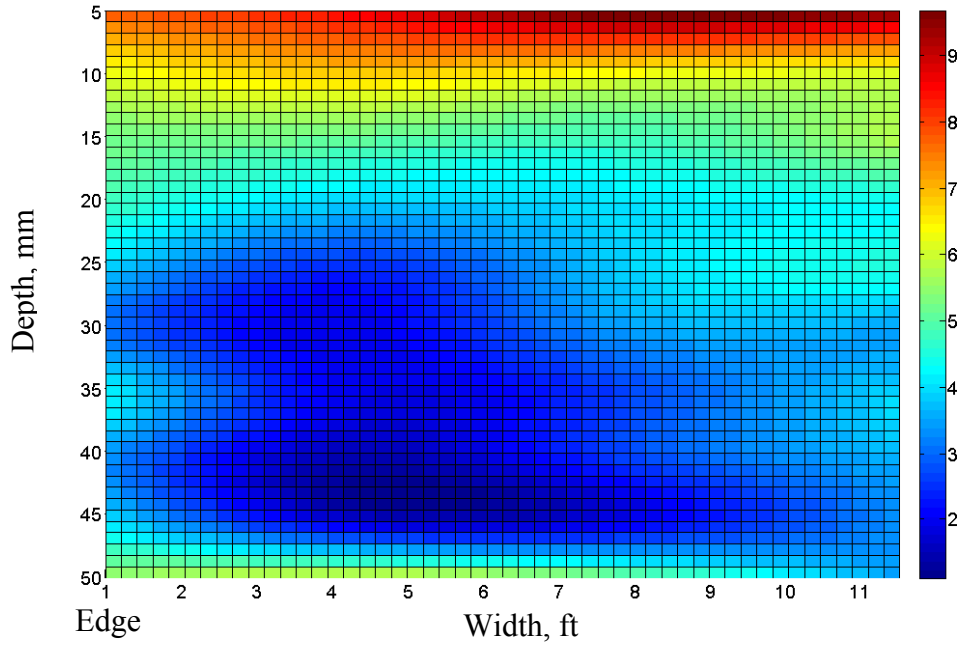

Note: the Total Width of the Mat is 12.5 ft.

Figure A-32. Air Void Distribution (%) along the Depth of the Mat for SL-1 Test Section.

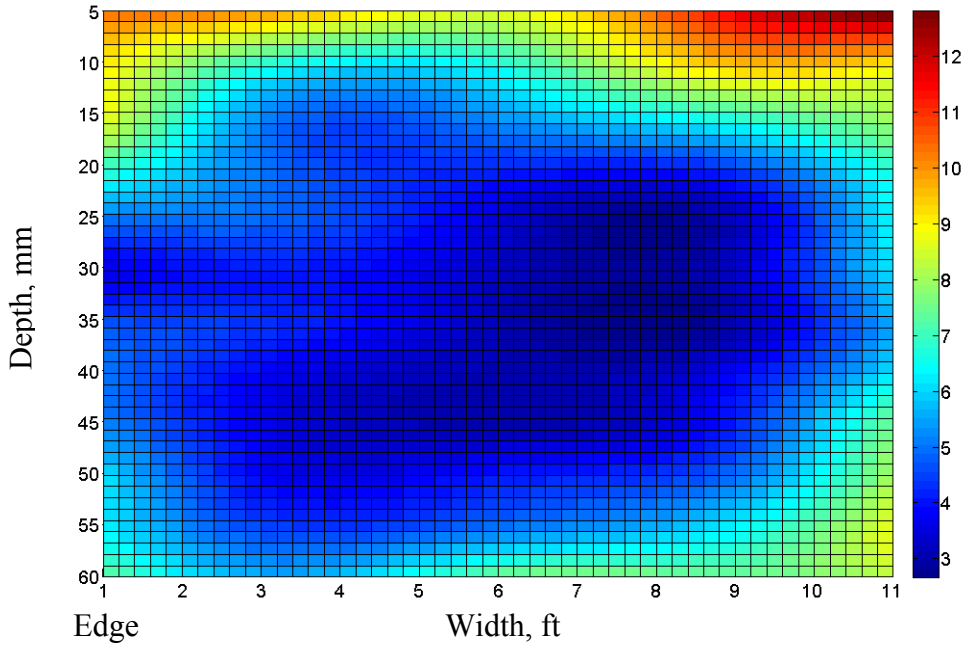

Note: the Total Width of the Mat is 12 ft.

Figure A-33. Air Void Distribution (%) along the Depth of the Mat for SH-44 Test Section.

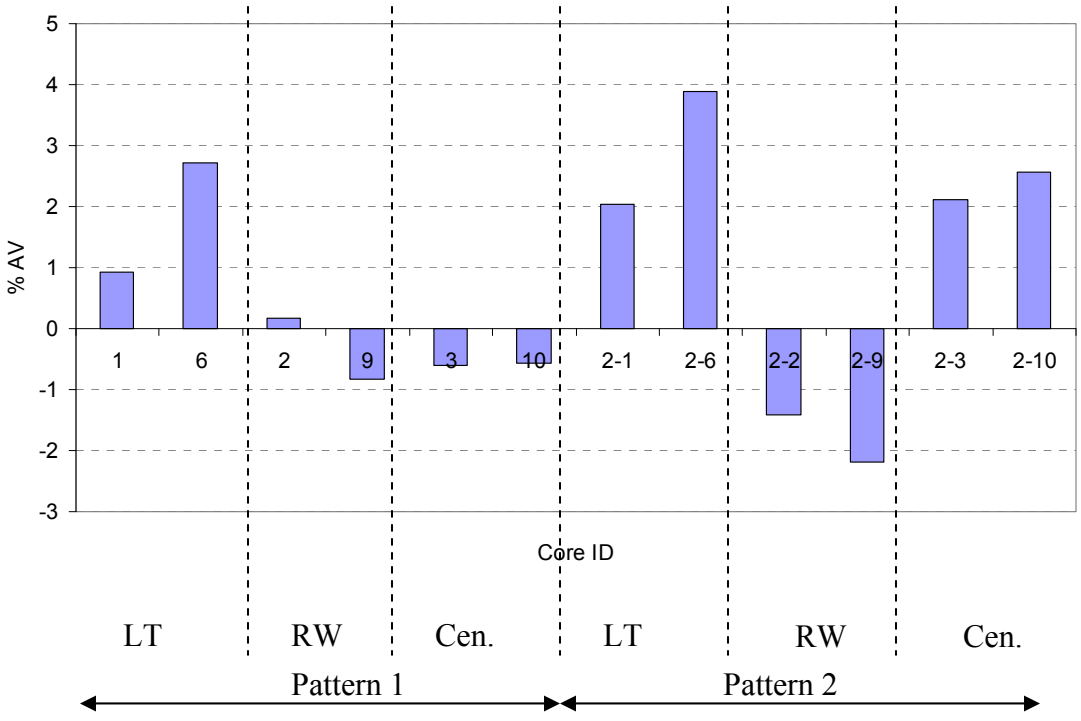

Figure A-34. Difference between the Percent of Air Voids at the Top and the Bottom Parts for SH-36 Test Section.

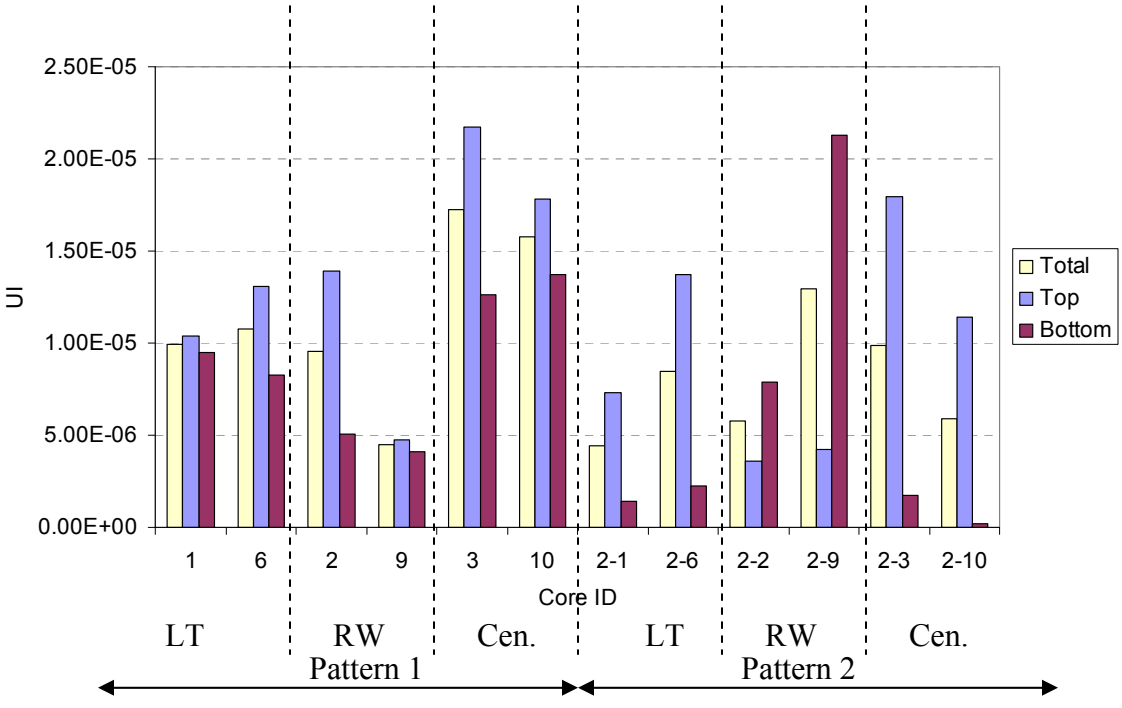

Figure A-35. UI for the SH-36 Test Section.

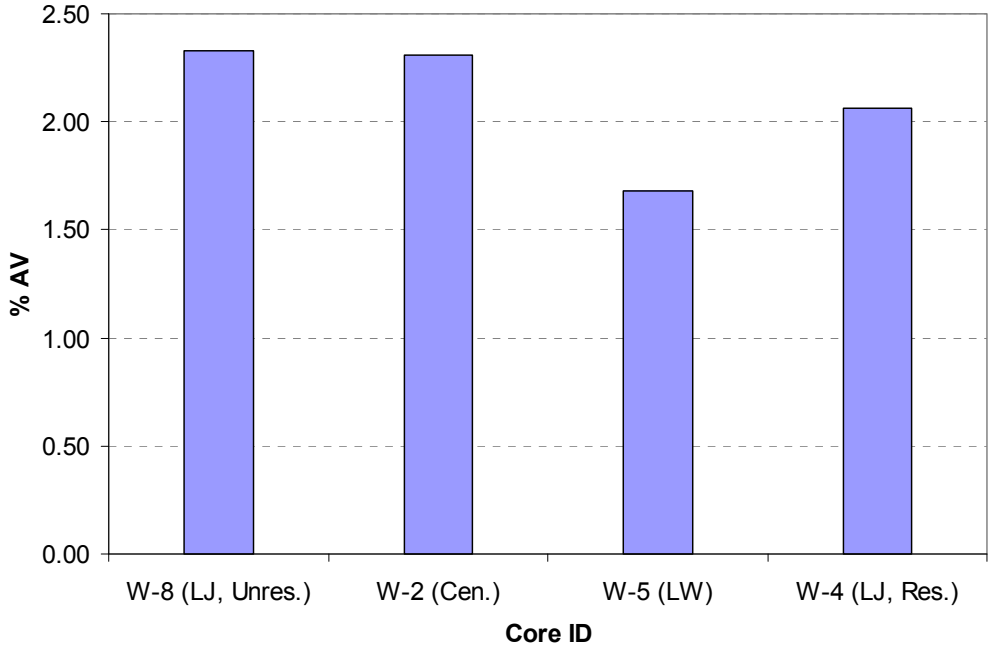

Figure A-36. Difference between the Percent of Air Voids at the Top and the Bottom Parts for IH-35 Test Section.

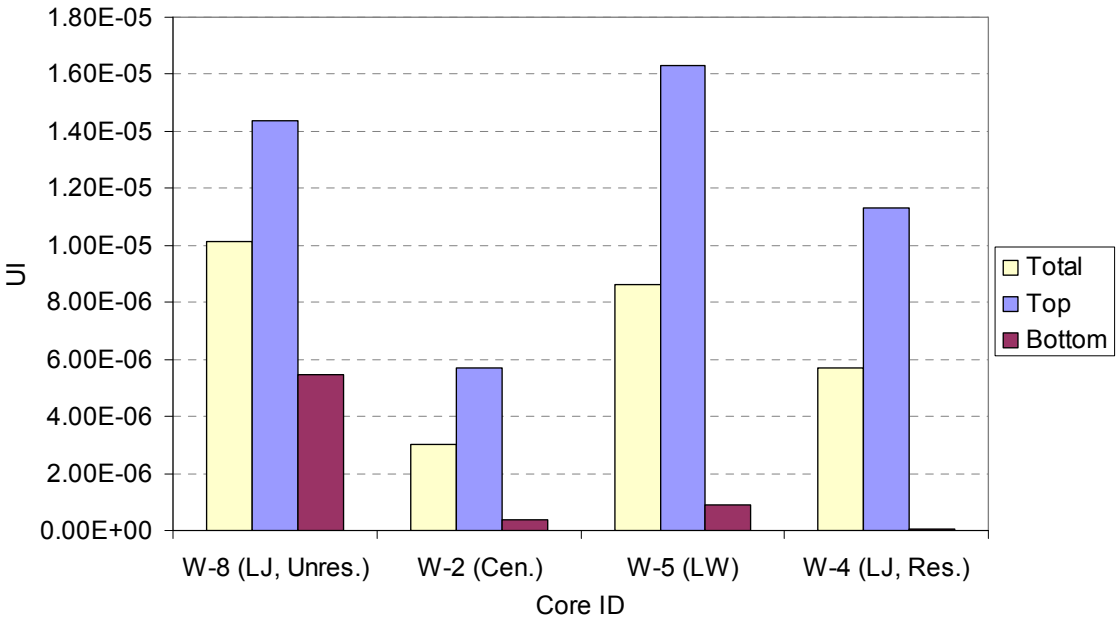

Figure A-37. UI for the IH-35 Test Section.

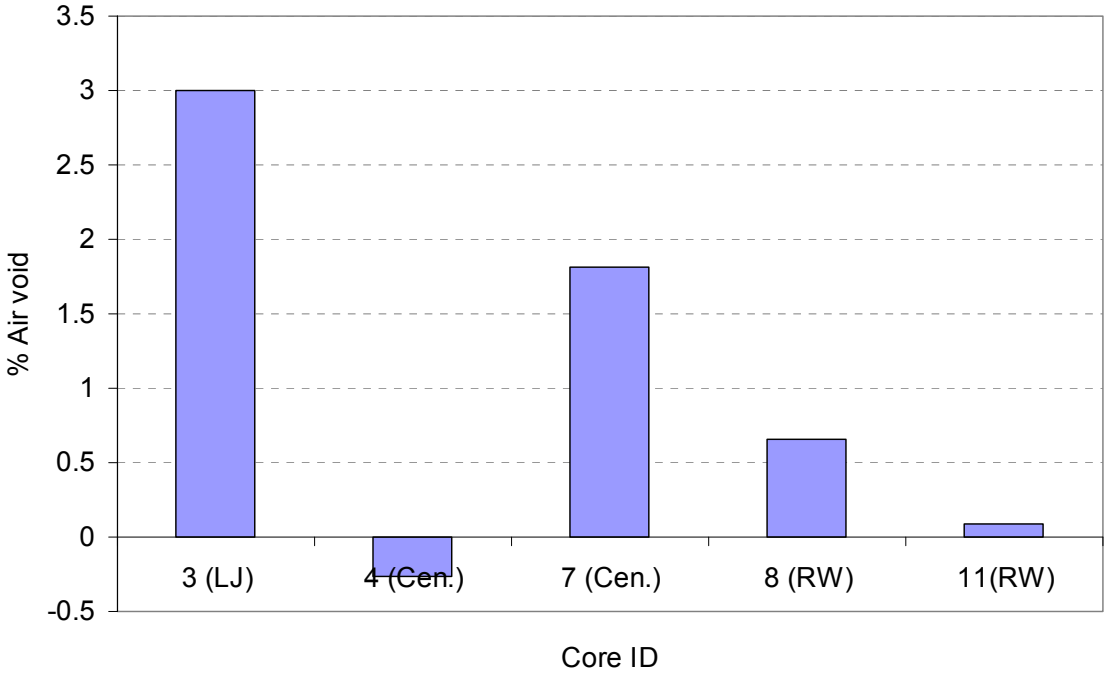

Figure A-38. Difference between the Percent of Air Voids at the Top and the Bottom Parts for US-281 Test Section.

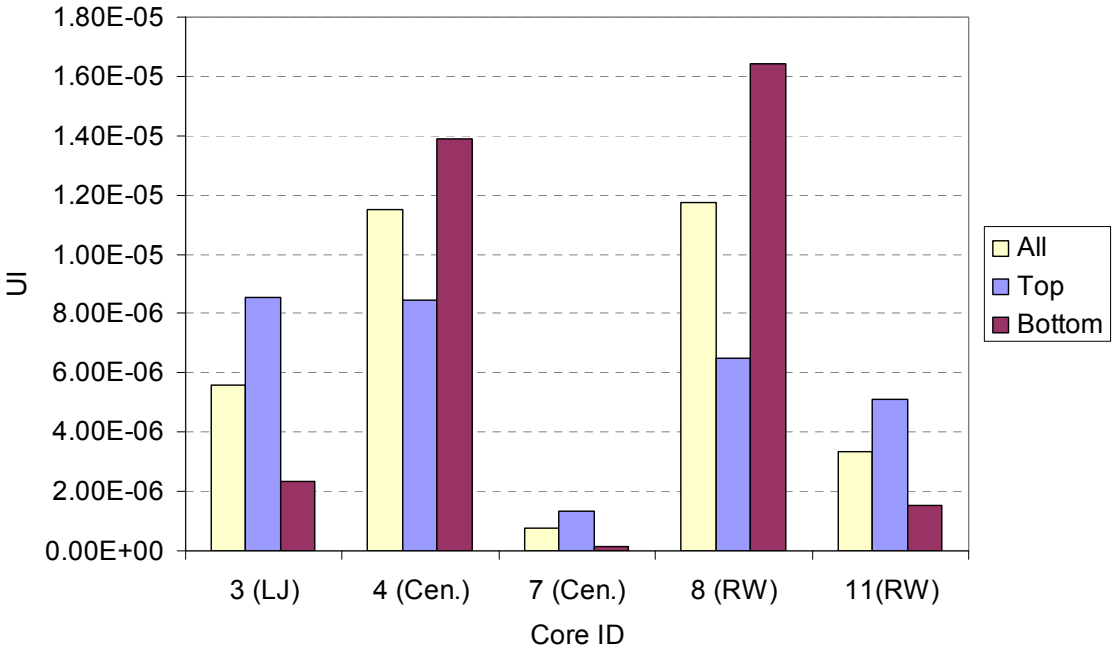

Figure A-39. UI for the US-281 Test Section.

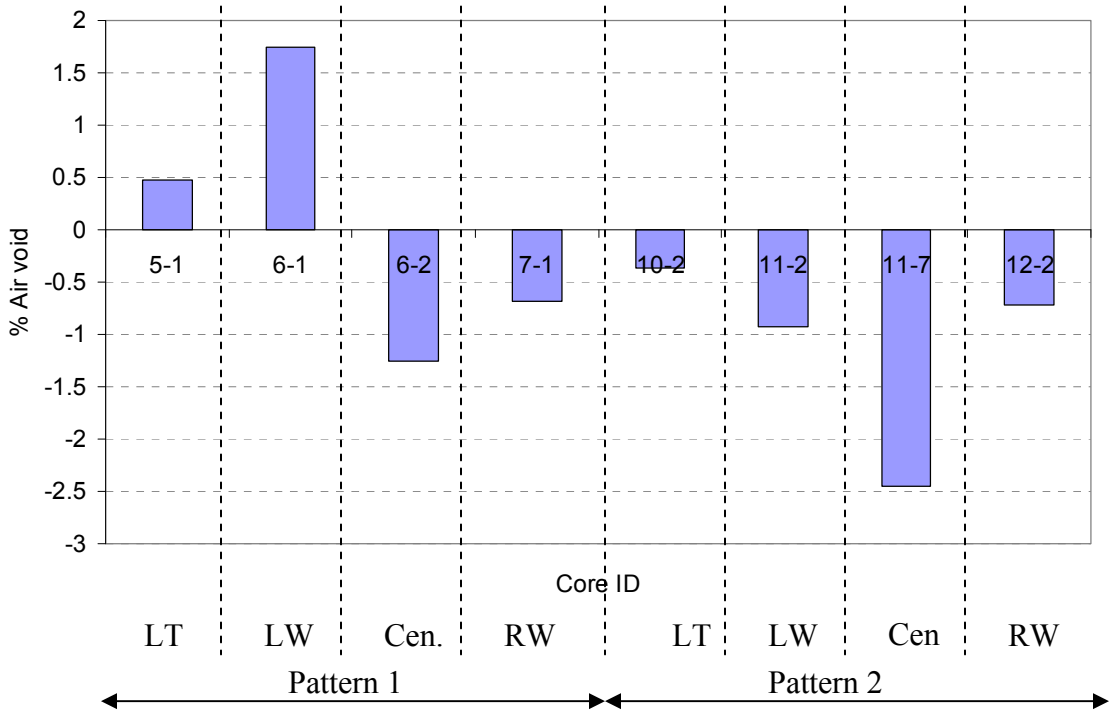

Figure A-40. Difference between the Percent of Air Voids at the Top and the Bottom Parts for FM-649 Test Section.

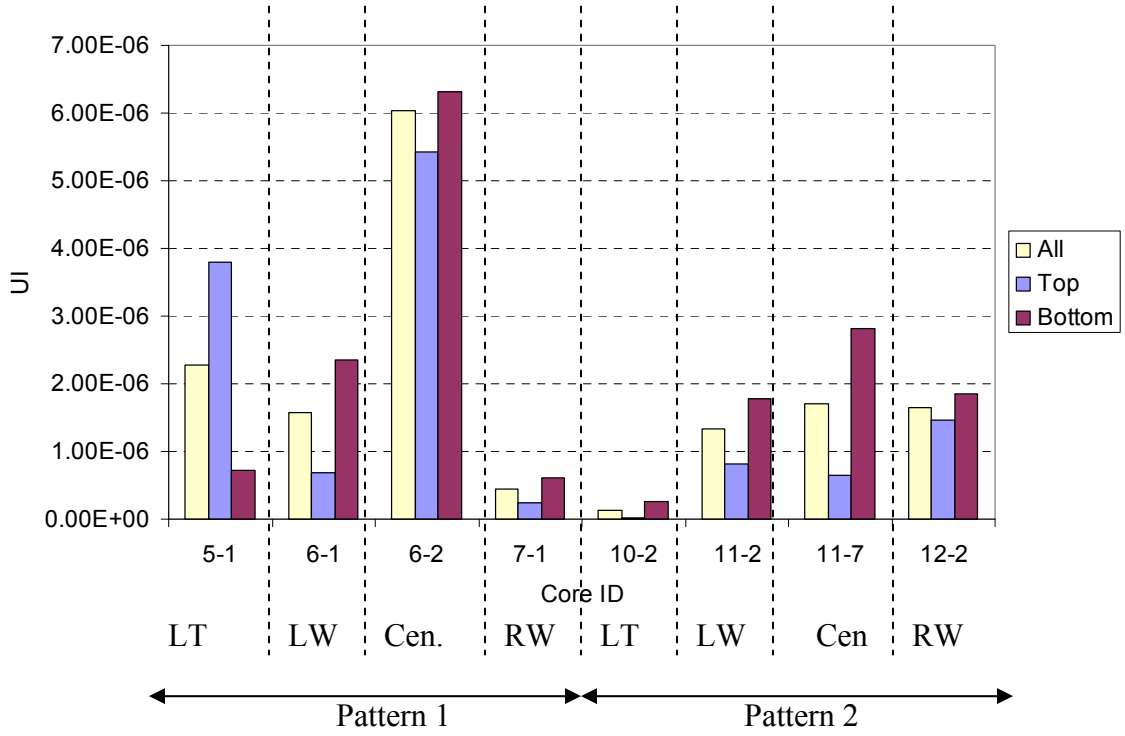

Figure A-41. UI for the FM-649 Test Section.

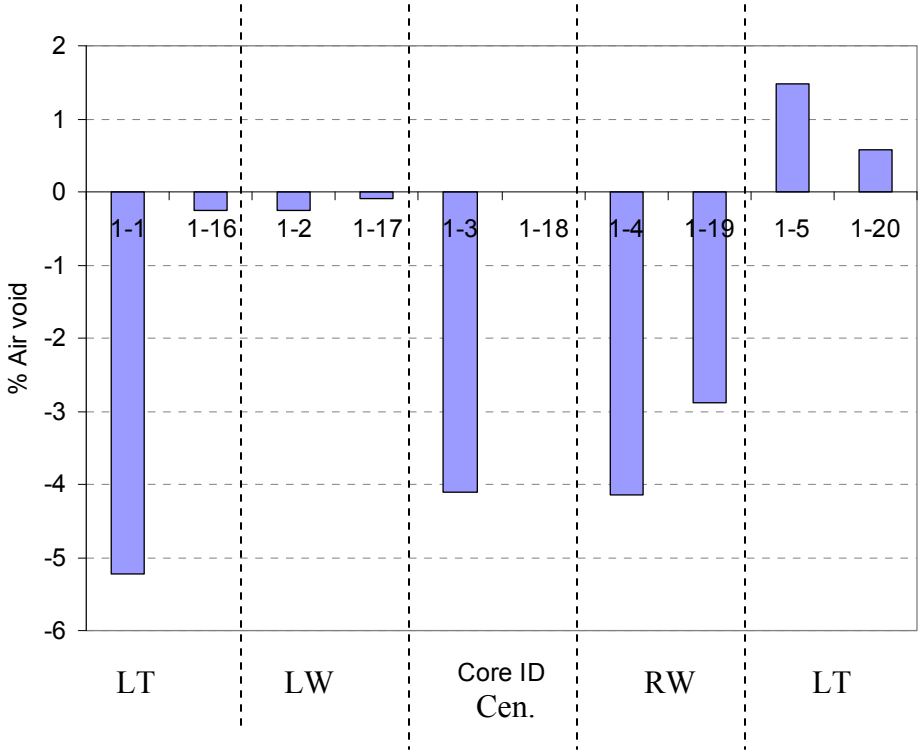

Figure A-42. Difference between the Percent of Air Voids at the Top and the Bottom Parts for US-259 Test Section (Pattern 1).

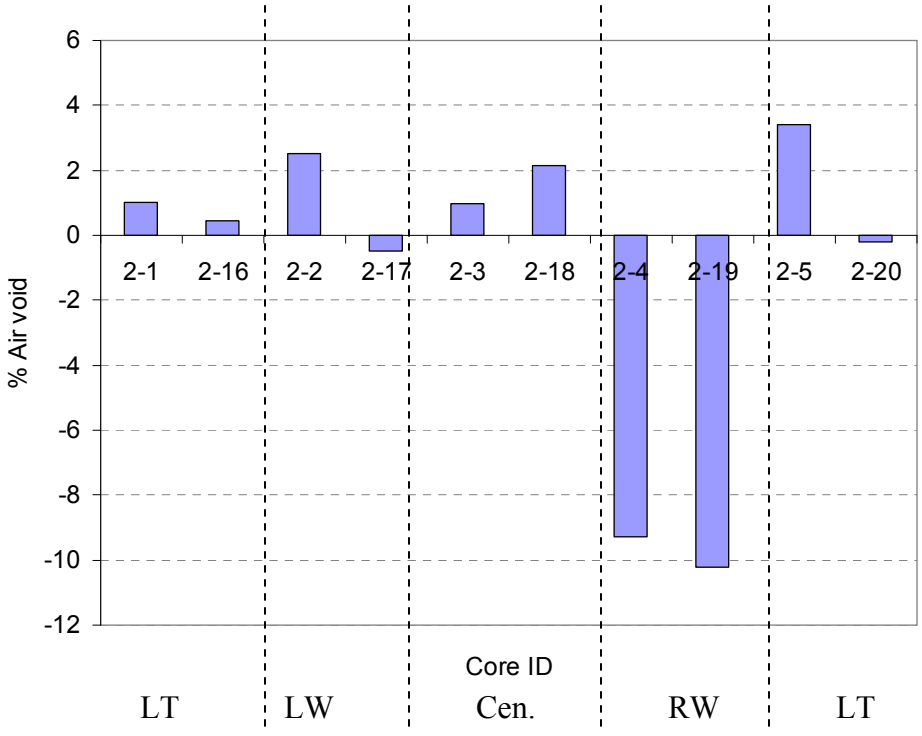

Figure A-43. Difference between the Percent of Air Voids at the Top. and the Bottom Parts for US-259 Test Section (Pattern 2).

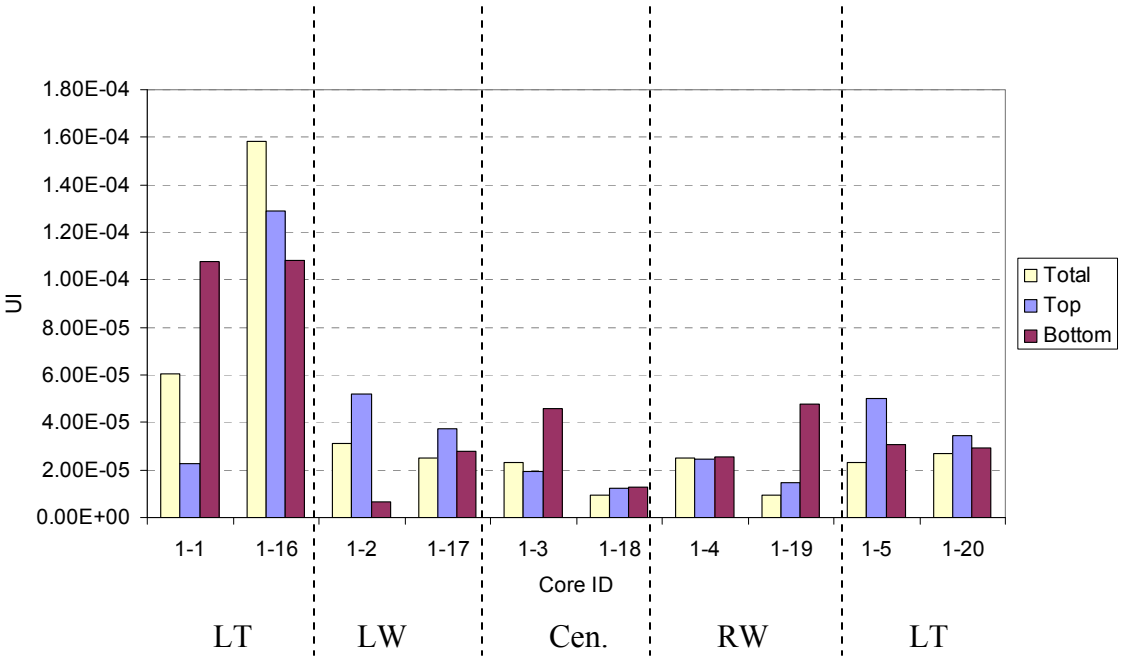

Figure A-44. UI for the US-259 Test Section (Pattern 1).

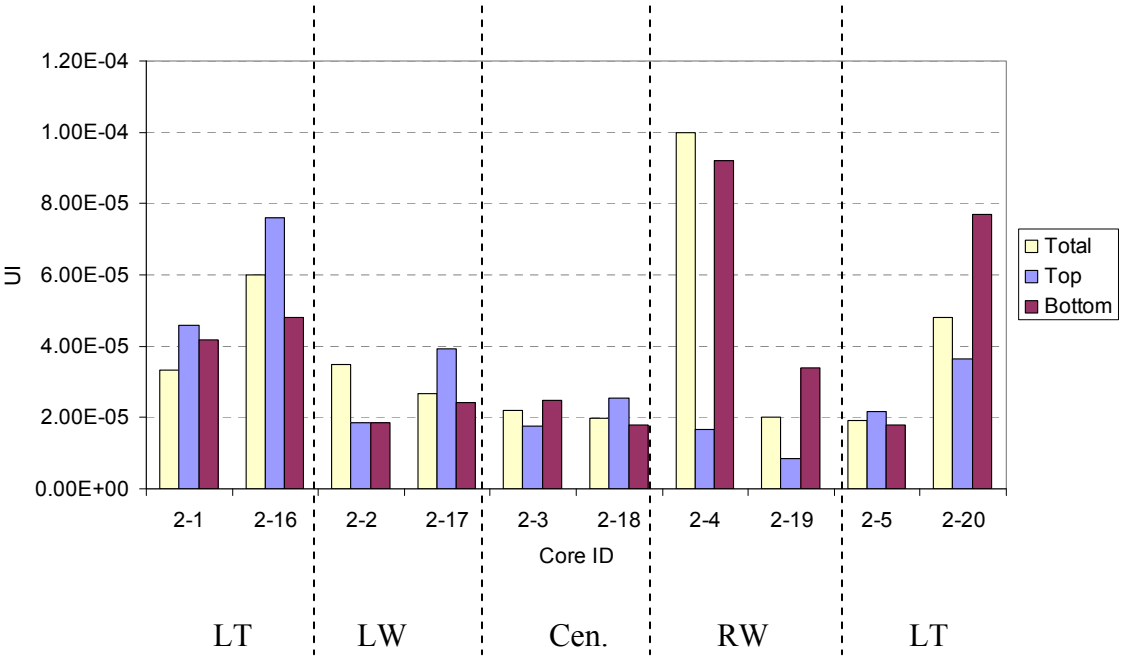

Figure A-45. UI for the US-259 Test Section (Pattern 2).

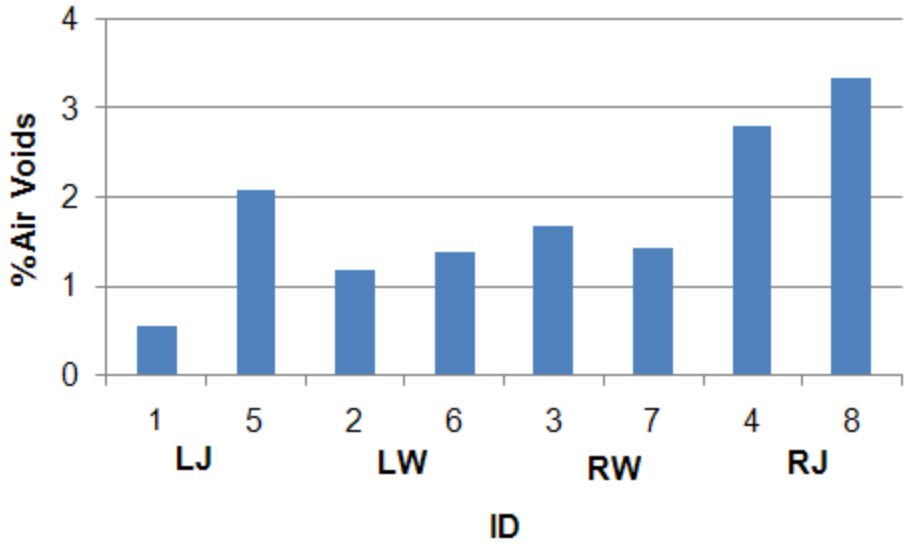

Figure A-46. Difference between the Percent of Air Voids at the Top and the Bottom Parts for SH-6 Test Section.

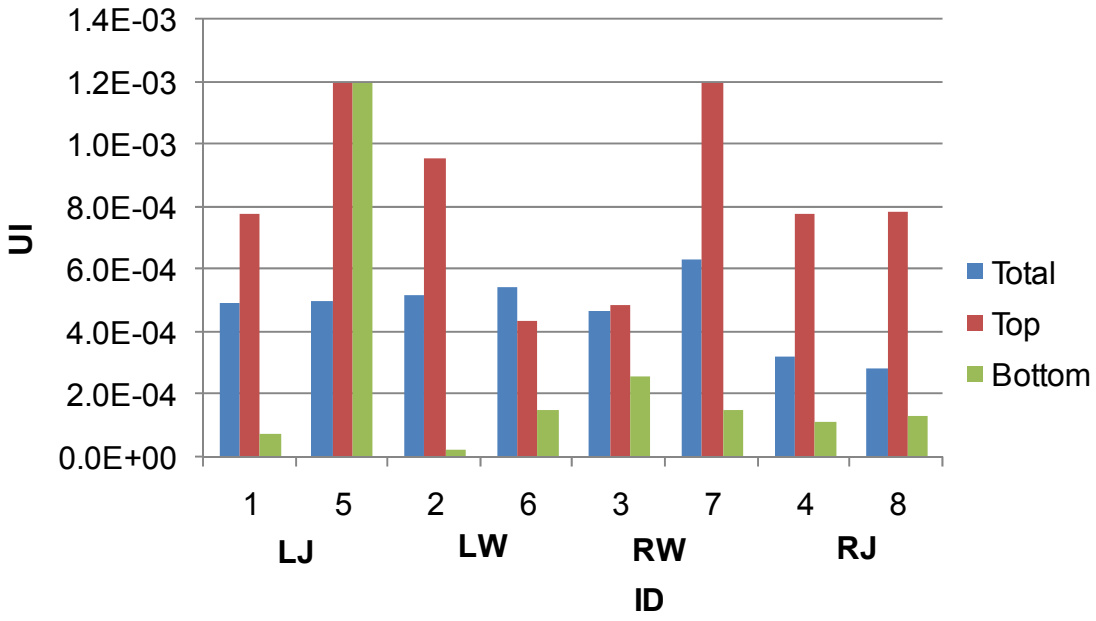

Figure A-47. UI for the SH-6 Test Section.

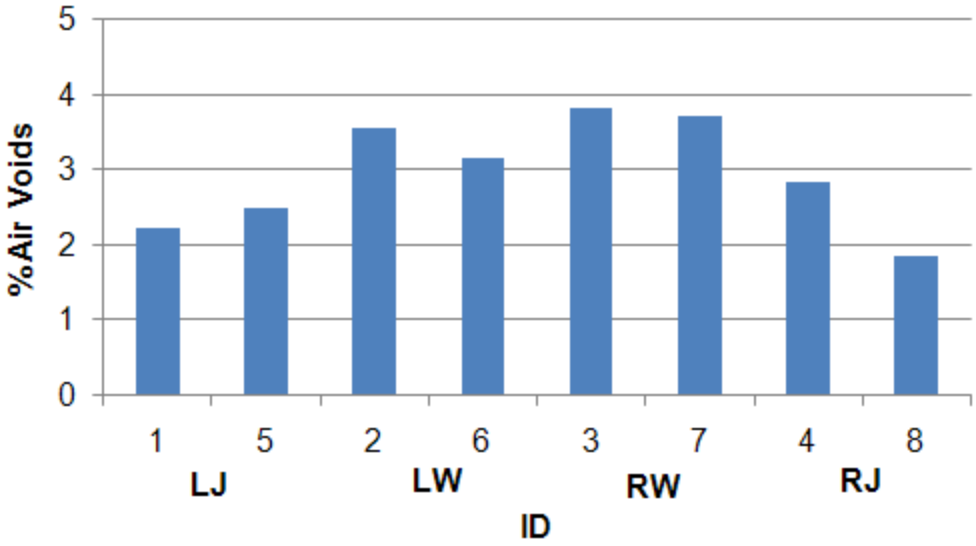

Figure A-48. Difference between the Percent of Air Voids at the Top and the Bottom Parts for SL-1 Test Section.

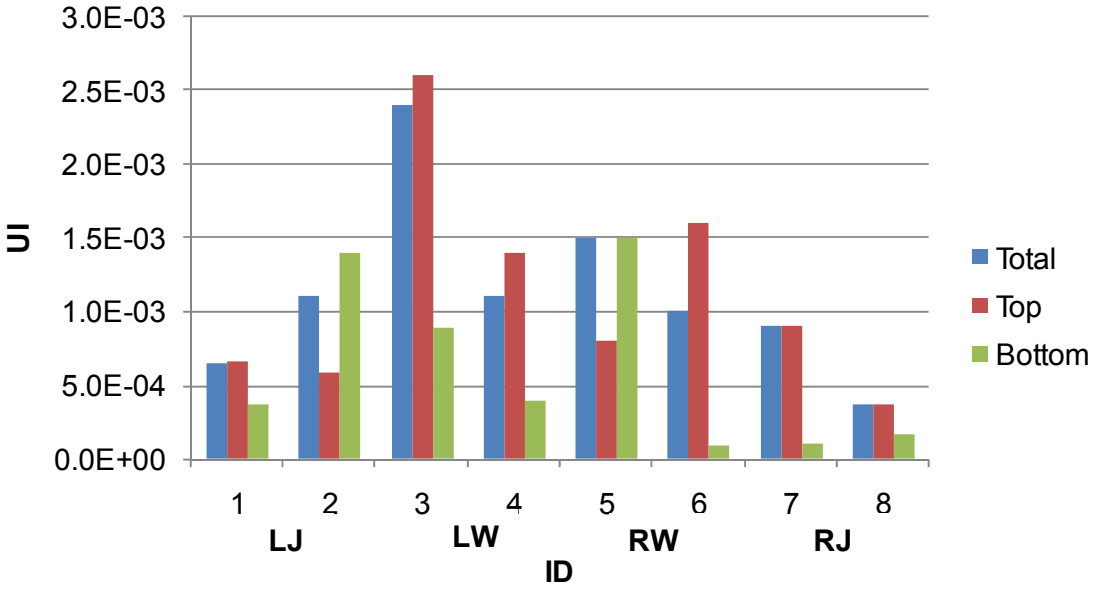

Figure A-49. UI for the SL-1 Test Section.

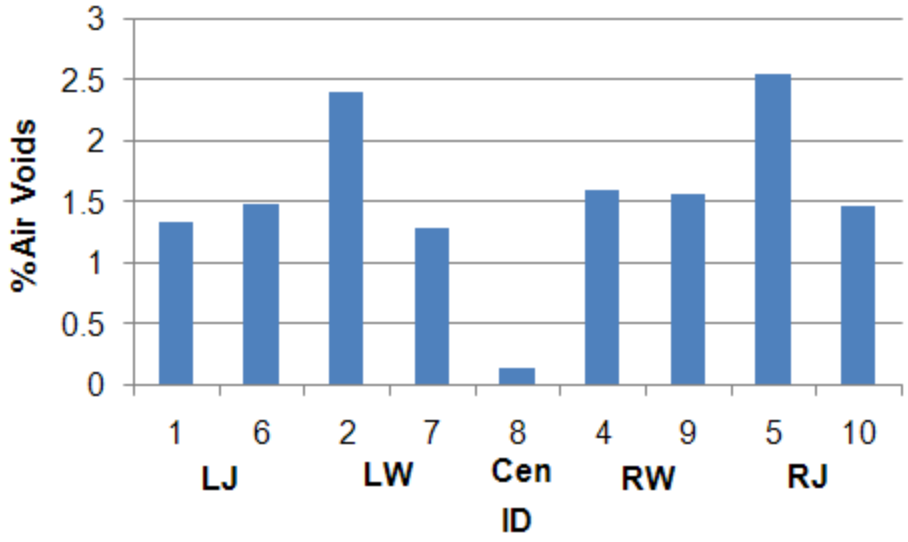

Figure A-50. Difference between the Percent of Air Voids at the Top and the Bottom Parts for SH-44 Test Section.

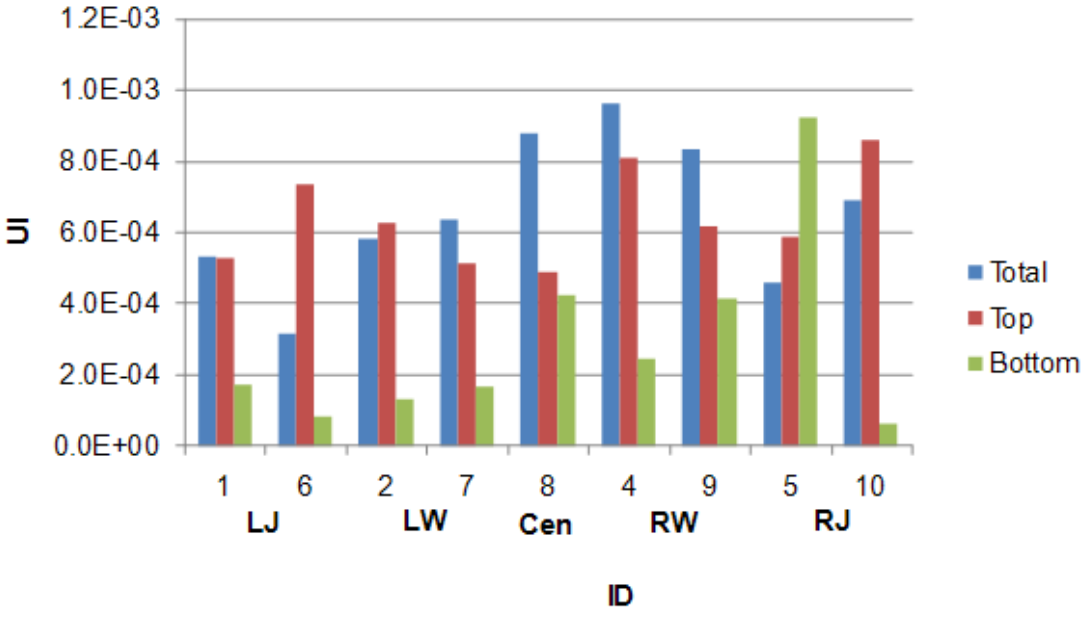

Figure A-51. UI for the SH-44 Test Section.

APPENDIX B
FORENSIC EVALUATION OF AIR VOID DISTRIBUTION

SL 368 IN SAN ANTONIO (WARM MIX)

Introduction

This construction project represents the first warm mix asphalt (WMA) trial placed by the Texas Department of Transportation (TxDOT). Evotherm, developed by MeadWestvaco Asphalt Innovations, Charleston, South Carolina, uses a non proprietary technology that is based on a chemical package that includes emulsification agents; additives to improve aggregate coating, mixture workability, and compaction; as well as adhesion promoters (anti-stripping agents). Evotherm utilizes a high residue emulsion (about 70 percent binder) that improves adhesion of the asphalt to the aggregate. The product enhances mixture workability, while lowering mixing temperatures to as low as 200°F. No plant modifications are required, the mix can be stored in silos, and may be utilized with or without polymer modifier.

The objectives of TxDOT in conducting this field trial include the following:

- to evaluate the production, laydown, and compaction of warm mix as compared with a conventional hot mix control using a standard TxDOT mixture design, and
- to evaluate the short and long-term performance of the warm mix versus a control hot mix.

The research team participated in this project in order to examine the compaction of both control and warm mix as a part of forensic study.

Project Description

This project was in Bexar County within the city limits of San Antonio. The project located on Loop 368 (Old Austin Highway), is a four-lane roadway divided by a median, with curb and gutter and many businesses along each side.

The existing pavement (prior to placement of the warm mix and control) consisted of a cold-milled asphalt surface which had been seal coated with AC-15P and a Grade 4 precoated aggregate. The seal coat had been under traffic for about a month prior to the overlay. All of the paving for this project was conducted at night.

The warm and control mixes were produced by Vulcan Materials of San Antonio and placed by Dean Word Company of New Braunfels. It should also be noted that the field trials were placed within the limits of a much larger HMAC paving project (CSJ 0016-08-027) that was both produced and placed by Dean Word Company.

Mixture Design

The control and warm mixtures met the gradation requirements of a TxDOT Item 341, Type C, Dense-Graded HMAC. The mixture designs were performed by Vulcan Materials laboratory. The asphalt used for the control HMAC was Valero PG 76-22. The base asphalt for the warm mix started as a Valero PG 64-22 prior to modification by MeadWestvaco. Once modified, the warm mix binder met the specifications of PG 76-22. The modified asphalt was then emulsified and provided to Vulcan Materials laboratory to perform the mixture design. Two aggregate sources were used for the mixtures: Vulcan's Helotes Pit limestone and the Harris Pit field sand. Note that the same aggregate sources and gradations were used for both the warm mix and the control. Both warm and control mixtures were designed using a Texas gyratory compactor with a target density of 96.5 percent.

Performance Testing and X-ray CT with Warm Mix

The research team was able to obtain only a limited number of roadway samples from warm mix and control sections. As a result only X-ray CT and permeability tests were conducted with these samples. Figure B-1 shows the test permeability test results with the roadway cores from both control and warm mix sections. Specimens from the control mix yield a little higher permeability than the warm mix specimens. The bottom of the warm mix samples were all saw cut except two cores (2A-1 and 2B-1) as explained in Table B-1 while the control specimens were not saw cut. Research team obtained the

specimens that way from TxDOT. The compaction pattern at different days of mixture placement and mixture types did not vary significantly.

Table B-1 shows the locations of road cores and their air voids. There were only two specimens from the control mixture (mixed and compacted at 315 °F and 305 °F, respectively). These two samples had relatively higher air voids and their air voids distributions were dissimilar. WMA specimens compacted (Lot 1 and Sublot 1) in center lane had relatively low air voids (5.4 to 5.8 percent). All four specimens had similar air voids distribution: high air voids at the top and bottom but low air voids at the center. Four other WMA road cores obtained from a close proximity but different lanes and different sublots (Lot 1 Sublot 2; specimens 2E, 2F, 2G, 2H) all had relatively high air voids (7.9 to 8.9 percent). Both Sublot 1 and Sublot 2 both had the same asphalt content and comparable compaction temperature. The only possible explanation could be the change in aggregate gradation which needs to be measured. When the average air voids were similar the control mixture and WMA had similar air voids distribution. Figures B-2 through B-12 show the air void distribution and the air void size along the depth of the test samples.

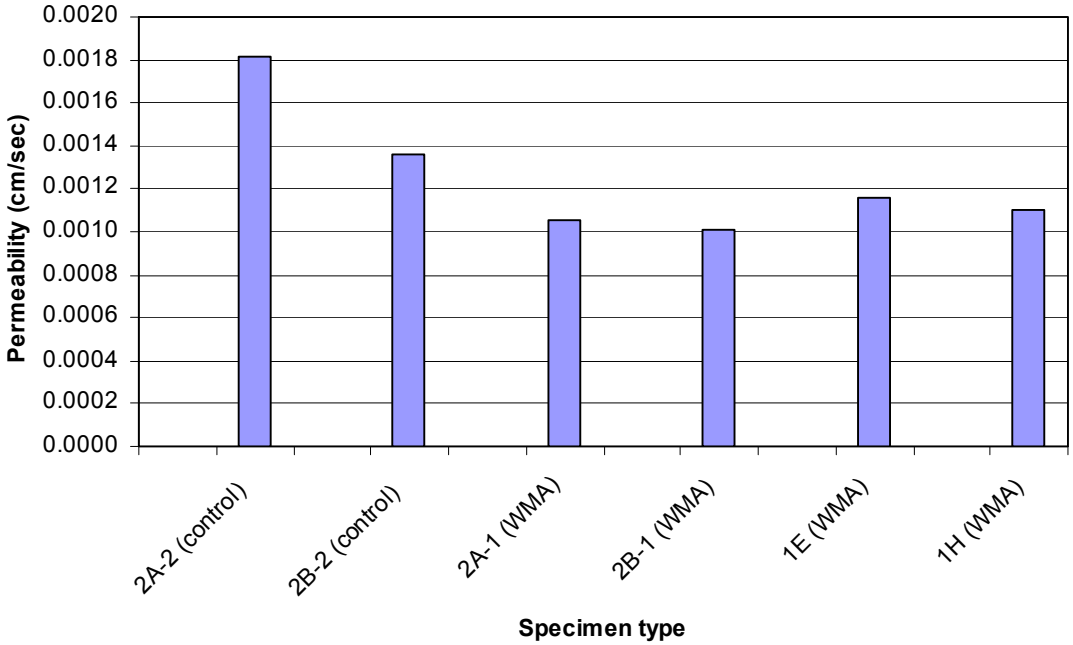

Figure B-1. Comparison of Permeability Test Results between Control and Warm Mix.

Table B-1. Description of Road Cores and Air Voids.

Sample ID	Location	Type	Remark	Air Void Percent
2A-2	36+50, NBOS Lane	Control Mix	uneven bottom	9.3
2B-2	36+50, NBOS Lane	Control Mix	uneven bottom	8.9
2A-1	56+00	WMA, 3rd night	uneven bottom	9.2
2B-1	56+00	WMA, 3rd night	uneven bottom	9.0
1E	15+00, Centerlane; 6 ft offset	WMA, 1st night, Lot 1, Sublot 1	Sawcut Bottom	5.4
1F	15+00, Centerlane; 6 ft offset	WMA, 1st night, Lot 1, Sublot 1	Sawcut Bottom	5.5
1G	15+00, Centerlane; 6 ft offset	WMA, 1st night, Lot 1, Sublot 1	Sawcut Bottom	5.6
1H	15+00, Centerlane; 6 ft offset	WMA, 1st night, Lot 1, Sublot 1	Sawcut Bottom	5.8
2E	15+60 SBOS lane, 7 ft offset	WMA, Lot 1, Sublot 2;	Sawcut Bottom	7.9
2F	15+60 SBOS lane, 7 ft offset	WMA, Lot 1, Sublot 2;	Sawcut Bottom	8.7
2G	15+60 SBOS lane, 7 ft offset	WMA, Lot 1, Sublot 2;	Sawcut Bottom	8.9
2H	15+60 SBOS lane, 7 ft offset	WMA, Lot 1, Sublot 2;	Sawcut Bottom	8.2

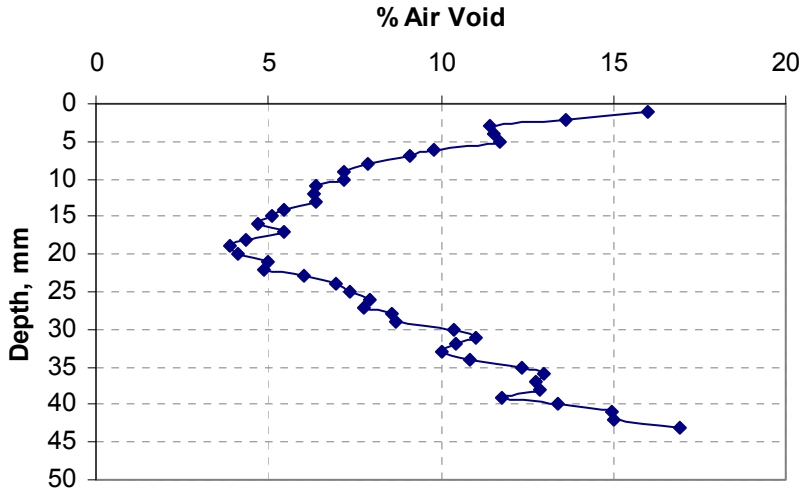

(a)

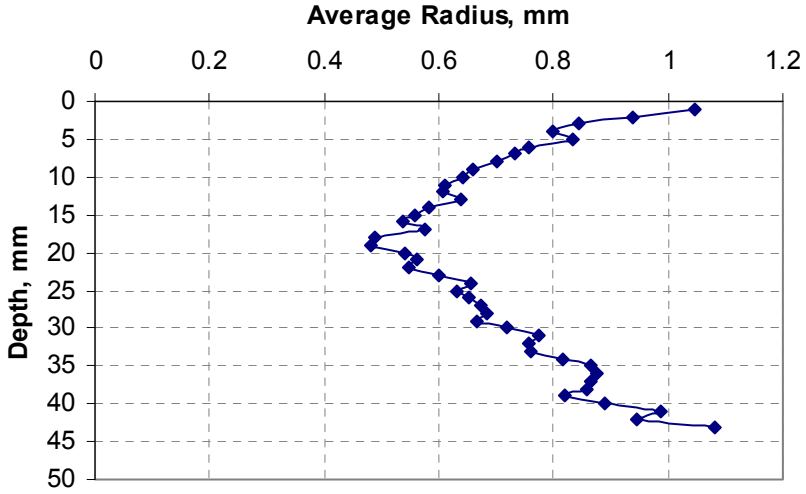

(b)

Figure B-2. (a) Air Void Distribution along the Depth of Core 2A-2, (b) Air Void Size Distribution along the Depth of Core 2A-2.

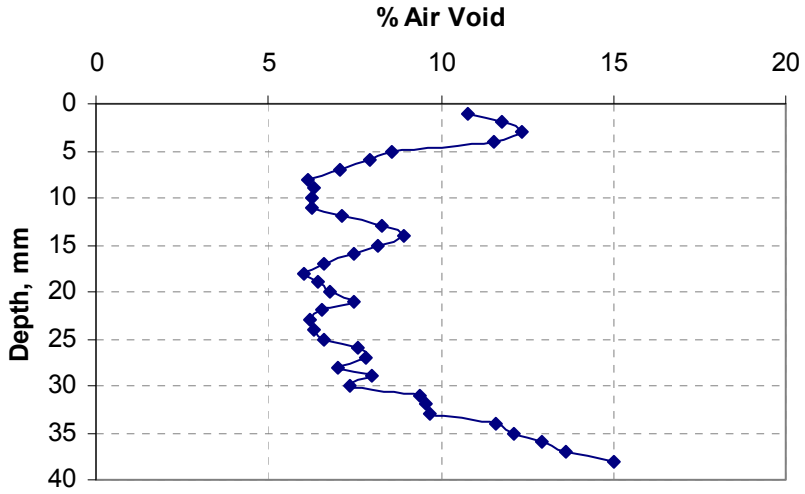

(a)

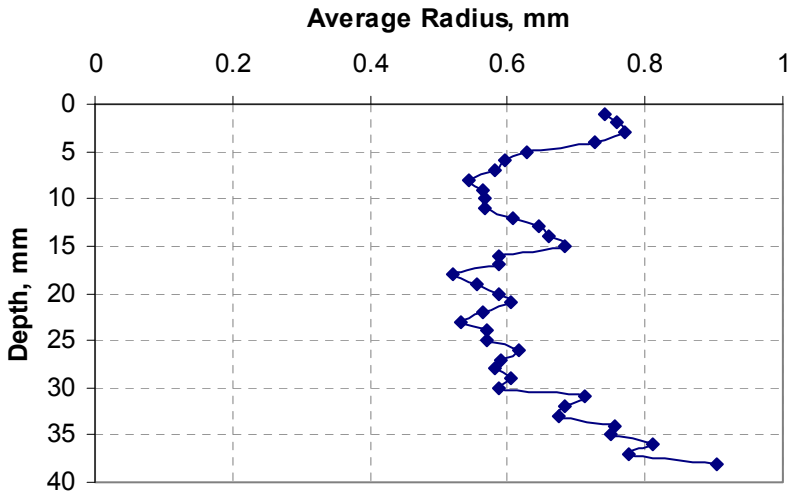

(b)

Figure B-3. (a) Air Void Distribution along the Depth of Core 2B-2, (b) Air Void Size Distribution along the Depth of Core 2B-2.

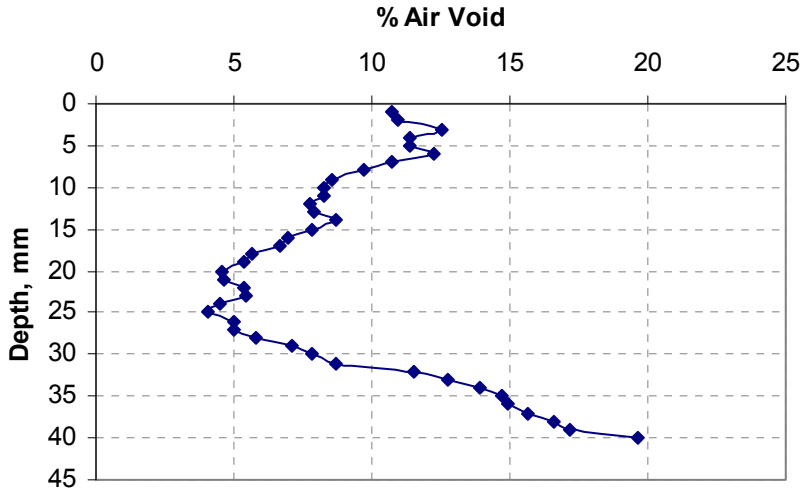

(a)

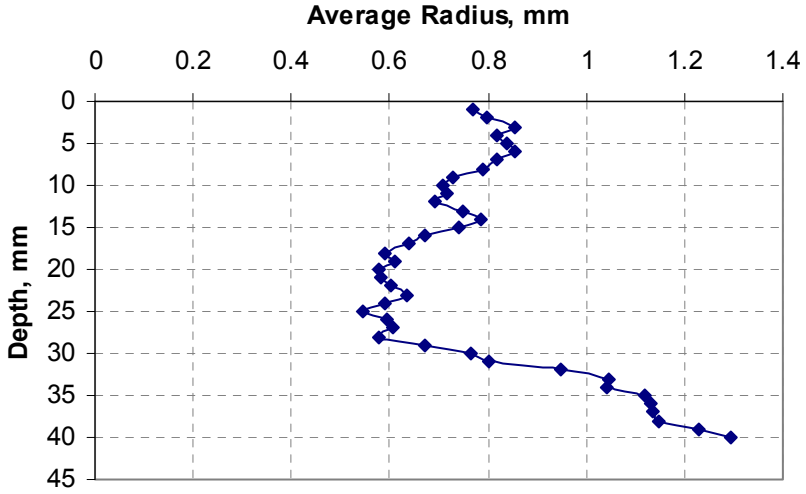

(b)

Figure B-4. (a) Air Void Distribution along the Depth of Core 2A-1, (b) Air Void Size Distribution along the Depth of Core 2A-1.

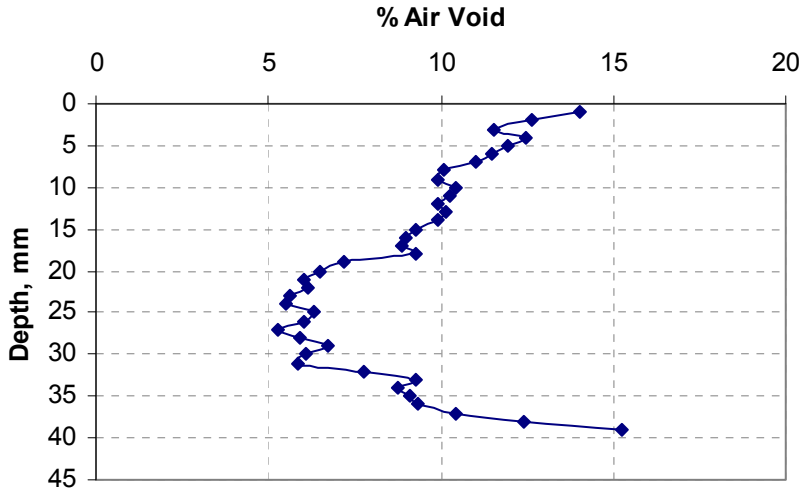

(a)

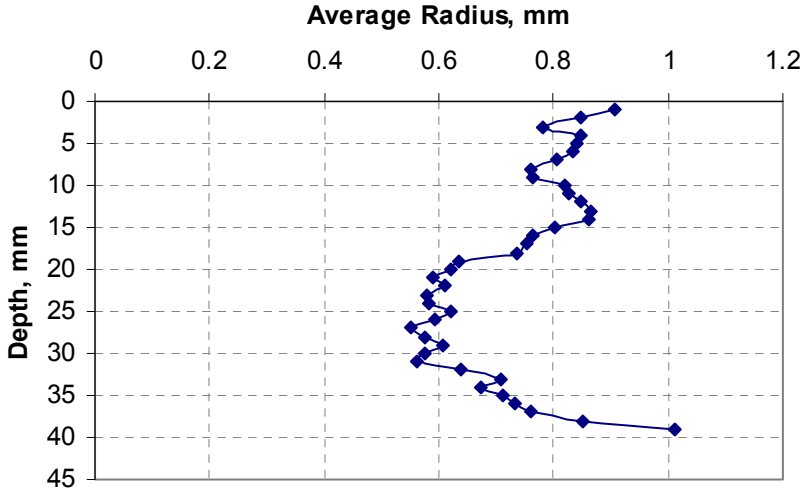

(b)

Figure B-5. (a) Air Void Distribution along the Depth of Core 2B-1, (b) Air Void Size Distribution along the Depth of Core 2B-1.

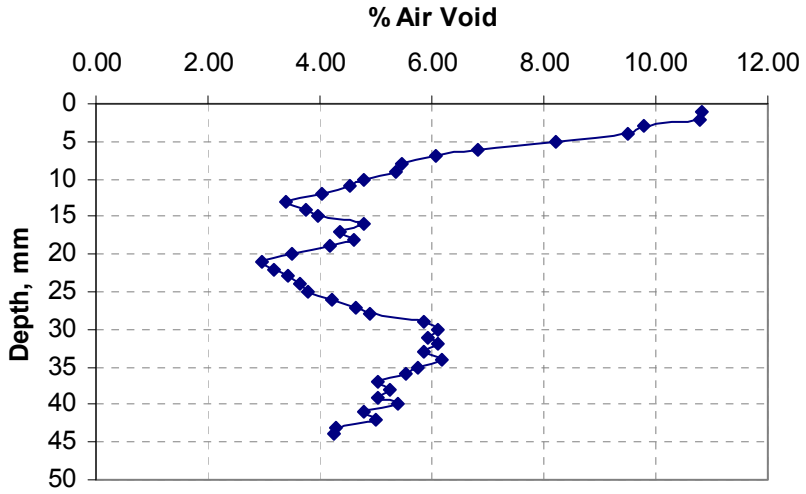

(a)

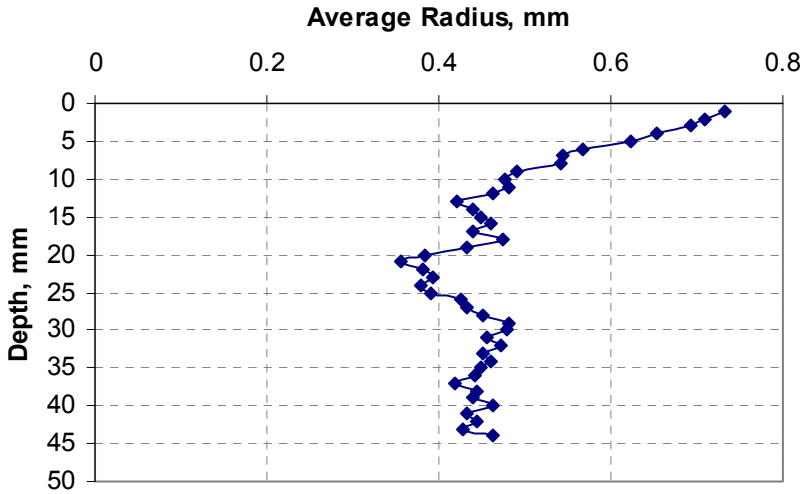

(b)

Figure B-6. (a) Air Void Distribution along the Depth of Core 1E, (b) Air Void Size Distribution along the Depth of Core 1E.

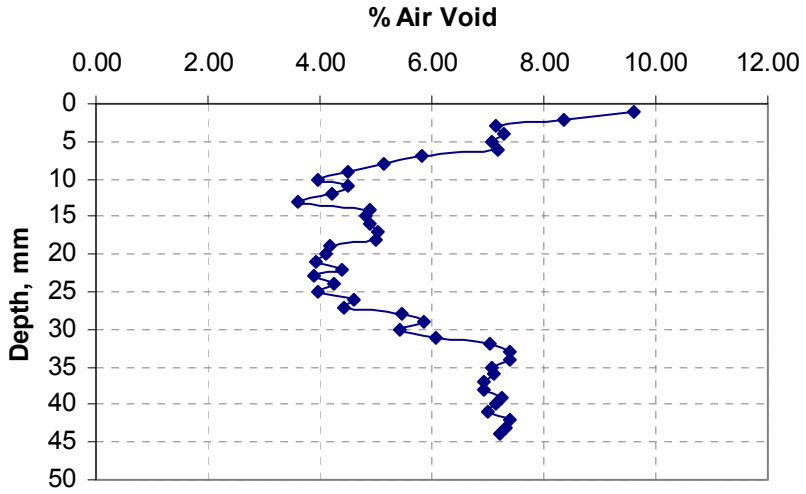

(a)

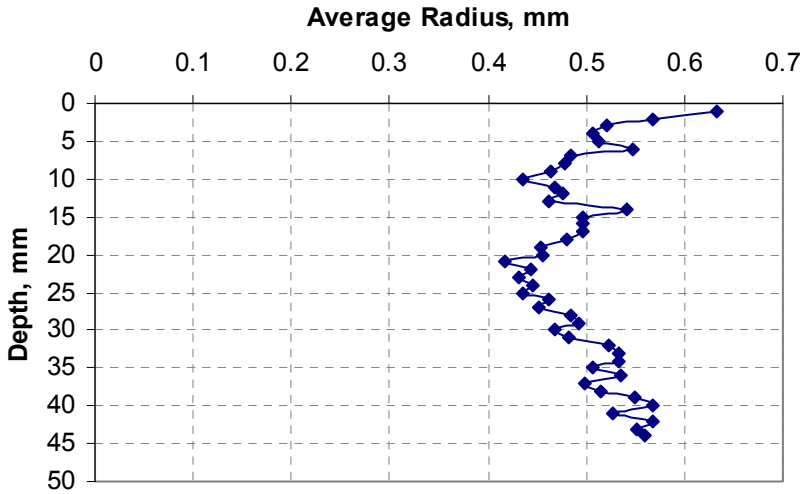

(b)

Figure B-7. (a) Air Void Distribution along the Depth of Core 1F, (b) Air Void Size Distribution along the Depth of Core 1F.

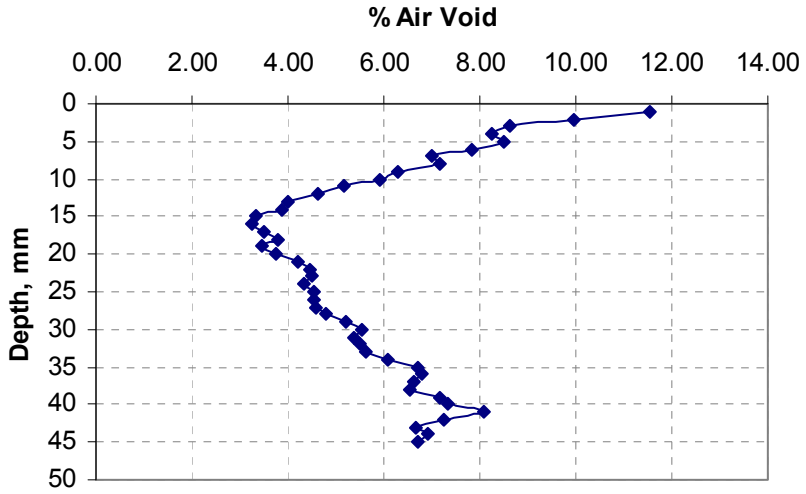

(a)

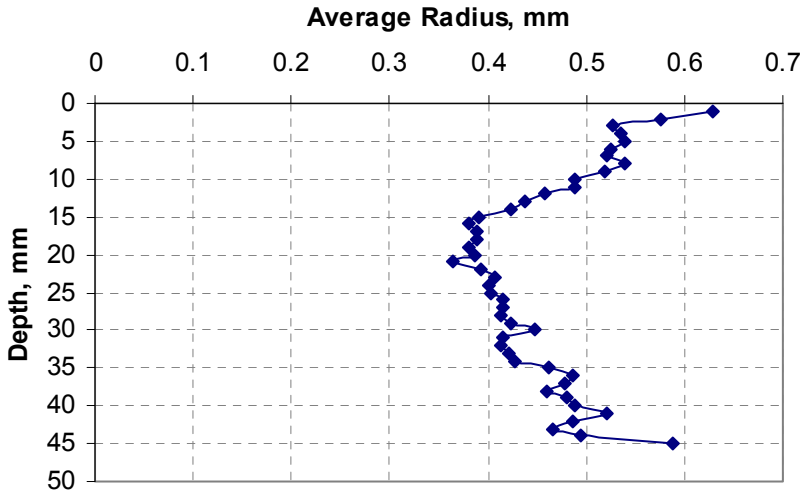

(b)

Figure B-8. (a) Air Void Distribution along the Depth of Core 1G, (b) Air Void Size Distribution along the Depth of Core 1G.

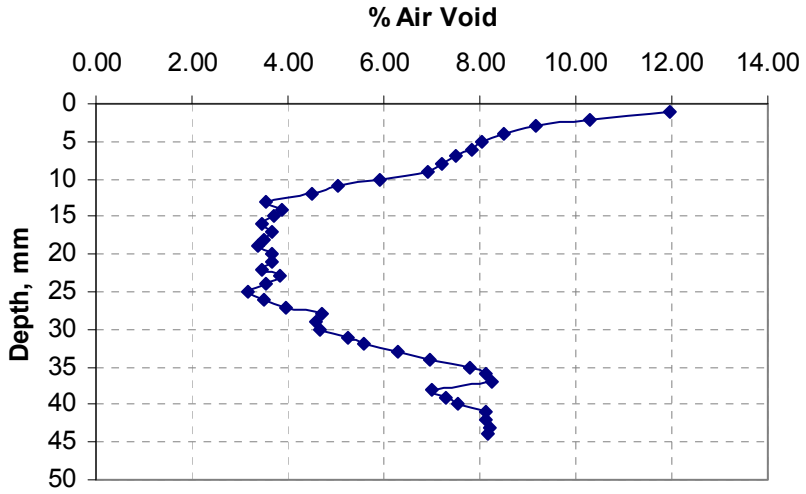

(a)

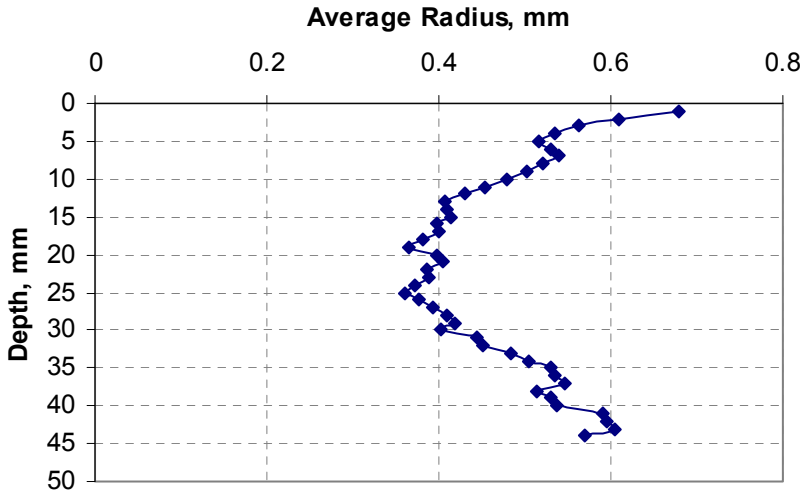

(b)

Figure B-9. (a) Air Void Distribution along the Depth of Core 1H, (b) Air Void Size Distribution along the Depth of Core 1H.

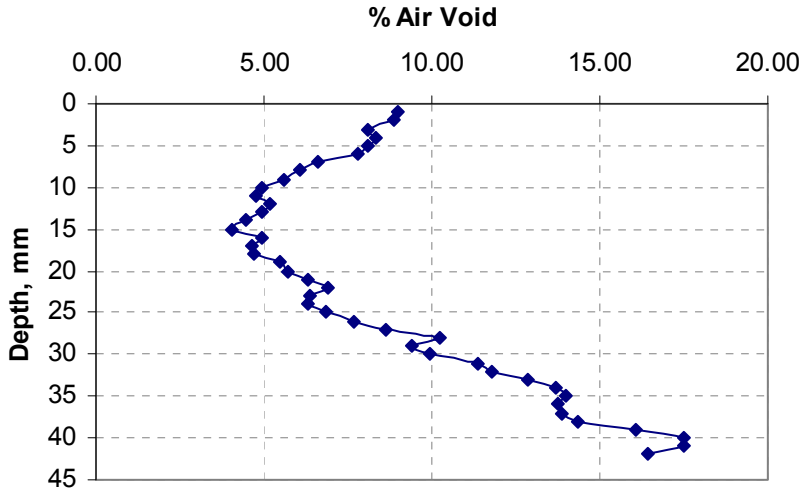

(a)

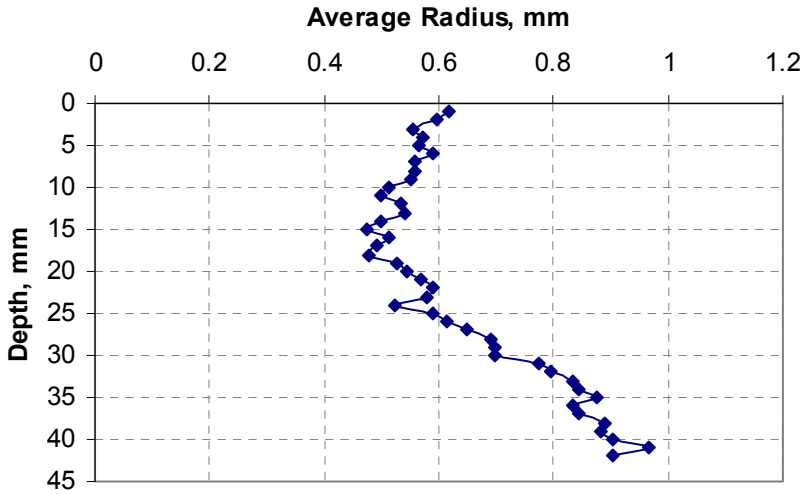

(b)

Figure B-10. (a) Air Void Distribution along the Depth of Core 2F, (b) Air Void Size Distribution along the Depth of Core 2F.

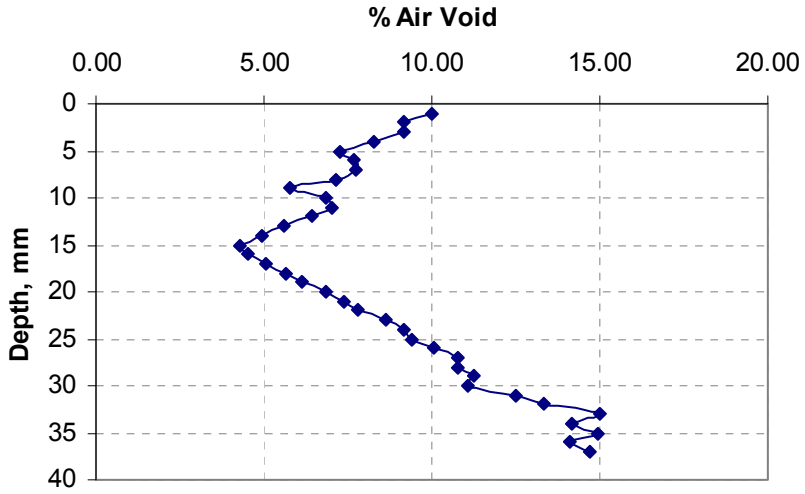

(a)

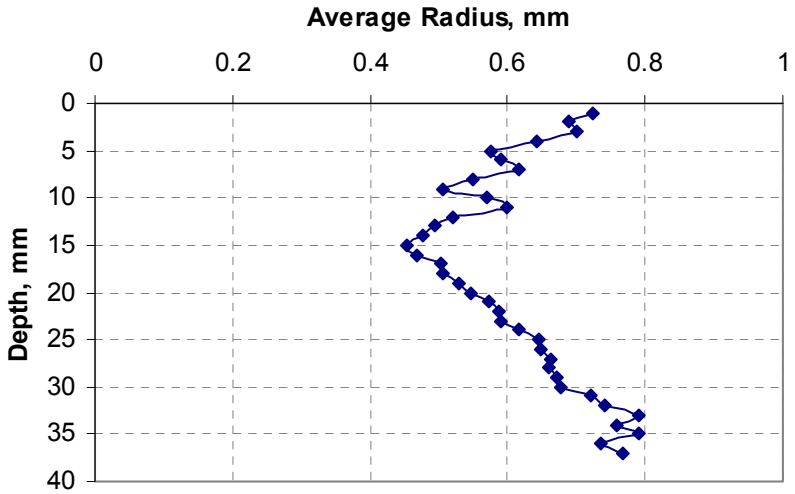

(b)

Figure B-11. (a) Air Void Distribution along the Depth of Core 2G, (b) Air Void Size Distribution along the Depth of Core 2G.

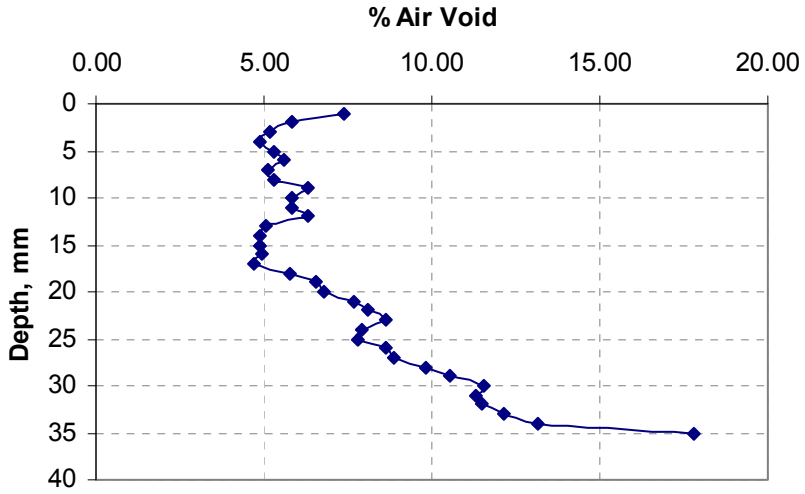

(a)

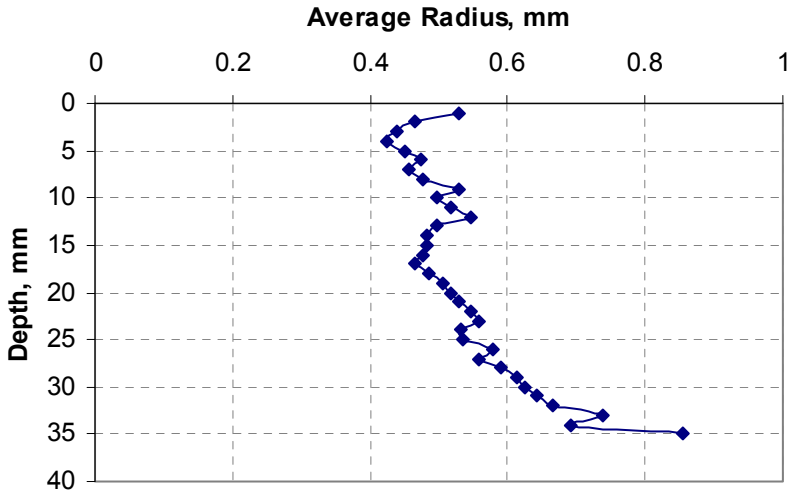

(b)

Figure B-12. (a) Air Void Distribution along the Depth of Core 2H, (b) Air Void Size Distribution along the Depth of Core 2H.

US 290 AND FM 529

Consulting with engineers from the Houston District, the research team included certain parts of US 290 and FM 529 in Waller County for further forensic study. Seven cores were obtained from US 290 in Waller County with the assistance from TxDOT's Houston District. The cores were obtained approximately 0.2 mile west of Heger road on the westbound outside lane. The coring layout is shown in Figure B-13.

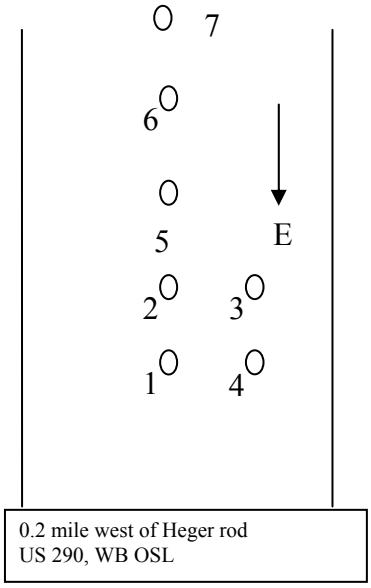

Figure B-13. US 290 Coring Layout.

Cores 3 and 4 are from the right wheel path, whereas cores 1, 2, 5, 6, and 7 are from between wheel paths. The primary focus of this investigation was the top layer which was a 2 inch thick Type C HMA layer. Cores labeled 4 and 6 were tested with X-ray Computed Tomography. Permeability and Hamburg testing were conducted on specimens 3 and 7. The results are shown in Table B-2.

Table B-2. Results from Testing US 290 Cores.

Test	Results
Rutting in Hamburg Test	3.4 mm at 20,000 cycles
Permeability	9.8×10^{-4} cm/sec

Based on the results in Table B-2, the findings from US 290 are summarized as follows:

- Rutting is not a concern for this layer.
- Permeability values are low. It is noted that this layer has been in service under heavy traffic for a few years.

Ten specimens were obtained from FM 529 in Waller County. The coring site was located approximately 1500 ft west of the Harris county line on westbound lane. The coring layout is shown in Figure B-14. Cores LJ1 and LJ2 were taken near the longitudinal joint, cores WP-3 and WP-4 were from the left wheel path, cores BW1 to BW4 were recovered between the wheel paths, while WP1 and WP2 were taken from the right wheel path. The primary focus of this investigation was the surface layer which was constructed in Fall 2005. The cores were obtained in February 2006. The surface layer was designed as Type F mixture with very high asphalt content. Cores LJ1, BW1 and BW4 were tested for permeability and rutting in Hamburg. Cores WP1, LJ1, WP2, and BW 1 were evaluated using X-ray CT.

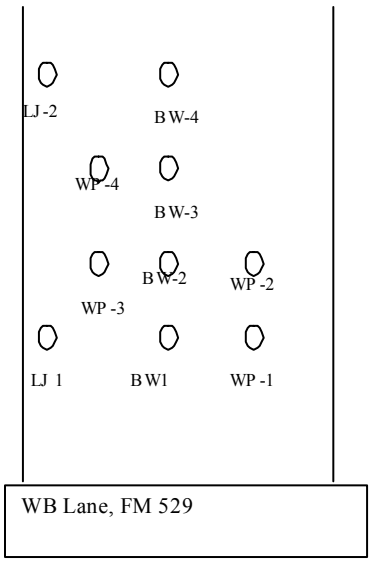

Figure B-14. Coring Layout for FM 529.

The results from testing the FM 529 cores are shown in Table B-3. Based on these results the findings can be summarized as follows:

- Rutting is not a concern for this layer.
- Permeability values are very low.
- Although the percent air voids is relatively high (about 10 percent), the permeability values are very small. This might suggest that the air void sizes in FM 529 are small and not connected.
- There was a very small difference (only 8 percent) between the permeability of the core taken near the longitudinal joint (LJ1) and the two cores from between wheel path (BW1 and BW4).

Table B-3. Results from Testing FM 529 Cores.

Test	Results
Rutting in Hamburg Test	4.25 mm at 20,000 cycles
Permeability	8.85×10^{-4} cm/sec
Percent Air Voids	10.40% (LJ1) 9.45% (Average of WP1 and WP4)

Air Void Distribution Using X-ray Computed Tomography

The X-ray CT and image analysis methods were used to determine the distribution of percent air voids and the radius of air voids across each specimen thickness. The analysis results are summarized in Table B-4. The detailed results for FM 529 are shown in Figures B-15 to B-22 while the results from US 290 are shown in Figures B-23 to B-26. The following is a summary of the findings:

- The comparison of percent air voids from X-ray CT in Table B-4 with the percent air voids measured in the laboratory based on specific gravity in Table B-3 shows that the difference is only 1 percent. This small difference supports the accuracy of X-Ray CT in determining the percent air voids in the whole specimen.
- As shown in Figures B-15 and B-17, the air void distributions in the cores recovered from the right and left wheel paths are very similar.
- The comparison of Figures B-15 and B-17 with Figure B-21 reveals that there are similar air void distributions within and outside the wheel paths. The primary difference is in the top 10 mm where the cores within the wheel paths have less percent air voids. This is expected due to the traffic effect on percent air voids close to the surface.
- The comparison between LJ1 in Figure B-19 and cores within the wheel paths in Figures B-15 and B-17 show that the main difference in percent air voids is in the top 10 mm where the cores near the longitudinal joint have more percent air voids.

- The small coefficient of variation for the radius of air voids in FM 529 compared with US 290 indicates that there are less large air voids in FM 529 compared with US 290. This finding explains the low permeability in FM 529 in spite of the relatively high percent air voids (about 10 percent).

Conclusions

- It is clear from Table B-3 that the FM 529 cores had more uniform distributions of percent air voids and size of air voids compared with US 290 cores. This can be seen in the lower standard deviation and lower coefficient of variation for both percent air voids and size of air voids in FM 529.
- The FM 529 mixture has very low permeability in spite of the relatively high percent air voids. This indicates that the air voids in FM 529 are not interconnected. Based on the limited rutting tests conducted in this study, it appears that the FM 529 mix type F has high resistance to rutting.
- A thin asphalt layer such as the one used in FM 529 is expected to have high stresses within the mix. Therefore, it is highly recommended to use aggregates with high abrasion resistance in these types of mixtures.

Table B-4. Summary of the Air Void Distribution Results.

Highway	Specimen ID	Percent Air Voids			Air Void Radius		
		Average (%)	St. Dev.	Coeff. Var.	Average (mm)	St. Dev.	Coeff. Var.
FM 529	WP1	10.739	1.014	9.44	0.688	0.039	5.67
FM 529	LJ1	11.657	0.812	6.97	0.722	0.032	4.43
FM 529	WP2	10.155	0.69	6.79	0.67	0.03	4.48
FM 529	BW1	10.348	1.008	9.74	0.689	0.043	6.24
US 290	4	8.509	1.698	19.96	0.616	0.065	10.55
US 290	6	6.061	1.733	28.59	0.51	0.073	14.31

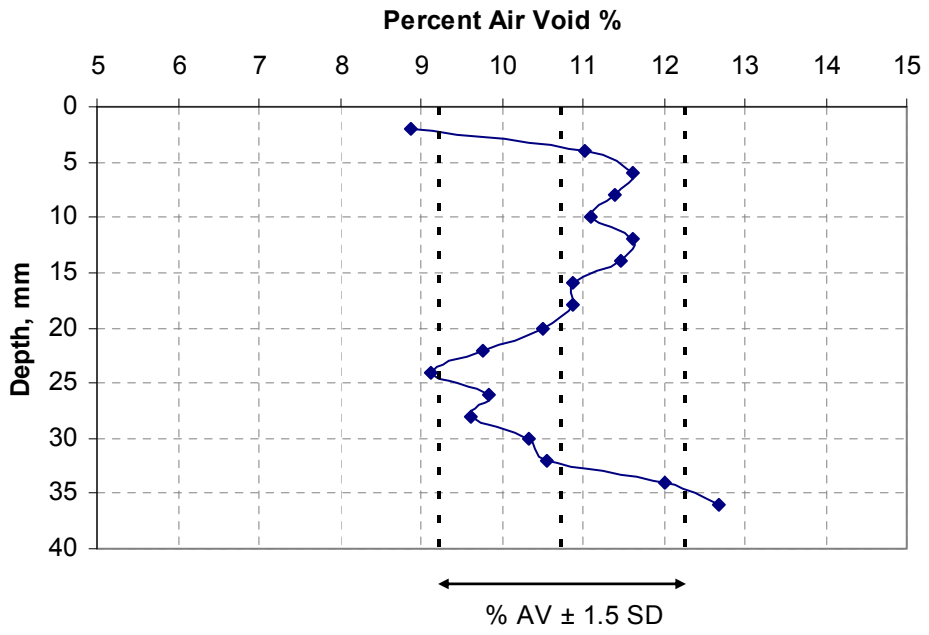

Figure B-15. Percent Air Distribution in Core ID: WP1; Highway: FM 529 and Location: Right Wheel Path.

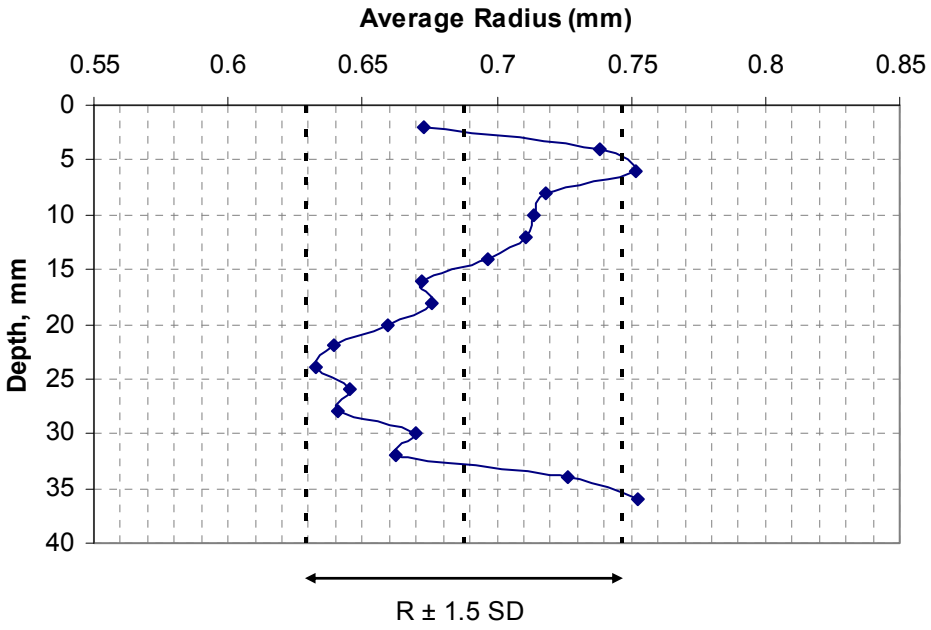

Figure B-16. Air Void Radius Distribution in Core ID: WP1; Highway: FM 529 and Location: Right Wheel Path.

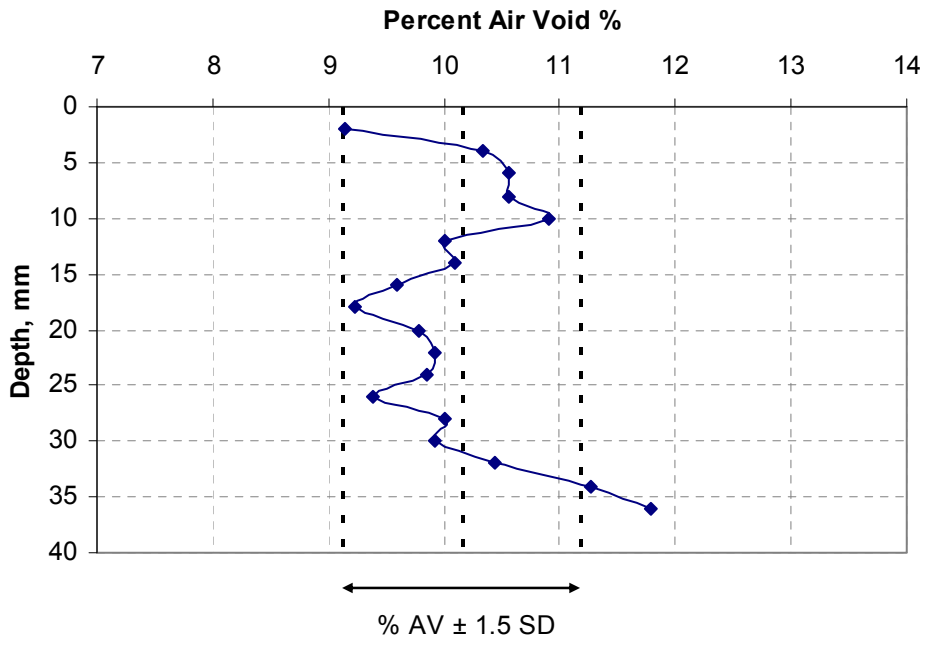

Figure B-17. Percent Air Voids Distribution in Core ID: WP2; Highway: FM 529 and Location: Left Wheel Path.

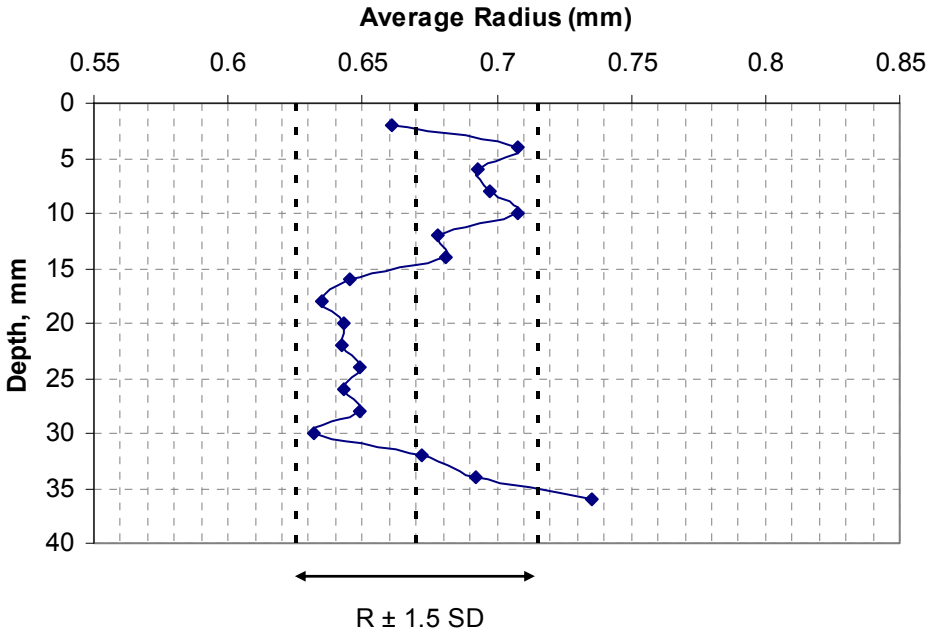

Figure B-18. Air Void Radius Distribution in Core ID: WP2; Highway: FM 529 and Location: Left Wheel Path.

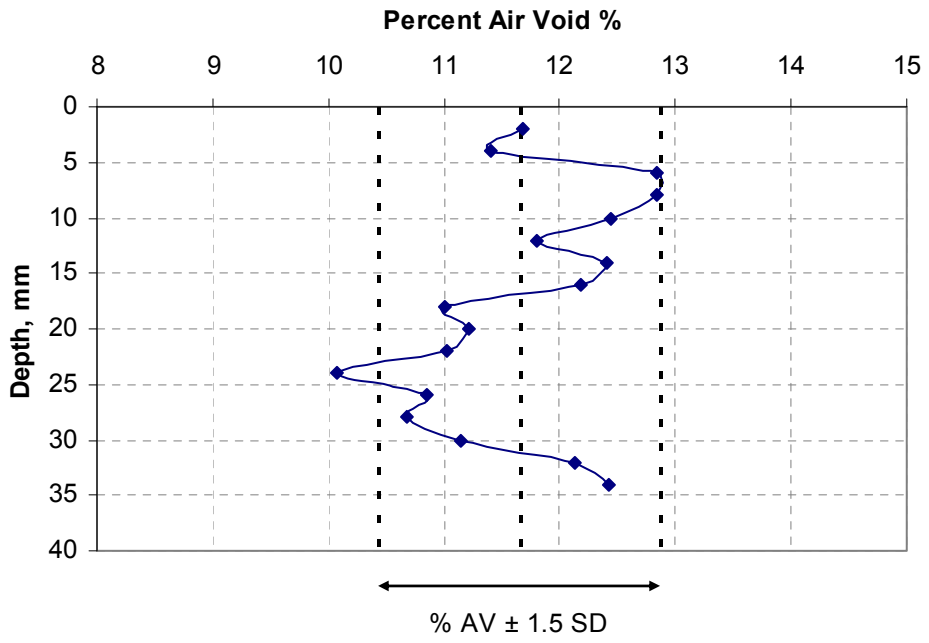

Figure B-19. Percent Air Voids Distribution in Core ID: LJ1; Highway: FM 529 and Location: Near Longitudinal Joint.

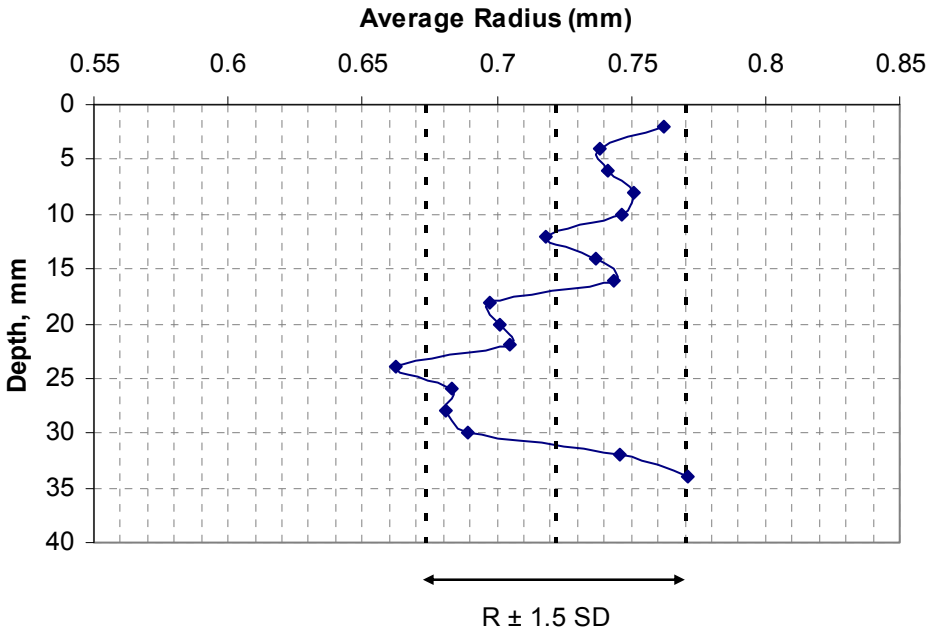

Figure B-20. Air Void Radius Distribution in Core ID: LJ1; Highway: FM 529 and Location: Near Longitudinal Joint.

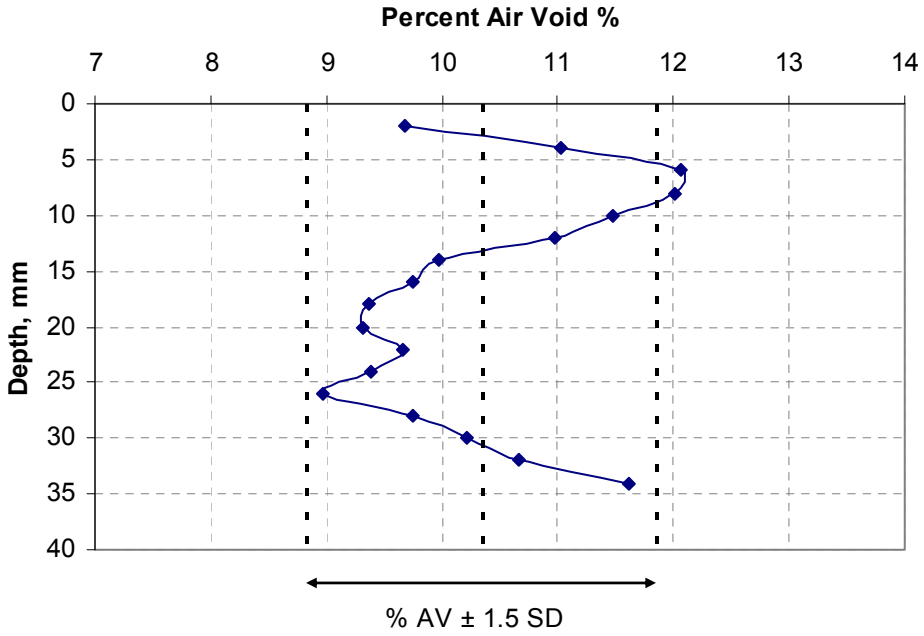

Figure B-21. Percent Air Voids Distribution in Core ID: BW1; Highway: FM 529 and Location: Center of the Lane.

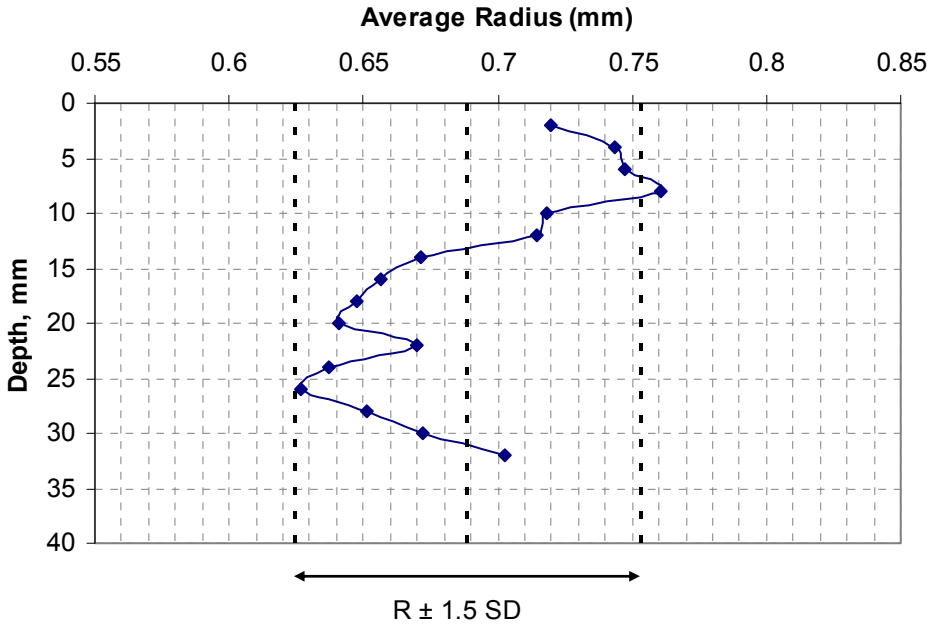

Figure B-22. Air Void Radius Distribution in Core ID: BW1; Highway: FM 529 and Location: Center of the Lane.

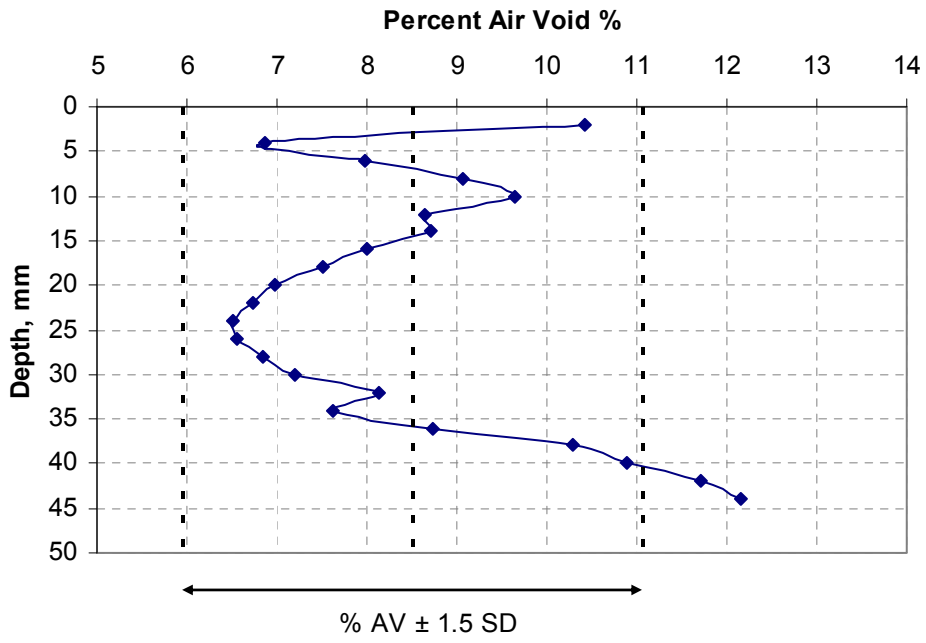

Figure B-23. Percent Air Voids Distribution in Core ID: 4; Highway: US 290 and Location: Right Wheel Path.

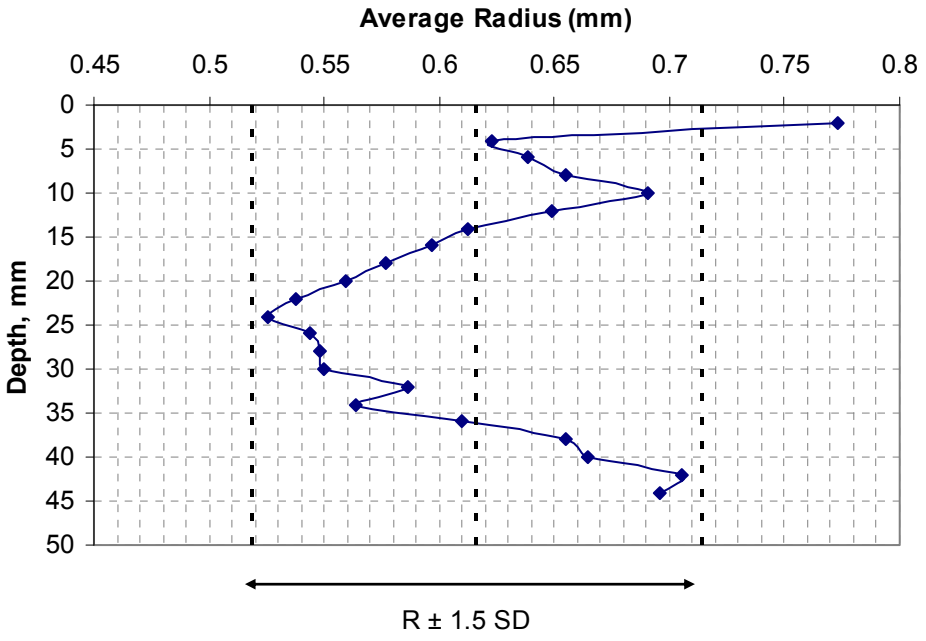

Figure B-24. Air Void Radius Distribution in Core ID: 4; Highway: US 290 and Location: Right Wheel Path.

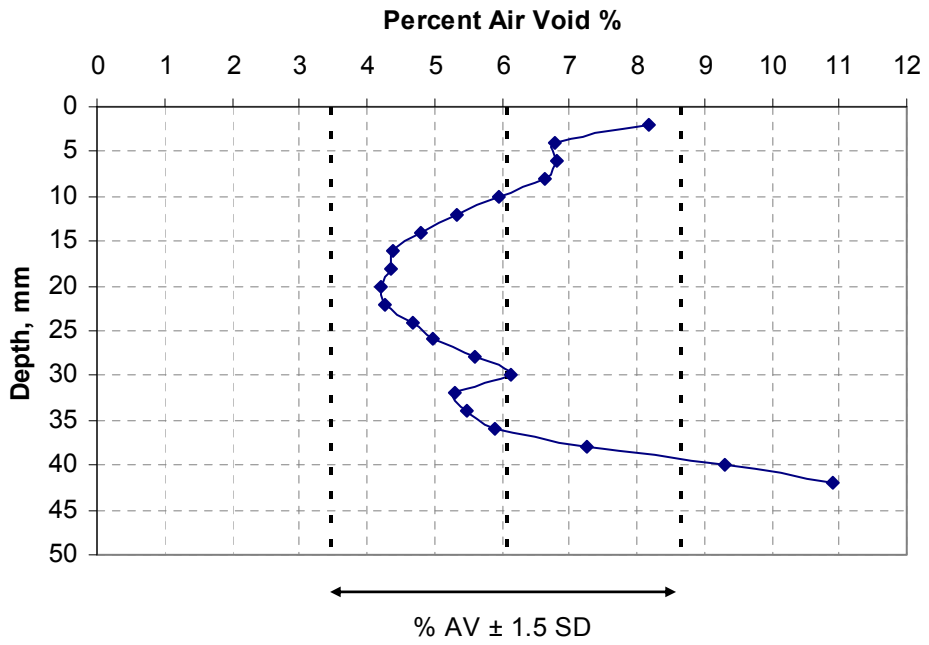

Figure B-25. Percent Air Voids Distribution in Core ID: 6; Highway: US 290 and Location: Between Wheel Paths.

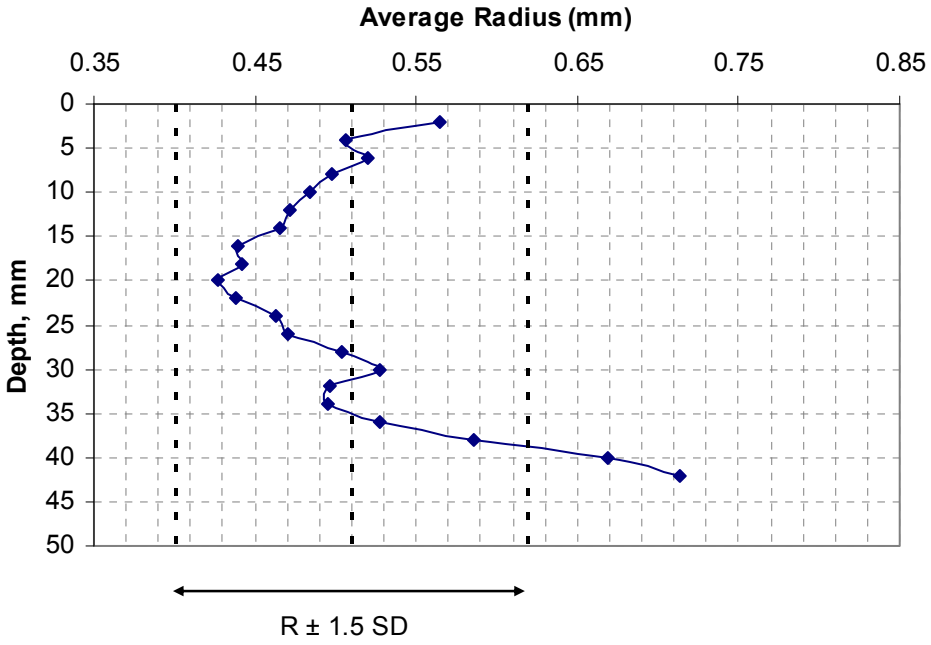

Figure B-26. Air Void Radius Distribution in Core ID: 6; Highway: US 290 and Location: Between Wheel Paths.

VITA

Name:

Emad Abdel-Rahman Kassem

Address:

Texas Transportation Institute
Texas A&M University System
3135 TAMU, College Station, Texas 77843

Email:

emad.kassem@gmail.com

Education:

Ph.D. in Civil Engineering, Texas A&M University, December 2008
M.S. in Civil Engineering, Texas A&M University, August 2005
B.S. in Civil Engineering, Zagazig University, Egypt, May 2001

Work History:

Graduate Research Assistant
Civil Engineering Department, Texas A&M University
College Station, Texas
May 2008 – December 2008

Graduate Teaching Assistant
Civil Engineering Department, Texas A&M University
College Station, Texas
January 2008 – May 2008

Graduate Research Assistant
Texas Transportation Institute, Texas A&M University
College Station, Texas
January 2004 – January 2008

Civil Engineer
Misr Consult (Environmental & Infrastructure Studies)
Cairo, Egypt
December 2002 – December 2003

Site Supervisor, Military Duty
Cairo, Egypt
October 2001 – November 2002